UNIVERSITY OF TRENTO - Italy
Department of Civil, Environmental
and Mechanical Engineering



Doctoral Programme in Civil, Environmental and Mechanical Engineering
Curriculum 3. Modelling and Simulation - 38th cycle 2022/2025

Doctoral Thesis – June 2026

Alessandro Lotti

Advancements in Satellite SAR Methods for Monitoring Civil Infrastructure

Supervisors
Prof. Daniele Zonta, University of Trento, Italy
Prof. Marco Broccardo, University of Trento, Italy

Credits of the cover image belong to the University of Trento.



Contents of this book are licensed under a Creative Common Attribution
Non Commercial – No Derivatives
4.0 International License, excepts for the parts already published by others publishers

University of Trento
Doctoral Programme in Civil, Environmental and Mechanical Engineering
http://web.unitn.it/en/dicam
Via Mesiano 77, I-38123 Trento
Tel. +39 0461 282670/2611 – *dicamphd@unitn.it*

From space, there are no borders – only pixels.

Buzz Aldrin

Acknowledgements

Before diving into the boring stuff, I would like to take a moment to thank all the people who made this achievement possible.

My first thanks goes to Prof. Daniele Zonta, my advisor, for guiding me with care throughout the PhD journey and for opening the door to such innovative research topics, which are first a great passion of mine.

Thanks to my colleagues and friends in Glasgow: Aleks, Prof. Carmine Clemente, and above all Prof. Enrico Tubaldi, who gave me a second home in a city I never imagined I could call one.

I would also like to thank the EO59 team for their valuable support throughout my research, in particular Alfredo and Daniele.

A special thanks goes to my friends at UniTN. Each of them should deserve a page of their own, but I hope you'll forgive me for not naming you one by one. I have never thought of you as mere colleagues, because to me you are truly friends. It is thanks to you and everything you have given to me that I have become the person I am today.

Thank you mom, dad, and Bea, for always standing by my side and for your unconditional love. I always took for granted what it means to have a family that loves you, but over these years I have truly come to understand its value.

Lastly, thank you Elena. This achievement is yours too, because you worked just as hard for it as I did. Thank you for being by my side every day, even when nothing seems to go right, and for giving me the strength to keep going.

Alessandro

Ringraziamenti

Prima di addentrarmi nelle cose noiose, vorrei prendermi un momento per ringraziare tutte le persone che hanno reso possibile questo traguardo.

Il primo grazie va al Prof. Daniele Zonta, mio advisor, per avermi guidato con attenzione durante il dottorato e per avermi aperto le porte a temi di ricerca così innovativi, che per me sono prima di tutto una grande passione.

Grazie ai colleghi e amici di Glasgow: Aleks, Prof. Carmine Clemente e soprattutto Prof. Enrico Tubaldi, che mi ha regalato una seconda casa in una città che non avrei mai immaginato di poter chiamare tale.

Un ringraziamento va anche al gruppo EO59 per il prezioso supporto alla mia ricerca, in particolare ad Alfredo e Daniele.

Un grazie speciale va agli amici di UniTN. Ognuno di loro meriterebbe una pagina intera, ma spero mi perdonerete se non vi nomino uno ad uno. Non vi ho mai considerati semplici colleghi, perché per me siete davvero degli amici. È grazie a voi e a tutto quello che mi avete dato che sono diventato la persona che sono oggi.

Grazie a mamma, papà e Bea, per essermi sempre stati accanto e per il vostro amore incondizionato. Ho sempre dato per scontato cosa significhi avere una famiglia che ti ama, ma in questi anni ne ho capito davvero il valore.

Infine, grazie ad Elena. Questo traguardo è anche tuo, perché te lo sei sudato tanto quanto me. Grazie per essere al mio fianco ogni giorno, anche quando nulla sembra andare per il verso giusto, e per darmi la forza di non mollare.

Alessandro

Abstract

Synthetic Aperture Radar (SAR) imaging enables large-scale, remote monitoring of civil infrastructure. SAR allows for monitoring without installation or maintenance, unlike traditional contact-type sensors. Whilst SAR interferometry (InSAR) is widely used for land monitoring, its application to bridge monitoring is still constrained by important limitations of the technique. Moreover, the use of SAR imagery for vibration-based structural health monitoring (VBSHM) remains largely unexplored in the current literature. This thesis investigates two complementary SAR-based approaches for bridge monitoring: spatio-temporal InSAR (ST-InSAR) for measuring long-term displacement and micro-Doppler SAR (MDSAR) for measuring structural vibrations.

The first part of the thesis discusses the issues of conventional InSAR for bridge applications, including phase ambiguity and the use of deformation models that do not accurately represent structural behaviour. These factors degrade temporal coherence and reduce the number of reliable measurement points on bridges. A new physics-based ST-InSAR framework is introduced that accounts for the spatial correlation of persistent scatterers (PSs) on the bridge within the InSAR processing pipeline, thereby resolving InSAR issues. By applying physical constraints obtained from feasible structural deformation fields, the interpretation of InSAR phase data is enhanced. ST-InSAR is then applied to the Colle Isarco viaduct case study, where PSs with near-zero temporal coherence achieve values of 0.70–0.80, and displacement errors are reduced to levels comparable to those of topographic surveying.

The second part of the thesis investigates vibration measurements from single-spaceborne SAR acquisitions, using MDSAR to estimate the line-of-sight (LOS) velocity time histories. On-site experiments on isolated targets demonstrate the successful measurement of controlled vibrations, even though they are affected by significant noise. The identification of dominant frequencies is successful for velocities as low as $1\ \mathrm{mm/s}$, and the accuracy of the frequency estimation depends solely on the SAR acquisition duration. Typically achievable resolutions are 0.03–$0.06\ \mathrm{Hz}$ for acquisition durations of 20–30 seconds. Experimental results obtained on a real bridge, specifically the South Portland Street suspension bridge, are consistent with those found in the isolated target tests. Dominant frequencies are identified for independent SAR acquisitions. However, full modal extraction, including mode shapes and damping ratios, is not currently achievable with available technology but is expected to become possible with future developments in satellite SAR systems.

Contents

Abbreviations and Notation **XIII**

1 Overview **1**
1.1 Civil infrastructure health worldwide . . . 1
1.1.1 Structural health monitoring of civil infrastructure . . . 2
1.2 Motivation . . . 3
1.2.1 The problem of SHM . . . 3
1.2.2 Spaceborne SAR monitoring . . . 4
1.2.3 Scientific gap . . . 5
1.3 Objectives of the thesis . . . 6
1.4 Publications . . . 6
1.5 Outline . . . 7
1.5.1 Chapters content . . . 8

I State of the Art **15**

2 Synthetic Aperture Radar **17**
2.1 SAR Technology . . . 17
2.2 SAR Acquisitions . . . 18
2.3 SAR Data . . . 21
2.4 SAR Image formation . . . 22
2.5 SAR Image Distortions . . . 24
2.6 Satellite SAR Missions . . . 25

3 Interferometric SAR for Bridge Monitoring **29**
3.1 Interferometry Principles . . . 29
3.2 Interferometric Phase modelling . . . 30
3.3 Interferogram generation . . . 31
3.4 Multi-Temporal InSAR . . . 32
Selection of Persistent Scatterer Candidate Points . . . 32
Temporal Coherence . . . 32
3.5 Challenges of InSAR for Bridge Monitoring . . . 33
3.5.1 Reconstruction of three-dimensional displacement . . . 33
3.5.2 Temporal Sampling . . . 33
3.5.3 Displacement ambiguity . . . 34
3.5.4 Displacement mismodelling . . . 34

3.6 Literature Gap 34
3.7 Motivation and Research Objectives 35

4 Micro-Doppler SAR for Bridge Monitoring 37
4.1 Micro-Doppler Principles 37
4.2 Vibrations and micro-Doppler 38
4.3 Sub-Pixel Offset Tracking Method 40
4.4 Challenges of MDSAR for Bridge Monitoring 41
4.4.1 Controlled experimental studies 42
4.4.2 Existing studies on real-world structures 42
4.5 Literature gap 42
4.6 Motivation and Research Objectives 43

II Publications 55

5 Spatio-temporal InSAR for bridge monitoring: integrating physics-based models with persistent scatterer interferometry 57
5.1 Introduction 58
5.1.1 Research Objectives 61
5.2 SAR Background 61
5.2.1 SAR Interferometry 62
5.2.2 Multi-Temporal InSAR and persistent scatterer interferometry 63
5.2.3 PSI limitations in bridge monitoring 65
5.3 Method 66
5.3.1 Structural Model 66
5.3.2 Integration of the structural model with the SAR Geometry 68
5.3.3 InSAR phase model with structural constraints 69
5.4 Case study 70
5.4.1 Colle Isarco Viaduct 70
5.4.2 PSI analysis of the viaduct 71
5.4.3 ST-InSAR analysis 74
Dataset 74
Structural Model 75
Parameters identification 77
5.4.4 Experimental comparison methodology 77
5.5 Results 78

5.5.1 Comparison of ST-InSAR and PSI with benchmark measurements . . . 78
5.5.2 Analysis of temporal coherence . . . 82
5.5.3 Temperature gradient estimation . . . 83
5.6 Discussion . . . 83
5.6.1 Why PSI fails at specific locations . . . 83
5.6.2 Why ST-InSAR performs well where PSI fails . . . 84
5.6.3 Metrological accuracy of ST-InSAR . . . 85
5.6.4 Using ST-InSAR to identify the thermal field . . . 86
5.6.5 Drawbacks of using ST-InSAR . . . 86
5.7 Conclusions . . . 88

6 Assessment of spaceborne SAR micro-motion measurement for vibration-based SHM 97
6.1 Introduction . . . 98
6.1.1 Remote sensing alternatives . . . 98
6.1.2 Motivation for SAR vibrometry . . . 99
6.1.3 Statement of novelty . . . 100
6.2 SAR background . . . 101
6.2.1 The micro-Doppler effect in SAR . . . 103
6.2.2 Micro-Doppler measurement from SAR . . . 104
Time-frequency analysis . . . 104
Phase domain . . . 105
Image domain . . . 106
6.3 SPOT METHOD . . . 107
6.3.1 Sub-aperture generation . . . 107
6.3.2 Motion tracking . . . 109
6.4 Experimental data and ground truth comparison . . . 110
6.4.1 Ground truth data . . . 110
Experiment locations . . . 110
Instrumentation . . . 111
Procedure . . . 111
6.4.2 SAR data . . . 113
6.4.3 Ground truth comparison . . . 113
Processing of ground truth . . . 113
Comparison metrics . . . 114
6.5 Results . . . 115
6.5.1 Single frequency . . . 117
Processing parameters . . . 117

Qualitative analysis . . . 117
Quantitative results . . . 118
6.5.2 Amplitude modulation . . . 118
Processing parameters . . . 118
Qualitative analysis . . . 121
Quantitative results . . . 122
6.5.3 Superposition and linear frequency modulation . . . 122
Processing parameters . . . 122
Qualitative analysis . . . 124
Quantitative results . . . 124
6.6 Discussion . . . 125
6.6.1 General measurement performance . . . 125
Effect of oscillation amplitude . . . 125
Effect of dominant frequency . . . 125
Effect of signal complexity . . . 126
Processing parameters . . . 126
6.6.2 Frequency measurement performance . . . 128
6.6.3 Suitability for SHM . . . 128
6.6.4 Future developments . . . 130
6.7 Conclusions . . . 131

7 Monitoring bridge vibrations via spaceborne SAR micro-Doppler 139
7.1 Introduction . . . 140
7.2 Materials and Methods . . . 145
7.2.1 Principles of SAR technology . . . 145
7.2.2 Micro-motion in SAR imagery . . . 148
7.2.3 Sub-Pixel Offset Tracking . . . 149
7.2.4 Case Study: South Portland St. suspension bridge . . . 152
7.2.5 Operational modal analysis . . . 155
7.2.6 SAR acquisitions and experimental validation . . . 160
SAR data . . . 160
Experimental comparison . . . 162
7.3 Results and discussion . . . 163
7.3.1 Acquisition 1 . . . 164
7.3.2 Acquisition 2 . . . 167
7.3.3 Discussion . . . 169
7.4 Conclusions . . . 173

III Summary, conclusions and future perspectives 183

8 Summary and discussion of research results 185

8.1 Research question 1:
Is it possible to overcome InSAR current limitations for bridge monitoring? . . . 187
8.1.1 Answer to question 1 . . . 187
8.1.2 Evaluation of ST-InSAR . . . 188
Quantity of Interest . . . 188
Direction of Measurement . . . 189
Accuracy . . . 189
Sampling frequency . . . 189
SAR acquisition compatibility . . . 189
Temporal coverage . . . 189
Summary table of metrological characteristics of ST-InSAR . . . 190

8.2 Research question 2:
Can MDSAR be used for vibration-based monitoring of bridges? 191
8.2.1 Answer to question 2 . . . 191
8.2.2 Evaluation of MDSAR . . . 193
Quantity of Interest . . . 193
Direction of Measurement . . . 193
Accuracy in the time domain . . . 193
Accuracy in the frequency domain . . . 193
Sampling frequency . . . 194
SAR acquisition compatibility . . . 195
SAR revisit time . . . 195
Temporal coverage . . . 195
Summary table of metrological characteristics of MDSAR 195

8.3 Are spaceborne SAR techniques ready to replace contact-based SHM? . . . 195
8.3.1 SAR and long-term displacement monitoring . . . 196
8.3.2 SAR and vibration-based monitoring . . . 196
Measuring the time history of vibration . . . 196
Extract natural frequencies . . . 196
Reconstruct mode shapes . . . 197

9 Conclusions and Future Works 199

9.1 Open challenges and future directions . . . 200

9.1.1 ST-InSAR 200
9.1.2 MDSAR 200

A Appendix **203**
A.1 Scopus search and queries 204
A.2 Publications list 205

List of abbreviations and notations

Abbreviations

AM	Amplitude Modulated
ASI	Amplitude Stability Index
CNR	National Research Council of Italy
CPHD	Complex Phase History Data
CPS	Candidate Persistent Scatterer
CR	Corner Reflector
DEM	Digital Elevation Model
DFT	Discrete Fourier Transform
DInSAR	Differential Interferogram
EM	Electromagnetic
FDD	Frequency Domain Decomposition
FEM	Finite Element Model
FFT	Fast Fourier Transform
FHWA	Federal Highway Administration
GB-PSO	Global Best PSO
HAF	High-order Ambiguity Functions
IFFT	Inverse Fast Fourier Transform
InSAR	SAR Interferometry
LEO	Low Earth Orbit
LiDAR	Light Detection and Ranging
LOS	Line of Sight
LTSHM	Long-term Structural Health Monitoring
LVDT	Linear Variable Differential Transformer
max	Maximum value
MDSAR	SAR micro-Doppler
MLE	Maximum Likelihood Estimation
MLC	Multi-Look Complex
MT-InSAR	Multi-Temporal InSAR
m-D	Micro Doppler
m-m	Micro-motion
NBIS	National Bridge Inspection Standards
PO	Polar Orbit
PPS	Polynomial Phase Function

PRF	Pulse Repetition Frequency
PS	Persistent Scatterer
PSI	Persistent Scatterer Interferometry
PSO	Particle Swarm Optimisation
QPS	Quasi-Persistent Scatterers
RAR	Real Aperture Radar
RCMC	Range Migration Cell Mitigation
RMS	Root Mean Square
RMSE	Root Mean Square Error
ROI	Region of Interest
SAR	Synthetic Aperture Radar
SBAS	Small Baseline Subset
SHM	Structural Health Monitoring
SICD	Sensor Independent Complex Data
SLC	Single-Look Complex
SNR	Signal-to-Noise Ratio
SP	State Parameters
SPOT	Sub-Pixel Offset Tracking
SSI	Stochastic Subspace Identification
SSO	Sun-Synchronised Orbit
STFT	Short-Time Fourier Transform
ST-InSAR	Spatio-Temporal InSAR
STSHM	Short-Term Structural Health Monitoring
StaMPS	Stanford Method for Persistent Scatterers
UAV	Uncrewed Aerial Vehicles
UNITN	University of Trento
USD	United States Dollar
UTC	Coordinated Universal Time
VBSHM	Vibration-Based Structural Health Monitoring
WVD	Wigner–Ville Distribution

Notations

x	Ground range direction
y	Azimuth direction
z	Vertical direction
r	Range (LOS) direction
d	Interferometric LOS displacement

β	Incidence angle
α	Azimuth angle
v_{s}	Satellite velocity
t_a	Acquisition duration
L	Synthetic aperture length
B	Signal Bandwidth
λ	Radar centre wavelength
c	Speed of light
Δr	Range resolution
Δy	Azimuth resolution
dt	Sampling interval
f_{s}	Sampling frequency
Δf	Frequency resolution
ρ	Pearson's correlation coefficient
ϵ_f	Frequency residual

SAR Interferometry

φ	Interferometric phase
d_{lim}	Displacement ambiguity
μ	Reflectivity variation
σ	Reflectivity standard deviation
φ_{atmo}	Atmospheric component
φ_{flat}	Flat terrain component
φ_{height}	Topographic component
φ_{disp}	LOS displacement component
φ_{noise}	Noise component
h_p	Residual height
$B_n^{(i)}$	Normal baseline
$d_p^{(i)}$	LOS differential displacement relative to pixel p
$\boldsymbol{u}_p^{(i)}$	Differential displacement vector
${}_t d_p$	Linear displacement rate
${}_T d_p$	Linear thermal expansion rate
$t^{(i)}$	Time interval (Temporal baseline)
$T_p^{(i)}$	Air temperature at instant i
$\Delta T^{(i)}$	Temperature gradient at instant i
$\mathcal{M}$	Structural model of the bridge
$\boldsymbol{\theta}$	State parameters vector
N	Number of state parameters
N_t	Number of time-varying state parameters

N_s	Number of space-varying state parameters
M	Number of acquisitions
P	Number of PSs on the bridge deck
j	Imaginary unit
γ_p	MT-InSAR objective function
Γ_p	ST-InSAR objective function
$\Delta\gamma_{p,t}$	Increase of temporal coherence

SAR micro-Doppler

f_D	Doppler frequency shift
v_r	Range (LOS) velocity
v_z	Vertical velocity
R	Slant-range distance
B_D	Full Doppler bandwidth
b_D	Partial Doppler bandwidth
t_{sap}	Sub-aperture duration
t_{ol}	Overlap duration
ξ	Aperture fraction
Ω	Overlap ratio
η	Observation ratio
T	Natural period of the oscillation
N	Number of sub-apertures
k_{grid}	Sub-aperture upsampling factor
k_{sinc}	Sinc-interpolation upsampling factor
W_r	Patch size along range direction
W_y	Patch size along azimuth direction

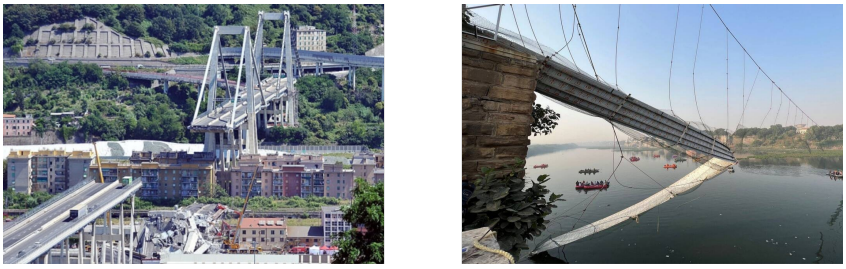
1. Overview

1.1 Civil infrastructure health worldwide

Bridges and viaducts are fundamental parts of civil infrastructure networks. Worldwide, many bridges and viaducts constructed in the mid-20th century are now reaching or exceeding their typical design service life of approximately 50 years [1]. Countries are, therefore, experiencing challenges related to maintenance and safety, making ageing infrastructure a serious concern [2]. In Italy, technical analyses conducted by the National Research Council of Italy (CNR) indicate that tens of thousands of bridges have exceeded their intended service life. Furthermore, studies report that more than 50% of Italian bridges are over 50 years old [3]. Likewise, this situation is witnessed across Europe. In France, as of 2018, 33% of the 12′000 state-managed bridges required repairs, while approximately 7% were so deteriorated that they posed a risk of collapse if not closed or rehabilitated [4]. In Germany, as of 2017, only 12.5% of highway bridges were rated in good condition, whereas a comparable proportion (12.4%) was rated in poor condition [4]. Moving to the United States, the 2025 ASCE Report Card states that approximately 45% of U.S. bridges are over 50 years old, and about one bridge out of fourteen is classified as being in poor condition [5]. As civil infrastructure exceeds its design life, a decline in structural health conditions increasingly follows. Although catastrophic bridge collapses are relatively rare, several failures in the past decade have raised public concern about the conditions of bridges [6]. The cases discussed below represent only a limited selection of such events.

In August 2018, the Morandi Bridge in Genoa (Italy, Figure 1.1(a)) collapsed suddenly, causing the death of 43 people [7]. In 2022, a 145-year-old suspension footbridge in Morbi (India, Figure 1.1(b)) collapsed under pedestrian loading, resulting in 135 fatalities [8]. Even in the U.S., a country with well-established inspection standards, bridge failures occur: for example, Pittsburgh's Fern Hollow Bridge (built in 1970) fell in early 2022 – fortunately with no fatalities. Reports further suggest that smaller-span bridge collapses, which typically result in less severe social and economic impacts – and therefore receive minimal media attention – are more frequent than perceived. In the United States, for instance, approximately 128 bridge collapses have been reported per year [9]. A common factor in many of these failures is the accumulation of years of undetected material and structural component deterioration.

These events reveal the need for the continuous monitoring of bridge con-



(a) **(b)**

Figure 1.1: (a) Morandi Bridge collapse, taken from [10]; (b) Morbi bridge collapse, taken from [11].

ditions to provide high safety standards and prevent failures that can lead to tragic social and economic consequences [12]. To achieve this goal, infrastructure managers must assess the structural reliability and health status of their bridge stock over time [13]. Periodic inspections have traditionally represented the main method of maintaining bridge safety [14, 15]. Most countries schedule periodic visual inspections of bridges – typically every 2 to 6 years for in-depth inspections – to look for cracks, corrosion, or other deterioration signs [16]. However, conventional inspections have several limitations: they are time-consuming, subject to operator judgment, and may miss hidden or rapidly developing issues between inspections [17]. In recent years, these issues have motivated a strong push toward complementing visual inspections with modern monitoring technologies.

1.1.1 Structural health monitoring of civil infrastructure

To overcome the limitations of visual inspections, Structural Health Monitoring (SHM) has established as an innovative tool for assessing and managing civil infrastructure [18]. SHM refers to the practice of employing sensors and data acquisition systems installed on structures to continuously – or periodically – measure physical quantities related to the structural response, such as displacements, strains, velocities, accelerations, or other environmental parameters [19].

SHM systems can be designed for [18, 19, 20, 21]:

- *Short-term monitoring* (STSHM): usually employed to support diagnostic investigations, model calibration, or load testing;
- *long-term monitoring* (LTSHM): aimed at providing the continuous investigation of critical infrastructures throughout their service life.

Among the various SHM approaches, vibration-based SHM (VBSHM) has received particular attention, as changes in modal properties (e.g., natural frequencies, mode shapes, and damping ratios) can deliver valuable information on the global structural condition [22].

Given the acknowledged potential of SHM, several countries have explicitly introduced monitoring technologies within their regulatory and management frameworks. In Italy, immediately after the collapse of the Morandi Bridge in Genoa, the government enacted the Decree-Law 109/2018 (the so-called "Genoa Decree"), which mandated the development of standardised national guidelines for risk classification, safety assessment, and monitoring of existing bridges and viaducts [23]. This regulatory framework formally introduced the role of monitoring technologies as a complement to traditional inspection procedures. In the U.S., the Federal Highway Administration (FHWA) continues to enforce strict inspection regimes through the National Bridge Inspection Standards (NBIS) [15]. The 2022 NBIS Final Rule further promotes a risk-based approach to bridge management and introduces procedures for the reporting and monitoring of critical findings, explicitly recognising the role of monitoring systems in supporting inspection activities and decision-making procedures.

1.2 Motivation

1.2.1 The problem of SHM

Whilst SHM has become an essential part of current bridge management systems, its large-scale implementation brings considerable practical challenges [24]. Even when the structures requiring monitoring are clearly identified, deploying and sustaining SHM systems at a network scale is limited by both economic and operational factors. In particular, the overall cost of SHM systems surpasses the sensing technology and includes [17, 19, 25, 26]:

- *Hardware and installation*: sensors, cabling, power, enclosures, access equipment, traffic management;
- *Connectivity and data*: fiber, gateways, cloud/on-prem storage, cybersecurity;
- *Processing operations*: calibration, sensor replacement, false alarms, software updates;
- *Human cost*: engineers who interpret data and inspectors who verify anomalies.

1.2.2 Spaceborne SAR monitoring

In this context, remote sensing techniques based on spaceborne Synthetic Aperture Radar (SAR) have developed as a promising complementary solution for large-scale bridge monitoring. In opposition to traditional contact-based SHM systems, SAR does not require sensor installation, on-site operators, or traffic disruptions and enables repeated observations of thousands of structures over wide areas from space [27]. Compared to classical optical satellite imagery, SAR offers several alternative advantages, including all-weather and day-night acquisition capability, as well as spatial resolutions on the order of meters or sub-meters [28]. Furthermore, by exploiting multi-temporal SAR acquisitions, it is possible to detect millimetric-scale displacements and long-term deformation trends [29, 30, 31, 32].

Owing to its unique features, SAR is especially suitable for large-scale monitoring and prioritisation rather than for detailed local diagnosis [27, 33]. Satellite-based monitoring can support infrastructure owners in identifying structures that may require closer inspection or permanent SHM deployment, consequently reducing the cost, time, and logistical limitations associated with contact-type instrumentation [34]. To summarise, spaceborne SAR is a scalable, non-intrusive tool that complements traditional inspection and monitoring strategies.

Though originally developed for land and environmental surveillance [35], SAR has attracted a growing interest in civil infrastructure monitoring applications. In the context of civil SHM, an analysis of the existing literature [27, 28, 30, 36, 37, 38, 39] identifies two main SAR-based techniques to retrieve long-term deformation and dynamics information of ground targets:

- *SAR interferometry* (InSAR), which exploits multiple images over the same target to measure long-term displacements;
- *SAR micro-Doppler* (MDSAR), which uses a single SAR acquisition, is used to estimate dynamic characteristics of targets, such as vibrations or velocities.

The growing relevance of satellite interferometric data for structural assessment has also been acknowledged at the national level. In Italy, the ReLUIS (*Rete dei Laboratori Universitari di Ingegneria Sismica e strutturale*) consortium has recently published dedicated guidelines for the use of InSAR data in the interpretation of the structural behavior of buildings [40], providing a reference framework that promotes the integration of satellite monitoring into engineering practice.

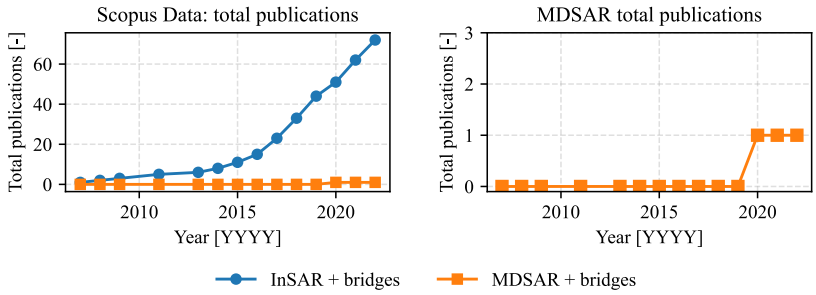


Figure 1.2: Total Scopus publications on InSAR and MDSAR bridge-based studies.

1.2.3 Scientific gap

Based on the discussion presented above, the application of spaceborne SAR is promising; however, existing SAR-based techniques for bridge monitoring remain a relatively recent and limited research topic. A bibliometric analysis performed using the Scopus database [41] indicates that, between 2015 and 2022, only 72 journal publications addressed the use of InSAR for bridge monitoring, whereas a single publication investigated the application of MDSAR to bridges (Figure 1.2). The analysis was intentionally limited to 2022, corresponding to the start of this PhD research, in order to define the state of the art at the time the research activities began. Additional details of the search strategy and queries are reported in Appendix A.1.

The number of InSAR-related publications demonstrates growing but limited academic interest. Nonetheless, the technique still suffers from a set of well-recognised limitations arising from the intrinsic interferometric nature of the measurement, which often undermine its adoption in engineering practice. Among these limitations, this thesis focuses on constraints related to the maximum measurable displacement and on the modelling assumptions required to retrieve displacement from SAR data, which will be discussed in detail in the following chapters. Therefore, a significant research effort is still required to improve the robustness, reliability, and operational applicability of InSAR for bridge-scale monitoring.

The research gap is more pronounced for MDSAR-based bridge monitoring. As of 2022, only a single study by Biondi et al. [39] had investigated the application of MDSAR to bridge structures. In this work, the authors examined several bridge case studies and identified anomalies in the structure vibrational behaviour from MDSAR measurements. This investigation clearly identified lo-

cations of cracks and expansion joints in the deck, which were validated by photographic documentation. However, no direct quantitative comparison between MDSAR vibrations and benchmark measurements was provided. Overall, the current literature lacks experimental confirmation, case studies, and rigorous metrological assessment of MDSAR for bridge monitoring. In particular, the accuracy, reliability, and practical feasibility of measuring structural vibrations from spaceborne SAR platforms remain largely unexplored.

1.3 Objectives of the thesis

Building on the scientific gaps identified in the previous section, this thesis studies the potential of spaceborne SAR for monitoring civil infrastructure, with particular emphasis on bridge applications. The main objective of the research is to address the following research questions:

1. Can InSAR be enhanced for bridge monitoring applications? In particular, is it possible to overcome the limitations that currently restrict its reliability and applicability in bridge structural health monitoring?
2. Can MDSAR be employed for VBSHM of bridges? Specifically, can satellite SAR sensors measure structural vibrations with sufficient accuracy, and can dynamic features, in terms of modal parameters, be extracted from spaceborne observations?

The answers to these research questions are discussed and supported through the experimental evidence presented throughout the thesis. The overall contribution of this work is to systematically assess the extent to which spaceborne SAR currently supports bridge monitoring and to identify the conditions under which it can be considered competitive with, or complementary to, traditional contact-based monitoring systems.

1.4 Publications

As a result of the work conducted during my PhD program, the following research products have been produced from the following research projects, funded by:

- the **ReLUIS Interuniversity Consortium** under the agreement *DPC-ReLUIS 2024-2026 WP 6 "Monitoring and satellite data"*, funded by the Italian Civil Protection Department;
- and the **European Space Agency** (ESA) under the project *Bridge Monitoring Based on Single Pass SAR Images*.

These research activities led to the production of the journal articles that constitute the core of this thesis and that are listed below. The complete list of journal and conference publications, including works not included in this thesis, is reported in Appendix A.2.

Journal Papers and Manuscripts

The following are the main journal papers produced. Papers J.1, J.2 and J.3 have been published in the journals *Structural Health Monitoring* (SAGE), *IEEE Access* (IEEE) and *Structural Control and Health Monitoring* (John Wiley & Sons), respectively.

(J.1) **Lotti, A.**, Zorzi, S., Tubaldi, E., Rocca, A., Perissin, D., Zonta, D. (2026). Spatio-temporal InSAR for bridge monitoring: integrating physics-based models with persistent scatterer interferometry, *Structural Health Monitoring*, https://doi.org/10.1177/14759217261453023.

(J.2) Vattulainen, A.B., **Lotti, A.**, Diaz Riofrio, S., Suppi, C., Tubaldi, E., Zonta, D., Milillo, P., Clemente, C. (2026). Assessment of spaceborne SAR micro-motion measurement for vibration-based SHM, *IEEE Access*, Volume: 14, https://doi.org/10.1109/ACCESS.2026.3652346.

(J.3) **Lotti, A.**, Vattulainen, A.B., Diaz Riofrio, S., Suppi, C., Tubaldi, E., Zonta, D., Milillo, P., Clemente, C. (2026). Monitoring bridge vibrations via spaceborne SAR micro-Doppler, *Structural Control and Health Monitoring*, https://doi.org/10.1155/stc/3858095.

1.5 Outline

This thesis is organised into three parts (I, II, and III) and nine chapters.

Part I, *State of the Art*, comprises three chapters that introduce the spaceborne SAR technology and review the state of the art in SAR imagery, Interferometric SAR, and micro-Doppler SAR, focusing on their working principles and current limitations for bridge monitoring.

Part II, *Publications*, consists of three chapters that constitute the core scientific contribution of this thesis. Each chapter corresponds to a post-print or pre-print of the selected authored publication.

Part III, *Summary, Conclusions and Future Perspectives*, summarises the results presented in Part II, discusses the overall achievement of this thesis, and includes future research directions.

1.5.1 Chapters content

More specifically, the content of each chapter is summarised as follows:

- **Chapter 2** introduces the SAR technology, its operating principles, the available sensor technologies, acquisition modes, and current satellite missions. The chapter also outlines the main steps of SAR data processing to generate focused SAR images.
- **Chapter 3** reports the fundamentals of SAR interferometry, with a particular emphasis on the modelling and the assumptions at the basis of persistent scatterer interferometry. The chapter ends by discussing the open challenges of applying InSAR to bridge monitoring and by linking these limitations to the research objectives of the thesis.
- **Chapter 4** describes the principles of micro-Doppler SAR, starting from the physical origin of the micro-Doppler effect and its appearance in SAR imagery. The chapter reviews existing applications of MDSAR applied to vibration monitoring, points out the main open challenges, and links them to the research objectives addressed in the following chapters.
- **Chapter 5** reports the pre-print of Paper (J.1), which proposes a novel spatio-temporal InSAR framework for bridge monitoring applied to persistent scatterer interferometry. The method integrates physics-based structural models into PSI to exploit spatial correlation among persistent scatterers. This approach tackles the main limitations of conventional PSI for civil infrastructure monitoring, including displacement ambiguity and weak correlation with air temperature.
- **Chapter 6** reports the post-print of Paper (J.2), which presents a comprehensive metrological assessment of MDSAR for vibration-based structural health monitoring. Using a processing strategy based on the subpixel offset tracking method, the study explores MDSAR capability to retrieve vibration time histories of isolated targets from SAR data. The validation is carried out using synchronous ground-based reference measurements. The accuracy, reliability, and limitations of the technique for measuring structural vibrations relevant to SHM are explored.
- **Chapter 7** reports the post-print of Paper (J.3), which demonstrates the application of spaceborne MDSAR for measuring the vibrations of the South Portland St. Suspension bridge. The chapter presents measurements of the line of sight velocity time histories of the bridge deck, validated against synchronous ground-truth data. The results show that MDSAR can reliably capture dominant vibration frequencies from independent satellite acquisitions, while still presenting important limitations

on measuring the true vibration time histories. The chapter concludes by discussing whether this technique can currently be used to retrieve modal parameters of civil infrastructure.

- **Chapter 8** provides a summary and discussion of the research results. The main research questions posed at the beginning of the thesis are addressed based on the experimental evidence presented throughout the work. The chapter also discusses the metrological characteristics of the proposed methods and outlines some practical guidelines for bridge monitoring using spaceborne SAR. Finally, the chapter clarifies current capabilities and limitations of the technology.
- **Chapter 9** presents the overall conclusions of this thesis to the field of spaceborne SAR for infrastructure monitoring. The chapter also describes possible future research directions and technological developments.

Bibliography

[1] International Organization for Standardization, *Buildings and constructed assets – Service life planning – Part 1: General principles and framework*, International Organization for Standardization Std. ISO 15 686-1:2011, 2011. [Online]. Available: https://store.uni.com/en/iso-15686-1-2011

[2] D. M. Frangopol and Y. Tsompanakis, *Maintenance and safety of aging infrastructure*. CRC press Boca Raton, FL, USA:, 2014, vol. 10.

[3] A. Occhiuzzi, "Autostrade, ecco lo stato di salute dei viadotti. L'analisi di Occhiuzzi (Cnr)," Nov. 2019, accessed: 2025. [Online]. Available: https://www.startmag.it/smartcity/autostrade-ecco-lo-stato-di-salute-dei-viadotti-lanalisi-di-occhiuzzi-cnr/

[4] T. Guardian, "Bridges across europe are in a dangerous state, warn experts," Aug. 2018, accessed: 2025. [Online]. Available: https://www.theguardian.com/world/2018/aug/16/bridges-across-europe-are-in-a-dangerous-state-warn-experts

[5] American Society of Civil Engineers, "2025 infrastructure report card," Reston, VA, USA, 2025, accessed: 2025. [Online]. Available: https://infrastructurereportcard.org

[6] T. N. Bittencourt, D. Frangopol, and A. Beck, *Maintenance, monitoring, safety, risk and resilience of bridges and bridge networks*. CRC Press, 2016.

[7] Ministero delle Infrastrutture e dei Trasporti, "Relazione della commissione ispettiva sul crollo del viadotto polcevera (ponte morandi)," Ministero delle Infrastrutture e dei Trasporti, Rome, Italy, Tech. Rep., 2019.

[8] BBC News, "Morbi bridge collapse: A death trap for indian children," 2022, accessed: February 2026. [Online]. Available: https://www.bbc.com/news/world-asia-india-63496684

[9] North Carolina Department of Transportation, "Bridge failure rates, consequences, and predictive trends," North Carolina Department of Transportation, Raleigh, NC, USA, Tech. Rep., 2020, accessed: 2025. [Online]. Available: https://connect.ncdot.gov/resources/LBIP2026-I95US301/Documents/Bridge%20Failure%20Rates%20Consequences%20and%20Predictive%20Trends.pdf

[10] C. N. dei Geologi, "1° anniversario crollo ponte Morandi, geologi: criticità innanzitutto idrogeologica," Aug. 2019, accessed: 2025. [Online]. Available: https://www.cngeologi.it/2019/08/13/1-anniversario-crollo-ponte-morandi-geologi-criticita-innanzitutto-idrogeologica/

[11] S. Fatma, "Morbi Bridge Collapse: The Apparent Concession Dysfunctionality," Dec. 2022, accessed: 2025. [Online]. Available: https://ijpiel.com/index.php/2022/12/30/morbi-bridge-collapse-the-apparent-concession-dysfunctionality/

[12] H. Wenzel, R. Veit-Egerer, M. Widmann, U. Santa, and C. Costa, "Colle Isarco Viaduct – Dynamic bridge behaviour based on periodic and permanent monitoring with BRIMOS®," in *Experimental Vibration Analysis for Civil Engineering Structures*, Oct. 2009.

[13] M. F. Bado, D. Tonelli, F. Poli, D. Zonta, and J. R. Casas, "Digital Twin for Civil Engineering Systems: An Exploratory Review for Distributed Sensing Updating," *Sensors*, vol. 22, no. 9, p. 3168, Apr. 2022. [Online]. Available: https://www.mdpi.com/1424-8220/22/9/3168

[14] European Commission, "Bridge management in europe," Publications Office of the European Union, Luxembourg, Tech. Rep., 2018.

[15] F. H. Administration, "Bridge Inspection - Safety Inspection - Bridges & Structures." [Online]. Available: https://www.fhwa.dot.gov/bridge/inspection/

[16] A. M. Abdallah, R. A. Atadero, and M. E. Ozbek, "A State-of-the-Art Review of Bridge Inspection Planning: Current Situation and Future Needs," *Journal of Bridge Engineering*, vol. 27, no. 2, p. 03121001, Feb. 2022, publisher: American Society of Civil Engineers. [Online]. Available: https://ascelibrary.org/doi/10.1061/%28ASCE%29BE.1943-5592.0001812

[17] D. M. Frangopol and M. Soliman, "Life-cycle of structural systems: recent achievements and future directions," *Structure and Infrastructure Engineering*, vol. 12, no. 1, pp. 1–20, 2016. [Online]. Available: https://doi.org/10.1080/15732479.2014.999794

[18] C. R. Farrar and K. Worden, "An introduction to structural health monitoring," *Philosophical Transactions of the Royal Society A: Mathematical, Physical and Engineering Sciences*, vol. 365, no. 1851, pp. 303–315, Feb. 2007. [Online]. Available: https://doi.org/10.1098/rsta.2006.1928

[19] J. Brownjohn, "Structural health monitoring of civil infrastructure," *Philosophical Transactions of the Royal Society A: Mathematical, Physical and Engineering Sciences*, vol. 365, no. 1851, pp. 589–622, 2 2007. [Online]. Available: https://royalsocietypublishing.org/doi/10.1098/rsta.2006.1925

[20] H. Sohn, C. R. Farrar, F. M. Hemez, D. D. Shunk, D. W. Stinemates, B. R. Nadler, and J. J. Czarnecki, "A review of structural health monitoring literature: 1996–2001," *Los Alamos National Laboratory, USA*, vol. 1, no. 16, pp. 10–12 989, 2003.

[21] V. R. Gharehbaghi, E. Noroozinejad Farsangi, M. Noori *et al.*, "A critical review on structural health monitoring: Definitions, methods, and perspectives," *Archives of Computational Methods in Engineering*, vol. 29, pp. 2209–2235, 2022. [Online]. Available: https://doi.org/10.1007/s11831-021-09665-9

[22] Wei Fan and Pizhong Qiao, "Vibration-based Damage Identification Methods: A Review and Comparative Study," *Structural Health Monitoring*, vol. 10, no. 1, pp. 83–111, Jan. 2011. [Online]. Available: https://journals.sagepub.com/doi/10.1177/1475921710365419

[23] Repubblica Italiana, "Decreto-legge 28 settembre 2018, n. 109, convertito con modificazioni dalla legge 16 novembre 2018, n. 130," Gazzetta Uffi-

ciale della Repubblica Italiana, 2018, disposizioni urgenti per la sicurezza delle infrastrutture e dei trasporti, a seguito del crollo del ponte Morandi.

[24] M. AlHamaydeh and N. G. Aswad, "Structural health monitoring techniques and technologies for large-scale structures: Challenges, limitations, and recommendations," *Practice Periodical on Structural Design and Construction*, vol. 27, no. 3, p. 03122004, 2022. [Online]. Available: https://doi.org/10.1061/(ASCE)SC.1943-5576.0000703

[25] C. R. Farrar and K. Worden, *Structural health monitoring: a machine learning perspective*. John Wiley & Sons, 2012. [Online]. Available: https://onlinelibrary.wiley.com/doi/book/10.1002/9781118443118

[26] M. Torti, I. Venanzi, S. Laflamme, and F. Ubertini, "Life-cycle management cost analysis of transportation bridges equipped with seismic structural health monitoring systems," *Structural Health Monitoring*, vol. 21, no. 1, pp. 100–117, 2021.

[27] M. Crosetto, O. Monserrat, M. Cuevas-González, N. Devanthéry, and B. Crippa, "Persistent Scatterer Interferometry: A review," *ISPRS Journal of Photogrammetry and Remote Sensing*, vol. 115, pp. 78–89, May 2016. [Online]. Available: https://www.sciencedirect.com/science/article/pii/S0924271615002415

[28] A. Ferretti, *Satellite InSAR Data: Reservoir Monitoring from Space*, ser. Education Tour Series. DB Houten: EAGE, 2014, no. 9.

[29] A. Ferretti, C. Prati, and F. Rocca, "Permanent scatterers in SAR interferometry," *IEEE Trans. Geosci. Remote Sensing*, vol. 39, no. 1, pp. 8–20, Jan. 2001. [Online]. Available: http://ieeexplore.ieee.org/document/898661/

[30] D. Perissin, "Interferometric SAR Multitemporal Processing: Techniques and Applications," in *Multitemporal Remote Sensing*, Y. Ban, Ed. Cham: Springer International Publishing, 2016, vol. 20, pp. 145–176, series Title: Remote Sensing and Digital Image Processing. [Online]. Available: https://link.springer.com/chapter/10.1007/978-3-319-47037-5_8

[31] D. Tonelli, A. Valentini, A. Rocca, S. Zorzi, A. Lotti, and D. Zonta, "Uncertainty quantification of satellite InSAR-monitoring of bridges: a case study," *ce/papers*, vol. 6, no. 5, pp. 900–906, 9 2023. [Online]. Available: https://onlinelibrary.wiley.com/doi/10.1002/cepa.1991

[32] D. Tonelli, M. Zini, L. Simeoni, A. Rocca, D. Perissin, and D. Zonta, "Integrating satellite insar and topographic data for long-term displacement monitoring of bridge crossing slow-moving landslides," *Structural Control and Health Monitoring*, vol. 2025, no. 1, p. 2106133, 2025. [Online]. Available: https://onlinelibrary.wiley.com/doi/abs/10.1155/stc/2106133

[33] D. Cusson, K. Trischuk, D. Hébert, G. Hewus, M. Gara, and P. Ghuman, "Satellite-Based InSAR Monitoring of Highway Bridges: Validation Case Study on the North Channel Bridge in Ontario, Canada," *Transportation Research Record*, vol. 2672, no. 45, pp. 76–86, Dec. 2018, publisher: SAGE Publications Inc. [Online]. Available: https://doi.org/10.1177/0361198118795013

[34] V. Macchiarulo, P. Milillo, C. Blenkinsopp, C. Reale, and G. Giardina, "Multi-temporal InSAR for transport infrastructure monitoring: recent trends and challenges," *Proceedings of the Institution of Civil Engineers - Bridge Engineering*, vol. 176, no. 2, pp. 92–117, Dec. 2021. [Online]. Available: https://doi.org/10.1680/jbren.21.00039

[35] J. C. Curlander and R. N. McDonough, *Synthetic aperture radar*. Wiley, New York, 1991, vol. 11.

[36] V. Macchiarulo, P. Milillo, M. J. DeJong, J. González Martí, J. Sánchez, and G. Giardina, "Integrated InSAR monitoring and structural assessment of tunnelling-induced building deformations," *Structural Contr & Hlth*, vol. 28, no. 9, Sep. 2021. [Online]. Available: https://onlinelibrary.wiley.com/doi/10.1002/stc.2781

[37] V. C. Chen, *The Micro-Doppler Effect in Radar*, 2nd ed. Artech house, 2019, accessed: 2025.

[38] F. C. Ponzo, C. Iacovino, R. Ditommaso, M. Bonano, R. Lanari, F. Soldovieri, V. Cuomo, F. Bozzano, P. Ciampi, and M. Rompato, "Transport infrastructure shm using integrated sar data and on-site vibrational acquisitions: "ponte della musica–armando trovajoli" case study," *Applied Sciences*, vol. 11, no. 14, 2021. [Online]. Available: https://www.mdpi.com/2076-3417/11/14/6504

[39] F. Biondi, P. Addabbo, C. Clemente, S. L. Ullo, and D. Orlando, "Monitoring of Critical Infrastructures by Micromotion Estimation: The Mosul Dam Destabilization," *IEEE Journal of Selected Topics in Applied*

Earth Observations and Remote Sensing, vol. 13, pp. 6337–6351, 2020. [Online]. Available: https://ieeexplore.ieee.org/document/9224142/

[40] A. Prota, M. Savoia, and F. C. Ponzo, *Linee guida per l'utilizzo dei dati interferometrici satellitari ai fini dell'interpretazione del comportamento strutturale delle costruzioni*. IT: Doppiavoce, 2025. [Online]. Available: https://doi.org/10.57580/RELUIS.LGDS

[41] Elsevier, "Scopus database," https://www.scopus.com, 2024, accessed November 2025.

Part I

State of the Art

2. Synthetic Aperture Radar

This state-of-the-art part of the thesis delivers a comprehensive overview of SAR principles and technologies, as well as current InSAR and MDSAR practices relevant to bridge monitoring applications.

As this thesis is structured as a thesis by publications, Chapters 5, 6, and 7 correspond to independent journal articles, each including a summarised introduction and a literature review. Consequently, partial overlap with this part is intentional. Readers who have already consulted this overview may choose to skim the introductory sections of those chapters.

2.1 SAR Technology

A radar is a remote sensing technology that operates by transmitting electromagnetic (EM) waves and recording the backscattered (i.e., reflected) signal from targets [1]. Conventional real-aperture radars (RAR) are characterised by an azimuthal resolution that is directly dependent on the physical length of the antenna, thereby limiting the achievable spatial resolution. To overcome this limitation, SAR technology exploits relative motion between the sensor and the target and combines echoes collected along the sensor trajectory [2]. As a result, SAR synthesises a larger antenna, hence the name *synthetic aperture*. This allows the sensor to achieve fine spatial resolution in the *azimuth* (i.e., along-track) direction, in addition to the *range* (i.e., sensor-to-target) direction. SAR systems can be deployed on different platforms, including ground-based installations, airborne sensors, and satellites [3]. In this thesis, the focus is exclusively on satellite-based systems; therefore, the term SAR is hereafter used to refer specifically to *spaceborne synthetic aperture radar*.

Compared to optical remote sensing systems, SAR sensors exhibit significant differences [4]. First, optical sensors are passive, as they record radiation emitted by another source (e.g., the Sun or artificial light) that is reflected by the object. In contrast, SAR sensors are active systems, meaning that they emit microwave radiation and measure the portion of the signal reflected by an object. Consequently, these sensors can operate both during the day and at night, without depending on sunlight or certain weather conditions.

Another important difference is the operating wavelength. Optical sensors typically operate in the visible and near-infrared portions of the electromagnetic spectrum, with wavelengths ranging from $0.3\ \mu\mathrm{m}$ to $0.7\ \mu\mathrm{m}$. Radar sensors, on the other hand, transmit and receive signals in the microwave domain, with

wavelengths typically in the centimetre range. These longer wavelengths allow microwave signals to penetrate clouds, fog, and precipitation, making SAR particularly well-suited for all-weather and continuous monitoring applications [5].

2.2 SAR Acquisitions

A SAR system can determine the distance and/or speed of a target by transmitting and receiving electromagnetic waves at regular time intervals [1]. This is achieved by measuring the time elapsed (or by calculating the phase and frequency differences) between the transmitted and backscattered signals [6]. The images acquired by a SAR sensor are two-dimensional and can be represented as complex-valued matrices. Rows and columns of these matrices are associated with the two main directions of the satellite geometry [5]:

1. *Azimuth direction* (y): Corresponding to the satellite motion path.
2. *Range direction* (r): corresponding to the radial direction, sensor to target and defined by the line of sight (LOS) of the satellite (as illustrated in Figure 2.1).

The ground projection of the LOS is called *ground range* (x). The Nadir represents the vertical line (z) connecting the satellite to the Earth's centre, and the incidence angle (β) is defined as the angle between the LOS and the local vertical direction at the target location. This angle typically ranges from $10°$ to $50°$. As shown in Figure 2.1, the satellite moves along its orbit with a velocity v_s, generating a synthetic antenna of length L [5].

SAR sensors can operate in several acquisition modes, most notably *ScanSAR*, *Stripmap*, and *Spotlight*, which can provide different trade-offs between spatial resolution and ground coverage [8]:

(a) *ScanSAR*: used when wider coverage is needed. In this mode, the radar sequentially switches between different elevation angles, covering multiple sub-swaths, as shown in Figure 2.2(a).

(b) *Stripmap*: the basic mode in which the radar remains fixed on a single strip (swath), capturing a continuous image along a line as illustrated in Figure 2.2(b).

(c) *Spotlight*: designed for finer resolution. In this case, the radar is focused on a fixed area on the ground, exploiting a longer aperture time (see Figure 2.2(c)).

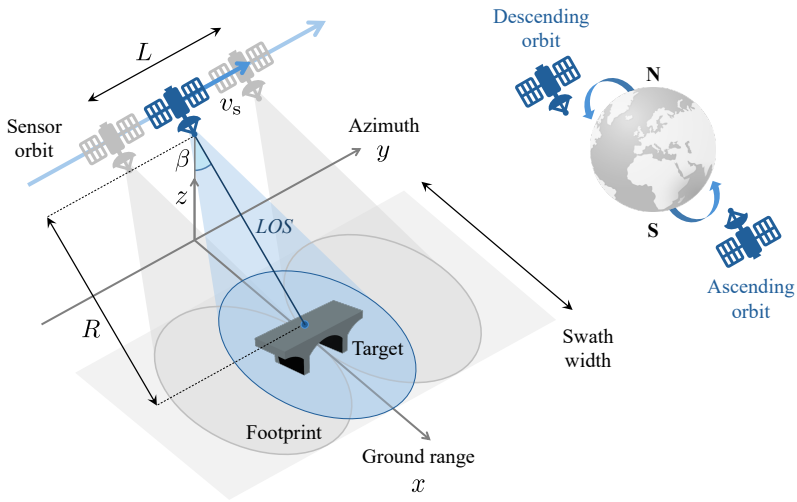


Figure 2.1: Typical stripmap acquisition geometry of a satellite-based SAR, adapted from [7]

In addition to the acquisition mode, SAR observation characteristics are influenced by the satellite orbit. This parameter determines key quantities, including revisit time, viewing geometry, and global coverage. Common orbital configurations adopted by spaceborne SAR missions are [9]:

- *Low Earth Orbit* (LEO): Satellites operate at an altitude of 600-700 km, travelling at a speed of 7.5 $\mathrm{km/s}$, completing an orbit around the Earth in about 90 minutes.
- *Polar Orbit* (PO): The satellite alternates its movement from south to north and vice versa, while the Earth rotates on its axis, allowing global coverage. Each area is acquired in both ascending orbit (south to north) and descending orbit (north to south).
- *Sun-Synchronised Orbit* (SSO): This specific polar orbit allows the satellite to observe the same Earth's location at the same time daily, minimising the effects of daily thermal variations.

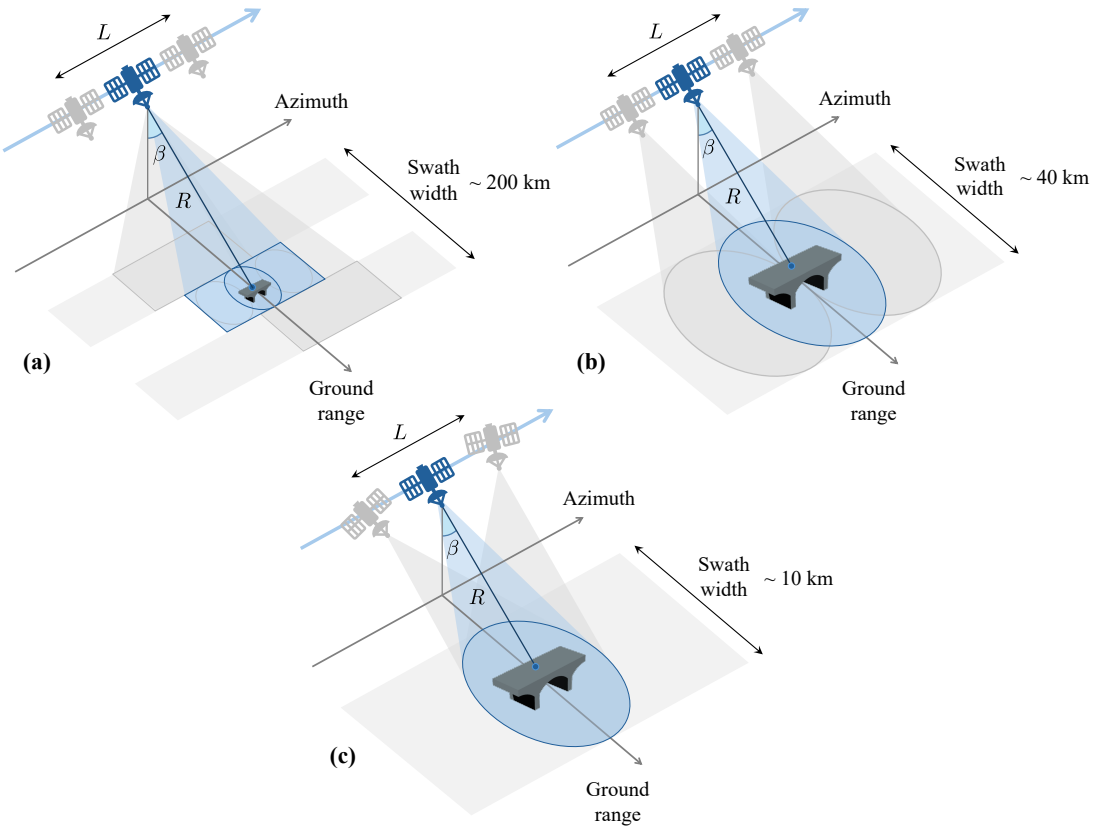


Figure 2.2: SAR acquisition modes: (a) ScanSAR, (b) Stripmap, (c) Spotlight

2.3 SAR Data

A SAR image effectively appears as a matrix of complex-valued numbers, in which each pixel contains [5]:

- A *magnitude*, representing the intensity of the backscattered signal.
- A *phase*, representing the delay of the recorded backscatter relative to the transmitted signal.

From these components, two main products can be derived [5], which are also illustrated in Figure 2.3:

- *Reflectivity map*: derived from signal intensity, representing an object's ability to reflect radar waves.
- *Phase map*: derived from the phase component, containing information on the relative distance and position of objects with respect to the SAR sensor.

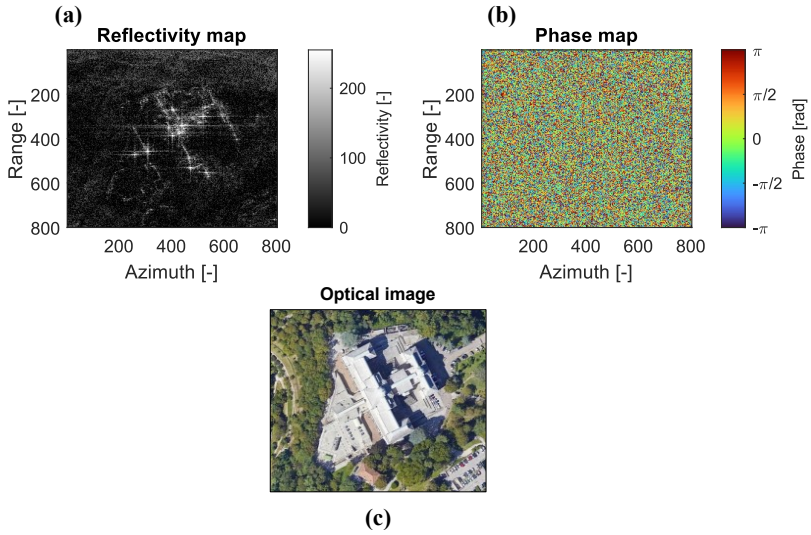


Figure 2.3: Reflectivity map (a), phase map (b), and optical image (c) of the DICAM building in Mesiano, University of Trento.

Optical images may appear more intuitive than radar images due to their often finer resolution, natural colour representation, and absence of noise. However, they do not directly provide information on the distance or velocity of ground targets. Reflectivity is typically high for metallic objects and structures with sharp geometries, as shown in Figure 2.3(a). The phase measured from a single SAR acquisition, although highly sensitive to small variations in dis-

tance, often appears noisy and difficult to interpret (Figure 2.3(b)). However, by comparing multiple SAR acquisitions using interferometric techniques, it is possible to exploit phase information to analyse temporal variations in distance.

The size, in metres, of each cell in both directions represents the azimuth and range resolution of the SAR image. SAR image resolution is crucial, as it determines the level of detail of the observable Earth's surface; finer resolution enables more precise observations. The range resolution is determined by Equation 2.1 [5]:

$$\Delta r = \frac{c}{2B} \tag{2.1}$$

where B is the signal bandwidth, and c is the speed of light. From the relationship, it follows that higher bandwidth improves radar resolution. For stripmap acquisition mode, azimuth resolution is given by the following relationship [5]:

$$\Delta y = \frac{L}{2} \tag{2.2}$$

where L is the synthetic antenna length. A smaller antenna yields a better azimuth resolution. However, real systems are subjected to noise, and the antenna design must account for the signal-to-noise ratio (SNR). An antenna that is too small would fail to illuminate ground targets with sufficient energy. Therefore, for a given maximum peak power and minimum SNR, the radar antenna must have a minimum size [5].

Azimuth resolution can be further improved by employing the spotlight acquisition mode, which extends the duration of target illumination. When combined with appropriate focusing algorithms, this approach enhances resolution by maximising the acquisition time for a given target. For spotlight mode, under small angles approximation, the azimuth resolution is given by [10]:

$$\Delta y = \frac{\lambda\, R}{2\, v_{\mathrm{s}}\, t_{\mathrm{a}}} \tag{2.3}$$

where λ is the radar centre wavelength, and t_{a} is the SAR acquisition – or collection – duration (i.e., how long the target remains illuminated by the radar beam).

2.4 SAR Image formation

The SAR image, in the form of a complex-valued matrix, is the final product of the elaboration of a sequence of radar pulses transmitted and received throughout the entire acquisition.

Depending on the level of processing applied to the raw data, SAR prod-

ucts can be provided in different formats, the most common of which are summarised below [11, 12, 13]:

- *Complex Phase History Data* (CPHD): the lowest-level data product, contains raw radar pulses collected over the entire acquisition time (t_a). These datasets are characterised by very large file sizes.
- *Single-Look Complex* (SLC): focused SAR image represented as a complex-valued matrix (magnitude and phase), generated from raw data using a single, unaveraged look over the full acquisition time (t_a). This product preserves the full spatial resolution and typically has a medium file size.
- *Multi-Look Complex* (MLC): a focused SAR image obtained by averaging multiple independent looks – of shorter duration – throughout the acquisition time. While this process reduces noise, it also degrades azimuth resolution. File sizes are generally smaller than those of SLC products.
- *Geocoded products* (e.g., GIS- or Google Earth–compatible formats): focused SAR images projected onto the ground-range-azimuth plane and orthorectified. These products have the smallest file size but do not contain the original complex phase information.

For SAR data focusing, several image formation algorithms have been developed. A comprehensive review of SAR image formation techniques is provided in [14]. Here, a representative example of stripmap SAR image formation using the *range-Doppler algorithm* is briefly described. A practical implementation of this approach is also available as a tutorial in [15]. Figure 2.4 illustrates the principal processing steps involved in SAR image formation for two representative point targets located at the same azimuth position.

The main steps are summarised as follows [16]:

1. *Raw SAR data acquisition*: the radar collects the backscattered signals as a function of range (fast time) and azimuth (slow time) (Figure 2.4(b)).

2. *Range compression*: each received pulse is compressed in the range direction using a matched filtering – typically cross-correlation – between the transmitted and received signals (Figure 2.4(c)).

3. *Range cell migration correction*: as the radar platform moves, the slant range to a target varies. This effect is compensated by applying range cell migration correction (RCMC), after which data are further processed in azimuth to produce the final focused image (Figure 2.4(d)).

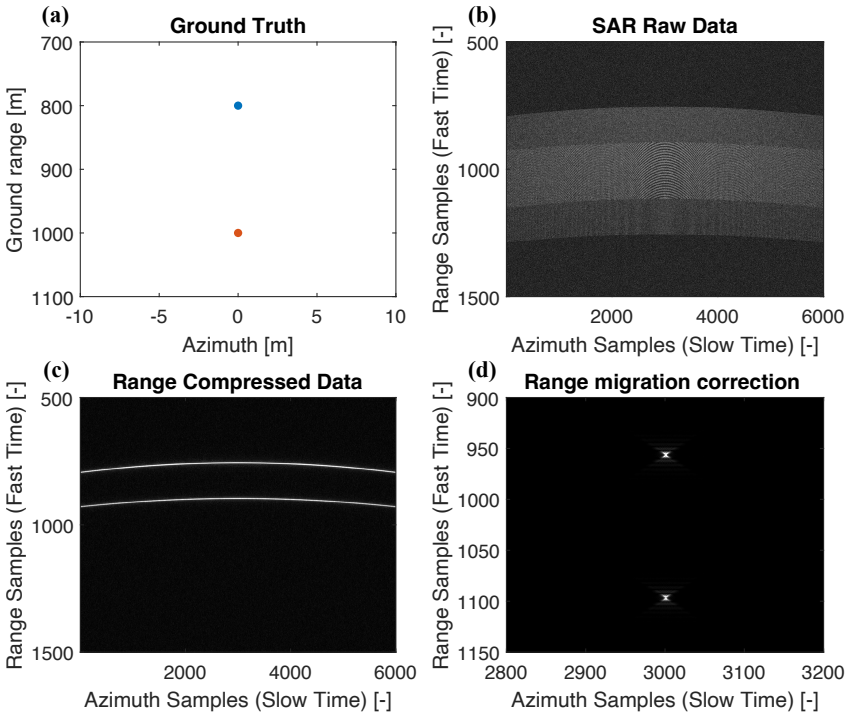


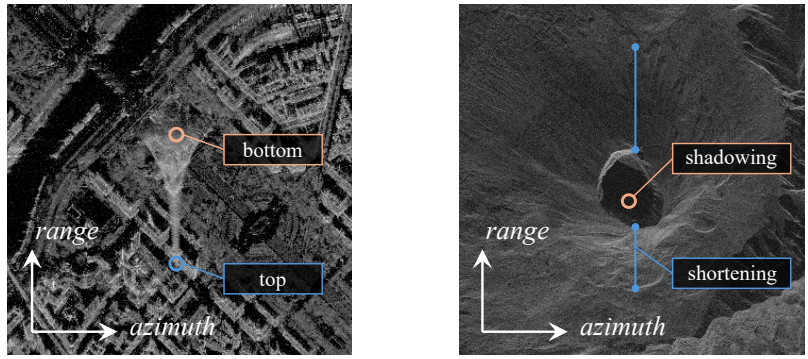
Figure 2.4: Stripmap SAR image formation: (a) target locations, (b) raw SAR data, (c) range-compressed data, and (d) the focused image after the range migration correction.

2.5 SAR Image Distortions

SAR images can exhibit several types of geometric distortions that affect target visibility and may lead to misinterpretation of the illuminated scene. The three main distortion effects are [5]:

- *Layover*: occurs when the radar signal reaches the top of a tall object before its base. The image inverts the order, displaying the top before the base. This effect is more pronounced at small incidence angles (β).
- *Foreshortening*: a less severe form of layover that occurs when the radar signal reaches the base of an object before its top, causing a compression of the object along the range direction. Conversely, slopes facing away from the radar appear elongated.
- *Shadowing*: occurs when steep slopes or objects block the radar signal, preventing the illumination of certain areas. These regions appear completely dark due to the absence of a backscattered signal.

These effects must be carefully considered to ensure accurate interpretation



(a) **(b)**

Figure 2.5: SAR distortion effects (a) layover on the Eiffel Tower, (b) foreshortening and shadowing on the Vesuvius.

of SAR imagery. Examples of these distortions are represented in Figure 2.5, which shows (a) the layover effect on the Eiffel Tower in a spotlight acquisition from the Capella mission (taken from its open database program [17]), and (b) foreshortening and shadowing effects on Mount Vesuvius in a spotlight acquisition from the Umbra mission (taken from its open database program [18]).

2.6 Satellite SAR Missions

Satellite missions equipped with SAR sensors differ in terms of operating frequency band, wavelength, acquisition mode, revisit time, and data accessibility. These characteristics strongly influence spatial resolution, temporal sampling, interferometric performance, and, most importantly, the practical feasibility of SAR monitoring applications. A comprehensive review of currently available SAR missions is provided by [19].

SAR sensors operate over various frequency bands, ranging from X- to L-band, each delivering distinct advantages and limitations [20]. As summarised in Table 2.1, X-band systems provide very fine spatial resolution and are therefore well suited for detailed observation of structures. However, shorter wavelengths are more susceptible to phase ambiguity (and therefore to temporal decorrelation), an issue addressed later in this thesis. In addition to spatial resolution, wavelength also affects signal penetration. In general, radar penetration increases with wavelength [5], making longer-wavelength systems more suitable for sensing subsurface objects.

Revisit time is another important parameter, which is defined as the temporal interval between successive acquisitions over the same area for a given

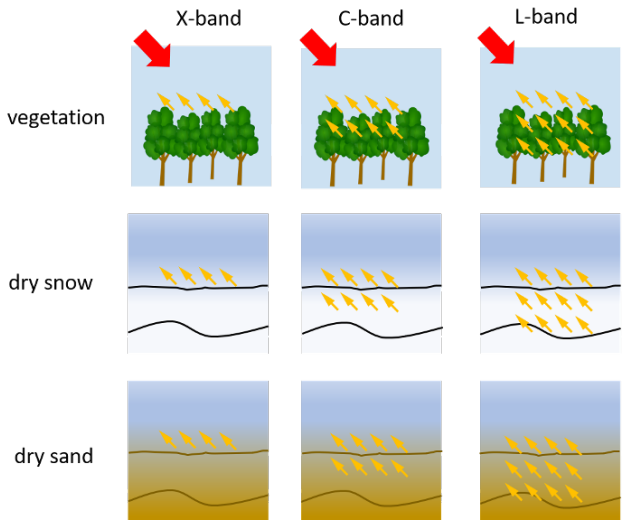


Figure 2.6: Radar penetration by frequency band, taken from [21].

orbit geometry. For example, Sentinel-1 has a revisit time of 12 days, but it is reduced to 6 days when combining ascending and descending orbits. Missions operating constellations of multiple satellites, such as Capella Space and Umbra, can achieve effective revisit times of less than one day [22, 23].

Data availability in mission archives is another major advantage of satellite SAR imagery. For example, Sentinel-1 provides systematic global acquisitions with open and free access [24], resulting in extensive historical archives that are particularly valuable for retrospective analyses. Other commercial missions routinely acquire data in stripmap and scanSAR modes, which are also available in their databases. These modes offer a balance between spatial coverage and resolution and are commonly accessible without the need for tasking. In contrast, spotlight acquisitions, while providing the highest spatial resolution, are rarely available in mission archives due to their limited swath and targeted tasks. As a result, spotlight data typically require advanced tasking, which introduces higher costs (up to a few thousand USD [25]), longer planning times, and reduced flexibility for retrospective studies.

Consequently, the choice of mission and acquisition mode must balance spatial resolution, temporal sampling, cost, and data availability to meet the specific requirements of structural monitoring. A summary of key mission characteristics, including revisit time, available acquisition modes, swath width, spatial resolution, data cost, and temporal coverage, is reported in Table 2.1.

Table 2.1: Synthetic Aperture Radar (SAR) satellite missions and main characteristics.

Mission	Band	Wavelength λ [cm]	Revisit Time [days]	Mode	Swath [km]	Resolution [m]	Cost [€]	Temporal coverage
Sentinel-1	C	3.8–7.5	12	StripMap, ScanSAR	up to 400	5–40	Free	from 2014
NovaSAR-1	S	7.5–15	16	StripMap, ScanSAR	up to 750	6–30	n.a.$^{(*)}$	from 2018
TerraSAR-X	X	2.4–3.8	11	Spotlight, StripMap, ScanSAR	10–100	down to 1	1000–4000	from 2007
COSMO-SkyMed	X	2.4–3.8	16	Spotlight, StripMap, ScanSAR	10–200	1–100	100–200	from 2007
SAOCOM	L	15–30	16	StripMap, ScanSAR	50–400	7–100	n.a.$^{(*)}$	from 2018
Umbra	X	2.4–3.8	n.a.$^{(*)}$	Spotlight	5–10	0.25–1	1000–3000	from 2021
Capella	X	2.4–3.8	n.a.$^{(*)}$	Spotlight, StripMap	5–10 10–100	0.25–1.2	n.a.$^{(*)}$	from 2018

$^{(*)}$no publicly available

3. Interferometric SAR for Bridge Monitoring

Interferometric Synthetic Aperture Radar (InSAR) exploits the phase differences of radar backscattered signals from ground targets observed in different SAR acquisitions [26]. When images are collected over time, this technique enables the measurement of surface displacements along the sensor LOS. Although originally developed for large-scale monitoring of land deformation [2], the advantages of InSAR remote sensing discussed previously have led researchers and practitioners to apply the technique to infrastructure monitoring. The advantages include the ability to provide long-term displacement trends, high spatial resolution, and historical data analysis.

InSAR approaches that analyse a set of SAR acquisitions distributed over time are generally referred to as *Multi-Temporal InSAR* (MT-InSAR), within which several algorithms have been developed over the years [27, 28, 29]. A comprehensive review of MT-InSAR techniques is provided by Crosetto et al. [20]. Among these methods, the most established technique – that is also the foundation for many subsequent MT-InSAR methods – is *Persistent Scatterer Interferometry* (PSI).

PSI focuses on targets that behave as stable radar reflectors over time, typically associated with metallic elements or geometrically sharp features. For these persistent scatterers (PSs), displacement time series can be extracted along the satellite LOS with millimetric accuracy. The scientific literature reports numerous case studies where PSI was successfully applied to infrastructure monitoring – and related phenomena – such as reinforced [30, 31] and prestressed concrete bridges [32, 33], railway bridges [34], cable-stayed bridges [35, 36], arch bridges [37], dam foundations [38] and even scour-related processes [39].

In the following sections, the fundamental principles of InSAR are introduced in order to facilitate the understanding of the technique limitations and of the methodological developments presented in the remainder of this thesis.

3.1 Interferometry Principles

A differential displacement along the sensor LOS d generates a delay in the backscattered radar signal, quantifiable by the interferometric phase shift [26]:

$$\varphi = \frac{4\pi}{\lambda} d \tag{3.1}$$

where λ is the central wavelength of the radar.

Since the interferometric phase is wrapped within the interval $[-\pi, \pi)$, the

maximum LOS displacement that can be measured without ambiguity, in terms of both magnitude and sign, is limited to $\pm\lambda/4$. This displacement ambiguity limit is defined as [40]:

$$d_{\text{lim}} = \frac{\lambda}{4} \tag{3.2}$$

3.2 Interferometric Phase modelling

Modelling the interferometric phase is a fundamental component of InSAR analysis, as it enables the separation of the phase contribution associated with LOS displacement – the primary quantity of interest in monitoring applications [26, 5].

It is important to note that the interferometric phase does not depend only on surface displacement but is the superposition of several contributions. A detailed derivation of each term can be found in [5].

Referring to a generic pixel p and acquisition i relative to a reference acquisition r and reference point O, the interferometric phase can be written as:

$$\varphi_p^{(i)} = \mu_p^{(i)} + \varphi_{p,\text{flat}}^{(i)} + \varphi_{p,\text{atmo}}^{(i)} + \varphi_{p,\text{height}}^{(i)} + \varphi_{p,\text{disp}}^{(i)} + \varphi_{p,\text{noise}}^{(i)} \tag{3.3}$$

where the individual terms are:

- *Reflectivity variations* $\mu_p^{(i)}$: contribution due to changes in the target reflectivity between acquisitions. This term is often neglected for persistent and highly reflective targets (e.g., corner reflectors that provide a high signal-to-noise ratio and temporal stability).
- *Flat-terrain* $\varphi_{p,\text{flat}}^{(i)}$: contribution caused by the Earth's curvature and the differences in the orbit geometries between the two acquisitions. It depends on the acquisition geometry and can be computed from known orbital parameters.
- *Atmosphere* $\varphi_{p,\text{atmo}}^{(i)}$: phase delay introduced when the radar signal travels through the atmosphere, mainly due to tropospheric water vapour and variations in temperature and pressure.
- *Topography* $\varphi_{p,\text{height}}^{(i)}$: phase contribution generated by the relative height difference between pixel p and the reference point, representing the effect of surface elevation (e.g. orography, man-made structures) on the interferometric phase.
- *Displacement* $\varphi_{p,\text{disp}}^{(i)}$: contribution relative to the motion of targets along the LOS between acquisitions r and i. it is directly proportional to $d_p^{(i)}$ via Eq. 3.1.

- *Noise* $\varphi^{(i)}_{p,\text{noise}}$: residual phase term that accounts for noise and modelling uncertainties.

Once the computable quantities are removed, the remaining interferometric phase depends primarily on the residual height h_p of the scatterer and the LOS displacement $d^{(i)}_p$. The full reduced-phase model and the associated geometry are presented in Chapter 5 (Section 5.2), where they form the basis of the proposed interferometric framework.

3.3 Interferogram generation

An interferogram is a two-dimensional representation of the phase difference between two SAR acquisitions of the same area [41], in which each fringe cycle – from $-\pi$ to π – represents a phase variation equivalent to the radar wavelength λ [26]. An example of an interferogram is shown in Figure 3.1(a).

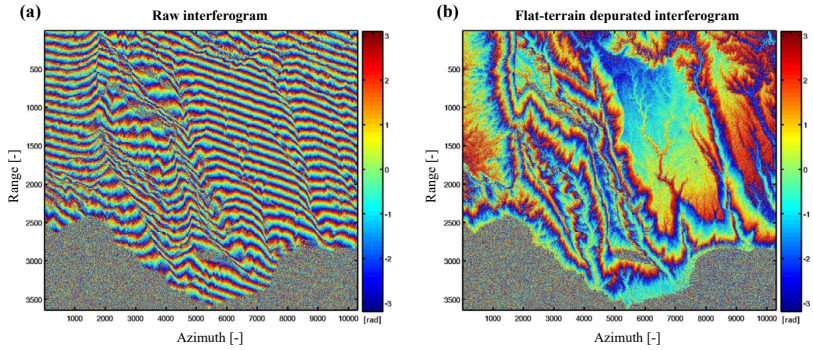


Figure 3.1: Example of an interferogram: (a) before and (b) after removing the flat terrain; taken from [26].

The overall objective of InSAR processing is to isolate the displacement component of the interferometric phase by removing the other contributions in Eq. 3.3. In general, the flat-terrain component can be easily removed (Figure 3.1(b)), as it depends only on known orbital geometry parameters. Over small areas such as individual bridges, the atmospheric phase contribution can be reasonably assumed to be spatially constant and is therefore cancelled when computing phase differences with respect to a reference point [27]. A Digital Elevation Model (DEM) can be used to remove the topographic phase contribution. When a DEM is employed for this purpose, the resulting interferogram is referred to as a *Differential Interferogram* (DInSAR) [5].

For civil infrastructure monitoring, the primary unknowns remaining from the interferometric phase are therefore the residual height h_p relative to the

DEM and the LOS displacements $d_p^{(i)}$.

3.4 Multi-Temporal InSAR

Multi-Temporal SAR Interferometry (MT-InSAR) is an advanced class of techniques developed to overcome some of the main limitations of conventional DInSAR. By exploiting a large stack of SAR acquisitions, rather than a single interferogram, MT-InSAR allows for reconstructing long-term surface displacement over time. Among MT-InSAR approaches, Persistent Scatterer Interferometry (PSI), developed by Ferretti et al. [27], represents one of the most used methodologies and has served as the starting point for several subsequent techniques [28, 29].

The PSI processing chain consists of four key steps: (1) selection of a single master image as reference to generate all interferograms; (2) identification of pixels with stable amplitude behaviour over time, referred to as Candidate Persistent Scatterers (CPS), using the Amplitude Stability Index (ASI); (3) modelling and removal of quantifiable phase components (flat-terrain, topography, atmosphere); and (4) joint estimation of the unknown displacement parameters and residual heights for each CPS using a Maximum Likelihood Estimation (MLE) approach.

Selection of Persistent Scatterer Candidate Points

Candidate Persistent Scatterers (CPS) are identified across all pixels in the interferograms, by analysing the Amplitude Stability Index (ASI), defined as:

$$\text{ASI} = 1 - \frac{\sigma}{\mu} \tag{3.4}$$

where μ is the mean reflectivity and σ is the standard deviation of the pixel reflectivity over all acquisitions. ASI values close to 1 indicate high amplitude stability, a key requirement for reliable PS selection.

Temporal Coherence

Once the unknown displacement parameters and residual heights have been jointly estimated via MLE, the quality of the fit for each CPS is measured by the *temporal coherence* γ_t.

This scalar quantity – whose full mathematical definition is given in Chapter 5 – captures how consistently the modelled interferometric phase matches the observed phase over the entire acquisition stack. When the assumed model fits well, the complex residuals align and γ_t approaches 1; while when the model is a poor fit, residuals are random in phase and $\gamma_t \ll 1$.

Temporal coherence is the primary quality indicator used to accept or dis-

card CPS candidates. CPSs with high temporal coherence are considered reliable persistent scatterers, while those with low coherence are discarded. Typical empirical thresholds include [40]:

- *high reliability*: $\gamma_t > 0.9$, at the expense of discarding many CPSs.
- *moderate reliability*: $\gamma_t > 0.6$, allowing for higher spatial density of PSs but reduced confidence.

A commonly adopted compromise threshold is $\gamma_t > 0.75$ [42].

3.5 Challenges of InSAR for Bridge Monitoring

InSAR provides valuable displacement measurements; however, when applied to bridge monitoring, several practical challenges must be considered. These limitations range from both the intrinsic characteristics of InSAR measurements and the modelling assumptions commonly adopted in interferometric analyses.

3.5.1 Reconstruction of three-dimensional displacement

InSAR provides one-dimensional measurements of differential displacement along the radar LOS. Reconstruction of three-dimensional structural motion generally requires the combination of measurements obtained from different viewing geometries – typically ascending and descending orbits [5]. However, this approach introduces additional sources of uncertainty related to spatial and temporal misalignment between the displacement time series. Giordano et al. recently proposed a framework to quantify these uncertainties when merging multi-orbit observations [43]. In areas characterised by complex topography the combination of multiple orbits is often not feasible due to shadowing and layover effects caused by surrounding mountains and steep terrain. This limitation significantly reduces the ability to reconstruct the full three-dimensional displacement response of bridge structures [39]. Although some studies have attempted to overcome this issue by simplifying assumptions on the displacement direction, such approximations may lead to misinterpretation of the actual structural behaviour [44].

3.5.2 Temporal Sampling

The temporal sampling of InSAR measurements depends on the revisit time of the satellite sensor. For widely used missions such as Sentinel-1 and COSMO-SkyMed (first- and second-generation), revisit intervals typically range from 6 to 16 days [45, 46]. Newer commercial constellations, such as Umbra and Capella, can provide revisit times on the order of hours, but their use is limited

by data availability and cost [47, 48]. Regular temporal sampling is generally preferred, as long temporal baselines can lead to temporal decorrelation, particularly when significant displacements occur between acquisitions [26]. This issue is especially critical for bridge monitoring, where structural displacements may increase rapidly under variable loading or environmental conditions.

3.5.3 Displacement ambiguity

As discussed in Section 3.1, unambiguous interpretation of interferometric phase measurements requires that LOS displacements – relative to the reference image – remain below the ambiguity limit $d_{\text{lim}} = \lambda/4$. This limit ranges from $7.75\ \text{mm}$ for X-band (e.g., COSMO-SkyMed) to approximately $58\ \text{mm}$ for C-band sensors (e.g., SAOCOM). In bridge monitoring, high-resolution SAR imagery is often required to accurately distinguish structural components. However, high-resolution sensors typically operate at shorter wavelengths, which reduces the displacement ambiguity threshold.

Sandoli et al. [49] proposed a framework to estimate the expected performance of InSAR measurements for bridge monitoring prior to data acquisition, accounting for bridge typology, live loads, and thermal effects. Their analysis points out the importance of thermal effects, particularly for long-span bridges, where exceeding the ambiguity threshold is more likely to occur.

3.5.4 Displacement mismodelling

The standard PSI assumes a displacement model that evolves linearly with time and air temperature. While this assumption can be reasonable for slow-moving geophysical processes or for structural elements such as piers subjected primarily to uniform thermal expansion, it may not be valid for bridges. In bridges, thermal deformation is governed by structural temperature, which depends not only on air temperature but also on solar radiation, shading, and thermal gradients. Consequently, other deformation mechanisms, such as deck deflection induced by vertical temperature gradients, cannot be adequately captured by simple linear models based solely on air temperature.

3.6 Literature Gap

The aforementioned issues jointly contribute to a loss of temporal coherence in PSs, even with consistent scattering properties. As a result, large portions of bridge structures are often discarded during PS selection, resulting in sparse or unreliable monitoring data.

Several methods have been developed to deal with poor temporal coher-

ence, including the Small Baseline Subset (SBAS) approach [50], Quasi-Persistent Scatterers (QPS) [29], and the Stanford Method for Persistent Scatterers (StaMPS) [28]. These methods rely on multiple reference images and reduced temporal baselines to enhance coherence. Whilst such techniques perform well for many applications, including slow-moving land deformation, they still rely on similar assumptions about displacement modelling. In bridge monitoring scenarios, displacements may exceed $\lambda/4$ within 10–16 days.

Intuitively, overcoming these limitations requires combining more refined, physics-based structural deformation models. Physics-informed InSAR approaches have been proposed in the context of geotechnical engineering [51, 52, 53, 54], tunnelling, and bridge monitoring [36, 55, 37, 56, 57, 58] to improve displacement interpretation, resolve ambiguity issues, and infer potential structural damage.

However, such approaches are typically applied as a post-processing step, after InSAR displacement measurements have already been retrieved. To date, no study has integrated a physics-based structural deformation model directly into the interferometric SAR processing pipeline to jointly estimate displacement and height parameters from the observed interferometric phase.

3.7 Motivation and Research Objectives

Overall, the above-mentioned literature demonstrates that InSAR has considerable potential for infrastructure monitoring; however, its practical application to bridges is constrained by core limitations arising from both the intrinsic nature of interferometric measurements and the algorithms commonly used for data processing. Whilst aspects such as temporal sampling and three-dimensional displacement reconstruction are dominated by orbit geometry and sensor revisit time, there is still significant room for improvement in displacement ambiguity and mismodelling limitations.

Dealing with these challenges constitutes the core motivation behind the first research question of this thesis:

> Can InSAR be enhanced for bridge monitoring applications? In particular, is it possible to overcome the limitations that currently restrict its reliability and applicability in bridge structural health monitoring?

To achieve this objective, a novel framework that integrates physics-based structural deformation models into persistent scatterer interferometry is proposed. In contrast to existing studies, where physics-based models are typically

applied *a posteriori* – once PSI displacement measurements are available – the proposed framework is integrated into the interferometric processing pipeline to estimate the displacement time series from interferometric phases.

The proposed approach is described and validated on a real-world case study, namely the Colle Isarco Viaduct located in Vipiteno (Italy), presented in Chapter 5.

4. Micro-Doppler SAR for Bridge Monitoring

As the reader may infer from the previous sections, InSAR techniques are not well-suited for measuring the vibrational response of bridges and viaducts. InSAR relies on repeated acquisitions with revisit times ranging from hours to several days. This temporal sampling is incompatible with vibration monitoring, as the dominant natural frequencies of civil engineering structures can reach several hertz. Due to these inherent limitations, InSAR cannot be used to assess the vibrational behaviour of structures directly.

However, a different class of SAR-based techniques operates on single-pass (i.e., individual) SAR images and can extract vibrational information [16]. These approaches exploit micro-Doppler (m-D) effects induced by target motion and are referred to in this thesis as MDSAR.

In the following sections, the fundamental principles of MDSAR are introduced, along with a review of its current applications in the literature when employed for VBSHM of civil infrastructure. The discussion concludes with an overview of the main limitations and open challenges.

4.1 Micro-Doppler Principles

A focused SAR image is generated by coherently combining the information collected from multiple radar pulses transmitted along the sensor LOS, as described in Section 2.4. Standard SAR processing methods assume that the scene under observation is static (i.e., that the targets remain stationary over the synthetic aperture time) [3]. When this assumption is violated, and targets exhibit motion, artefacts are introduced in the final focused SAR image [59].

To show this effect, consider the example discussed in Section 2.4, which shows the range cell migration correction of two point-like scatterers. Let the lower scatterer move with a constant velocity $v_x = 1\ \mathrm{m/s}$ along the ground-range direction, as represented in Figure 4.1(a). Figure 4.1(b) shows the focused SAR image after RCMC. Unlike the top (stationary) scatterer, the moving scatterer appears displaced from its true position by a distance y along the azimuth. This distance depends on the LOS component of the scatterer velocity v_r.

When a target moves at constant velocity, this induces a frequency shift in the backscattered signal due to the Doppler effect, given by [59]:

$$f_D = \frac{2v_r}{\lambda} \tag{4.1}$$

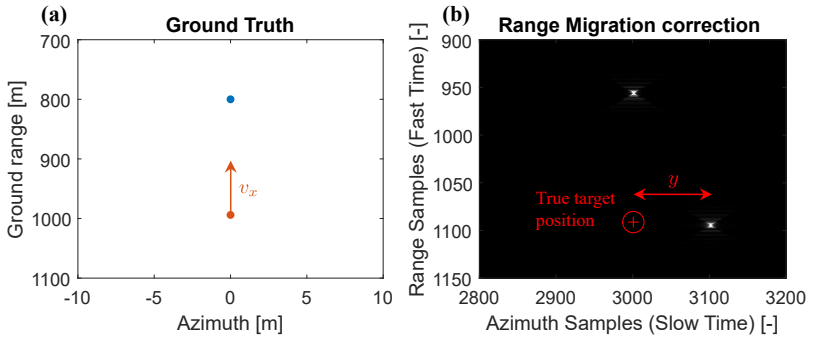


Figure 4.1: Simulated effect of a moving scatterer, with constant velocity, in the SAR image: (a) Ground truth image, (b) focused SAR image after RCMC.

where f_D is the Doppler frequency shift, v_r is the radial (LOS) velocity, and λ is the radar wavelength. Since the radar can only measure along the LOS, Doppler shifts arise exclusively from the target radial component of the velocity. The Doppler frequency shift – and the associated phase modulation – cause the target to appear defocused and displaced in the focused SAR image along the azimuth direction. The azimuth shift $y(t)$ can be expressed as [59]:

$$y(t) = \frac{v_r \, R(t)}{v_\mathrm{s}} \tag{4.2}$$

where $R(t)$ is the instantaneous slant-range distance and v_s is the SAR velocity.

4.2 Vibrations and micro-Doppler

The same phenomenon can also be observed at a much smaller scale in the presence of structural vibrations [60]. Consider the same example of the two point-like scatterers discussed above, where the bottom scatterer oscillates with a constant frequency of 5 Hz and an amplitude of 1 cm along the ground-range direction (see Figure 4.2(a)). The corresponding focused SAR image, after range cell migration correction, is shown in Figure 4.2(b).

In this case, a new artefact appears for the oscillating scatterer. The periodic change in the sign of the radial velocity causes the appearance of multiple *paired echoes* [61] centred around the true target position. In the context of radar, this is commonly referred to as *micro-Doppler*, and arises from micro-motions of targets, such as oscillations or vibrations.

The same micro-Doppler behaviour can also be observed in the *azimuth-Doppler* domain, which shows how the frequency content of the SAR signal evolves over slow time (i.e., throughout the acquisition). To visualise this tem-

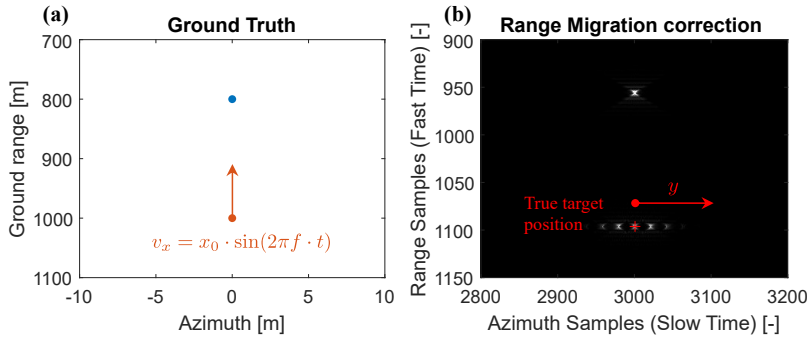


Figure 4.2: Simulated effect of a vibrating scatterer in the SAR focused image: (a) Ground truth image, (b) focused image after RCMC.

poral evolution, it is sufficient to focus on the range bin associated with the scatterer after the *range compression step* – prior to the final azimuth focusing [59]. A short-time Fourier transform (STFT) can then be computed on the extracted signal to visualise the temporal evolution of the Doppler frequency during the acquisition [59]. As shown in Figure 4.3, a static scatterer produces a nearly linear Doppler trend over time, while a vibrating scatterer produces a sinusoidal modulation in the Doppler spectrum, representing the spectral counterpart of the paired echoes in the image domain.

On the one hand, paired echoes represent the spatial realisation of time-varying Doppler shifts but do not preserve temporal information, as they result from the entire focusing process. On the other hand, the Doppler-domain representation explicitly reveals temporal evolution at the expense of spatial information along azimuth.

Methods for micro-Doppler measurement from SAR data depend on the product level they operate on, such as CPHD or SLC [62]. A comprehensive review of these techniques is beyond the scope of this thesis, and the reader is referred to the recent work of Rollo et al. [16].

This thesis focuses on a specific micro-Doppler measurement approach, namely the *sub-pixel offset tracking* (SPOT) method, first introduced by Biondi et al. [63] for measuring vibrations. The main idea of the algorithm is introduced in the following section, while the proposed technique and its validation are discussed in Chapters 6 and 7.

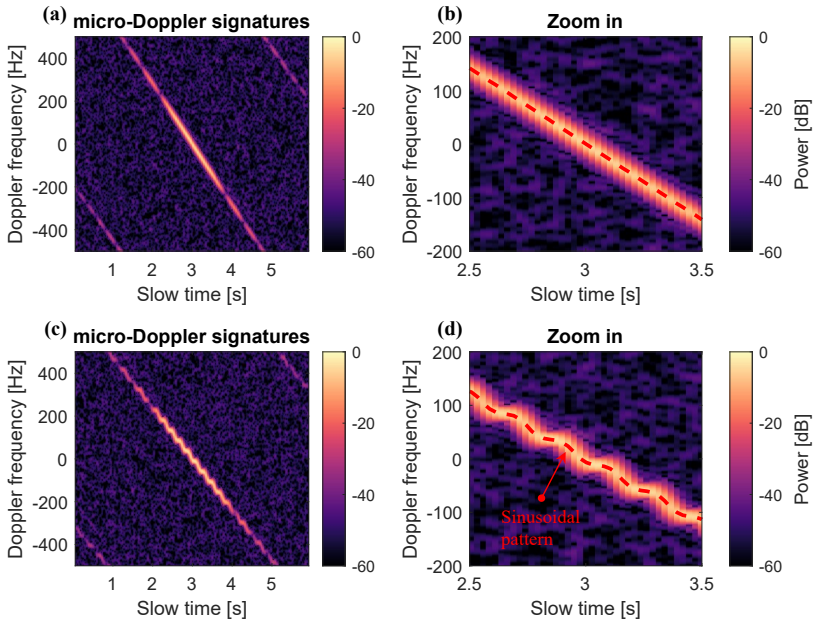


Figure 4.3: Micro-Doppler signatures in the azimuth-Doppler domain: (a) static scatterer, (b) zoomed-in view of (a), (c) vibrating scatterer, (d) zoomed-in view of (c) showing the sinusoidal Doppler modulation.

4.3 Sub-Pixel Offset Tracking Method

SPOT was originally developed to measure large-scale ground displacements from stacks of SAR images, exploiting amplitude (i.e., reflectivity) information rather than interferometric phase [64]. The authors used the method to estimate displacement in both the range and azimuth directions, complementing InSAR-based techniques.

At first glance, the applicability of SPOT to vibration monitoring may appear non-intuitive; however, it can also be employed for this purpose. To understand this, it is important to recall that a focused SAR image is generated by combining multiple radar pulses collected over the acquisition time t_a, often referred to as *aperture time*.

The key idea behind SPOT micro-Doppler analysis is to start from the full-aperture focused SAR image and segment it into multiple azimuth (or Doppler) sub-apertures [65]. Each sub-aperture corresponds to a shorter time window within the total acquisition time.

Selecting only a portion of the full Doppler bandwidth corresponds to selecting a subset of pulses acquired over a specific time window of the synthetic

aperture of duration t_{sap}. This process is commonly known as azimuth *sub-aperture segmentation*, and trades spatial resolution for temporal resolution: each sub-aperture image has degraded azimuth resolution compared to the full aperture t_a, but captures the target response corresponding to a specific time interval within the SAR acquisition.

It is worth noting that the azimuth shift of a target within each sub-aperture depends on the instantaneous value of the radial velocity during the corresponding sub-aperture window. As a result, moving or vibrating targets exhibit different azimuth shifts across the sub-aperture series [66]. By tracking the azimuth displacement of a reflective target across the sub-aperture sequence – within a single SAR acquisition – it is therefore possible to reconstruct the time series of the target LOS velocity. Very small shifts may fall within a single pixel; upsampling can be applied to preserve sub-pixel precision, hence the term sub-pixel offset tracking.

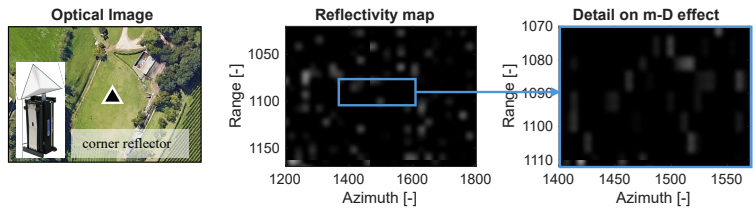


Figure 4.4: Effect of an isolated target oscillating vertically: (a) optical image with highlighted target, (b) full SAR image, and (c) zoomed-in view around the target showing paired echoes; adapted from [67].

The complete mathematical formulation of the sub-aperture segmentation and pixel-tracking algorithm is reported in Chapter 6, where it represents the basis of the proposed methodology and experimental validation, and is later recalled in Chapter 7.

4.4 Challenges of MDSAR for Bridge Monitoring

Micro-Doppler SAR is a promising tool that could enable a range of new possibilities for remote vibration-based monitoring of civil infrastructure [68]. However, its application to bridges remains at an early stage of development. Unlike InSAR, whose limitations are well documented in the literature, MDSAR lacks validation studies and, most importantly, a consolidated metrological framework. Consequently, it is difficult to draw general conclusions regarding MDSAR accuracy, robustness, and practical usage. Most existing studies focus on demonstrating feasibility under specific conditions rather than providing a

rigorous quantitative assessment of measurement uncertainty.

4.4.1 Controlled experimental studies

Early investigations of MDSAR aimed to extract vibration features of isolated targets in controlled environments to mitigate interference from the surroundings. In these works, mechanically actuated and controlled vibrations of corner reflectors were employed to reproduce vibrations, which were extracted using SAR imagery acquired both from airborne sensors [60, 69] and, more recently, spaceborne sensors [66, 70].

Under these conditions, these studies have demonstrated the detectability of micro-Doppler signatures and the ability to identify dominant vibration frequencies, primarily in the range of 1 to 2 Hz. However, they primarily focused on frequency detection rather than reconstruction of full vibration time series, and vibration amplitudes were often not compatible compared to those typically observed in bridges under operational conditions.

Moreover, most experiments were limited to a single acquisition, constraining repeatability and accuracy estimation across a broader range of vibration scenarios.

4.4.2 Existing studies on real-world structures

Regarding the applications of MDSAR to real civil infrastructure, Biondi et al. [68] first used SPOT to identify crack zones in the Mosul Dam from SAR imagery, validating results against PSI InSAR benchmark data. In a later study, Biondi et al. [71] applied SPOT MDSAR to five bridge case studies to detect anomalies in the vibrational behaviour of the deck; however, the extracted vibration amplitude and frequencies were not compared against independent benchmark measurements. Focsa et al. [72] estimated a bridge natural frequencies using azimuth sub-aperture processing, reporting errors of 0.03 to 0.5 Hz; though the accuracy remains uncertain due to asynchronous validation. Finally, Vattulainen et al. [73] used a modified back-projection algorithm and reported a frequency error of 0.04 Hz in the bridge dominant vibration frequency, but without the time-domain reconstruction of the vibrations.

4.5 Literature gap

In summary, the current literature highlights the feasibility of extracting vibrational information via MDSAR but leaves two major gaps unaddressed for bridge monitoring applications.

First, controlled experiments with isolated targets have demonstrated the

detectability of vibration frequencies; however, a comprehensive metrological evaluation of MDSAR capabilities remains lacking. In particular, no study has assessed the accuracy of MDSAR in reconstructing vibrations in the time domain – including the amplitude – under controlled conditions and across a wide range of vibration scenarios representative of operational bridge behaviour.

Secondly, the application of MDSAR to full-scale civil infrastructure remains limited and mainly qualitative. To date, no study has applied MDSAR to a real bridge while validating the measured vibration time histories against synchronous ground-based reference measurements in the time domain. Furthermore, an investigation is necessary to determine whether SAR data can be effectively used for conventional modal extraction, including the identification of natural frequencies, damping ratios, and mode shapes of the structure, which constitutes the main goal of VBSHM.

4.6 Motivation and Research Objectives

In summary, the reviewed literature indicates that Micro-Doppler SAR is a promising technique for remote vibration-based monitoring of civil infrastructure. In contrast to InSAR, MDSAR still lacks a consolidated metrological framework and systematic validation against independent reference measurements. In fact, the scientific gaps highlighted in the previous sections undermine its applicability to VBSHM. MDSAR application to bridge monitoring remains at a preliminary stage, with current studies largely limited to feasibility demonstrations under specific and often idealised conditions. Addressing MDSAR gaps constitutes the core motivation behind the second research question of this thesis:

> Can MDSAR be employed for vibration-based structural health monitoring of bridges? Specifically, can satellite SAR sensors measure structural vibrations with sufficient accuracy, and can dynamic features—such as modal parameters—be reliably extracted from spaceborne observations?

To answer these questions, this thesis follows a two-step validation strategy.

First, a comprehensive experimental validation of MDSAR is carried out under controlled conditions using isolated corner reflectors and shakers to simulate vibrations. In contrast to most existing studies, validation is performed synchronously with ground-based reference measurements in both the time and frequency domains. This enables a quantitative assessment of MDSAR accuracy in reconstructing vibration time histories over a wide range of amplitudes

and frequencies, from large, easily detectable levels to those representative of structural operating conditions. This investigation is presented in Chapter 6.

Secondly, the validated methodology is applied to a real-world bridge case study, the South Portland St. suspension bridge located in Glasgow (UK), where MDSAR measurements are compared against synchronous ground benchmark data. This further step enables evaluation of MDSAR performance under realistic operational conditions and exploration of its ability to extract dynamic features relevant to vibration-based monitoring. The results of this application are presented in Chapter 7.

Bibliography

[1] M. I. Skolnik, “Radar handbook,” *IEEE Aerospace Electronic Systems Magazine*, vol. 23, no. 5, pp. 41–41, 2008.

[2] J. C. Curlander and R. N. McDonough, *Synthetic aperture radar*. Wiley, New York, 1991, vol. 11.

[3] I. G. Cumming and F. H. Wong, “Digital processing of synthetic aperture radar data,” *Artech house*, vol. 1, no. 3, pp. 108–110, 2005. [Online]. Available: https://www.researchgate.net/profile/Ahmed-Azouz/post/Could_anyone_suggest_good_and_simple_reference_for_synthetic_aperture_radar_SAR/attachment/623282a9d411a95e64e84e40/AS%3A1134416655056897%401647477415675/download/Digital+Processing+of+Synthetic+Aperture+Radar+Data_+Algorithms+and+Implementation-Artech+House+%282005%29.pdf

[4] T. Lillesand, R. W. Kiefer, and J. Chipman, *Remote sensing and image interpretation*. John Wiley & Sons, 2015.

[5] A. Ferretti, *Satellite InSAR Data: Reservoir Monitoring from Space*, ser. Education Tour Series. DB Houten: EAGE, 2014, no. 9.

[6] B. Wang, *Digital Signal Processing Techniques and Applications in Radar Image Processing*, 1st ed. Wiley, Aug. 2008. [Online]. Available: https://onlinelibrary.wiley.com/doi/book/10.1002/9780470377765

[7] A. Lotti, S. Zorzi, E. Tubaldi, A. Rocca, D. Perissin, and D. Zonta, “Spatio-temporal insar for bridge monitoring: Integrating physics-based models with persistent scatterer interferometry,” *Structural Health Monitoring*, 2026, submitted.

[8] A. Moreira, P. Prats-Iraola, M. Younis, G. Krieger, I. Hajnsek, and K. P. Papathanassiou, “A tutorial on synthetic aperture radar,” *IEEE Geoscience and Remote Sensing Magazine*, vol. 1, no. 1, pp. 6–43, 2013.

[9] European Space Agency, “Types of orbits,” 2020, accessed: December 2025. [Online]. Available: https://www.esa.int/Enabling_Support/Space_Transportation/Types_of_orbits

[10] C. V. Jakowatz, D. E. Wahl, P. H. Eichel, D. C. Ghiglia, and P. A. Thompson, “A Tomographic Foundation for Spotlight-Mode Sar Imaging,” in *Spotlight-Mode Synthetic Aperture Radar: A Signal*

Processing Approach, C. V. Jakowatz, D. E. Wahl, P. H. Eichel, D. C. Ghiglia, and P. A. Thompson, Eds. Boston, MA: Springer US, 1996, pp. 33–103. [Online]. Available: https://doi.org/10.1007/978-1-4613-1333-5_2

[11] UP42, "Sar processing levels," 2026, accessed: February 2026. [Online]. Available: https://docs.up42.com/data/sar-processing

[12] Capella Space, "What sar imagery products are available with capella?" 2025, accessed: February 2026. [Online]. Available: https://support.capellaspace.com/what-sar-imagery-products-are-available-with-capella

[13] NASA Earthdata, "Types of sar products," https://www.earthdata.nasa.gov/learn/earth-observation-data-basics/types-sar-products, 2025, accessed: February 2026.

[14] H. Cruz, M. Véstias, J. Monteiro, H. Neto, R. P. Duarte, H. Cruz, M. Véstias, J. Monteiro, H. Neto, and R. P. Duarte, "A Review of Synthetic-Aperture Radar Image Formation Algorithms and Implementations: A Computational Perspective," *Remote Sensing*, vol. 14, no. 5, Mar. 2022, company: Multidisciplinary Digital Publishing Institute Distributor: Multidisciplinary Digital Publishing Institute Institution: Multidisciplinary Digital Publishing Institute Label: Multidisciplinary Digital Publishing Institute Publisher: publisher. [Online]. Available: https://www.mdpi.com/2072-4292/14/5/1258

[15] MathWorks, "Stripmap Synthetic Aperture Radar (SAR) Image Formation - MATLAB & Simulink." [Online]. Available: https://it.mathworks.com/help/radar/ug/stripmap-synthetic-aperture-radar-sar-image-formation.html

[16] F. Rollo, C. Ilioudis, and C. Clemente, "Advances in Micro-Doppler Processing in Synthetic Aperture Radar: A review of techniques, results, and future trends," *IEEE Geoscience and Remote Sensing Magazine*, pp. 2–24, 2025. [Online]. Available: https://ieeexplore.ieee.org/document/11029265/

[17] C. Space, "Capella Open Data Gallery." [Online]. Available: https://www.capellaspace.com/earth-observation/gallery

[18] U. Space, "Umbra Synthetic Aperture Radar (SAR) Open Data - Registry of Open Data on AWS," accessed: 2025. [Online]. Available: https://registry.opendata.aws/umbra-open-data/

[19] C. Hu, Y. Li, Z. Chen, F. Liu, Q. Zhang, A. V. Monti-Guarnieri, S. Hobbs, A. Anghel, and M. Datcu, "Distributed Spaceborne SAR: A review of systems, applications, and the road ahead," *IEEE Geoscience and Remote Sensing Magazine*, vol. 13, no. 2, pp. 329–361, Jun. 2025. [Online]. Available: https://ieeexplore.ieee.org/document/10936987/

[20] M. Crosetto, O. Monserrat, M. Cuevas-González, N. Devanthéry, and B. Crippa, "Persistent Scatterer Interferometry: A review," *ISPRS Journal of Photogrammetry and Remote Sensing*, vol. 115, pp. 78–89, May 2016. [Online]. Available: https://www.sciencedirect.com/science/article/pii/S0924271615002415

[21] C. Space, "SAR 101: An Introduction to Synthetic Aperture Radar." [Online]. Available: https://www.capellaspace.com/blog/sar-101-an-introduction-to-synthetic-aperture-radar

[22] EoPortal, "Capella Space X-Band Synthetic Aperture Radar," 2025. [Online]. Available: https://www.eoportal.org/satellite-missions/capella-x-sar#mission-capabilities

[23] ——, "Umbra SAR Constellation," 2025. [Online]. Available: https://www.eoportal.org/satellite-missions/umbra-sar

[24] E. S. Agency, "Sentinel-1," https://www.esa.int/Applications/Observing_the_Earth/Copernicus/Sentinel-1, 2025.

[25] D. Amitrano, G. Di Martino, R. Guida, P. Iervolino, A. Iodice, M. N. Papa, D. Riccio, and G. Ruello, "Earth Environmental Monitoring Using Multi-Temporal Synthetic Aperture Radar: A Critical Review of Selected Applications," *Remote Sensing*, vol. 13, no. 4, p. 604, Feb. 2021. [Online]. Available: https://www.mdpi.com/2072-4292/13/4/604

[26] D. Perissin, "Interferometric SAR Multitemporal Processing: Techniques and Applications," in *Multitemporal Remote Sensing*, Y. Ban, Ed. Cham: Springer International Publishing, 2016, vol. 20, pp. 145–176, series Title: Remote Sensing and Digital Image Processing. [Online]. Available: https://link.springer.com/chapter/10.1007/978-3-319-47037-5_8

[27] A. Ferretti, C. Prati, and F. Rocca, "Permanent scatterers in SAR interferometry," *IEEE Trans. Geosci. Remote Sensing*, vol. 39, no. 1, pp. 8–20, Jan. 2001. [Online]. Available: http://ieeexplore.ieee.org/document/898661/

[28] A. Hooper, P. Segall, and H. Zebker, "Persistent scatterer interferometric synthetic aperture radar for crustal deformation analysis, with application to Volcán Alcedo, Galápagos," *Journal of Geophysical Research: Solid Earth*, vol. 112, no. B7, 2007, _eprint: https://agupubs.onlinelibrary.wiley.com/doi/pdf/10.1029/2006JB004763. [Online]. Available: https://onlinelibrary.wiley.com/doi/abs/10.1029/2006JB004763

[29] D. Perissin and T. Wang, "Repeat-Pass SAR Interferometry With Partially Coherent Targets," *IEEE Trans. Geosci. Remote Sensing*, vol. 50, no. 1, pp. 271–280, Jan. 2012. [Online]. Available: http://ieeexplore.ieee.org/document/5978217/

[30] R. Wang, J. Zhang, and X. Liu, "A Most-Unfavorable-Condition Method for Bridge-Damage Detection and Analysis Using PSP-InSAR," *Remote Sensing*, vol. 14, no. 1, p. 137, Jan. 2022, publisher: Multidisciplinary Digital Publishing Institute. [Online]. Available: https://www.mdpi.com/2072-4292/14/1/137

[31] M. Schlögl, P. Dorninger, M. Kwapisz, M. Ralbovsky, and R. Spielhofer, "Remote Sensing Techniques for Bridge Deformation Monitoring at Millimetric Scale: Investigating the Potential of Satellite Radar Interferometry, Airborne Laser Scanning and Ground-Based Mobile Laser Scanning," *PFG – Journal of Photogrammetry, Remote Sensing and Geoinformation Science*, vol. 90, no. 4, pp. 391–411, Aug. 2022. [Online]. Available: https://link.springer.com/10.1007/s41064-022-00210-2

[32] D. Tonelli, A. Valentini, A. Rocca, S. Zorzi, A. Lotti, and D. Zonta, "Uncertainty quantification of satellite InSAR-monitoring of bridges: a case study," *ce/papers*, vol. 6, no. 5, pp. 900–906, 9 2023. [Online]. Available: https://onlinelibrary.wiley.com/doi/10.1002/cepa.1991

[33] P. F. Giordano, M. Kwapisz, A. Miano, R. Liuzzo, A. Vorwagner, M. P. Limongelli, A. Prota, and M. Ralbovsky, "Monitoring of a multi-span prestressed concrete bridge using satellite interferometric data and comparison with on-site sensor results," *Structural Concrete*, p. suco.202400881, Feb. 2025. [Online]. Available: https://onlinelibrary.wiley.com/doi/10.1002/suco.202400881

[34] F. D'Amico, V. Gagliardi, L. Bianchini Ciampoli, and F. Tosti, "Integration of InSAR and GPR techniques for monitoring transition

areas in railway bridges," *NDT & E International*, vol. 115, p. 102291, Oct. 2020. [Online]. Available: https://www.sciencedirect.com/science/article/pii/S0963869520303157

[35] S. Xiong, C. Wang, X. Qin, B. Zhang, and Q. Li, "Time-Series Analysis on Persistent Scatter-Interferometric Synthetic Aperture Radar (PS-InSAR) Derived Displacements of the Hong Kong–Zhuhai–Macao Bridge (HZMB) from Sentinel-1A Observations," *Remote Sensing*, vol. 13, no. 4, p. 546, Jan. 2021, publisher: Multidisciplinary Digital Publishing Institute. [Online]. Available: https://www.mdpi.com/2072-4292/13/4/546

[36] X. Qin, Q. Li, X. Ding, L. Xie, C. Wang, M. Liao, L. Zhang, B. Zhang, and S. Xiong, "A structure knowledge-synthetic aperture radar interferometry integration method for high-precision deformation monitoring and risk identification of sea-crossing bridges," *International Journal of Applied Earth Observation and Geoinformation*, vol. 103, p. 102476, Dec. 2021. [Online]. Available: https://www.sciencedirect.com/science/article/pii/S0303243421001835

[37] F. C. Ponzo, G. Auletta, P. Ielpo, and R. Ditommaso, "DInSAR–SBAS satellite monitoring of infrastructures: how temperature affects the "Ponte della Musica" case study," *Journal of Civil Structural Health Monitoring*, vol. 14, no. 3, pp. 745–761, Mar. 2024. [Online]. Available: https://link.springer.com/10.1007/s13349-023-00751-z

[38] P. Milillo, R. Bürgmann, P. Lundgren, J. Salzer, D. Perissin, E. Fielding, F. Biondi, and G. Milillo, "Space geodetic monitoring of engineered structures: The ongoing destabilization of the Mosul dam, Iraq," *Scientific Reports*, vol. 6, no. 1, p. 37408, 12 2016. [Online]. Available: https://www.nature.com/articles/srep37408

[39] S. Selvakumaran, S. Plank, C. Geiß, C. Rossi, and C. Middleton, "Remote monitoring to predict bridge scour failure using Interferometric Synthetic Aperture Radar (InSAR) stacking techniques," *International Journal of Applied Earth Observation and Geoinformation*, vol. 73, pp. 463–470, Dec. 2018. [Online]. Available: https://linkinghub.elsevier.com/retrieve/pii/S0303243418303052

[40] V. Macchiarulo, P. Milillo, C. Blenkinsopp, C. Reale, and G. Giardina, "Multi-temporal InSAR for transport infrastructure monitoring: recent

trends and challenges," *Proceedings of the Institution of Civil Engineers - Bridge Engineering*, vol. 176, no. 2, pp. 92–117, Dec. 2021. [Online]. Available: https://doi.org/10.1680/jbren.21.00039

[41] D. Massonnet and K. L. Feigl, "Radar interferometry and its application to changes in the Earth's surface," *Reviews of Geophysics*, vol. 36, no. 4, pp. 441–500, 1998, _eprint: https://agupubs.onlinelibrary.wiley.com/doi/pdf/10.1029/97RG03139. [Online]. Available: https://onlinelibrary.wiley.com/doi/abs/10.1029/97RG03139

[42] S. Fikri, I. M. Anjasmara, and M. Taufik, "Application of Different Coherence Threshold on PS-InSAR Technique for Monitoring Deformation on the LUSI Affected Area During 2017 and 2019," *IOP Conference Series: Earth and Environmental Science*, vol. 731, no. 1, p. 012036, Apr. 2021. [Online]. Available: https://iopscience.iop.org/article/10.1088/1755-1315/731/1/012036

[43] P. F. Giordano, A. Kamariotis, G. Giardina, E. Chatzi, and M. P. Limongelli, "Uncertainty propagation in satellite InSAR data analysis for structural health monitoring," *Automation in Construction*, vol. 177, p. 106371, Sep. 2025. [Online]. Available: https://www.sciencedirect.com/science/article/pii/S092658052500411X

[44] R. F. Hanssen, *Radar interferometry: data interpretation and error analysis*. Springer, 2001.

[45] Copernicus SentiWiki, "Sentinel-1 mission," 2026, accessed: February 2026. [Online]. Available: https://sentiwiki.copernicus.eu/web/s1-mission

[46] European Space Agency, "Cosmo-skymed mission," 2026, accessed: February 2026. [Online]. Available: https://earth.esa.int/eogateway/missions/cosmo-skymed

[47] Umbra, "Delivering Global Omniscience • Umbra Space," 2023, accessed: 2025. [Online]. Available: https://umbra.space/

[48] C. Space, "Capella Space - Amplify Intelligence," 2025. [Online]. Available: https://www.capellaspace.com/

[49] A. Sandoli, E. Petracca, C. Rainieri, and G. Fabbrocino, "Operation of Interferometric SBAS-DInSAR Data for Remote Structural Monitoring

of Existing Bridges," *J. Bridge Eng.*, vol. 29, no. 11, p. 04024085, Nov. 2024. [Online]. Available: https://ascelibrary.org/doi/10.1061/JBENF2.BEENG-6850

[50] P. Berardino, G. Fornaro, R. Lanari, and E. Sansosti, "A new algorithm for surface deformation monitoring based on small baseline differential SAR interferograms," *IEEE Trans. Geosci. Remote Sensing*, vol. 40, no. 11, pp. 2375–2383, Nov. 2002. [Online]. Available: http://ieeexplore.ieee.org/document/1166596/

[51] V. Macchiarulo, P. Milillo, M. J. DeJong, J. González Martí, J. Sánchez, and G. Giardina, "Integrated InSAR monitoring and structural assessment of tunnelling-induced building deformations," *Structural Contr & Hlth*, vol. 28, no. 9, Sep. 2021. [Online]. Available: https://onlinelibrary.wiley.com/doi/10.1002/stc.2781

[52] K. J. Reinders, R. F. Hanssen, F. J. Van Leijen, and M. Korff, "Augmented satellite InSAR for assessing short-term and long-term surface deformation due to shield tunnelling," *Tunnelling and Underground Space Technology*, vol. 110, p. 103745, Apr. 2021. [Online]. Available: https://linkinghub.elsevier.com/retrieve/pii/S0886779820306994

[53] L. Sun, H. Li, S. Guo, X. Li, P. Chen, and J. Chen, "Incorporating Physical Constraint in Three-Dimensional Time Series InSAR Inversion for Urban Deformation Monitoring," *IEEE Journal of Selected Topics in Applied Earth Observations and Remote Sensing*, vol. 18, pp. 13 967–13 985, 2025. [Online]. Available: https://ieeexplore.ieee.org/abstract/document/11015766

[54] E. Cernuto, D. Salciarini, F. Ubertini, and G. Giardina, "Landslide-Bridge Interaction: A combined approach based on InSAR data and numerical modelling," *International Journal of Disaster Risk Reduction*, vol. 126, p. 105568, Aug. 2025. [Online]. Available: https://www.sciencedirect.com/science/article/pii/S2212420925003929

[55] E. Farneti, N. Cavalagli, M. Costantini, F. Trillo, F. Minati, I. Venanzi, and F. Ubertini, "A method for structural monitoring of multispan bridges using satellite InSAR data with uncertainty quantification and its pre-collapse application to the Albiano-Magra Bridge in Italy," *Structural Health Monitoring*, vol. 22, no. 1, pp. 353–371, Jan. 2023, publisher: SAGE Publications. [Online]. Available: https://doi.org/10.1177/14759217221083609

[56] G. M. Guzman-Acevedo, G. E. Vazquez-Becerra, J. A. Quintana-Rodriguez, J. R. Gaxiola-Camacho, M. Anaya-Diaz, J. C. Mediano-Martinez, and F. J. Carrión Viramontes, "Structural health monitoring and risk assessment of bridges integrating InSAR and a calibrated FE model," *Structures*, vol. 63, p. 106353, May 2024. [Online]. Available: https://www.sciencedirect.com/science/article/pii/S2352012424005058

[57] Y. Zhou, G. Hao, X. Qin, F. Yi, and Z. Tan, "A refined DS-InSAR technique for long-term deformation monitoring of low-coherence bridge groups," *Engineering Structures*, vol. 335, p. 120335, Jul. 2025. [Online]. Available: https://www.sciencedirect.com/science/article/pii/S0141029625007266

[58] H. Kuai, V. Macchiarulo, S. Sharma, P. Karamitopoulos, F. Messali, A. Cicirello, and G. Giardina, "Identification of mechanism-specific persistent scatterers for enhancing MT-InSAR in Structural Health Monitoring applications," *Engineering Structures*, vol. 352, p. 122103, Apr. 2026. [Online]. Available: https://www.sciencedirect.com/science/article/pii/S0141029626000155

[59] V. C. Chen, *The Micro-Doppler Effect in Radar*, 2nd ed. Artech house, 2019, accessed: 2025.

[60] V. Chen, Fayin Li, Shen-Shyang Ho, and H. Wechsler, "Micro-doppler effect in radar: phenomenon, model, and simulation study," *IEEE Transactions on Aerospace and Electronic Systems*, vol. 42, no. 1, pp. 2–21, 1 2006. [Online]. Available: http://ieeexplore.ieee.org/document/1603402/

[61] M. Ruegg, E. Meier, and D. Nuesch, "Vibration and Rotation in Millimeter-Wave SAR," *IEEE Transactions on Geoscience and Remote Sensing*, vol. 45, no. 2, pp. 293–304, Feb. 2007. [Online]. Available: http://ieeexplore.ieee.org/document/4069119/

[62] A. B. Vattulainen, A. Lotti, S. D. Riofrío, C. Suppi, E. Tubaldi, D. Zonta, P. Milillo, and C. Clemente, "Assessment of spaceborne SAR micro-motion measurement for vibration-based SHM," *IEEE Access*, pp. 1–1, 2026. [Online]. Available: https://ieeexplore.ieee.org/document/11343745

[63] F. Biondi, P. Addabbo, D. Orlando, and C. Clemente, "Micro-Motion Estimation of Maritime Targets Using Pixel Tracking in Cosmo-

Skymed Synthetic Aperture Radar Data—An Operative Assessment," *Remote Sensing*, vol. 11, no. 14, Jul. 2019. [Online]. Available: https://www.mdpi.com/2072-4292/11/14/1637

[64] A. Singleton, Z. Li, T. Hoey, and J. P. Muller, "Evaluating sub-pixel offset techniques as an alternative to D-InSAR for monitoring episodic landslide movements in vegetated terrain," *Remote Sensing of Environment*, vol. 147, pp. 133–144, May 2014. [Online]. Available: https://www.sciencedirect.com/science/article/pii/S0034425714000686

[65] A. Focsa, A. Anghel, G. Nico, J. Patruno, and M. Datcu, "Large scene micro-doppler analysis on sar images," in *IGARSS 2024 - 2024 IEEE International Geoscience and Remote Sensing Symposium*, 2024, pp. 11 343–11 346.

[66] C. Clemente, D. Tonelli, A. Lotti, F. Rollo, C. Ilioudis, S. D. Riofrio, F. Biondi, E. Tubaldi, M. Macdonald, D. Zonta, M. Zavagli, M. Costantini, F. Minati, F. Vecchioli, P. Milillo, M. Zimmermanns, E. Imbembo, and M. Corvino, "On Micro-Motion Extraction from High Resolution X-band SAR products," in *IGARSS 2024 - 2024 IEEE International Geoscience and Remote Sensing Symposium*. Athens, Greece: IEEE, 7 2024, pp. 1182–1186. [Online]. Available: https://ieeexplore.ieee.org/document/10642825/

[67] A. Lotti, A. Vattulainen, S. D. Riofrio, C. Suppi, D. Tonelli, F. Rollo, C. Ilioudis, P. Milillo, E. Tubaldi, C. Clemente *et al.*, "Vibration-based structural health monitoring from single-pass sar images," in *International Conference on Experimental Vibration Analysis for Civil Engineering Structures*. Springer, 2025, pp. 402–411. [Online]. Available: https://doi.org/10.1007/978-3-031-96110-6_38

[68] F. Biondi, P. Addabbo, C. Clemente, S. L. Ullo, and D. Orlando, "Monitoring of Critical Infrastructures by Micromotion Estimation: The Mosul Dam Destabilization," *IEEE Journal of Selected Topics in Applied Earth Observations and Remote Sensing*, vol. 13, pp. 6337–6351, 2020. [Online]. Available: https://ieeexplore.ieee.org/document/9224142/

[69] M. Rüegg, E. Meier, and D. Nüesch, "Vibration and Rotation in Millimeter-Wave SAR," *IEEE Transactions on Geoscience and Remote Sensing*, vol. 45, no. 2, pp. 293–304, 2 2007. [Online]. Available: http://ieeexplore.ieee.org/document/4069119/

[70] F. Rollo, C. V. Ilioudis, G. Zefi, A. Lotti, D. Tonelli, M. Zavagli, M. Constantini, D. Zonta, E. Tubaldi, P. Milillo, M. Macdonald, and C. Clemente, "Micro-motion extraction from spotlight SAR using a modified backprojection approach," in *Microwave Remote Sensing: Data Processing and Applications III*, E. Santi, F. Bovenga, C. Notarnicola, and N. Pierdicca, Eds. SPIE, 11 2024, p. 12. [Online]. Available: https://www.spiedigitallibrary.org/conference-proceedings-of-spie/13195/3031678/Micro-motion-extraction-from-spotlight-SAR-using-a-modified-backprojection/10.1117/12.3031678.full

[71] F. Biondi, P. Addabbo, S. L. Ullo, C. Clemente, and D. Orlando, "Perspectives on the Structural Health Monitoring of Bridges by Synthetic Aperture Radar," *Remote Sensing*, vol. 12, no. 23, p. 3852, Nov. 2020. [Online]. Available: https://www.mdpi.com/2072-4292/12/23/3852

[72] A. Focsa, A. Anghel, G. Nico, I. Maggio, M. Datcu, and M. Corvino, "Vibration-Induced Micro-Doppler Estimation in Spaceborne SAR Images Using Doppler Centroid Tracking Across Azimuth Sub-Apertures," in *2025 IEEE International Radar Conference (RADAR)*. IEEE, 5 2025, pp. 1–6. [Online]. Available: https://ieeexplore.ieee.org/document/11031947/

[73] A. B. Vattulainen, F. Rollo, A. Lotti, D. Tonelli, S. D. Riofrio, E. Tubaldi, D. Zonta, C. Ilioudis, P. Milillo, and C. Clemente, "Bridge Vibration Measurements from Very High-Resolution Spaceborne SAR," in *2024 IEEE SENSORS*. IEEE, 10 2024, pp. 1–4. [Online]. Available: https://ieeexplore.ieee.org/document/10785004/

Part II

Publications

5. Spatio-temporal InSAR for bridge monitoring: integrating physics-based models with persistent scatterer interferometry

Context and contribution to the thesis

This chapter addresses the first research question of the thesis by investigating whether InSAR can be enhanced for long-term bridge monitoring. A spatio-temporal InSAR (ST-InSAR) framework is proposed that employs a physics-based structural model within the interferometric analysis.

The following pages present the post-print of

> **Lotti, A.**, Zorzi, S., Tubaldi, E., Rocca, A., Perissin, D., Zonta, D. (2026). Spatio-temporal InSAR for bridge monitoring: integrating physics-based models with persistent scatterer interferometry, *Structural Health Monitoring*, https://doi.org/10.1177/14759217261453023

as published in the Journal *Structural Health Monitoring*, differing only from the published article in terms of layout, formatting, and notation.

Authors' contributions:

Lotti, A.: conceptualisation, methodology, investigation, formal analysis, visualisation, software, writing (original draft), review. **Zorzi, S.**: methodology, software, review. **Tubaldi, E.**: methodology, review, supervision. **Rocca, A.**: methodology, review. **Perissin, D.**: methodology, review. **Zonta, D.**: methodology, review, supervision, funding acquisition.

Abstract

This work presents a novel spatio–temporal InSAR (ST-InSAR) framework that integrates physics-based structural models into persistent scatterer interferometry (PSI) for bridge monitoring. The proposed approach mitigates the limitations of conventional PSI in civil infrastructure applications, namely, large displacements that exceed ambiguity limits and the lack of correlation with air temperature. ST-InSAR exploits spatial correlation among PSs to jointly estimate the displacements across the entire structure. The framework is applied to the Colle Isarco Viaduct (Italy), where its performance is compared with that of conventional multi-temporal PSI, using benchmark topographic measurements. Results show that ST-InSAR can detect structural displacements with an accuracy on the order of $2\ \mathrm{mm}$, even at locations where PSI fails. Additionally, temporal coherence values increase from approximately 0.08 (PSI) to over 0.9. Finally, the proposed framework enables the estimation of the temperature gradient across the bridge deck with an accuracy better than $1\ ^{\circ}\mathrm{C}$, providing information about the structural thermal state beyond displacement monitoring.

Keywords: structural health monitoring, remote sensing, InSAR, persistent scatterer, physics-based extraction

5.1 Introduction

Structural Health Monitoring (SHM) of bridges and viaducts is traditionally performed with contact-sensors directly installed on the structure of interest. Recourse to these technologies requires high economic investments, including the initial sensor costs, the installation, and the maintenance [1, 2]. As a consequence, the number of infrastructures that can be equipped with continuous monitoring systems remains limited. This condition is particularly problematic in regions with large stocks of ageing bridges, where widespread monitoring is promptly needed but conventional SHM strategies are impractical [3].

Practitioners and researchers have progressively shifted attention towards remote-sensing alternatives [4], which do not require any physical intervention on the structure and can overcome the scalability issues inherent to contact-based approaches. Among these, synthetic aperture radar (SAR) has emerged as a powerful solution for large-scale infrastructure monitoring. SAR is an active microwave imaging technique capable of acquiring high-resolution images of the Earth's surface. Operating from space or ground, SAR sensors illuminate the target surface and measure the backscattered signal, which is characterised by its amplitude (reflectivity) and phase. Because satellite acquisitions cover

wide areas at regular intervals – usually one acquisition per 12-16 days for each satellite– SAR enables simultaneous monitoring of networks of infrastructures [5]. Moreover, SAR data are relatively inexpensive, with image costs ranging from free (e.g., from open-access missions such as Sentinel-1 [6]) up to a few thousand USD for ultra-fine-resolution commercial products [7].

Within SAR-based methods, multi-temporal interferometric SAR (MT-InSAR) exploits the phase difference between multiple SAR images acquired over the same target, and detects slow displacement over time [8]. One widely applied MT-InSAR technique is Persistent Scatterer Interferometry (PSI), which was first introduced by [9] and subsequently refined in numerous studies and comprehensively reviewed by Crosetto et al. [10]. PSI focuses on pixels that behave as stable radar reflectors – typically metallic or geometrically sharp-like features – and extracts their displacement time series along the radar line of sight (LOS) with millimetric precision. PSI have been successfully employed for the monitoring of reinforced [11, 12] and prestressed concrete bridges [13, 14], railway bridges [15, 16], cable-stayed bridges [17, 18], arch bridges [19], dam foundations [20] and even scour-related processes [21].

Despite its advantages, PSI performance significantly depends on the temporal stability of the pixel amplitude and phase. Candidate persistent scatterers (CPS) are typically selected based on the *amplitude stability index* (ASI) and later validated using *temporal coherence*, which quantifies how well a pixel phase time series follows the assumed interferometric phase model. However, several factors can lead to coherence loss, including [22]: changes in the scatterer properties (i.e. temporal decorrelation); changes in the orbit geometries (i.e. geometrical decorrelation); errors in the assumed deformation model; and displacements exceeding the radar measurement ambiguity interval. Because the interferometric phase is wrapped within the interval $[-\pi, \pi)$, two LOS displacements that differ by $\lambda/2$ produce identical wrapped interferometric phase values (Figure 5.1). This periodicity implies that the phase measurement is inherently ambiguous. However, the maximum LOS displacement that can be measured unambiguously, in terms of both magnitude and sign, is limited to $\pm\lambda/4$, since larger displacements cause the interferometric phase to exceed the $\pm\pi$ domain [23].

Several methods have been developed to deal with poorly coherent PSs, such as Quasi-PS (QPS) [24] and the Stanford Method for PS (StaMPS) [22]. These techniques perform well for several classes of problems, including land deformation monitoring, as long as the monitored displacements are slow (i.e., limited magnitude between satellite passes) and exhibit strong correlation with time and air temperature. In contrast, bridge displacement presents different

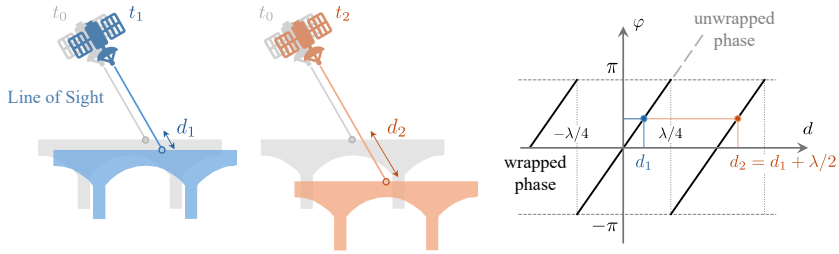


Figure 5.1: Phase ambiguity issue in which two bridge LOS displacements d_1 and d_2, that differ by $\lambda/2$, correspond to the same wrapped interferometric phase value.

characteristics:

- In terms of magnitude, differential displacements between successive acquisitions can be large – especially for medium and long-span bridges – and may exceed the unambiguous displacement limit $\lambda/4$.
- Bridge displacements are not directly correlated with air temperature but rather with the structural temperature of the bridge, which is often governed by temperature gradients across the deck.

Another important limitation of conventional interferometric methods is that scatterers are treated independently, which inherently implies no spatial correlation between closely-spaced points. This assumption is particularly limiting for bridge monitoring, where scatterers should exhibit space-correlated displacement given by the mechanics of structural deformation. Consequently, a natural extension of the InSAR techniques is to integrate into the analysis a physics-based model capable of predicting the spatial deformed shape of the structure of interest.

Physics-augmented approaches have been integrated with InSAR data regarding geotechnical and tunnelling applications to help resolve phase ambiguities [25, 26, 27, 28]. Regarding bridge monitoring, several studies have integrated structural models to interpret observed displacement patterns, solve phase-ambiguity issues, and infer potential material changes and damages [18, 29, 19, 30, 31, 32, 33]. However, in these cases, bridge models were employed in a post-processing phase, once InSAR displacement measurements were already available.

To the best of the authors' knowledge, no prior work has integrated a physics-based structural deformation model directly into the PSI extraction process itself in order to account for refined spatial and temporal bridge behaviour during the displacement time series estimation.

5.1.1 Research Objectives

This paper proposes a novel framework that directly integrates a physics-based structural model of the bridge into the interferometric phase formulation of PSI, explicitly accounting for spatial and temporal deformation. This integration is achieved by relaxing some conventional PSI assumptions, specifically the linear correlation of deck displacement with time and with air temperature, and by introducing spatial dependency of the PSs located on the bridge deck, according to the expected and compatible structural deflection.

The proposed framework is able to recover displacement information at locations that are typically discarded due to low temporal coherence. By mitigating the factors that typically lead to coherence loss in InSAR bridge monitoring, the method improves the reliability of displacement time series estimates that would normally be rejected. More specifically, it reduces displacement estimation errors and enhances the temporal coherence of PSI discarded pixels

This methodology is applied to the Colle Isarco Viaduct in Vipiteno (Italy), a long-span prestressed concrete highway bridge consisting of two parallel decks with cantilever–Gerber beam structural configurations. The results are compared with those obtained using conventional PSI and validated against benchmark topographic surveying measurements on the bridge.

The remainder of the paper is organized as follows: Section 5.2 reviews the fundamentals of InSAR and the conventional PSI technique; Section 5.3 describes the proposed methodology; Section 5.4 presents the case study; Section 5.5 presents the results and compares the performance of the proposed framework with that of PSI; Section 5.6 discusses the experimental results; and Section 5.7 concludes the paper.

5.2 SAR Background

This section briefly revisits the fundamental concepts of SAR interferometry required to understand the methodology proposed in this work, with particular emphasis on the PSI technique. The objective is to introduce the key principles, assumptions, and processing steps underlying traditional PSI, in order to clarify its limitations when applied to bridge monitoring and to provide the motivations for this study.

In the remainder of this paper, the term PSI refers to the traditional persistent scatterer interferometry approach.

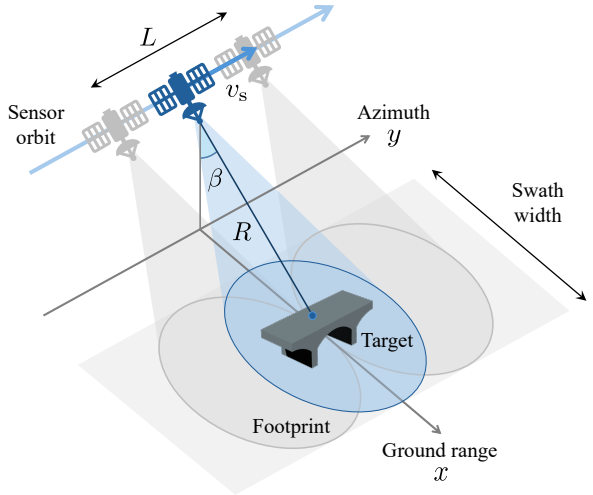


Figure 5.2: SAR geometry orbit in stripmap acquisition mode.

5.2.1 SAR Interferometry

In SAR imaging, the sensor emits a radar signal with an incidence angle β, measured relative to the vertical direction. The distance from a ground target (e.g. the monitored bridge) to the sensor is called slant-range distance, R, which defines the sensor line of sight. During the acquisition, the sensor travels at a constant velocity v_s along a straight orbital path in the azimuth direction y, synthetically extending the antenna aperture L – hence the term *synthetic aperture radar*. Figure 5.2 shows the orbital geometry for a *stripmap* acquisition mode, in which the antenna beam is fixed to illuminate a continuous strip of the ground surface.

A displacement d along the LOS, with respect to a reference acquisition, generates a phase shift φ in the backscattered radar signal (Figure 5.1). This relationship is expressed as:

$$\varphi = \frac{4\pi}{\lambda} d \tag{5.1}$$

where λ is the radar centre wavelength.

Given a reference acquisition r, the interferometric phase at acquisition i for a generic p-th pixel in the image, relative to a reference point O, is defined as the double difference [34]:

$$\varphi_{po}^{(r,i)} = \left[\varphi_p^{(r)} - \varphi_o^{(r)}\right] - \left[\varphi_p^{(i)} - \varphi_o^{(i)}\right] \tag{5.2}$$

where $\varphi_p^{(r)}$ and $\varphi_p^{(i)}$ are the phases of pixel p in acquisitions r and i, respectively,

and $\varphi_o^{(r)}$ and $\varphi_o^{(i)}$ are the corresponding measured phases of the reference point O. For brevity, the reference instant r and point O are omitted from now on.

The interferometric phase $\varphi_p^{(i)}$ is composed of several physical contributions [8]:

$$\varphi_p^{(i)} = \varphi_{p,\text{flat}}^{(i)} + \varphi_{p,\text{atmo}}^{(i)} + \varphi_{p,\text{height}}^{(i)} + \varphi_{p,\text{disp}}^{(i)} + \varphi_{p,\text{noise}}^{(i)} \tag{5.3}$$

where:

- $\varphi_{p,\text{flat}}^{(i)}$ is the flat-terrain component, due to the different geometric locations of the reference point and the pixel of interest.
- $\varphi_{p,\text{atmo}}^{(i)}$ is the atmospheric component, due to tropospheric refractivity variations.
- $\varphi_{p,\text{height}}^{(i)}$ is the topographic component, relative to the height difference between the points considered.
- $\varphi_{p,\text{disp}}^{(i)}$ is the LOS displacement component.
- $\varphi_{p,\text{noise}}^{(i)}$ is the noise introduced by the model uncertainty and the multiple scatterers within the same resolution cell.

The contributions $\varphi_{p,\text{flat}}^{(i)}$, $\varphi_{p,\text{atmo}}^{(i)}$ can be estimated and removed using standard interferometric processing techniques [8, 9]. After correcting for these components – and neglecting the residual noise term – the remaining interferometric phase can be modelled as a function of only the scatterer height and the LOS displacement [34]:

$$\varphi_p^{(i)}\left(h_p, d_p^{(i)}\right) = \varphi_{p,\text{height}}^{(i)}\left(h_p\right) + \varphi_{p,\text{disp}}^{(i)}\left(d_p^{(i)}\right) = \frac{4\pi}{\lambda}\frac{B_n^{(i)}}{R\sin\beta}h_p + \frac{4\pi}{\lambda}d_p^{(i)} \tag{5.4}$$

The first term describes the sensitivity of the interferometric phase to the scatterer height h_p, which depends on the acquisition geometry; more specifically, on the incidence angle β, the slant-range distance R and the normal baseline $B_n^{(i)}$. This latter is defined as the distance between the sensor positions of the reference acquisition and acquisition i, orthogonal to the range direction, as illustrated in Figure 5.3. The second term is directly proportional to the LOS displacement $d_p^{(i)}$ that occurs between the two acquisitions.

5.2.2 Multi-Temporal InSAR and persistent scatterer interferometry

Multi-temporal InSAR uses a set of SAR acquisitions to reconstruct the entire time series of LOS displacement [9]. Let M be the total number of acquisitions collected over the same target. In the classic PSI method, the LOS

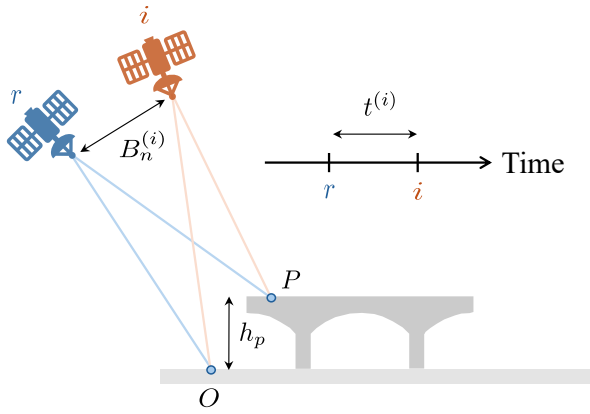


Figure 5.3: Interferometric geometry showing the reference orbit and the acquisition orbit at time $t^{(i)}$.

displacement is assumed to be a linear function of both time t and air temperature T – typically measured at the nearest weather station. The displacement model can be expressed as [34]:

$$d_p^{(i)} = {}_t d_p \cdot t^{(i)} + {}_T d_p \cdot T^{(i)} \tag{5.5}$$

where ${}_t d_p$ and ${}_T d_p$ are two constant coefficients that represent the linear displacement velocity and the thermal expansion coefficient, respectively. These coefficients correspond to the partial derivatives of the LOS displacement with respect to time and air temperature, which explains the adopted subscript notation.

By substituting the displacement model in Eq.5.4, the interferometric phase can be written as a function of the scatterer height and the displacement coefficients:

$$\varphi_p^{(i)}\left(h_p, {}_t d_p, {}_T d_p\right) = \frac{4\pi}{\lambda} \frac{B_n^{(i)}}{R \sin\beta} h_p + \frac{4\pi}{\lambda} \left[{}_t d_p \cdot t^{(i)} + {}_T d_p \cdot T^{(i)} \right] \tag{5.6}$$

where $i = 1, 2, \ldots, M$ denotes the interferogram generated with respect to the reference image r.

The three unknown parameters $[h_p, {}_t d_p, {}_T d_p]$ are assumed to be constant for each pixel and are jointly estimated – exploiting the full interferometric set – using a Maximum Likelihood Estimation (MLE) approach. The estimation is performed on the magnitude of the following objective function [34]:

$$\gamma_p\left(h_p, {}_t d_p, {}_T d_p\right) = \frac{1}{M} \sum_{i=1}^{M} \exp\left\{ j \cdot \left[\phi_p^{(i)} - \varphi_p^{(i)}\left(h_p, {}_t d_p, {}_T d_p\right) \right] \right\} \tag{5.7}$$

where $\phi_p^{(i)}$ represents the measured interferometric phase, depurated from the flat terrain and atmospheric components, while $\varphi_p^{(i)}$ is the modelled interferometric phase given by Eq.5.6, and expressed as a function of the unknown parameters, and j represent the imaginary unit.

The optimal parameter estimates are obtained by maximising the magnitude of the objective function:

$$\{\tilde{h}_p, {}_t\tilde{d}_p, {}_T\tilde{d}_p\} = \arg \max_{h_p, {}_td_p, {}_Td_p} \left|\gamma_p \left(h_p, {}_td_p, {}_Td_p\right)\right| \tag{5.8}$$

Once the optimal parameters are determined, the displacement time series for each PS can be reconstructed by substituting the optimal values ${}_td_p$ and ${}_Td_p$ into the displacement model of Eq. 5.5, yielding $d_p^{(i)} = {}_td_p \cdot t^{(i)} + {}_Td_p \cdot T^{(i)}$ for each interferogram.

Finally, the temporal coherence $\gamma_{p,t}$ of the pixel is evaluated with the following relationship:

$$\gamma_{p,t} = \left|\gamma_p \left(\tilde{h}_p, {}_t\tilde{d}_p, {}_T\tilde{d}_p\right)\right| \tag{5.9}$$

where, in this case, the subscript $_{\mathrm{t}}$ is written on the right and in roman font to denote *temporal* coherence, rather than a time derivative. The pixel (i.e., candidate persistent scatterer) is typically accepted as a permanent scatterer if its temporal coherence exceeds a certain threshold (usually preferably higher than 0.75 [35]).

5.2.3 PSI limitations in bridge monitoring

In summary, conventional PSI techniques approximate the behaviour of each persistent scatterer using a parametric displacement model assumed to be a linear function of time and air temperature, and spatially uncorrelated between neighbouring pixels. While these assumptions are often acceptable for monitoring slow-moving geophysical phenomena, they are often violated in the case of bridge monitoring, leading to a loss of performance.

The main limitations can be summarised as follows:

1. Long-span bridges often exhibit relatively large displacements that can exceed in magnitude the ambiguity limit $d_{\text{lim}} = \lambda/4$. For bridge monitoring, shorter radar wavelengths are typically employed to increase spatial resolution and identify a larger number of scatterers on the structure. However, shorter wavelengths further reduce the displacement ambiguity limit. For example, in X-band systems $\lambda/4 \simeq 8$ mm.

2. The assumption of spatially independent PSs is generally not valid for

bridges, where closely-spaced scatterers are mechanically dependent and must follow physically admissible deformation shapes given by the structural behaviour of the bridge.

3. Thermal deformation is governed by structural temperature, which is influenced not only by air temperature but also by solar radiation and thermal gradients. While the deformation of some structural components (e.g., piers or deck longitudinal expansion) may be primarily correlated with air temperature, other deformation mechanisms (e.g., deck deflection induced by vertical temperature gradients) cannot be adequately described using the above model.

As a consequence of these limitations, even pixels with stable reflectivity across all SAR acquisitions may result in having low temporal coherence and end up being discarded by conventional PSI analyses.

The methodology proposed in the next section addresses these limitations by jointly processing all stable scatterers, including those that would normally be discarded due to low temporal coherence, and by explicitly accounting for the physical behaviour of the structure.

5.3 Method

The general idea of the proposed framework is to employ, within the InSAR processing pipeline, a time-varying geometrical model that describes the expected structural deformation of the bridge. This key step allows one to constrain the space of admissible solutions to a limited set of physically feasible configurations, consistent with the expected spatial and temporal deformation behaviour of the structure. For this reason, the proposed approach is referred to as spatio-temporal InSAR (ST-InSAR).

In this section, the general ST-InSAR framework is presented, first describing the structural model employed and then illustrating its integration into the PSI analysis. Its application to a real-world case study is discussed in Section 5.4.

5.3.1 Structural Model

The first step consists of defining a structural model of the bridge – specifically the deck – to capture the spatial deformation affecting different PSs. This model replaces the generic deformation law of Eq. 5.5, and explicitly describes the physical mechanisms responsible for the observed displacement. Defining a structural model can be done with several layers of approximations, ranging from simplified 1D beam finite-element (FE) representations to more detailed

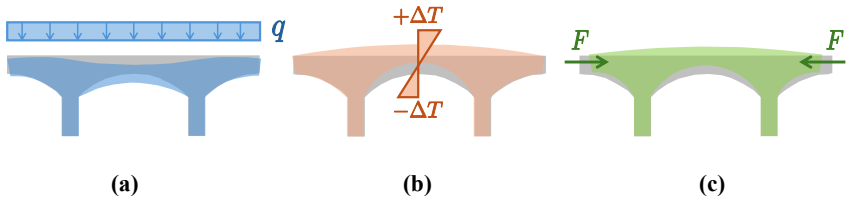


Figure 5.4: Illustration of some of the different causes of bridge deformation: (a) dead load q, (b) temperature gradient ΔT, and (c) creep effects due to the horizontal prestressing force F.

shell or full 3D models. Regardless of the chosen complexity, the deck deformation is mainly influenced by the following effects:

1. Permanent and live loads, that generate an elastic deformation, mostly vertical (Figure 5.4a).
2. Temperature, that generates an expansion along the deck direction, expansion of the piers and vertical deflection (Figure 5.4b).
3. Slow phenomena, such as *creep* or *prestressing relaxation*, affecting both vertical and horizontal displacements (Figure 5.4c).

The unknown quantities that represent the deformation mechanisms listed above are collected in the vector θ of the state parameters (SP).

The displacement is expressed in a local reference system fixed to the bridge deck and denoted as $\{x', y', z'\}$; where x' is the longitudinal direction, y' is the transversal (horizontal) direction, and z' is the vertical direction.

The structural model uses known quantities such as time $t^{(i)}$ and air temperature $T^{(i)}$ – retrieved from SAR acquisition metadata and external weather stations – and the SP to compute the three-dimensional differential displacement $\boldsymbol{u}_p^{(i)}$ at each PS p and for every acquisition i:

$$\boldsymbol{u}_p^{(i)} = \left[u_p^{(i)}, v_p^{(i)}, w_p^{(i)}\right]^{\mathrm{T}} = \mathcal{M}_p\left(\theta, t^{(i)}, T^{(i)}\right) \tag{5.10}$$

where $u_p^{(i)}$, $v_p^{(i)}$, and $w_p^{(i)}$ are the longitudinal, transversal and vertical differential displacements, respectively. A schematic representation of this reference system is represented in Figure 5.5.

A further assumption, which covers the vast majority of practical cases, is that the state parameters controlling the model can be classified into two groups:

- *Time-varying and space-constant parameters*, e.g., a temperature gradient $\Delta T^{(i)}$ assumed uniform along the deck at time $t^{(i)}$.

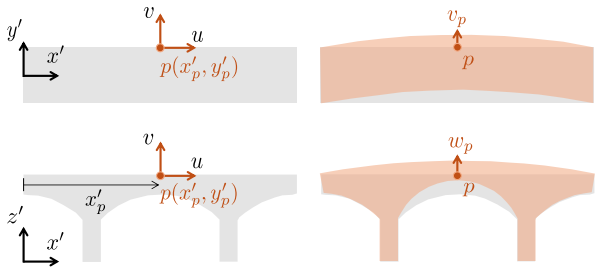


Figure 5.5: Scheme of the reference system adopted to describe the three-dimensional deck displacement.

- *Space-varying and time-constant parameters*, e.g., a linear deformation rate or thermal expansion coefficient that differs from pier to pier but remains constant over the acquisition series.

Let N_t and N_s, be the number of time-varying and space-varying parameters, respectively; the total number of structural unknowns equals:

$$N = N_t + N_s \tag{5.11}$$

5.3.2 Integration of the structural model with the SAR Geometry

InSAR provides, for each PS, a sequence of interferometric phases $\varphi_p^{(i)}$ that depends on the LOS displacement $d_p^{(i)}$. The key idea is to replace the displacement model of Eq.5.5 with the structural model described in the previous section. Figure 5.6 shows their geometric relationship. The LOS displacement of PS p at an instant i can be obtained from the three-dimensional displacement $\boldsymbol{u}_p^{(i)}$ via the transformation:

$$d_p^{(i)} = [\cos\alpha \;\; \sin\beta, \; -\sin\alpha \, \sin\beta, \; -\cos\beta] \; \cdot \boldsymbol{u}_p^{(i)} = \boldsymbol{A} \cdot \boldsymbol{u}_p^{(i)} \tag{5.12}$$

where α is the relative azimuth angle between the bridge longitudinal axis and the SAR azimuth direction, β is the SAR incidence angle, and $\boldsymbol{A}$ is the LOS transformation vector. By substituting the structural model into this expression, one obtains:

$$d_p^{(i)} = \boldsymbol{A} \cdot \mathcal{M}_p \left(\boldsymbol{\theta}, t^{(i)}, T^{(i)} \right) = \mathcal{F}_p \left(\boldsymbol{\theta}, t^{(i)}, T^{(i)} \right) \tag{5.13}$$

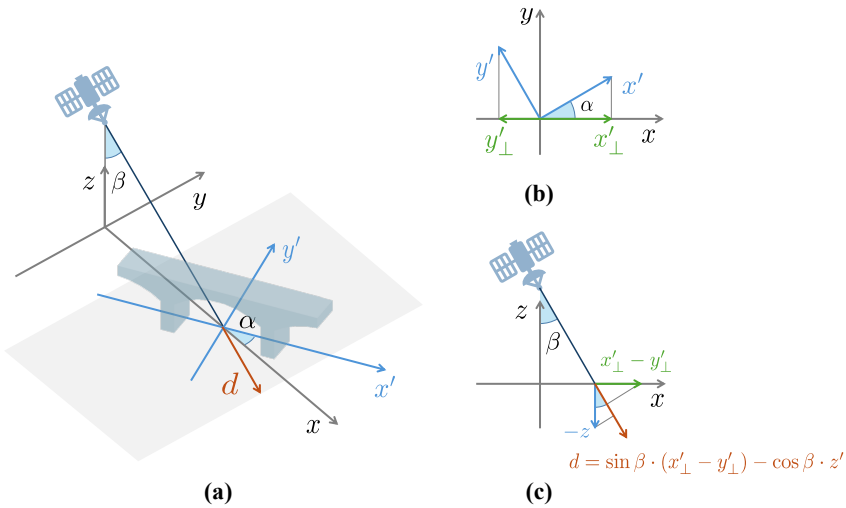


Figure 5.6: Satellite reference system $\{x, y, z\}$ and bridge reference system $\{x', y', z'\}$: (a) three-dimensional view, (b) $x - y$ plane, (c) $x - z$ plane.

5.3.3 InSAR phase model with structural constraints

Replacing the LOS displacement term in the PSI phase model (Eq.5.4) returns:

$$\varphi_p^{(i)}\left(h_p, \boldsymbol{\theta}, t^{(i)}, T^{(i)}\right) = \frac{4\pi}{\lambda}\frac{B_n^{(i)}}{R\sin\beta}h_p + \frac{4\pi}{\lambda}\mathcal{F}_p(\boldsymbol{\theta}, t^{(i)}, T^{(i)}) \tag{5.14}$$

To estimate the unknown parameters h_p and $\boldsymbol{\theta}$ for all PSs located on the bridge deck, the MT-InSAR objective function (Eq.5.7) can be rewritten as:

$$\Gamma\left(h_p, \boldsymbol{\theta}\right) = \frac{1}{P\,M}\sum_{p=1}^{P}\sum_{i=1}^{M}\exp\left\{j\left[\phi_p^{(i)} - \frac{4\pi}{\lambda}\frac{B_n^{(i)}}{R\,\sin\beta}\,h_p - \frac{4\pi}{\lambda}\,\mathcal{F}_p\left(\boldsymbol{\theta}, t^{(i)}, T^{(i)}\right)\right]\right\} \tag{5.15}$$

where P represents the number of identified PSs on the bridge, while M is the number of interferograms available. The optimal estimates of the unknowns h_p and $\boldsymbol{\theta}$ are obtained by maximising the magnitude of the objective function $|\Gamma_p\left(h_p, \boldsymbol{\theta}\right)|$. The total number of unknowns is therefore $N + P$, consisting of the N model state parameters and the P different PS heights. Since the total number of observations is $M \cdot P$, well-poseness requires that $N + P \leq M \cdot P$ (ideally $N + P << M \cdot P$).

Several efficient global optimisation algorithms have been presented in the scientific literature [36], and most widely used scientific programming envi-

ronments offer reliable implementations of these methods. In this work, the Particle Swarm Optimisation (PSO) technique [37, 38, 39] is used to solve the optimisation problem. Additional information is provided in Section 5.4.

It should be noted that the precise location of PSs can be affected by uncertainty, as they could be located not only in the surroundings but also on structural elements other than those modelled [40]. However, the consistency between the structural model and the actual PSs spatial distribution can be verified by recomputing the temporal coherence – substituting the modelled phase of Eq. 5.14 into Eq. 5.9. PSs whose displacement phase time series is not consistent with the assumed deformation model will produce low temporal coherence and can be filtered out of the processing data. If a further consistency check is required, PSs with an estimated height falling outside the expected deck elevation (within a tolerance given by the scatterer height sensitivity) can be excluded.

5.4 Case study

5.4.1 Colle Isarco Viaduct

The case study selected for the application of the framework is the Colle Isarco Viaduct in Vipiteno, Italy. This structure was constructed in 1968 and opened later in 1971 and is now part of the A22 Highway. It has a total length of 1028 metres, consisting of two parallel and independent decks and 13 spans.

The portion of major interest is the main spans between Piers 7–8 and 9–10, consisting of symmetrical prestressed concrete Niagara box girders, with a filler beam (Gerber beam) connecting them. Each of the two elements is divided into a main span of length $91\ \mathrm{m}$ and a cantilever span of $59\ \mathrm{m}$. Supported by the two cantilevers, there is a suspended beam of length $45\ \mathrm{m}$. The box girders have a height $10.93\ \mathrm{m}$ on top of Piers 8 and 9, and decrease to $2.57\ \mathrm{m}$ at the half-joints. Technical drawings of the plan and section views are reported in Figure 5.7.

The viaduct underwent progressive deflection over time, which led to major retrofitting interventions, first in 1988 and then in 2014. Since the 2014 intervention, the spans between piers 7 and 10 have been instrumented with 72 optical prisms, 50 of which are on the deck (see Figure 5.9a and Figure 5.9b), for displacement monitoring. Additionally, fibre-optic sensors (FOS) and thermocouples were installed on both the top and bottom slabs at the midspan, Pier 8, and the cantilever half-joint, to measure deck deformations and local temperature, respectively. For these sections, it is therefore possible to estimate the temperature gradient, computed as the difference between the temperature recorded in the upper slab and the one measured in the bottom slab.

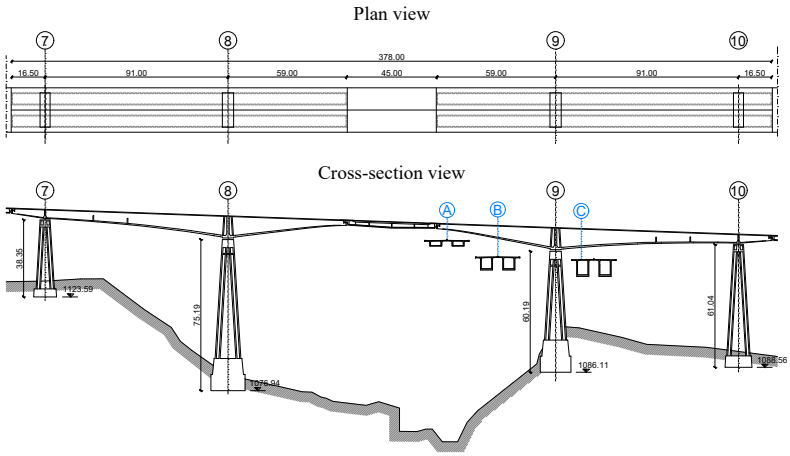


Figure 5.7: Plan and side views of the viaduct portion between Piers 7 *and* 10*.*

5.4.2 PSI analysis of the viaduct

A PSI analysis of the viaduct was carried out by Tonelli et al. [13] using a dataset of 62 COSMO-SkyMed X-band images acquired in stripmap HIMAGE mode, in descending orbit, between 5 July 2016 and 25 June 2020, with reference image corresponding to 18th March 2018 (shown in the star-graph of Figure 5.8(a)). The analysis resulted in the identification of 173 PSs on the Pier 7–10 segment.

As shown in the plan distribution in Figure 5.8 and 5.9, the PSs align along three longitudinal lines, corresponding to the backscatter from the guardrails. The central line contains the reflection from both carriageways, which fall within the same SAR resolution cell. This phenomenon is visible in the reflectivity map of the Piers 7–8 segment in Figure 5.8(b). Both figures also report the temporal coherence γ_t of the extracted PSs.

In both figures, a significant reduction in temporal coherence can be observed near the ends of the cantilevers, in the vicinity of the half-joints, and on the Gerber beam, with values as low as 0.08. Temporal coherence progressively increases towards the piers and the main span, where overall high values are observed – particularly at the piers, with coherence values reaching up to 0.90.

To understand this phenomenon, it is useful to recall the two fundamental assumptions of PSI monitoring (explained in Section 5.2): (i) displacement

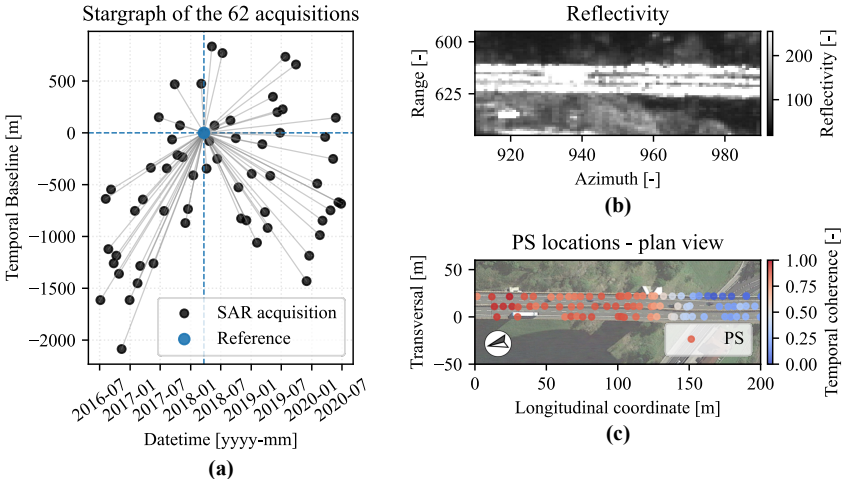


Figure 5.8: (a) Star graph showing temporal and perpendicular baselines of the 62 SAR images, (b) reflectivity map; and (c) PSs distribution coloured by temporal coherence.

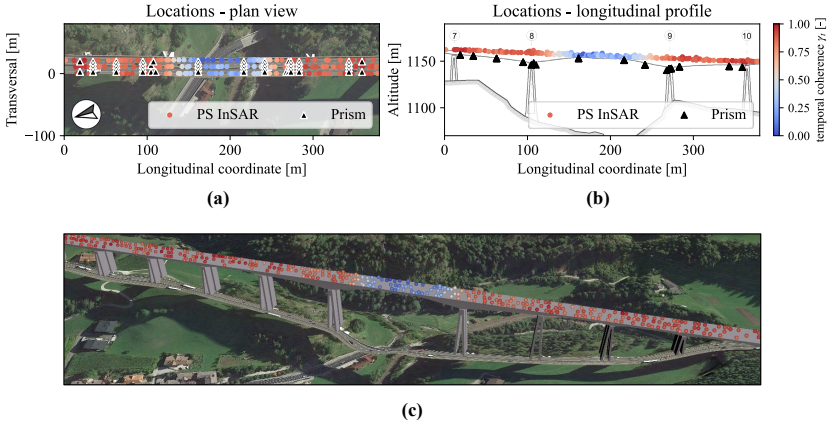


Figure 5.9: PSs distribution coloured by temporal coherence γ_t: (a) plan view, (b) side view, and (c) 3D view in Google Earth Engine. Topographic prism locations are shown as triangles.

magnitudes shorter than $\lambda/4$ to avoid phase ambiguity, and (ii) displacements are assumed to be linearly varying with time and air temperature, according to the model given in Eq.5.5.

In order to verify whether these assumptions are satisfied for the actual structural behaviour, topographic measurements (i.e., true displacements) were projected on the satellite LOS. The displacement time series, relative to the ref-

erence acquisition, are reported in Figure 5.10, and their Pearson's correlation indexes with air temperature and temperature gradient at selected locations. In the figure, four representative points on the north carriageway are considered: at Pier 7 (blue), at the middle of the main span (orange), at Pier 8 (green), and at the half-joint (red).

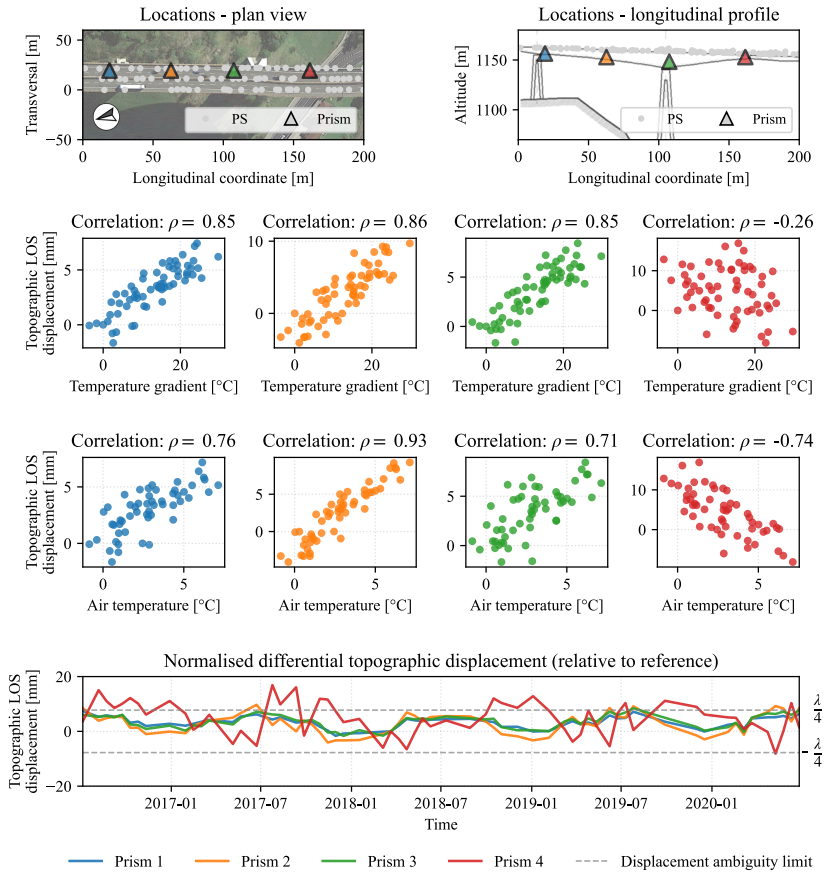


Figure 5.10: LOS-projected topographic displacements at four locations, their correlation with air temperature, temperature gradient across the section, and corresponding displacement time histories.

At the piers and at the midspan, LOS displacements are relatively contained within the ambiguity bounds and have strong correlation with air temperature $\rho \geq 0.85$ for all cases. These locations, therefore, satisfy the fundamental PSI assumptions, which explains the high temporal coherence observed in the corresponding areas.

Conversely, displacements at the half-joint frequently exceed the ambiguity

limit and are poorly correlated with air temperature $\rho = -0.26$, therefore violating the assumptions and resulting in a significant loss of temporal coherence.

When considering correlation with the deck temperature gradient, a different behaviour is observed. All points exhibit a significant correlation with the temperature gradient; however, the relative importance of this parameter varies spatially. At Pier 7 and Pier 8, the correlation with temperature gradient is weaker ($\rho = 0.76$ and 0.71, respectively) than that associated with air temperature, indicating that pier displacements are primarily governed by uniform thermal expansion.

In contrast, the midspan and the cantilever half-joint show higher correlation with temperature gradient ($\rho = 0.93$ and $\rho = -0.74$, respectively), exceeding that associated with air temperature. This behaviour is consistent with the expected structural behaviour, as the temperature gradient induces vertical thermal deflections that become more dominant when moving from the piers towards the main span and the cantilever.

For brevity, results for the southern carriageway are not reported, but they exhibit the same behaviour.

In summary, PSI analysis is expected to perform well for some of the viaduct points, whereas it is expected to fail on the cantilever span where the fundamental assumptions are violated, as will be confirmed by the experimental results presented in Section 5.5. In this region, displacements are dominated by temperature gradient, which is not represented in the conventional PSI displacement model.

5.4.3 ST-InSAR analysis

To overcome the limitations discussed in the previous sections, the proposed ST-InSAR framework is applied following the methodology explained in Section 5.3. The principal task is to define a structural model of the viaduct that describes its expected spatio-temporal deformation behaviour, therefore enabling the spatial correlation among PSs located on the deck. The parameters of this structural model are then jointly estimated within the interferometric analysis, and the correct LOS displacements are subsequently evaluated.

Dataset

The same dataset used for the PSI analysis was employed, consisting of $M = 62$ SAR images. The reference acquisition corresponds to 18 March 2018. The northern and southern carriageways were analysed separately. To ensure a fair comparison between ST-InSAR and PSI, only the PSs previously identified on the Piers 7–8 segment by the previous PSI analysis were processed. A total of $P = 26$ PSs were identified on the northern carriageway and $P = 19$

on the southern carriageway. The interferometric phase time series of the PSs located on the deck were retrieved using the commercial software SARPROZ©.

Structural Model

In order to apply the ST-InSAR framework to the interferometric phase time series, it is first necessary to define an appropriate structural model of the viaduct case study. The structural analysis focuses on the main span and cantilever span supported by piers 7 and 8. This segment behaves as an isolated structural system, independent from the rest of the viaduct. Since SAR acquisitions primarily illuminate the bridge deck, the structural model is defined for the deck itself. Given the spatial distribution of the persistent scatterers, it is reasonable to assume that the structure behaves predominantly as a linear (i.e. one-dimensional) system that develops along its longitudinal axis.

InSAR measures the displacement along the satellite LOS, which represents a projection of the actual three-dimensional displacement field, composed of longitudinal, transversal and vertical components. For the Colle Isarco viaduct, the satellite descending orbit creates a very small angle with the longitudinal axis of the bridge, which is approximately $\alpha = 2^\circ$ (see Figure 5.11(a) and 5.11(b)). Consequently, the contribution of longitudinal differential displacement $u_p^{(i)}$ to the LOS displacement is negligible in Eq.5.13. Moreover, long-span concrete bridges exhibit transverse displacements that are typically small compared to vertical and longitudinal ones. Under these conditions, the LOS displacement $d_p^{(i)}$ can therefore be assumed to depend primarily on the vertical component $w_p^{(i)}$ (see Figure 5.11(c)).

The vertical deflection of the viaduct at acquisition i is governed mainly by the temperature gradient $\Delta T^{(i)}$ between the upper and lower deck slabs, relative to the reference acquisition. This gradient induces curvature of the deck cross-section, resulting in vertical deflections that vary spatially depending on the local cross-section height. Since $\Delta T^{(i)}$ depends on several environmental factors – such as solar radiation, shading, and wind – it cannot be reliably predicted from air temperature measurements alone. For this reason, $\Delta T^{(i)}$ is treated as an independent parameter for each of the M interferograms.

Deck displacement is also influenced by the expansion of the supporting piers. In contrast to the deck behaviour, the piers displacement is well correlated with time and air temperature. Pier motion is modelled as the superposition of a linear temporal trend and a uniform thermal expansion component, consistent with the conventional PSI displacement model (Eq.5.5). Therefore, for each carriageway, the displacement parameters include one linear displacement rate ${}_t w_{\text{pier}}$ and one thermal-expansion coefficient ${}_T w_{\text{pier}}$ for each of the two piers.

To summarise, the proposed model for the Colle Isarco Viaduct relies on

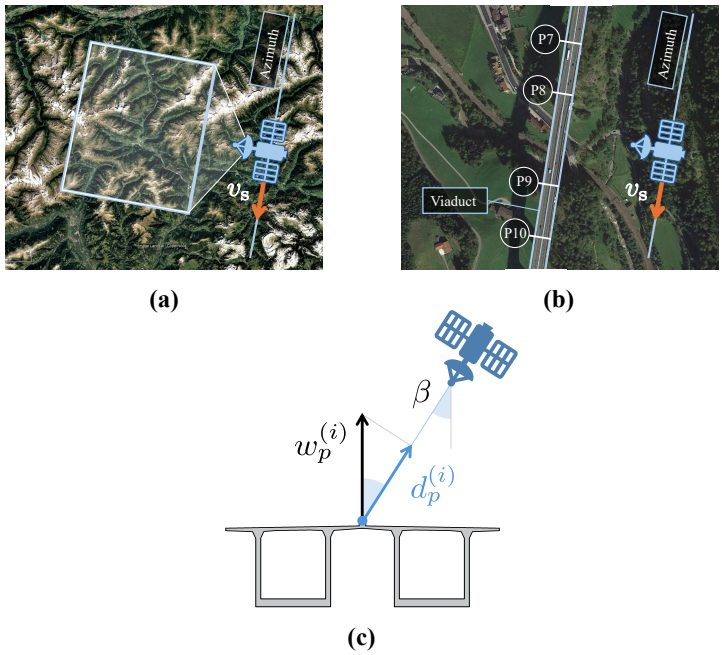


Figure 5.11: (a) Footprint reference SAR image; (b) zoomed-in view of the viaduct P7–P10 with satellite azimuth direction; (c) projection of vertical displacement along the LOS.

the following assumptions:

1. Each carriageway is modelled as a one-dimensional Euler–Bernoulli beam with cubic shape functions. The model computes the displacement response at the deck edges, where the PSs are located.
2. Due to acquisition geometry and bridge type, the LOS displacement is assumed to depend only on the vertical displacement component;
3. Vertical deck deflection is driven by the temperature gradient between the upper and lower deck slabs. The gradient is treated as a separate parameter for each acquisition and, at a given time, is assumed spatially constant over the deck.
4. Pier displacements are treated as imposed boundary conditions and are modelled using a linear relationship with respect to time and air temperature.

The scheme of the model employed is illustrated in Figure 5.12.

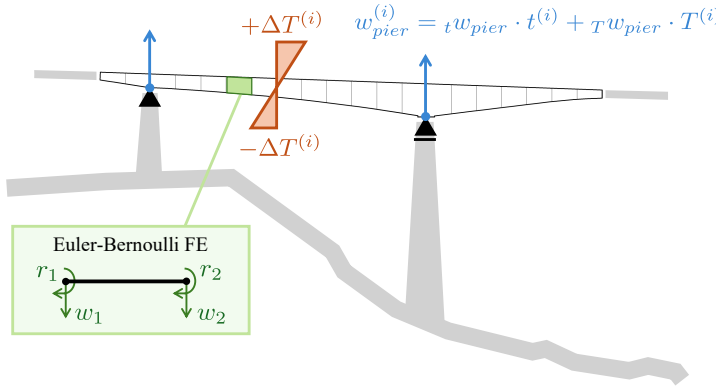


Figure 5.12: 1D Euler-Bernoulli model employed for each carriageway of the segment Pier 7–8.

The resulting state parameter vector for each carriageway is therefore:

$$\theta = \left[\Delta T^{(1)}, \Delta T^{(2)}, ..., \Delta T^{(M)}, {}_t w_{\text{pier},1}, {}_T w_{\text{pier},1}, {}_t w_{\text{pier},2}, {}_T w_{\text{pier},2}\right]^{\mathrm{T}} \quad (5.16)$$

where $\theta \in \mathcal{R}^{(M+4)\times 1}$, where $M = 62$ is the total number of interferograms available. Regarding the number of PSs, a total of $P = 26$ were identified on the northern carriageway and $P = 19$ on the southern.

Parameters identification

To find the optimal estimates of the parameters h_p and θ, which maximise the objective function $|\Gamma(h_p, \theta)|$, the Particle Swarm Optimisation (PSO) algorithm was selected, specifically the Global Best PSO (GB-PSO) implementation provided by the `pyswarms.single.GlobalBestPSO` function in the PySwarms library [41]. For the implementation, the algorithm was configured with 2000 particles and 5000 iterations, a cognitive coefficient of 0.6, a social coefficient of 0.4, and an inertia weight of 0.9. Default settings were maintained for initialisation, velocity management, and clamping options.

5.4.4 Experimental comparison methodology

The LOS displacements measured using ST-InSAR are compared against both the conventional PSI displacement time series and the topographic prism measurements used as a validation benchmark. The performance of ST-InSAR is evaluated using the following metrics:

- Root mean square of the error (RMSE) between SAR and topographic displacements time series, computed after removing the mean value to eliminate bias;

- Pearson's correlation coefficient (ρ) computed on the displacement time series;
- Updated temporal coherence (γ_t) obtained with ST-InSAR, by using the new interferometric phase model in Eq.5.14.

Finally, the estimated temperature gradients $\Delta T^{(i)}$ are validated against thermocouple measurements installed inside the deck.

It is important to note that even the benchmark data are affected by uncertainty, which is due to:

- *Lack of temporal synchronisation*, as topographic measurements timestamps do not coincide with SAR acquisitions, requiring interpolation;
- *Spatial misalignment*, as PSs and prisms do not coincide exactly, so each PS is compared to its closest optical prism.

Consequently, the error observed in the performance evaluation reflects the combined effect of InSAR measurement errors and the spatial and temporal misalignment relative to the validation benchmark.

5.5 Results

This section presents the results obtained from the proposed ST-InSAR analysis. The performance of ST-InSAR is assessed through a comparison with that of PSI. Furthermore, both methods are validated against independent topographic benchmark measurements.

The comparison is carried out both graphically, through Figures 5.13 to 5.15, and numerically using the metrics reported in Table 5.1. The results corresponding to eight different points are reported, selected as the closest available persistent scatterers to the monitored topographic prisms on the viaduct deck.

In addition, temporal coherence obtained by both PSI and ST-InSAR is analysed for all the extracted PSs along the structure. Finally, temperature gradients estimated by ST-InSAR are compared with independent measurements collected from thermocouples embedded in the viaduct deck.

5.5.1 Comparison of ST-InSAR and PSI with benchmark measurements

The analysis first focuses on the northern carriageway. Figure 5.13 illustrates the comparison between the performance of ST-InSAR and PSI, both validated against the benchmark topographic measurements. At the top of the figure, the locations of the analysed PSs, together with the corresponding optical prisms used for topographic measurements, are shown in the plan and longitudi-

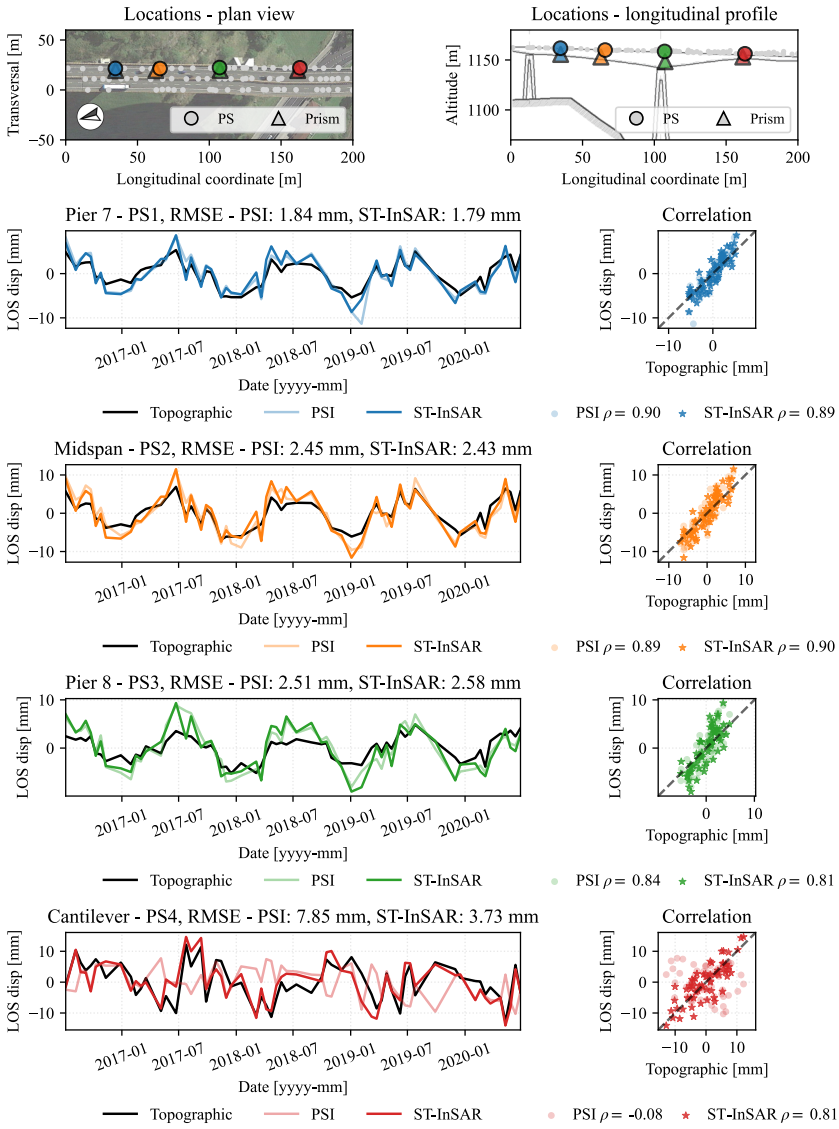


Figure 5.13: North carriageway, PS 1 (Pier 7), PS 2 (Midspan), PS 3 (Pier 8), PS 4 (Cantilever) - ST-InSAR results, compared with PSI and topographic measurements.

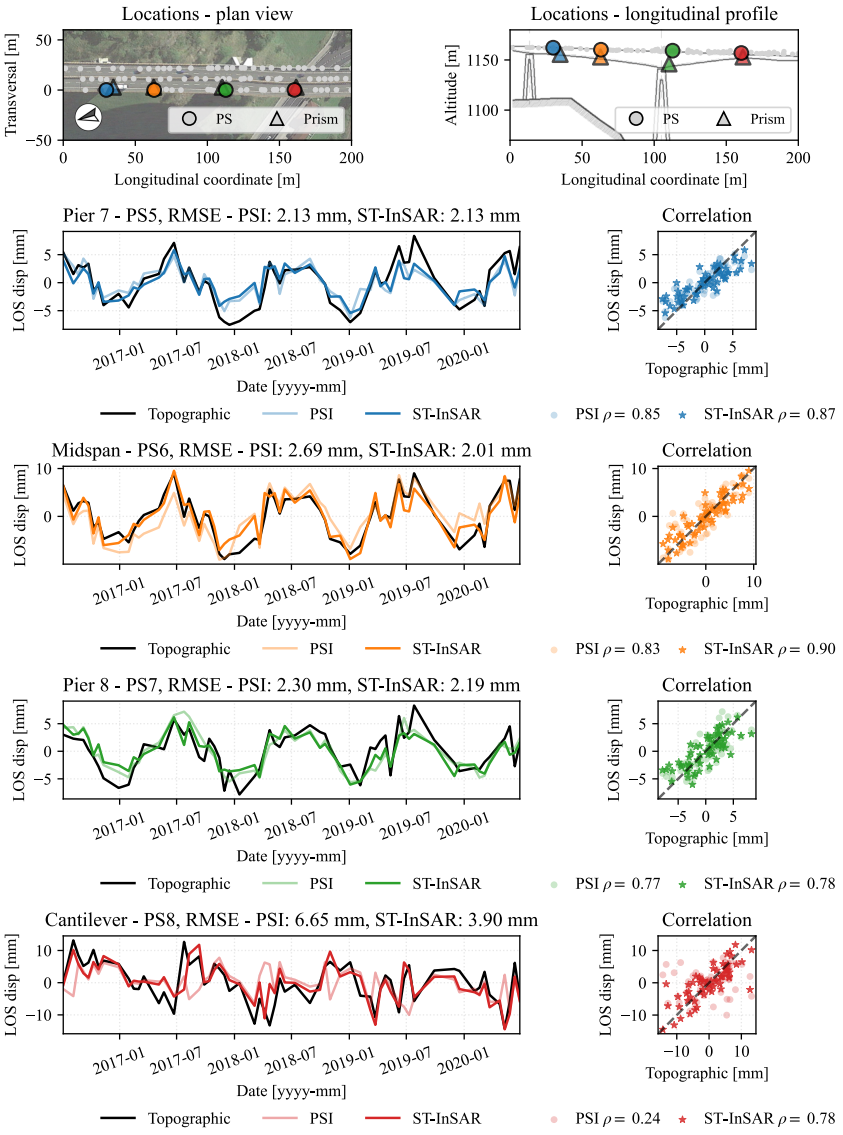


Figure 5.14: South carriageway, PS 5 (Pier 7), PS 6 (Midspan), PS 7 (Pier 8), PS 8 (Cantilever) - ST-InSAR results, compared with PSI and topographic measurements.

PS	Carriageway	Location	RMSE [mm]		Correlation [-]		Coherence [-]	
			PSI	ST-InSAR	PSI	ST-InSAR	PSI	ST-InSAR
1	north	Pier 7	1.84	1.79	0.90	0.89	0.89	0.89
2	north	Midspan	2.45	2.43	0.89	0.90	0.79	0.77
3	north	Pier 8	2.51	2.58	0.84	0.81	0.85	0.83
4	north	Cantilever	7.85	3.73	-0.08	0.81	0.08	0.95
5	south	Pier 7	2.13	2.13	0.85	0.87	0.88	0.89
6	south	Midspan	1.85	1.99	0.92	0.91	0.89	0.88
7	south	Pier 8	2.30	2.19	0.77	0.78	0.85	0.89
8	south	Cantilever	6.65	3.90	0.24	0.78	0.29	0.94

Table 5.1: Performance comparison of ST-InSAR and PSI.

nal profile. The lower panels report the LOS displacement time series (left) and correlation plots (right), where topographic measurements are shown in black, ST-InSAR results are indicated by bold lines, and PSI results by lightly transparent lines. The points reported are PS 1 close to Pier 7 (blue), PS 2 at the midspan (orange), PS 3 at Pier 8 (green), and PS 4 at the cantilever half-joint (red).

It can be observed that ST-InSAR and PSI show very similar performance for PS 1, 2, and 3. Qualitatively, the LOS displacement time series estimated by the two techniques match well, although small discrepancies with respect to the topographic measurements are visible. This behaviour is expected, as discussed previously, since the benchmark measurements are affected by uncertainty due to temporal resampling and spatial misalignment relative to the SAR acquisitions. Figure 5.13 also shows the correlation between InSAR-derived displacements and the topographic measurements (right). Again, for PS 1, 2, and 3, the distributions obtained using ST-InSAR and PSI largely overlap and strongly align along the principal correlation direction.

These observations are supported by the quantitative metrics reported in Table 5.1. For PS 1, 2, and 3, correlation coefficients of both methods are very similar, with overall satisfactory values greater than 0.8, meaning that PSI and ST-InSAR produce very similar displacements. Temporal coherence shows a similar trend: PSs located at the piers and midspan exhibit high PSI coherence (0.79–0.89), and similar values are obtained with ST-InSAR (0.77—0.89). In terms of accuracy, for the same locations, the two techniques substantially produce comparable results with an error on the order of around 2 mm. More specifically, RMSE values range between 1.84-–2.51 mm for PSI and 1.79—2.51 mm for ST-InSAR.

A marked difference in behaviour is observed for PS 4, located at the cantilever half-joint. At this location, PSI fails to correctly estimate the displacement time series, whereas ST-InSAR shows satisfactory agreement with the

topographic measurements. The better performance of ST-InSAR is visible in both the displacement time series and the correlation plot (Figure 5.13 bottom panels). This is also evident by the correlation indexes in Table 5.1. For PS 4, PSI correlation coefficient drops to -0.08, together with a very low temporal coherence of 0.08, indicating poor modelling of the observed interferometric phase. Conversely, ST-InSAR achieves a correlation coefficient of 0.81 and a temporal coherence of 0.95 at the same point. RMSE is significantly lower for ST-InSAR $3.73\ \mathrm{mm}$ compared to that of PSI $7.85\ \mathrm{mm}$, particularly considering that the true signal amplitude at this point is on the order of $10\ \mathrm{mm}$.

Very similar insights can be drawn for the southern carriageway, based on the displacement time series and correlation plots shown in Figure 5.14, and the performance metrics reported in Table 5.1.

5.5.2 Analysis of temporal coherence

It is reminded that temporal coherence quantifies the similarity between the observed and the modelled interferometric phase, and therefore does not depend on the availability of benchmark measurements. Consequently, temporal coherence can be evaluated for all persistent scatterers on the viaduct.

Figure 5.15 shows the temporal coherence values obtained with PSI (orange) and ST-InSAR (blue) for the various PSs along the deck, on both carriageways, together with the corresponding increases (black) brought by the proposed method with respect to PSI.

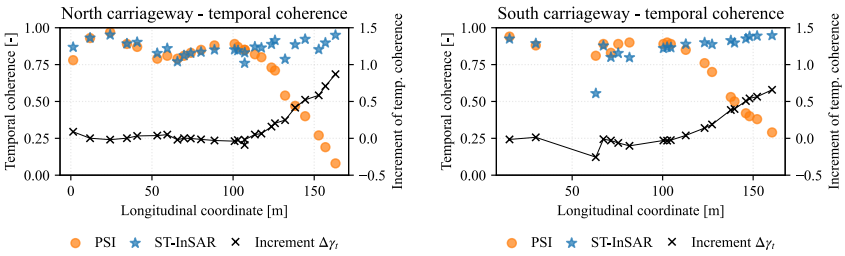


Figure 5.15: Temporal coherence of PSI and of ST-InSAR along the viaduct.

The figure shows a spatial trend for PSI, where coherence is highest near the piers (at longitudinal coordinates of approximately $16.5\ \mathrm{m}$ and $105\ \mathrm{m}$) and remain overall high in the main span (greater than 0.75), while it progressively decreases towards the cantilever half-joints.

ST-InSAR coherence exceeds the 0.75 threshold for nearly all points on the structure, with one exception on the south carriageway, where coherence decreases from 0.81 (PSI) to 0.55 (ST-InSAR).

5.5.3 Temperature gradient estimation

The deck temperature gradient, estimated by ST-InSAR as one of the model parameters, is compared with measurements acquired by the installed thermocouples embedded in the deck concrete beams. Figure 5.16 shows the measured temperature gradient ΔT for both carriageways (black), obtained by averaging the gradients recorded at three sections located at the midspan, Pier 8, and at the cantilever end, together with the temperature gradient estimated using ST-InSAR (blue line). The confidence bounds of the measured signal are also reported in black, corresponding to a standard deviation of 0.71 °C.

A strong agreement between the measured and estimated temperature gradients can be observed. In particular, the correlation coefficients between the thermocouple measurements and ST-InSAR estimates are 0.90 for the northern carriageway and 0.89 for the southern carriageway. The RMSE – which quantifies the discrepancy between the estimated temperature gradient ΔT and the values measured by the monitoring system – is below 1 °C for both carriageways, with values of 0.90 °C and 0.75 °C for the northern and southern carriageway, respectively.

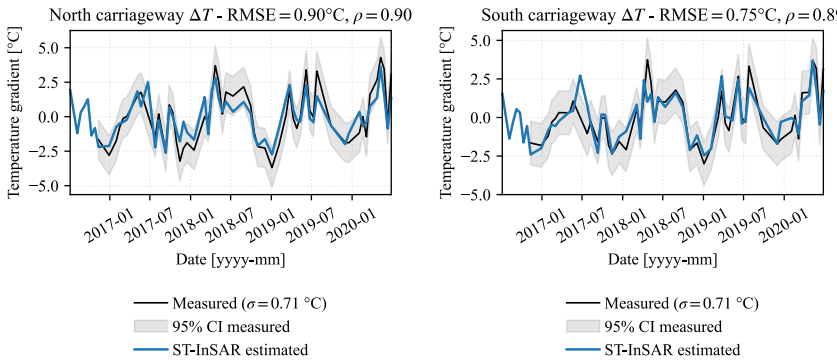


Figure 5.16: Extracted temperature gradient time series compared to average gradient measured

5.6 Discussion

5.6.1 Why PSI fails at specific locations

The results presented in Section 5.5 highlight a clear spatial dependence of PSI performance along the Colle Isarco viaduct. The technique is effective at piers and at the midspan, while its performance degrades along the cantilever spans.

To interpret this behaviour, it is recalled that conventional PSI assumes that the displacement is a linear function of time and air temperature, and that it remains within the ambiguity limit $\lambda/4$. These assumptions are well suited for deformation mechanisms dominated by uniform thermal expansion or long-term trends; however, they may be violated for bridge and viaduct structural elements.

Based on the ground monitoring system installed on the Colle Isarco viaduct, it is expected that PSI performs well in structural regions where these assumptions are valid and degrades where they are violated. The true LOS displacement analysis presented in Section 5.4 – through Figure 5.10 – supports this expectation:

- At the piers, structural displacements are primarily dominated by uniform thermal expansion and, therefore, show strong correlation with air temperature. Consequently, the PSI displacement model (Eq.5.5) remains representative of the observed interferometric phase, resulting in high temporal coherence.
- High temporal coherence is also obtained at the midspan, where the air-temperature correlation is less but still significant
- Moving away from Pier 8 towards the cantilever half-joints, the structural response becomes increasingly dominated by temperature gradients, which induce vertical thermal deflection of the deck. Since this deformation mechanism is not explicitly represented in the conventional PSI model, this results in a gradual loss of PSI performance. This is supported by the spatial trend observed in the coherence maps and by the RMSE error estimated at the half-joints.

5.6.2 Why ST-InSAR performs well where PSI fails

Unlike PSI, the proposed ST-InSAR framework employs a structural deformation model that explicitly accounts for both the uniform thermal expansion of the piers and the effects of temperature gradients across the deck.

Effectively, this model captures more accurately the correct deformation mechanisms, making ST-InSAR more effective in regions where PSI particularly struggles, such as the cantilever spans. At these locations, evidence demonstrates that ST-InSAR provides displacement estimates that better describe the true structural response.

The improved deformation modelling naturally leads to a more accurate approximation of the interferometric phase, which in turn results in higher temporal coherence.

In regions where the assumptions of conventional PSI are satisfied, ST-InSAR performs comparably to PSI. However, it significantly outperforms PSI at the cantilever spans, producing better RMSE and correlation values associated with the displacement time series.

The key difference of the proposed approach is that it consists of simultaneously processing all the persistent scatterers located on the structure while defining spatial correlation compatible with the structural model. This constraint effectively limits the solution space only to physically feasible deformation configurations – compatible with the expected structural behaviour.

5.6.3 Metrological accuracy of ST-InSAR

Overall, ST-InSAR achieves an accuracy comparable across all stable reflective points on the bridge, validated against benchmark measurements. LOS displacement uncertainties (RMSE) are consistently of the order of $2\ \mathrm{mm}$ at the piers and midspan, while slightly higher, of the order of $3\ \mathrm{mm}$, at the cantilever half-joints. This happens because the error is a combination of, on one side, the metrological uncertainty of InSAR measurements and, on the other, the temporal and spatial misalignment of the topographic benchmark (as described in Section 5.4.4).

It is reasonable to assume that the metrological uncertainty of InSAR does not depend on the displacement amplitude, while the error associated with the benchmark misalignment does. Therefore, at points where displacement amplitudes are relatively small, the resulting RMSE is expected to be primarily governed by the measurement uncertainty of InSAR. On the contrary, at points undergoing larger displacements, the misalignment error becomes increasingly more significant.

More specifically, for Pier 7, Pier 8, and the midspan – where displacement amplitudes are limited – the RMSE is very similar, around $2\ \mathrm{mm}$ (between 1.79 mm and $2.58\ \mathrm{mm}$). Here, PSI returns comparable errors. This suggests that the metrological uncertainty of InSAR is approximately $2\ \mathrm{mm}$.

Conversely, as expected, the RMSE of ST-InSAR increases to about $3\ \mathrm{mm}$ at the half-joints, where larger displacements occur. It must be noted that this increase does not reflect a degradation of ST-InSAR accuracy, but rather results from the increasing contribution of benchmark misalignment. Overall, the InSAR metrological uncertainty is therefore expected to remain constant across the structure and approximately $2\ \mathrm{mm}$.

At the same locations, on the contrary, the RMSE associated with PSI is comparable to the true magnitude of the displacements.

It is worth noting that an uncertainty of $2\ \mathrm{mm}$ is comparable to the or-

der of magnitude of the error typically associated with topographic surveying techniques. A key difference, however, is that topographic measurements are not collected synchronously, as total stations acquire sequentially at individual points, whereas InSAR measurements are acquired simultaneously over the entire structure. Therefore, ST-InSAR could also have potential for reconstructing the instantaneous deformed shape of the structure.

5.6.4 Using ST-InSAR to identify the thermal field

ST-InSAR employs a displacement model that depends on both air temperature and the temperature gradient across the bridge deck. Whilst air temperature is treated as a known input, as in conventional PSI, the temperature gradient is not directly measured and is assumed as an unknown parameter to be estimated from the analysis.

The results presented in Section 5.5.3 demonstrate that the temperature gradient estimated through ST-InSAR is actually very close to the true gradient, with an error smaller than $\Delta T = 1\ ^{\circ}\text{C}$. A by-product of this observation is that ST-InSAR could, in principle, be used to measure the thermal field of civil infrastructure without the need for expensive contact-type devices.

Notice that, in opposition, gaining information from PSI about the temperature field of the structure is not possible.

5.6.5 Drawbacks of using ST-InSAR

Based on the discussion above, ST-InSAR proves to be more effective than the conventional PSI approach. In spite of that, its application also introduces drawbacks compared to PSI.

Firstly, ST-InSAR requires the definition of a physics-based structural model that accounts for deformation mechanisms influencing the structure. If deformation sources are not represented in the model, their displacement contribution cannot be estimated. Therefore, the structural model must be sufficiently comprehensive to describe all the physical phenomena governing the structural response.

These limitations, however, do not constitute an additional requirement with respect to conventional contact-based SHM. In this context, structural geometry, construction details, and expected deformation mechanisms are also needed to design sensor layouts and interpret measurements.

Secondly, applying the framework to a bridge or viaduct requires a preliminary investigation to define the geometry, orientation – as well as the appropriate modelling assumptions – for the structure of interest. It is also necessary to precisely identify the main structural components with their corresponding

scattering elements in the SAR reflectivity map. For instance, when piers are particularly tall, radar shadowing can assist in identifying their positions. Alternatively, corner reflectors (CRs) may be installed to enhance the backscattering of selected locations and ensure accurate correspondence between structural nodes and persistent scatterers.

It is noteworthy that the applicability of ST-InSAR is constrained by the need for a physics-based representation of deformation mechanisms, geometry, and structural orientation, thereby limiting the intrinsic benefits of synthetic radar interferometry in terms of cost-effectiveness, deployment efficiency, and large-scale scalability.

As mentioned in Section 5.3, the spatial uncertainty in PS distribution can be addressed by examining the recomputed temporal coherence. In the present case study, this issue is further mitigated by the fact that only PSs previously identified on the deck by the preceding PSI analysis were processed, ensuring that both methods operated on the same set of scatterers. The high temporal coherence values obtained further confirm that the identified PSs are consistent with the modelled deck deformation, supporting their correct structural assignment. However, this issue may become more challenging when merging data from multiple orbits or sensors, where differences in viewing geometry and resolution may require more explicit classification strategies such as that proposed by Giordano et al. [40].

A further consideration concerns the robustness of the estimation when the number of unknown parameters in Eq. 5.15 is large. As the structural complexity increases, the number of state parameters N is also expected to grow, potentially making the optimisation prone to multiple solutions. In the present case study, the structural behaviour is dominated by a relatively small number of parameters, as deformation is predominantly vertical and thermally induced – which keeps the parameter space manageable and the estimation well-posed. For more complex scenarios with multiple interacting deformation sources (e.g. non-linear long-term phenomena or non-uniform thermal gradients), the robustness of the estimation may require additional attention. In such cases, potential mitigation strategies include exploiting high-coherence PSI points as boundary conditions or increasing the number of SAR acquisitions M to improve the observation-to-unknowns ratio. For example, pier displacements with high temporal coherence in PSI could be imposed as fixed constraints, improving the identifiability of the remaining parameters and reducing the risk of having non-unique solutions. Beyond these strategies, Bayesian inference could further mitigate non-uniqueness by integrating prior structural knowledge into the estimation and therefore restricting the solution space.

Finally, although this work focuses on bridges and viaducts, the same methodology can be extended to other civil structures – such as dams, buildings, port facilities, and towers – provided that their displacement behaviour can be spatially correlated by an appropriate physical model.

5.7 Conclusions

This work presented a spatio-temporal framework that integrates physics-based structural models into the MT-InSAR processing pipeline. The proposed method exploits the structural model to simultaneously estimate displacement information from all persistent scatterers identified on the structure, explicitly accounting for spatial and temporal correlation.

The methodology was applied to the Colle Isarco viaduct as a case study, where the performance of the proposed ST-InSAR was compared with that of conventional multi-temporal PSI, by using benchmark topographic measurements.

Based on the experimental results, the following conclusions can be drawn:

- Conventional PSI presents several limitations when applied to bridges and viaducts. This technique performs well when displacements are limited and correlated with air temperature. Consequently, it fails when displacements are not well correlated with air temperature and exceed $\lambda/4$, leading to phase ambiguities.
- ST-InSAR performs well at all monitored locations, successfully identifying displacements at points where conventional PSI fails – where deformation is not correlated with air temperature and exceeds the ambiguity limit. This is achieved thanks to the integration of a more refined displacement model that accounts for deformation mechanisms typically neglected in conventional PSI, and jointly estimates the displacements across all persistent scatterers. As a result, temporal coherence at locations poorly identified by PSI increases significantly, from values close to zero (0.08) to highly satisfactory levels (up to 0.95).
- The comparison with the benchmark measurements suggests that the metrological error of ST-InSAR is on the order of $2\ \mathrm{mm}$, which is on the same order of magnitude achieved by topographic surveying monitoring. A significant advantage of ST-InSAR, however, is the capability of synchronously measuring all points on the structure. Under appropriate conditions, this makes ST-InSAR a promising alternative solution to topographic survey monitoring.
- A by-product of ST-InSAR is the identification of the thermal gradient

across the bridge deck. In this study, the deck temperature gradient was estimated with an accuracy below 1°C. Therefore, ST-InSAR could also be used to infer the thermal field of the structure, in addition to displacement monitoring.

- The proposed methodology can be extended to civil structures beyond bridges, provided that their displacement behaviour can be described through an appropriate physics-based spatial correlation model.
- The main limitation of ST-InSAR lies in the requirement of a physics-based structural model that captures the relevant deformation mechanisms, geometry, and orientation of the structure. This prerequisite may compromise key advantages of SAR interferometry, such as low-cost, rapid monitoring and scalability across large infrastructure typologies. This limitation may be mitigated by automating model generation via approaches such as parametric modelling, digital twins, and hybrid physics data-driven methods.
- Future work will focus on developing a Bayesian inference framework to enhance the robustness of the estimation, particularly in scenarios where multiple deformation mechanisms contribute to the structural response.

Bibliography

[1] T. Nagayama, S. Sim, Y. Miyamori, and B. J. Spencer, "Issues in structural health monitoring employing smart sensors," *Smart Structures and Systems*, vol. 3, no. 3, pp. 299–320, Jul. 2007. [Online]. Available: https://doi.org/10.12989/SSS.2007.3.3.299

[2] Z. E. Foden A., "Value and challenges of structural monitoring for long-span bridges," in *Risk-based strategies for bridge maintenance*. Boca Raton: CRC Press, Taylor & Francis Group, 2023.

[3] D. Li, B. Li, T. Wang, and J. Zhang, "Lightweight structural health monitoring and safety evaluation: Review and case studies," *Advances in Structural Engineering*, p. 13694332251325043, Mar. 2025. [Online]. Available: https://journals.sagepub.com/doi/10.1177/13694332251325043

[4] J. Valença, X. Qin, L. Chang, J. Dong, X. Shi, and J. R. Casas, "Remote Sensing-Based Structural Health Monitoring and Damage Assessment," *Remote Sensing*, vol. 16, no. 7, p. 1146, Mar. 2024. [Online]. Available: https://www.mdpi.com/2072-4292/16/7/1146

[5] V. Macchiarulo, P. Milillo, C. Blenkinsopp, and G. Giardina, "Monitoring deformations of infrastructure networks: A fully automated GIS integration and analysis of InSAR time-series," *Structural Health Monitoring*, vol. 21, no. 4, pp. 1849–1878, Jul. 2022, publisher: SAGE Publications. [Online]. Available: https://doi.org/10.1177/14759217211045912

[6] E. S. Agency, "Sentinel-1," https://www.esa.int/Applications/Observing_the_Earth/Copernicus/Sentinel-1, 2025.

[7] D. Amitrano, G. Di Martino, R. Guida, P. Iervolino, A. Iodice, M. N. Papa, D. Riccio, and G. Ruello, "Earth Environmental Monitoring Using Multi-Temporal Synthetic Aperture Radar: A Critical Review of Selected Applications," *Remote Sensing*, vol. 13, no. 4, p. 604, Feb. 2021. [Online]. Available: https://www.mdpi.com/2072-4292/13/4/604

[8] A. Ferretti, *Satellite InSAR Data: Reservoir Monitoring from Space*, ser. Education Tour Series. DB Houten: EAGE, 2014, no. 9.

[9] A. Ferretti, C. Prati, and F. Rocca, "Permanent scatterers in SAR interferometry," *IEEE Trans. Geosci. Remote Sensing*, vol. 39, no. 1,

pp. 8–20, Jan. 2001. [Online]. Available: http://ieeexplore.ieee.org/document/898661/

[10] M. Crosetto, O. Monserrat, M. Cuevas-González, N. Devanthéry, and B. Crippa, "Persistent Scatterer Interferometry: A review," *ISPRS Journal of Photogrammetry and Remote Sensing*, vol. 115, pp. 78–89, May 2016. [Online]. Available: https://www.sciencedirect.com/science/article/pii/S0924271615002415

[11] R. Wang, J. Zhang, and X. Liu, "A Most-Unfavorable-Condition Method for Bridge-Damage Detection and Analysis Using PSP-InSAR," *Remote Sensing*, vol. 14, no. 1, p. 137, Jan. 2022, publisher: Multidisciplinary Digital Publishing Institute. [Online]. Available: https://www.mdpi.com/2072-4292/14/1/137

[12] M. Schlögl, P. Dorninger, M. Kwapisz, M. Ralbovsky, and R. Spielhofer, "Remote Sensing Techniques for Bridge Deformation Monitoring at Millimetric Scale: Investigating the Potential of Satellite Radar Interferometry, Airborne Laser Scanning and Ground-Based Mobile Laser Scanning," *PFG – Journal of Photogrammetry, Remote Sensing and Geoinformation Science*, vol. 90, no. 4, pp. 391–411, Aug. 2022. [Online]. Available: https://link.springer.com/10.1007/s41064-022-00210-2

[13] D. Tonelli, A. Valentini, A. Rocca, S. Zorzi, A. Lotti, and D. Zonta, "Uncertainty quantification of satellite InSAR-monitoring of bridges: a case study," *ce/papers*, vol. 6, no. 5, pp. 900–906, 9 2023. [Online]. Available: https://onlinelibrary.wiley.com/doi/10.1002/cepa.1991

[14] P. F. Giordano, M. Kwapisz, A. Miano, R. Liuzzo, A. Vorwagner, M. P. Limongelli, A. Prota, and M. Ralbovsky, "Monitoring of a multi-span prestressed concrete bridge using satellite interferometric data and comparison with on-site sensor results," *Structural Concrete*, p. suco.202400881, Feb. 2025. [Online]. Available: https://onlinelibrary.wiley.com/doi/10.1002/suco.202400881

[15] F. D'Amico, V. Gagliardi, L. Bianchini Ciampoli, and F. Tosti, "Integration of InSAR and GPR techniques for monitoring transition areas in railway bridges," *NDT & E International*, vol. 115, p. 102291, Oct. 2020. [Online]. Available: https://www.sciencedirect.com/science/article/pii/S0963869520303157

[16] Y. Zhou, G. Hao, J. Chen, and J. Wei, "Time series forecasting and anomaly detection of bridge deformation based on PS-InSAR technique and seasonal-trend decomposition," *Structural Health Monitoring*, p. 14759217251365289, Sep. 2025. [Online]. Available: https://doi.org/10.1177/14759217251365289

[17] S. Xiong, C. Wang, X. Qin, B. Zhang, and Q. Li, "Time-Series Analysis on Persistent Scatter-Interferometric Synthetic Aperture Radar (PS-InSAR) Derived Displacements of the Hong Kong–Zhuhai–Macao Bridge (HZMB) from Sentinel-1A Observations," *Remote Sensing*, vol. 13, no. 4, p. 546, Jan. 2021, publisher: Multidisciplinary Digital Publishing Institute. [Online]. Available: https://www.mdpi.com/2072-4292/13/4/546

[18] X. Qin, Q. Li, X. Ding, L. Xie, C. Wang, M. Liao, L. Zhang, B. Zhang, and S. Xiong, "A structure knowledge-synthetic aperture radar interferometry integration method for high-precision deformation monitoring and risk identification of sea-crossing bridges," *International Journal of Applied Earth Observation and Geoinformation*, vol. 103, p. 102476, Dec. 2021. [Online]. Available: https://www.sciencedirect.com/science/article/pii/S0303243421001835

[19] F. C. Ponzo, G. Auletta, P. Ielpo, and R. Ditommaso, "DInSAR–SBAS satellite monitoring of infrastructures: how temperature affects the "Ponte della Musica" case study," *Journal of Civil Structural Health Monitoring*, vol. 14, no. 3, pp. 745–761, Mar. 2024. [Online]. Available: https://link.springer.com/10.1007/s13349-023-00751-z

[20] P. Milillo, R. Bürgmann, P. Lundgren, J. Salzer, D. Perissin, E. Fielding, F. Biondi, and G. Milillo, "Space geodetic monitoring of engineered structures: The ongoing destabilization of the Mosul dam, Iraq," *Sci Rep*, vol. 6, no. 1, p. 37408, Dec. 2016. [Online]. Available: https://www.nature.com/articles/srep37408

[21] S. Selvakumaran, S. Plank, C. Geiß, C. Rossi, and C. Middleton, "Remote monitoring to predict bridge scour failure using Interferometric Synthetic Aperture Radar (InSAR) stacking techniques," *International Journal of Applied Earth Observation and Geoinformation*, vol. 73, pp. 463–470, Dec. 2018. [Online]. Available: https://linkinghub.elsevier.com/retrieve/pii/S0303243418303052

[22] A. Hooper, P. Segall, and H. Zebker, "Persistent scatterer interferometric synthetic aperture radar for crustal deformation analysis, with application to Volcán Alcedo, Galápagos," *Journal of Geophysical Research: Solid Earth*, vol. 112, no. B7, 2007, _eprint: https://agupubs.onlinelibrary.wiley.com/doi/pdf/10.1029/2006JB004763. [Online]. Available: https://onlinelibrary.wiley.com/doi/abs/10.1029/2006JB004763

[23] V. Macchiarulo, P. Milillo, C. Blenkinsopp, C. Reale, and G. Giardina, "Multi-temporal InSAR for transport infrastructure monitoring: recent trends and challenges," *Proceedings of the Institution of Civil Engineers - Bridge Engineering*, vol. 176, no. 2, pp. 92–117, Dec. 2021. [Online]. Available: https://doi.org/10.1680/jbren.21.00039

[24] D. Perissin and T. Wang, "Repeat-Pass SAR Interferometry With Partially Coherent Targets," *IEEE Trans. Geosci. Remote Sensing*, vol. 50, no. 1, pp. 271–280, Jan. 2012. [Online]. Available: http://ieeexplore.ieee.org/document/5978217/

[25] V. Macchiarulo, P. Milillo, M. J. DeJong, J. González Martí, J. Sánchez, and G. Giardina, "Integrated InSAR monitoring and structural assessment of tunnelling-induced building deformations," *Structural Contr & Hlth*, vol. 28, no. 9, Sep. 2021. [Online]. Available: https://onlinelibrary.wiley.com/doi/10.1002/stc.2781

[26] K. J. Reinders, R. F. Hanssen, F. J. Van Leijen, and M. Korff, "Augmented satellite InSAR for assessing short-term and long-term surface deformation due to shield tunnelling," *Tunnelling and Underground Space Technology*, vol. 110, p. 103745, Apr. 2021. [Online]. Available: https://linkinghub.elsevier.com/retrieve/pii/S0886779820306994

[27] L. Sun, H. Li, S. Guo, X. Li, P. Chen, and J. Chen, "Incorporating Physical Constraint in Three-Dimensional Time Series InSAR Inversion for Urban Deformation Monitoring," *IEEE Journal of Selected Topics in Applied Earth Observations and Remote Sensing*, vol. 18, pp. 13 967–13 985, 2025. [Online]. Available: https://ieeexplore.ieee.org/abstract/document/11015766

[28] E. Cernuto, D. Salciarini, F. Ubertini, and G. Giardina, "Landslide-Bridge Interaction: A combined approach based on InSAR data and numerical modelling," *International Journal of Disaster Risk*

Reduction, vol. 126, p. 105568, Aug. 2025. [Online]. Available: https://www.sciencedirect.com/science/article/pii/S2212420925003929

[29] E. Farneti, N. Cavalagli, M. Costantini, F. Trillo, F. Minati, I. Venanzi, and F. Ubertini, "A method for structural monitoring of multispan bridges using satellite InSAR data with uncertainty quantification and its pre-collapse application to the Albiano-Magra Bridge in Italy," *Structural Health Monitoring*, vol. 22, no. 1, pp. 353–371, Jan. 2023, publisher: SAGE Publications. [Online]. Available: https://doi.org/10.1177/14759217221083609

[30] G. M. Guzman-Acevedo, G. E. Vazquez-Becerra, J. A. Quintana-Rodriguez, J. R. Gaxiola-Camacho, M. Anaya-Diaz, J. C. Mediano-Martinez, and F. J. Carrión Viramontes, "Structural health monitoring and risk assessment of bridges integrating InSAR and a calibrated FE model," *Structures*, vol. 63, p. 106353, May 2024. [Online]. Available: https://www.sciencedirect.com/science/article/pii/S2352012424005058

[31] Y. Zhou, G. Hao, X. Qin, F. Yi, and Z. Tan, "A refined DS-InSAR technique for long-term deformation monitoring of low-coherence bridge groups," *Engineering Structures*, vol. 335, p. 120335, Jul. 2025. [Online]. Available: https://www.sciencedirect.com/science/article/pii/S0141029625007266

[32] S. Quqa, A. Palermo, F. Ubertini, and A. Marzani, "Regional-scale bridge condition monitoring using InSAR displacements and environmental data," *Structural Health Monitoring*, vol. 24, no. 4, pp. 2271–2291, Jul. 2025. [Online]. Available: https://doi.org/10.1177/14759217241302369

[33] H. Kuai, V. Macchiarulo, S. Sharma, P. Karamitopoulos, F. Messali, A. Cicirello, and G. Giardina, "Identification of mechanism-specific persistent scatterers for enhancing MT-InSAR in Structural Health Monitoring applications," *Engineering Structures*, vol. 352, p. 122103, Apr. 2026. [Online]. Available: https://www.sciencedirect.com/science/article/pii/S0141029626000155

[34] D. Perissin, "Interferometric SAR Multitemporal Processing: Techniques and Applications," in *Multitemporal Remote Sensing*, Y. Ban, Ed. Cham: Springer International Publishing, 2016, vol. 20, pp. 145–176, series Title: Remote Sensing and Digital Image Processing. [Online]. Available: https://link.springer.com/chapter/10.1007/978-3-319-47037-5_8

[35] S. Fikri, I. M. Anjasmara, and M. Taufik, "Application of Different Coherence Threshold on PS-InSAR Technique for Monitoring Deformation on the LUSI Affected Area During 2017 and 2019," *IOP Conference Series: Earth and Environmental Science*, vol. 731, no. 1, p. 012036, Apr. 2021. [Online]. Available: https://iopscience.iop.org/article/10.1088/1755-1315/731/1/012036

[36] R. Horst, P. M. Pardalos, and N. V. Thoai, *Introduction to global optimization*, 2nd ed., ser. Nonconvex optimization and its applications. Dordrech Boston Londont: Kluwer Academic Publishers, 2000, no. volume 48.

[37] J. Kennedy and R. Eberhart, "Particle swarm optimization," in *Proceedings of ICNN'95 - International Conference on Neural Networks*, vol. 4. Perth, WA, Australia: IEEE, 1995, pp. 1942–1948. [Online]. Available: http://ieeexplore.ieee.org/document/488968/

[38] Y. Shi and R. Eberhart, "A modified particle swarm optimizer," in *1998 IEEE International Conference on Evolutionary Computation Proceedings. IEEE World Congress on Computational Intelligence (Cat. No.98TH8360)*. Anchorage, AK, USA: IEEE, 1998, pp. 69–73. [Online]. Available: http://ieeexplore.ieee.org/document/699146/

[39] A. G. Gad, "Particle Swarm Optimization Algorithm and Its Applications: A Systematic Review," *Arch Computat Methods Eng*, vol. 29, no. 5, pp. 2531–2561, Aug. 2022. [Online]. Available: https://link.springer.com/10.1007/s11831-021-09694-4

[40] P. F. Giordano, A. Kamariotis, G. Giardina, E. Chatzi, and M. P. Limongelli, "Uncertainty propagation in satellite InSAR data analysis for structural health monitoring," *Automation in Construction*, vol. 177, p. 106371, Sep. 2025. [Online]. Available: https://www.sciencedirect.com/science/article/pii/S092658052500411X

[41] L. J. V. Miranda, "PySwarms, a research-toolkit for Particle Swarm Optimization in Python," *Journal of Open Source Software*, vol. 3, 2018. [Online]. Available: https://doi.org/10.21105/joss.00433

6. Assessment of spaceborne SAR micro-motion measurement for vibration-based SHM

Context and contribution to the thesis

This chapter contributes to the second research question by assessing the feasibility of micro-Doppler SAR for vibration-based structural health monitoring of bridges. In this work, an MDSAR technique is proposed and tested through controlled shaker experiments on isolated targets. The results provide a proof of concept of the technique and define the metrological capabilities and limitations of MDSAR under controlled conditions.

The following pages present the post-print of

> Vattulainen, A.B., **Lotti, A.**, Diaz Riofrio, S., Suppi, C., Tubaldi, E., Zonta, D., Milillo, P., Clemente, C. (2026). Assessment of spaceborne SAR micro-motion measurement for vibration-based SHM, *IEEE Access*, Volume: 14, https://doi.org/10.1109/ACCESS.2026.3652346.

as published in the journal *IEEE Access*, differing only from the published article in terms of layout, formatting, and notation.

Authors' contributions:

Vattulainen, A.B.: methodology, investigation, formal analysis, visualisation, software, writing (original draft), review. **Lotti, A.**: methodology, investigation, formal analysis, visualisation, software, data collection, writing (original draft), review. **Diaz Riofrio, S.**: methodology, investigation, software. **Suppi, C.**: software, data collection. **Tubaldi, E.**: methodology, data collection, review, supervision. **Zonta, D.**: methodology, data collection, review, supervision. **Milillo, P.**: methodology, data collection, review, supervision. **Clemente, C.**: conceptualisation, methodology, data collection, review, supervision, funding acquisition.

Abstract

Remote sensing methods for vibration-based structural health monitoring (VBSHM) are gaining interest, given the benefits of non-contact sensing for this application: broader spatial coverage, easier measurement access to structures such as bridges, and cost savings from reducing the need for embedded sensor networks. Vibration measurement using micro-Doppler synthetic aperture radar (MDSAR) is an emerging technique enabling the measurement of structural vibrations from synthetic aperture radar (SAR) satellite data, exploiting recent advancements in high-resolution X-band radar imaging. This paper presents a detailed metrological assessment of MDSAR – using processing based on the pre-existing subpixel offset tracking (SPOT) concept as a representative method – to evaluate its applicability to VBSHM. Measurements are made from real SAR images of vibrating targets with synchronous ground truth data. The results verify that the technique can be used to measure target motion time histories with dynamics relevant to SHM, namely different modulations with frequencies from 1 to 4 Hz, and radial RMS displacement amplitudes from 10.43 to 0.10 mm. These results pave the way for future measurements of infrastructure.

Keywords: Frequency detection, micro-Doppler, micro-motion, SAR, vibration-based SHM, vibration measurement.

6.1 Introduction

Vibrometry is a popular method for structural health monitoring (SHM) due to its relative ease of implementation and potential effectiveness in identifying damage, usually achieved by observing changes in the modal parameters of a structure over time [1, 2]. Conventionally, accelerometers are used for vibration-based SHM (VBSHM). As these are contact sensors, they must be installed on the structure, where this can pose challenges in terms of hazardous working conditions and access – particularly in the case of bridges supporting arterial road or rail networks. Additionally, each sensor can only measure at a single fixed location, meaning that large structures typically require a network for adequate coverage [3]. All of these factors inflate costs and thus diminish the effectiveness of this method [4].

6.1.1 Remote sensing alternatives

Due to the issues mentioned above, the development of remote sensing alternatives has been of interest for some time. Approaches include motion-

tracking cameras using digital image correlation [5, 6] or LiDAR [7, 8], although other issues are associated with these methods: motion-tracking with cameras has the lowest measurement precision [9], is reliant on ambient lighting conditions, and along with LiDAR is sensitive to weather occlusion. Ground-based Doppler radar [10, 11, 12] solves these problems, however both LiDAR and radar sensors are very expensive, and are vulnerable to sensor movement caused by environmental conditions such as wind buffeting. If viable, passive Doppler radar making use of increasingly ubiquitous higher frequency communication signals such as 5G could help reduce costs [13], however these methods all suffer from being ground-based – requiring that they are *on-site* to make measurements – thus drastically reducing their coverage and increasing cost per monitored area.

Spaceborne sensing, such as synthetic aperture radar (SAR), presents an alternative paradigm. Interferometric SAR (InSAR) is an established technology being explored for SHM [14, 15, 16, 17, 18] and can cover very large areas (typically many kilometres), with interferometric techniques being used to measure changes in surface height. InSAR works by comparing the changes in signal phase between pixels in two registered SAR images collected at different times, which correspond to small changes in distance to the sensor at those positions. Although capable of measuring minute displacements, only very slow bulk movements can be measured as the images being compared are typically acquired days apart (if not longer) and so these techniques are not suitable for vibrometric studies.

This work instead investigates using micro-Doppler SAR (MDSAR) acting on single-pass (i.e. single acquisition) data which can observe target dynamics within the SAR acquisition time, with frequencies relevant for vibrometric SHM.

6.1.2 Motivation for SAR vibrometry

Like ground-based Doppler radar and LiDAR, SAR is a good candidate sensor for VBSHM given its sensitivity to the small changes in signal phase caused by moving targets via the Doppler effect [19]. SAR also offers the greatest possible spatial coverage of remote sensing techniques and an increasingly convenient level of temporal coverage – with highly predictable repeat passes of any area of interest – as commercial satellite constellations continue to grow. These companies include Umbra [20], Capella Space [21], and ICEYE [22], which have the capability to provide very high-resolution X-band (wavelength of $\lambda = 2.4$ to 3.8 cm) SAR images, with long dwell times/long acquisition times (t_a) – which enable MDSAR processing. Being spaceborne, these sen-

sors are not subject to any local vibration of the sensor, unlike ground-based methods. Additionally, MDSAR techniques could assess any non-networked structure of interest much faster than conventional methods, which would expedite interventions or inspections after natural disasters – presenting a significant advantage in time critical scenarios.

The purpose of this work is thus to carry out a metrological assessment of an MDSAR technique via experimental tests, where ground truth data were synchronised with satellite acquisitions. Whilst several MDSAR measurement techniques have been published, none have been comprehensively evaluated in this way previously. In this work, the sub-pixel offset tracking (SPOT) method is used to make vibration measurements from SAR data as a representative technique. Data of an isolated, high reflectivity target were collected with the target undergoing motion with a range of frequencies, amplitudes, and modulations. The majority of tests involved very low amplitudes relevant to SHM use cases, where the scope of the work is defined as an evaluation of the potential and limitations of MDSAR techniques for VBSHM.

6.1.3 Statement of novelty

The key novelty of this work is the metrological evaluation of MDSAR measurements of motion typical of civil infrastructure. It quantifies the capabilities and limitations of the SPOT method across a range of realistic scenarios, to the lowest verified amplitude and velocity motions to date. Another important novelty is the reconstruction of the full-time histories of target vibrations (including both frequency and amplitude) validated through synchronised ground truth measurements acquired during the spaceborne SAR data acquisitions, these having previously been demonstrated only in a very limited capacity [23, 24]. This assessment provides robust evidence that this information is captured in SAR data, and that this can already be recovered with relatively simple signal processing techniques such as SPOT.

Following the introduction in Section 6.1, Section 6.2 covers the basics of SAR as needed to interpret the results and provides a brief overview of SAR micro-motion measurement methods. Section 6.3 then explains the MDSAR processing method used in this work. Section 6.4 details the SAR and ground truth data collection, followed by the results of the study in Section 6.5. The paper then ends with Sections 6.6 and 6.7 with the discussion and conclusions.

6.2 SAR background

SAR is a radar imaging technique which exploits sensor movement to improve image azimuth resolution. During the data acquisition period, the SAR (mounted on a satellite) receives echoes of reflected pulses from the scene whilst moving some distance along its orbit. By recording information about the position and velocity of the SAR during acquisition, the phase changes these induce in the received signal can be compensated for, and the data from the full acquisition focused to form an image. By doing this, the section of the orbit covered during the acquisition is in effect *synthesised* to become the sensor antenna. The synthetic aperture greatly improves the image azimuth resolution (since this is inversely proportional to the aperture length) far beyond what is possible with the real aperture antenna on board [25].

The image azimuth direction is defined as parallel to the SAR movement, whereas range is perpendicular, as shown in the SAR imaging geometry diagram in Fig. 6.1, which shows a 'spotlight' mode acquisition. Several SAR imaging modes exist, however this study considers spotlight mode acquisitions due to the greater target observation time this provides[1]. In spotlight mode, the beam angle of the SAR antenna ('squint angle') is steered such that the centre of the target area remains illuminated as the platform moves (as shown in Fig. 6.1) for the entire observation time. The achievable azimuth resolution, Δy, is given in Eq.6.1:

$$\Delta y = \frac{\lambda \cdot R(t)}{2 \cdot v_{\mathrm{s}}.t_{\mathrm{a}}} \tag{6.1}$$

where λ is the centre wavelength of the transmitted signal and v_{s} is the platform (satellite) velocity[2].

Figure 6.1 also shows the definitions of the incidence angle, θ, the slant (also known as line of sight, LOS) range $R(t)$, and the *synthetic aperture* length L travelled by the platform over the acquisition time from $t = 0$ to $t = t_{\mathrm{a}}$.

An example of a SAR image formed from spotlight mode data is shown in Fig. 6.2, showing some basic phenomenology. The image grid has the axes of azimuth and (slant) range, where these are often simply given as pixel number but can be scaled to distances. Figure 6.2 is produced from a common SAR image product known as sensor independent complex data (SICD) [26]

[1]The mathematical concepts and algorithms shown in this work also apply to other image acquisition modes such as Stripmap, however the effectiveness of MDSAR in other modes is more limited due to the shorter achievable observation times.

[2]This formula is derived from the formula for the azimuth resolution of spotlight mode SAR, $\Delta y = \frac{\lambda}{2\phi}$, applying the small angle approximation for the subtended angle of the aperture, ϕ.

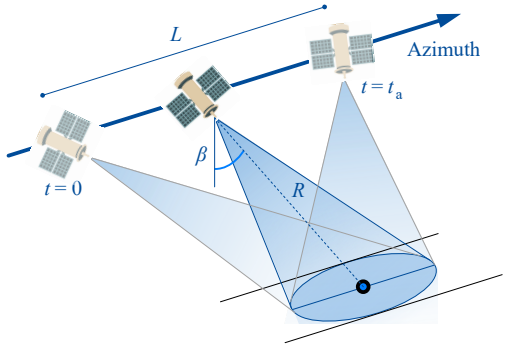


Figure 6.1: SAR imaging geometry for a spotlight mode acquisition. The diagram illustrates the squinting behaviour of the sensor whereby it changes the antenna pointing angle during the acquisition. Key features shown include the satellite flight direction (labelled as azimuth), the total acquisition duration (from $t = 0$ to $t = t_a$), the synthetic aperture length (L), the slant range (LOS) distance ($R(t)$), and the incidence angle (β).

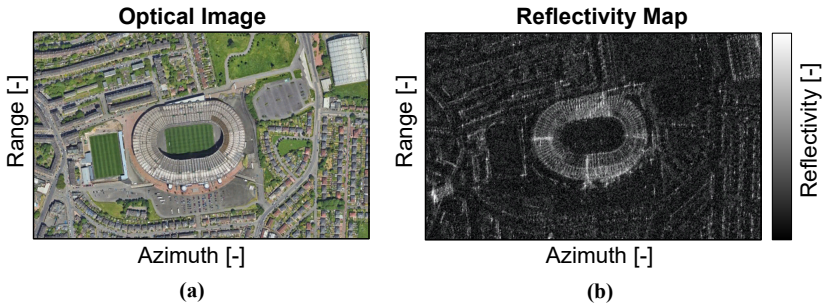


Figure 6.2: (a) Optical image, and (b) reflectivity map from a spotlight acquisition over Hampden Park Stadium in Glasgow, captured by the Umbra-04 sensor on the 14th of March 2024 at 20:35:48 (UTC).

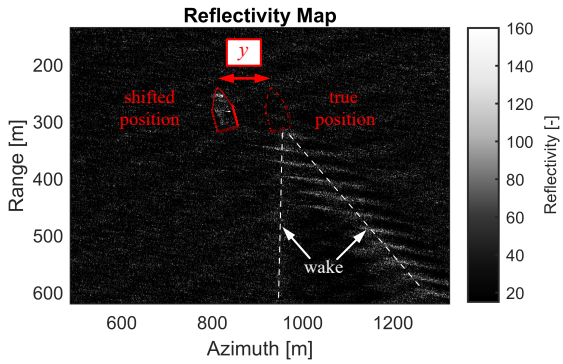


Figure 6.3: Example of the effects of a constant velocity target on SAR imaging. The figure shows the shifted position of a moving ship in the reflectivity map of a SAR image, captured by the Capella-10 sensor on the 5th of February 2025 at 11:49:46 (UTC).

which provides pixel intensity (reflectivity) and phase information. Complex data are necessary for the processing method described in this paper, where it must also be 'single-look complex' (SLC) data as opposed to 'multi-look complex' (MLC) data, as in the former only one continuous observation is used to form the image rather than the multiple integrated images in the latter. The use of multiple image acquisitions causes temporal averaging that corrupts any motion information in the data and renders this unusable for MDSAR.

6.2.1 The micro-Doppler effect in SAR

Numerous SAR image formation processes exist; however, typically they assume that the observed scene is stationary when performing the signal phase compensation methods that focus the image. Moving targets thus have uncompensated signal phase (due to the Doppler effect), which results in target displacements, distortions, or artefacts in the final image [19]. For example, a target moving with constant velocity will appear offset and smeared (defocused) along the azimuth direction in the SAR image. An example of these effects is shown in Fig. 6.3, which shows a moving ship displaced from its wake at sea due to the radial velocity component of the ship relative to the SAR observation. In the case of a strongly vibrating target, this results in the appearance of several 'paired echoes' centered around the true position of the target [27, 28], as seen in Fig. 6.5(a), for example.

The phase changes induced by the Doppler effect are caused by radial velocities, thus the radar can only observe motion in the LOS direction. Due to the one-to-one mapping of Doppler shift bins to azimuth bins in SAR imaging, the

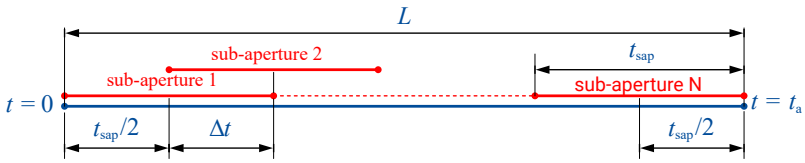


Figure 6.4: Diagram showing the segmentation of a synthetic aperture of length L, duration t_a, into N overlapping sub-apertures of duration t_{sap}, separated by the time resolution, Δt.

radial velocities manifest as artefacts predominantly in the azimuth direction rather than range [29]. This relationship is shown in Eq.6.2:

$$y(t) = -\frac{v_r \cdot R(t)}{v_s} \tag{6.2}$$

where $x(t)$ is the offset distance along the azimuth direction, and v_r is the radial velocity (along the LOS) of the target relative to the moving SAR sensor.

In the field of radar, the changing Doppler frequency shift observed from targets which are oscillating or vibrating (or in general undergoing some periodic or secondary motion) is known as *micro-Doppler*, and arises from the *micro-motion* (m-m) of the target. Vibrometric measurements with SAR (and radar more broadly) thus fall into the field of micro-Doppler measurement and phenomenology. To achieve the measurement of micro-Doppler, sampling of the signal as a function of time is required. The SLC SAR image product has no temporal resolution since it is formed from the integrated data from the whole aperture, however if the data is segmented to form *sub-aperture* images (where each image is formed from a smaller section of the full acquisition), time resolution can be achieved. This concept is illustrated in Fig. 6.4. Segmenting the data comes at the cost of coarser azimuth resolution in the resultant images as dictated by Eq.6.1, however this issue can be mitigated with the use of overlapping sub-aperture windows or by longer full aperture lengths such as those afforded by spotlight mode acquisitions.

6.2.2 Micro-Doppler measurement from SAR

Several different methods have been devised for the measurement of m-m from SAR data, and are discussed below as a small number of broad algorithm classes. For a deeper review, the reader is invited to refer to Rollo et al. [28].

Time-frequency analysis

These methods involve the use of different transforms to estimate the Doppler frequency in a given time window, producing measurements of target motion

over time. Long windows are often used to maintain sufficient frequency (and thus velocity) resolution, where these are then significantly overlapped to mitigate loss of time resolution. The most frequently used transform for this kind of processing is the short-time Fourier transform (STFT), generating the commonly known spectrogram. Many other transforms have been used for micro-Doppler analysis more broadly, with examples tabulated in Chen et al. [30] such as the Wigner-Ville distribution (WVD). The work by Chen et al. used time-frequency analysis to measure a vibrating corner reflector from SAR data with the reasonable accuracy of 2.3 Hz versus a ground truth value of 2.0 Hz, however the results were presented without additional amplitude verification. Rüegg et al. [27] used the smoothed pseudo-WVD and the Gabor transform to analyse vibrating and rotating targets in SAR images, where the changing Doppler frequency of a corner reflector rotating at 1 Hz was observed.

More recently, a modified back-projection approach was used as a new way to construct the signal of interest. This method has been used to measure a vibrating corner reflector with a frequency of 2.00 Hz and an amplitude of 15 mm, returning an accurate frequency estimate using a time-frequency method presented in Clemente et al. [23]. Similar time-frequency methods applied to back-projected data of a bridge in Glasgow yielded estimated vibrational spectra showing several modes of interest matching synchronous ground truth data collected using accelerometers. Whilst the technique correctly identified many vibrational modes, the relative amplitudes were not a match due to the limitations of the approach [31], although this work presents the first synchronous measurements of structural vibrations with conventional (accelerometer) sensors and SAR, to the authors' knowledge.

Phase domain

The second broad class of methods measure the changing signal phase directly. These include the discrete fractional Fourier transform (DFrFT), which is an extension of the discrete Fourier transform (DFT) which can be used to estimate rates of frequency change. This was used in papers by Wang et al. [32, 33] in efforts to suppress paired echo artefacts in SAR images. Experimental data of vibrating corner reflector targets were presented with good results in two scenarios, the first with settings of 1 Hz frequency and 1.5 cm amplitude, and the second with 5 Hz frequency and 1.5 mm amplitude. Amplitude estimates from the measurements were not reported, however the frequency accuracy of the results were good: 0.9 Hz was measured for the former experiment, and 5.2 Hz for the latter [32].

Another example of a phase signal estimator is the high-order ambiguity function (HAF). This works by assuming the phase can be modelled as a poly-

nomial phase function (PPS), and then iteratively estimating the coefficients of the PPS in each time window. This method has been applied in an SHM context, measuring movements of the PuyLaurent Dam in France. In this experiment the m-m of a corner reflector placed at the ridge of the dam was measured, producing vibrational frequency results which are consistent with previously reported in situ values, however without any simultaneous measurement or comparison of amplitude [34]. A recent approach which has been investigated involved measuring the Doppler centroid of targets over a sequence of sub-aperture images to estimate displacements over time. This was used on data of a water tower and a bridge in the Basilicata region of Italy, and compared favourably with asynchronous measurements by a ground-based radar [35].

Other approaches include the use of a quasi-maximum likelihood estimator to track the signal phase, showing promising results on simulated data and being remarkable as an example of a statistical approach [36].

The same modified back-projection approach as presented in Clemente et al. [23] above was initially pursued to allow the phase to be directly measured over time. A direct extraction of the signal phase from the back-projected data in Rollo et al. [24] yielded promising results of a frequency estimate of 2.01 Hz and amplitude of approximately 16 mm, however phase unwrapping errors and vulnerability to clutter remain an obstacle to this approach.

Image domain

The final class of SAR m-m measurement algorithms are those operating in the image domain, often known as pixel tracking methods. Clemente et al. [23] used a simple approach to measure the motion of a corner reflector with a nominal frequency of 2 Hz and 15 mm amplitude, where the position of the target intensity maximum was tracked over a sequence of sub-aperture image frames. This accurately estimated the frequency, and yielded an amplitude estimate of approximately 18 mm, and prior to this work was the only pixel tracking result with simultaneous ground truth verification.

The aforementioned SPOT method used in this work also belongs to this class, where for this technique 2D cross-correlation is used for image registration between each sub-aperture image to detect the apparent shift of the target due to the Doppler effect. The term ‘sub-pixel’ refers to the upsampling of the sub-aperture images which is used to increase the precision of the shift estimates. This method has been demonstrated for SHM using case studies of several bridges in Italy in Biondi et al. [37], where crack localisation matching photographs is shown, however without ground truth verification of vibrational dynamics with conventional sensing. A case study of the destabilisation of the Mosul Dam in Iraq has also been published [38], where some cracks identified

with SPOT coincide with those identified using interferometric SAR (InSAR) [39], these being very similar to damage identified by in situ measurements.

SPOT has in general shown many promising results in applications involving SHM and is likely the most established method for measuring m-m from SAR, having been applied to the most use cases and experimental data. The results presented in the literature have however lacked verification with synchronous ground truth measurements, where the results presented in this work aim to begin to fill this gap and improve the rigour of future measurements.

6.3 SPOT METHOD

This section outlines the method for estimating the vibrational velocities of ground targets from single-pass SAR images using the SPOT technique. This implementation of the SPOT algorithm is inspired by similar pixel-tracking methods [38, 37].

6.3.1 Sub-aperture generation

The processing begins with the generation of the azimuth sub-aperture sequence from the full acquisition data, taking as input a SAR SLC image. To reduce computational load, the SAR image is cropped around the target by defining a region of interest (ROI). A 1D Fast Fourier Transform (FFT) is then applied to the ROI along the azimuth dimension to convert the data from the range-azimuth domain to the *range-azimuth frequency* domain. The data for the sequence of N sub-apertures are then segmented from this by applying a series of N bandpass filters, where each is centred at increasing azimuth frequencies. The proportion of the full acquisition data (or bandwidth) used for each sub-aperture is described by the aperture fraction, ξ, defined as:

$$\xi := \frac{t_{\text{sap}}}{t_{\text{a}}} \tag{6.3}$$

where t_{sap} is the sub-aperture duration. This is the observation window of the instantaneous vibrational motion, where to facilitate comparison of processing parameters when observing vibrations with different periods, T, the observation ratio, η, is defined:

$$\eta := \frac{t_{\text{sap}}}{T} \tag{6.4}$$

where T is the natural period of the highest frequency component.

Similar to time-frequency analysis techniques such as the spectrogram, the windows used to segment the sub-aperture data can overlap to improve temporal resolution whilst maintaining a large aperture fraction, which corresponds to a

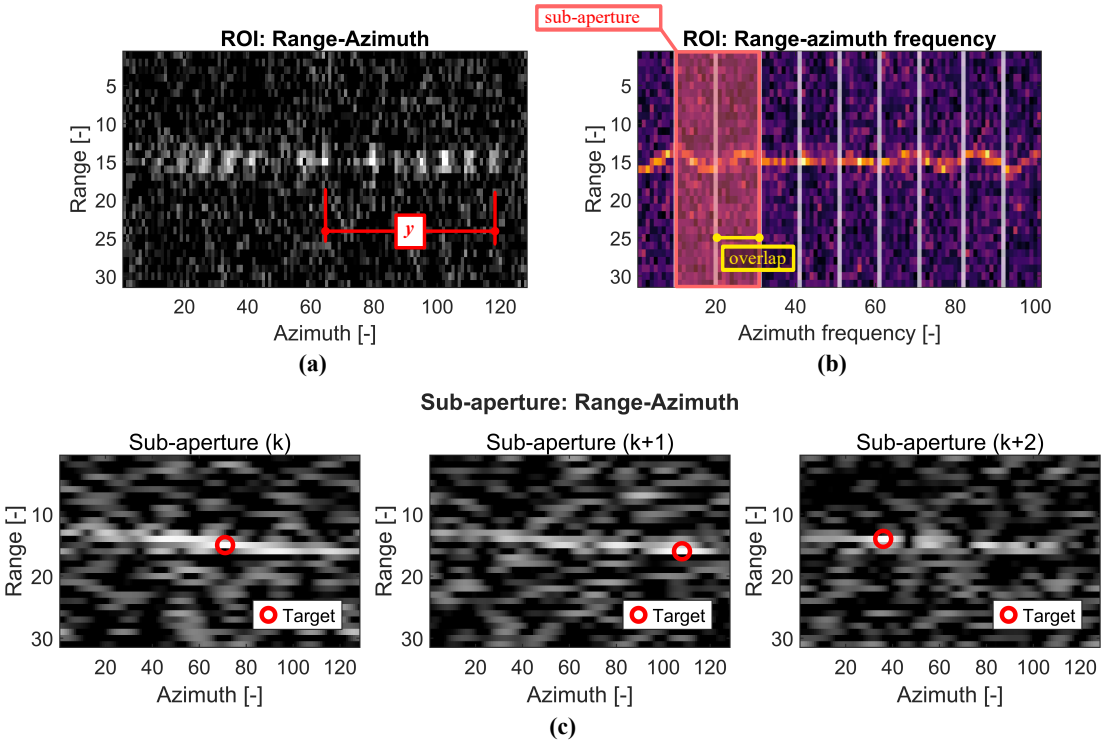


Figure 6.5: (a) ROI reflectivity image in range-azimuth coordinates, showing the azimuth displacement, y, of a vibrating ground target; (b) the range-azimuth frequency plot generated from the ROI using an FFT in the azimuth dimension, where the segmentation of this data into sub-apertures is determined by the sub-aperture fraction, ξ, and the overlap, Ω; and (c) examples of sub-apertures in range-azimuth coordinates indicating pixel tracking.

better azimuth resolution by Eq.6.1. In common with the general method for computing overlapping windows, the degree of overlap is parametrised by the overlap ratio Ω. The number of sub-apertures corresponding to the specified values of ξ and Ω is then computed using Eq.6.5.

$$N = \frac{t_{\mathrm{a}} - \Omega \cdot t_{\mathrm{sap}}}{t_{\mathrm{sap}} - \Omega \cdot t_{\mathrm{sap}}} = \frac{\xi^{-1} - \Omega}{1 - \Omega} \tag{6.5}$$

The segmented data are then transformed back into the range-azimuth domain using an inverse FFT (IFFT). Prior to this step, the segmented data are zero-padded to be of the same dimension as the input ROI, such that the pixel spacing of each sub-aperture image is the same as the original. The sub-aperture generation processing is summarised in Fig. 6.5.

6.3.2 Motion tracking

As shown in Eq.6.2, due to the instantaneous radial velocity v_{r} of the target at each time step, the target is observed as shifted by varying amounts in azimuth in each sub-aperture. This shift is tracked by identifying and following the azimuth position, y, of a bright pixel across the sequence of sub-apertures using 2D cross-correlation. The cross-correlation registers a reference and a test image patch, with each having matching azimuth and range widths (w_x and w_y, respectively) in terms of pixels. The reference patch is selected from the middle sub-aperture frame, with each test patch selected in sequence beginning from the first frame. During the registration process, the patches are further upsampled by a factor A to measure shifts with sub-pixel precision. Finally, the series of azimuth pixel displacements is then converted into a radial velocity time history using Eq.6.2.

The time axis of the reconstructed velocity signal is generated in the same way as for a spectrogram. Each velocity value is associated with the centre of its respective sub-aperture window. As such, the time axis is defined as a linearly spaced vector of N values, ranging from $t_{\mathrm{sap}}/2$ to $t_{\mathrm{a}} - t_{\mathrm{sap}}/2$, as shown in Fig. 6.4. This results in a temporal resolution (i.e. sampling period) as shown in Eq.6.6:

$$\Delta t = \frac{t_{\mathrm{a}} - t_{\mathrm{sap}}}{N - 1} \tag{6.6}$$

where the sampling frequency, f_{s}, is given by $1/\Delta t$. Since this method uses only a single acquisition, it can only resolve motion which has a maximal period on the scale of the observation time, t_{a}.

To enhance the temporal resolution of the SAR measured velocity signal, Whittaker–Shannon interpolation (better known as sinc interpolation) is applied. This technique allows for the reconstruction of a continuous-time signal from its discrete samples, under the assumption that the signal is band-limited [40]. In this work, sinc interpolation was used to upsample the coarse SAR measured velocity signal by a factor B, improving the extracted amplitude estimates while preserving the original frequency content.

The fundamental steps of the SPOT algorithm are summarised below:

1. Begin with the full SLC SAR image.
2. Crop the data to the ROI around the target.
3. Apply an FFT along the azimuth dimension of the ROI.
4. Segment the data into N sub-apertures, where N is given by Eq.6.5 based on the chosen aperture fraction ξ and overlap ratio Ω.

5. Zero-pad and apply an IFFT to each segment of the data to reconstruct a series of sub-aperture images in range-azimuth with the same pixel spacing as the ROI.
6. Select the brightest pixel within the scene on which to centre a patch of $W_r \cdot W_y$, and track the motion of this patch through the sequence of sub-aperture frames using 2D cross-correlation, using an upsampling factor k_{grid}.
7. Convert pixel shifts into radial velocity values using Eq.6.2 and apply sinc interpolation with an upsampling factor k_{sinc}.

Figure 6.6 graphically illustrates the overall SPOT algorithm workflow. Steps 3, 4, and 5, which correspond to the sub-aperture generation process, are further detailed in Fig. 6.5.

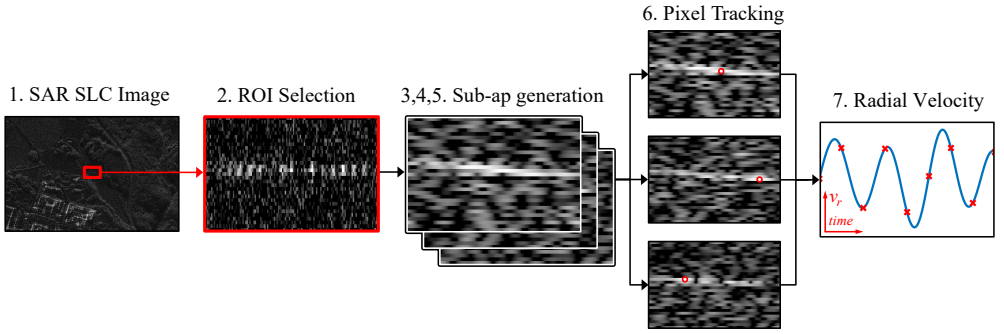


Figure 6.6: Diagram illustrating the SPOT algorithm workflow.

6.4 Experimental data and ground truth comparison

This section describes the experiments conducted to test the SPOT algorithm. The collection of the ground truth data is described first, followed by a description of the SAR data. Finally, the processing of the ground truth data and the subsequent analysis comparing the SAR measurements and ground truth values is explained.

6.4.1 Ground truth data

Experiment locations

To ensure a controlled environment and reduce potential sources of interference, the vibrating targets used in the experiments were placed in open grassy

areas far from other reflective objects such as large buildings or metal structures. The tests were conducted at two locations: Villa Gherta in Trento, Italy, and Glasgow Green, Glasgow, Scotland. These locations are shown in Fig. 6.7.

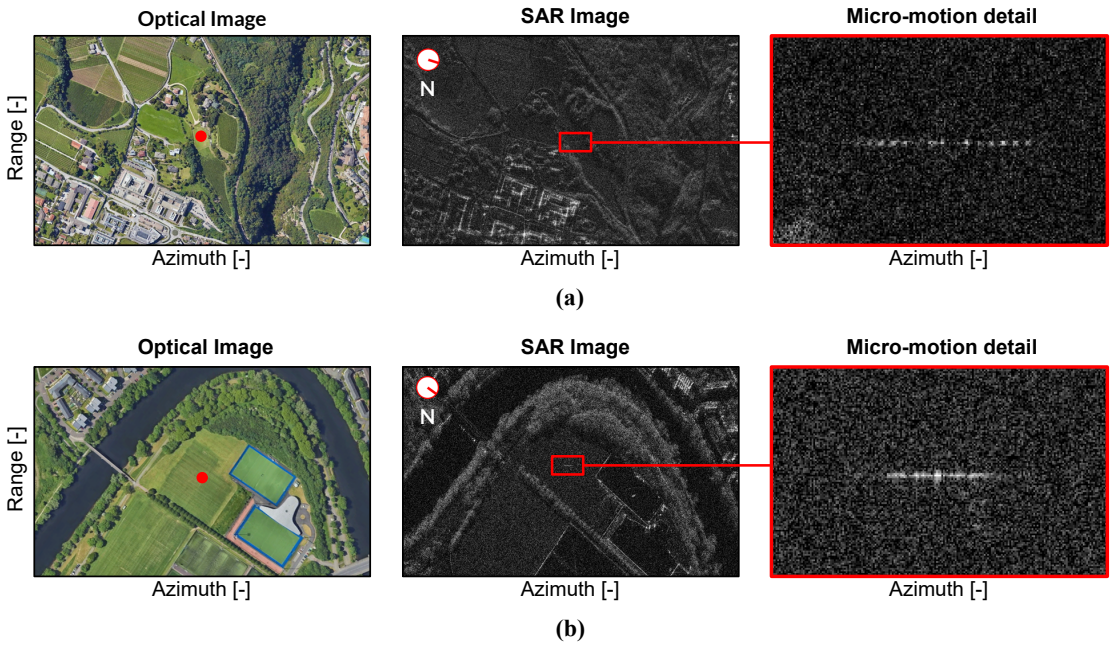


Figure 6.7: The test locations shown as both optical and SAR images, with detail of micro-motion seen from a shaker target in (a) Villa Gherta in Trento LAT: 46.06814°, LON:11.14684°; and (b) Glasgow Green in Glasgow LAT: 55.84379°, LON:−4.23634°.

Instrumentation

The vibrating 'shaker' targets were set up by mounting a corner reflector (CR) target on a linear actuator. CRs are commonly used in radar measurements to provide a point-like high intensity reflection which is stable over a wide angle [43]. The shaker in Glasgow used a TIRA-TV 51140 [44] whilst in Trento this was an APS-400 [45]. Photographs of the apparatus in situ are shown in Fig. 6.8(a)-(b). Both configurations produced only vertical motion to simplify the validation process, which was controlled using a signal generator input. A diagram of the SAR collection geometry in relation to the shaker movement is also shown in Fig. 6.8(c). The vertical displacements produced by the apparatus were recorded using a linear variable differential transformer (LVDT) sensor.

Procedure

First, the CR was tilted 20° vertically and then oriented in azimuth to face towards the direction of the satellite during its passage, taken as the oppos-

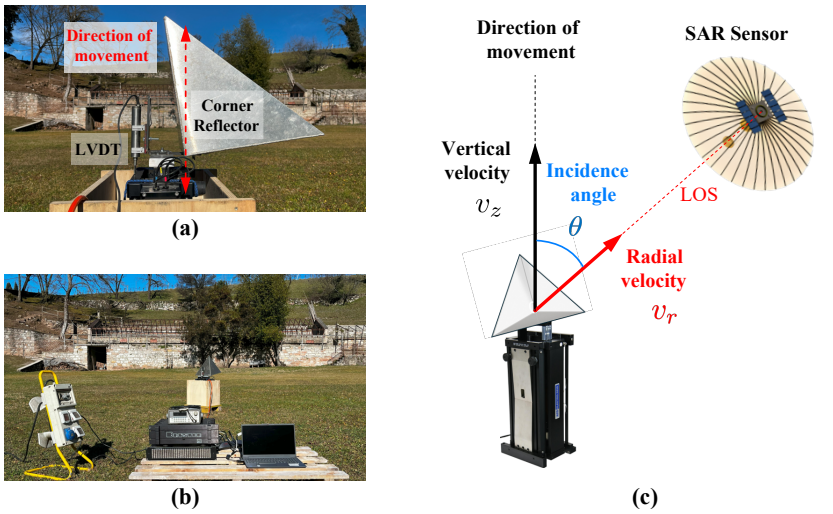


Figure 6.8: Photographs in (a) and (b) show the experimental apparatus in situ at the Villa Gherta site, including the actuator, CR, LVDT, and data acquisition system, and (c) shows a diagram of the SAR acquisition geometry in relation to the shaker setup. Images adapted from [41, 42].

ing angle to the mean azimuth angle of the acquisition. The instrumentation described above was then activated 10 minutes prior to the start of the scheduled satellite observation time (which has a degree of uncertainty) to ensure that coincident data were collected and that the shaker motion had settled to a steady state. Data collection continued for a further 10 minutes after the scheduled time, during which the LVDT sampled the displacement of the CR at a sampling rate of 50 Hz. The programme of tests involved motions with various amplitudes, frequencies, and modulations to comprehensively test the algorithm under different conditions in preparation for more complex case studies involving real structures.

The resultant tests included a variety of vibration signals, ranging from single tone sinusoids to more complex signals such as a linear frequency sweep, a superposition of multiple frequencies, and a number of amplitude-modulated (AM) signals with either a 1 or 2 Hz carrier frequency with a 0.2 Hz modulation. These signal types were selected to evaluate SPOT across a range of vibrational scenarios relevant to SHM. Single-tone signals reflect typical structural responses near fundamental modes, while amplitude-modulated signals mimic responses from multiple closely spaced modes (e.g. typically observed in long-span bridges and viaducts). Frequency-varying signals, although less common in SHM, allow the assessment of the technique under more complex conditions

that could be useful in other contexts. The SAR measures only the LOS projection of the target motion. For the sake of experimental simplicity, the shakers move only vertically. To disambiguate motion components along multiple axes, two or more measurements from different perspectives are needed; however, for bridges, the dominant direction of motion is vertical – this case matches the experiments well and can be measured with only a single observation given this prior knowledge.

In this study, 9 different configurations were tested, with the resulting peak radial displacement, $r_{\max}$, of the shaker being as large as $13.96\ \mathrm{mm}$ with a peak radial velocity, $v_{r,\max}$, of $95.52\ \mathrm{mm/s}$ down to a displacement of $0.19\ \mathrm{mm}$ and a peak radial velocity of $1.42\ \mathrm{mm/s}$. The experiment configurations are listed in Table 6.1.

6.4.2 SAR data

The SAR dataset consists of 9 Umbra acquisitions corresponding to the tests described in Table 6.1. Umbra is a constellation of X-band SAR satellites capable of providing high-resolution data promptly for both private and public use [20]. The radar sensors operate at a central frequency of 9.6 GHz, corresponding to a wavelength of $\lambda = 31\ \mathrm{mm}$. All of the acquisitions were collected using the Umbra spotlight high-resolution mode. The main acquisition parameters of the SAR images are reported in Table 6.2, including the SAR sensor satellite used for the acquisition, date and time of the acquisition, duration of the acquisition t_{a}, collection incidence angle β, pulse repetition frequency (PRF), SAR platform velocity v_{s}, slant range distance R, range resolution Δr, and azimuth resolution Δy.

6.4.3 Ground truth comparison

Processing of ground truth

The ground truth data were processed to LOS velocities and synchronised with the acquisition to provide a meaningful comparison with the SAR measurements. This processing involved:

1. **Numerical derivation**: the recorded vertical displacement data were differentiated to obtain vertical velocity values.
2. **Time cropping**: the velocity time history was cropped to match the satellite acquisition window by centring this on the centre of aperture time t_{COA}.
3. **Satellite geometry computation**: the satellite geometry during the acquisition was calculated to determine the LOS angle at each point in the

time history.

4. **Velocity projection**: the vertical velocity was projected onto the radial direction (LOS) of the satellite using the incidence angle β to compute the radial velocity v_r. This projection is shown in Fig. 6.8.

Comparison metrics

The following metrics were chosen to evaluate the quality of the SAR measurement with respect to the ground truth data, in both the time and frequency domains, for each individual test:

- RMSE: root mean square of the error (RMSE) between the two signals computed in the time domain by comparing the SAR and ground truth measured velocities at corresponding time instants,
- ϵ_f: absolute error between the dominant frequency peaks,
- ρ_t: Pearson's coefficient for correlation in the time domain,
- ρ_f: Pearson's coefficient for correlation in the frequency domain.

As discussed above, the SAR and ground truth time series were aligned using t_{COA}, however a small uncertainty in the synchronisation remained. To account for this, the SAR signal was allowed to shift within a time interval of half the period $[\text{-}T/2, T/2]$ of the lowest frequency component to maximise the time domain correlation ρ_t between the two signals. This was assumed to minimise the synchronisation error, and the same time shift was then applied when calculating the RMSE. To optimise the processing settings of sub-aperture duration, overlap ratio, and patch size, a parameter sweep was performed and the results selected based on maximising the temporal correlation with the corresponding ground truth.

Table 6.1: The configuration of the conducted tests, noting the test number, type of signal, the principal frequencies (f), the peak (z_{max}) and RMS (z_{RMS}) values of the vertical displacement, the peak ($v_{z,max}$) and RMS ($v_{z,RMS}$) values of the vertical velocity, the peak (r_{max}) and RMS (r_{RMS}) radial displacements, and the peak ($v_{r,max}$) and RMS ($v_{r,RMS}$) values of the radial velocity of the oscillations.

Test	Signal	f	z_{max}	z_{RMS}	$v_{z,\text{max}}$	$v_{z,\text{RMS}}$	r_{max}	r_{RMS}	$v_{r,\text{max}}$	$v_{r,\text{RMS}}$
–	–	[Hz]	[mm]	[mm]	[mm/s]	[mm/s]	[mm]	[mm]	[mm/s]	[mm/s]
1	Single tone	1	24.10	17.42	165.86	111.24	13.96	10.43	95.52	64.11
2	Single tone	2	3.43	2.53	48.26	31.79	2.24	1.65	31.38	20.70
3	Single tone	2	1.08	0.80	16.55	10.24	0.70	0.52	10.75	6.66
4	AM	2 (0.2)	0.52	0.26	7.12	3.17	0.39	0.19	5.25	2.34
5	AM	2 (0.2)	0.29	0.14	4.34	1.77	0.22	0.10	3.21	1.31
6	AM	1 (0.2)	0.53	0.28	3.83	1.78	0.43	0.23	3.13	1.46
7	AM	1 (0.2)	0.24	0.13	1.74	0.81	0.19	0.10	1.42	0.66
8	Superposition	2 and 4	2.60	1.56	51.63	29.27	1.11	0.66	21.99	12.47
9	Frequency sweep	1 to 4	4.03	2.81	84.33	38.47	2.81	1.98	58.04	26.53

Table 6.2: SAR acquisition parameters: test number, sensor name, acquisition date, time at the start of the acquisition in UTC, observation time (t_a), incidence angle (β), pulse repetition frequency (PRF), satellite velocity (v_s), slant range distance (R), range resolution (Δr), and azimuth resolution (Δy).

Test	Sensor	Date	Time (UTC)	t_{a}	β	PRF	v_{s}	R	Δr	Δy
–	–	[dd-mm-yy]	[HH:MM:SS]	[s]	[°]	[kHz]	[km/s]	[km]	[m]	[m]
1	Umbra05	18/11/23	20:46:27	6.04	54.80	5.75	7.69	844	0.18	0.22
2	Umbra04	14/03/24	20:35:48	5.41	49.36	6.37	7.70	716	0.17	0.22
3	Umbra05	14/03/24	21:29:22	5.95	49.43	6.31	7.67	795	0.17	0.21
4	Umbra09	24/02/25	10:53:09	16.01	42.29	7.44	7.65	749	0.15	0.08
5	Umbra10	25/02/25	10:52:49	15.93	42.00	6.92	7.65	745	0.15	0.08
6	Umbra09	30/01/25	10:46:27	14.70	34.49	7.75	7.65	683	0.13	0.07
7	Umbra09	31/01/25	10:46:52	14.79	35.05	7.71	7.65	687	0.13	0.07
8	Umbra08	29/03/24	20:57:41	7.98	64.78	6.11	7.66	1115	0.20	0.22
9	Umbra04	29/03/24	21:29:38	6.38	46.29	5.44	7.70	673	0.16	0.18

6.5 Results

In this section, the results of the SPOT technique are presented with comparison to the ground truth data. Each SAR acquisition was processed following the workflow described in Section 6.3, with Table 6.3 summarising the parameters used for each extraction and the resulting metric outputs. The presentation of results is structured into three parts according to signal type: single tone, AM, and superposition and frequency sweep.

The processing parameters listed in Table 6.3 include:

- The patch size in pixels along the range (W_r) and azimuth (W_y) directions.

Table 6.3: SPOT extraction parameters and metric results comparing the SAR measured velocities with ground truth data. The table lists the test number, patch range size (W_r), patch azimuth size (W_y), observation time (t_a), observation ratio (η), overlap percentage (Ω), sub-aperture number (N), sampling frequency (f_s), sub-aperture duration (t_{sap}), frequency resolution (Δf), absolute and percentage RMSE, absolute error between dominant frequency peaks (ϵ_f), correlation in the time domain (ρ_t), and correlation in the frequency domain (ρ_f).

Test	W_r	W_y	t_a	η	Ω	N	f_s	t_sap	Δf	RMSE	%RMSE	ϵ_f	ρ_t	ρ_f
–	[pixels]	[pixels]	[s]	–	[%]	–	[Hz]	[s]	[Hz]	[mm/s]	[%]	[Hz]	–	–
1	5	131	6.04	0.39	43	26	4.4	0.39	0.18	20.6	21.6	0.0090	0.95	0.97
2	5	101	5.41	0.48	38	35	6.6	0.24	0.19	9.6	30.6	0.091	0.89	0.96
3	5	101	5.95	0.57	38	33	5.6	0.28	0.18	4.9	45.6	0.045	0.73	0.87
4	5	51	16.01	0.58	23	71	4.5	0.29	0.064	2.3	43.8	0.050	0.61	0.71
5	5	71	15.93	0.62	31	74	4.7	0.31	0.064	2.2	68.5	0.015	0.45	0.73
6	5	51	14.70	0.66	49	42	2.9	0.66	0.071	1.2	38.3	0.0010	0.68	0.75
7	5	51	14.79	0.65	42	38	2.6	0.65	0.071	0.91	64.1	0.014	0.48	0.70
8	5	71	7.98	0.66	41	81	10.2	0.17	0.13	13.9	63.2	0.083	0.51	0.67
9	5	131	6.38	0.69	45	66	10.5	0.17	0.16	11.9	20.5	0.079	0.89	0.95

- The observation ratio (η), where this was computed relative to the period of the carrier frequency – for the superposition and frequency sweep signals, the period associated with the highest frequency component was used.
- The overlap ratio (Ω).
- The resulting number of sub-apertures (N).
- The sampling frequency (f_s).
- The sub-aperture duration (t_sap).
- The frequency resolution in the spectral domain (Δf).

Additionally, the ROI size during processing was defined as 650 range pixels by 3000 azimuth pixels, and upsampling factors of $k_\mathrm{grid} = 10$ and $k_\mathrm{sinc} = 20$ were used. The performance of the SPOT algorithm was assessed both graphically with Figures 6.9 to 6.17, and numerically using the metrics outlined in Section 6.4.3, with the results presented in Table 6.3. In the case of the RMSE, this is expressed both in terms of velocity and as a percentage of the maximum ground truth radial velocity to help facilitate comparison of the results. During the acquisition time, the range to the target observed by the SAR changes, however the image formation process fully compensates the change such that R is a constant in the image product used as input to the SPOT processing, with values as shown in Table 6.2.

6.5.1 Single frequency

Processing parameters

Tests 1 to 3 were of single frequency sinusoids with a frequency of either 1 Hz or 2 Hz, with maximum radial velocities ranging from $v_{r,\max} = 95.52$ to 10.75 mm/s (RMS radial values of $v_{r,\text{RMS}} = 64.11$ to 6.66 mm/s), with corresponding RMS radial displacements, r_{RMS}, of 10.43 mm to 0.52 mm. As summarised in Table 6.3, these were extracted with observation ratios η ranging from 0.39 to 0.57 corresponding to comparable t_{sap} values of 0.39 s to 0.24 s. The observation ratio used for the extraction in Test 3 exceeded 0.5 meaning that the sub-aperture duration was greater than half of the period being observed, however the overlap percentage of 38% ensured that the sampling frequency met the Nyquist criterion. In general, the overlap percentages for these tests were similar, ranging from 38% to 43%. The azimuth patch size was 131 for Test 1, after which it was decreased to 101 for Tests 2 and 3. This was found to improve tracking performance and was dependent on the target velocity, where it was observed that too small a patch size would result in the tracking underestimating the movement.

Qualitative analysis

Figures 6.9 to 6.11 show the time series and frequency spectra of the velocity measurements. These results indicate that the signals measured by SAR match the ground truth well both in the time and frequency domains. In all cases, the main vibration frequency was accurately detected, as shown by the spectrum results. The measured peak amplitude values are also satisfactory, however with a tendency to be slightly underestimated, indicating a measurement bias which is more pronounced in Tests 2 and 3. Test 2 (Fig. 6.10) exhibits a generally good match in the time series, however with some peaks being under- or overestimated, and with consequently a diminished spectral peak and spurious frequency components at 0.5 and 2.8 Hz. Test 3 (Fig. 6.11) shows similar results, confirming the overall measurement consistency although again with some minor measurement noise in the spectrum. A degradation in performance was observed as the vibration velocity decreases – in this case from 95.52 mm/s to 10.75 mm/s from Test 1 to Test 3 – which affected both the smoothness of the time series and the sharpness of the spectral peaks. The consistency of the tracking measurement appears to be better for the 1 Hz oscillation, however more single tone experiments would be required to confirm whether this is due to the oscillation amplitude or frequency since in this case the target was moving at a significantly greater velocity.

Quantitative results

The identified qualitative trends are supported by the metric results. The time domain correlation coefficients for these tests are high, ranging from 0.73 to 0.95, going from the lowest (Test 3) to the highest (Test 1) velocity cases, respectively. In the frequency domain, the values of the correlation coefficient range from 0.87 to 0.97, with better performance likewise associated with higher velocities (see Table 6.3). Despite the limited frequency resolution, Δf, due to the short acquisition duration, the dominant frequency peaks were accurately identified with absolute errors ranging from 0.009 Hz to 0.091 Hz, where these values are significantly less than Δf in all cases, indicating that the identified peaks are a match within measurement uncertainty. In terms of amplitude, the SAR measured velocities show a slight underestimation compared to the ground truth, where this discrepancy increases with decreasing target velocity. The RMSE confirms this trend – the relative RMSE increased consistently from 21.6% for Test 1 to 45.6% for Test 3. These findings all support the expectation that measurement accuracy decreases with decreasing target velocity.

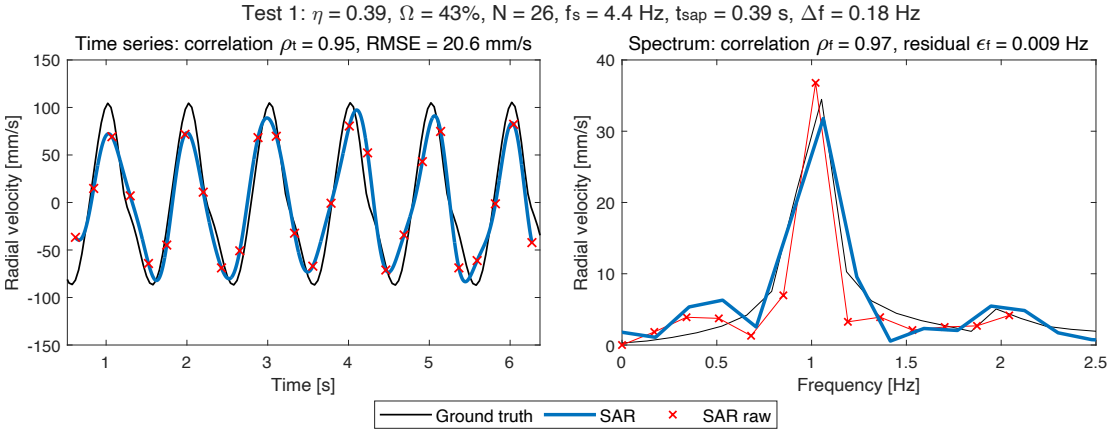


Figure 6.9: Radial velocity and corresponding frequency spectrum from Test 1*, with the shaker set to vibrate at* 1 *Hz with a peak radial velocity of* $v_{r,max} = 95.52$ *mms*$^{-1}$ *and an RMS of* $v_{r,RMS} = 64.11$ *mms*$^{-1}$*. The plots compare the ground truth velocity (black line) with the SAR measurement: the raw output (red line with markers) and the sinc-interpolated result (blue line).*

6.5.2 Amplitude modulation

Processing parameters

The measurement results of the AM signals in Tests 4 to 7 are shown in Figures 6.12, 6.13, 6.14, and 6.15. The target velocities in these tests were significantly lower compared to the single frequency experiments, with $v_{r,\max}$

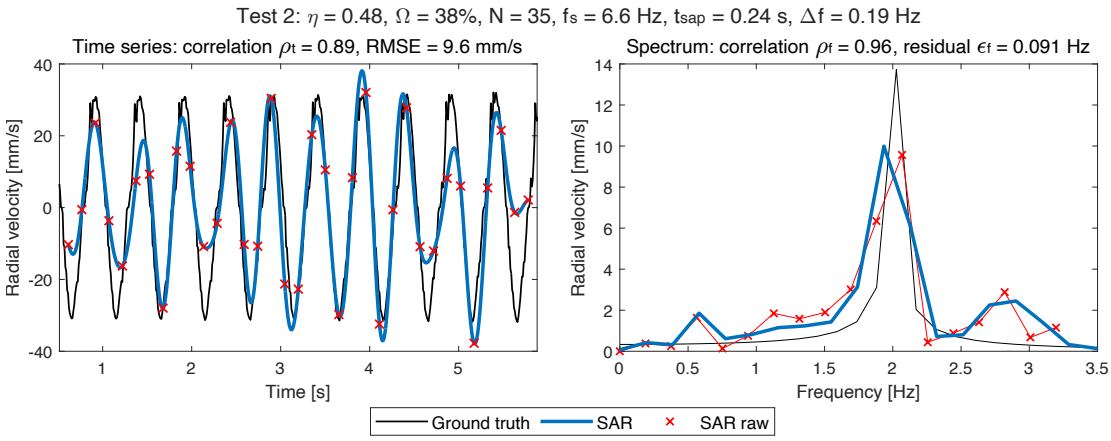


Figure 6.10: Time series and frequency spectrum results for Test 2, for 2 Hz single frequency, shaker motion with a $v_{r,max} = 31.38$ *mms*$^{-1}$ *and* $v_{r,RMS} = 20.70$ *mms*$^{-1}$.

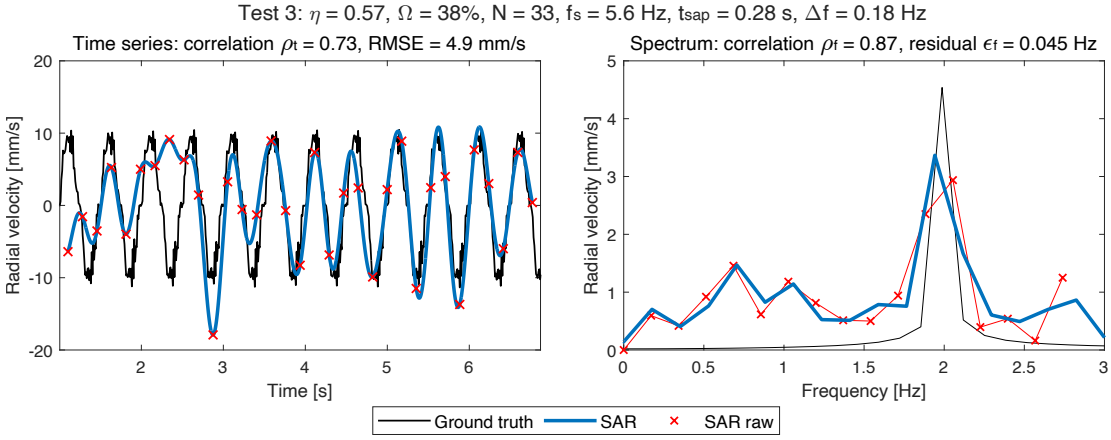


Figure 6.11: Time series and frequency spectrum results for Test 3, for 2 Hz single frequency, shaker motion with a $v_{r,max} = 10.75$ *mms*$^{-1}$ *and* $v_{r,RMS} = 6.66$ *mms*$^{-1}$.

ranging from 1.42 mm/s to 5.25 mm/s (0.66 to 2.34 mm/s RMS) making them more representative of the vibrations expected for real structures. The RMS radial displacements recorded for these tests were very low, ranging from 0.10 mm to 0.23 mm. To compensate for the lower amplitudes and increased waveform complexity, it was found that the observation ratio η needed to be increased compared to the single frequency measurements to values ranging from 0.58 to 0.66, whilst the optimal overlap percentage Ω was more variable but remained within a similar range of 23% to 49%. This resulted in reduced sampling frequencies overall when comparing measurements of signals with the same carrier frequency; Test 1 compared with 6 and 7 indicates an approximate

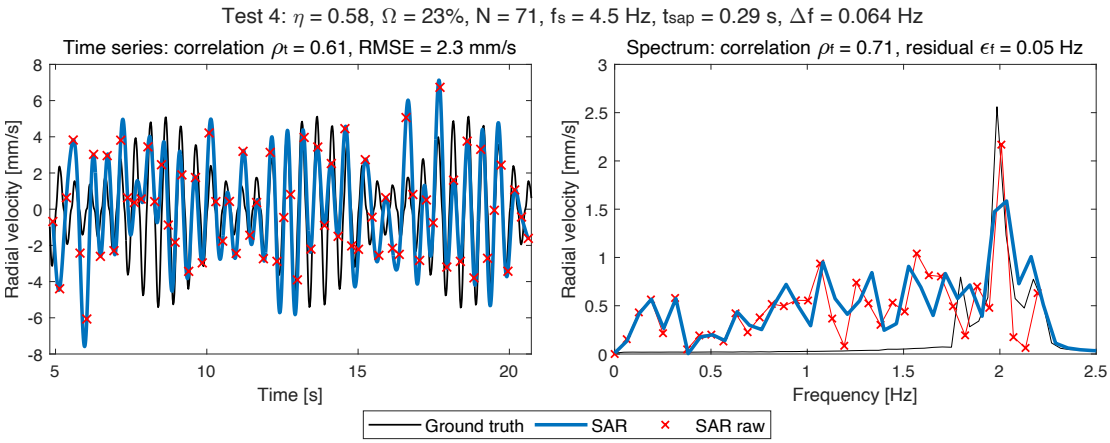


Figure 6.12: Time series and frequency spectrum results for Test 4*, for* 2 *Hz frequency and amplitude modulation of* 0.2 *Hz, shaker motion with a* $v_{r,max} = 5.25$ *mms*$^{-1}$ *and* $v_{r,RMS} = 2.34$ *mms*$^{-1}$.

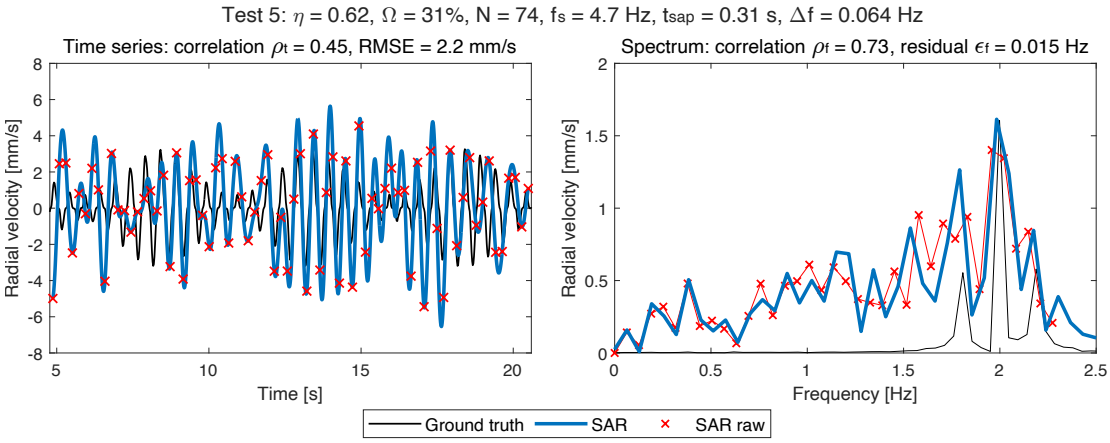


Figure 6.13: Time series and frequency spectrum results for Test 5*, for* 2 *Hz frequency and amplitude modulation of* 0.2 *Hz, shaker motion with a* $v_{r,max} = 3.21$ *mms*$^{-1}$ *and* $v_{r,RMS} = 1.31$ *mms*$^{-1}$.

40% drop in sampling frequency, and comparing Tests 2 and 3 with 4 and 5 shows an average decrease of approximately 25%. This led to a reduction in the maximum observable frequency, particularly in Tests 4 and 7, where the sampling frequency only marginally satisfied the Nyquist criterion of 4.4 and 2.4 Hz, respectively. Despite the reduction in f_s, t_{sap} was broadly similar to the single frequency measurements, except for Tests 6 and 7 involving the 1 Hz carrier which were significantly longer. For these measurements, the azimuth patch sizes were reduced to either 51 or 71 pixels, where this was due to the lower overall target velocity.

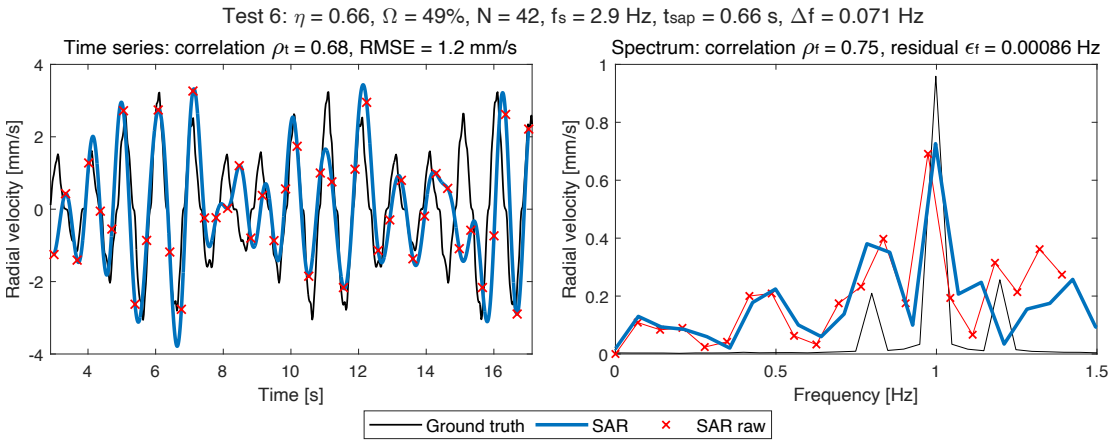


Figure 6.14: Time series and frequency spectrum results for Test 6*, for* 1 *Hz frequency and amplitude modulation of* 0.2 *Hz), shaker motion with a* $v_{r,max} = 3.13\ mms^{-1}$ *and* $v_{r,RMS} = 1.46\ mms^{-1}$.

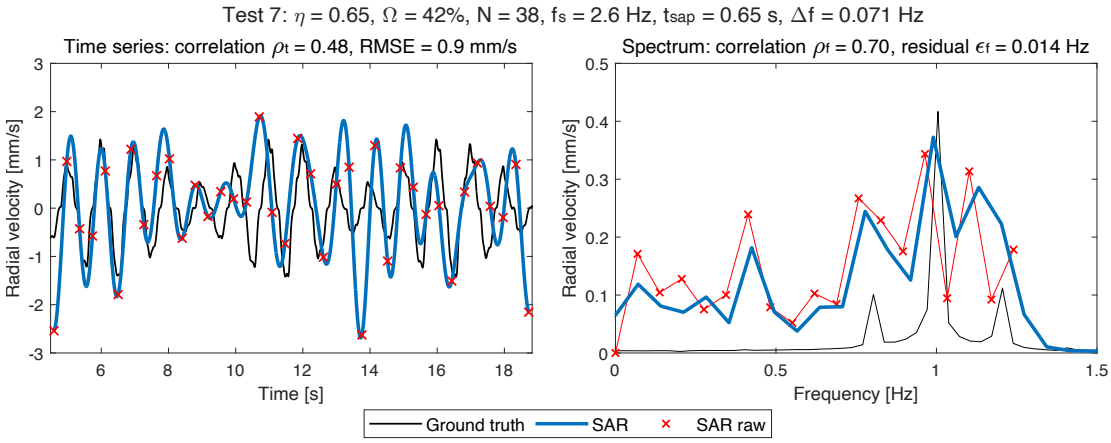


Figure 6.15: Time series and frequency spectrum results for Test 7*, for* 1 *Hz frequency and amplitude modulation of* 0.2 *Hz, shaker motion with a* $v_{r,max} = 1.42\ mms^{-1}$ *and* $v_{r,RMS} = 0.66\ mms^{-1}$.

Qualitative analysis

Compared to the higher velocity basic waveforms from Tests 1 to 3, a decrease in performance was observed for Tests 4 to 7. Despite this, the dominant frequency was accurately measured in all cases. Results from tests with a 2 Hz carrier (shown in Figures 6.12 and 6.13) were of generally lower quality. In Test 4, a secondary peak corresponding to the amplitude modulation was only marginally detectable, whilst in Test 5 both the modulation peaks were identified, although their amplitudes are comparable to the surrounding level of measurement uncertainty. Tests with a 1 Hz carrier (shown in Figures 6.14 and 6.15), showed clearer detections of the secondary peaks; in Test 7, these were

more distinct compared to those in Test 6. The frequency match of the lower peak tended to be better than that of the higher peak, which was in general slightly underestimated. The relative amplitudes of the peaks were generally poorly estimated, but in all cases they remained lower than that of the carrier peak, which was accurately measured in Test 5, although it was generally underestimated in the other tests. Additionally, when detectable, the amplitude of the secondary peaks tended to be overestimated compared to the ground truth values.

Quantitative results

As shown in Table 6.3, the time domain correlation coefficients for these tests range from 0.45 (Test 5) to 0.68 (Test 6), showing a decline compared to the single frequency tests. Frequency domain correlation values show a small variation from 0.70 (Test 7) to 0.75 (Test 6). The longer acquisition time of these tests resulted in an improved frequency spectrum resolution where $\Delta f \approx 0.07$ Hz. The frequency error, ϵ_f, for the dominant peak remained very good, ranging from 0.001 Hz to 0.050 Hz, and being consistently less than Δf. %RMSE values range from 38.3% (Test 6) to 68.5% (Test 5), with the error increasing as target velocity decreases for each carrier frequency, respectively.

Whilst Tests 5 and 6 had very similar target velocities of $v_{r,\text{RMS}} = 1.31$ mm/s and 1.46 mm/s, respectively, the measurement quality for Test 5 was significantly lower. This is indicated by the high RMSE and reduced time-domain correlation; the %RMSE for Test 5 reached 68.5%, compared to 38.3% for Test 6, and the time-domain correlation ρ_t was 0.45 versus 0.68. The frequency spectrum correlation, ρ_f, remained comparable however for the two tests, with only a slight decrease in Test 5 (0.73 versus 0.75). The decrease in performance can also be seen by visually comparing the measured signals in Fig. 6.13 and Fig. 6.14. These results suggest that the SPOT algorithm performs better measuring lower frequencies, and that the performance is not only dependent on the target velocity. Further support for this comes from Test 4, which featured a carrier frequency of 2 Hz and a higher velocity amplitude $v_{r,\text{RMS}}$ of 2.34 than Test 6 (1 Hz carrier), but still resulted in a higher %RMSE of 43.8%.

6.5.3 Superposition and linear frequency modulation

Processing parameters

Tests 8 and 9 (shown in Fig. 6.16 and 6.17) involved more complex target vibration signals, with additional frequency content and higher frequency components reaching up to 4 Hz. These tests also featured higher vibration ve-

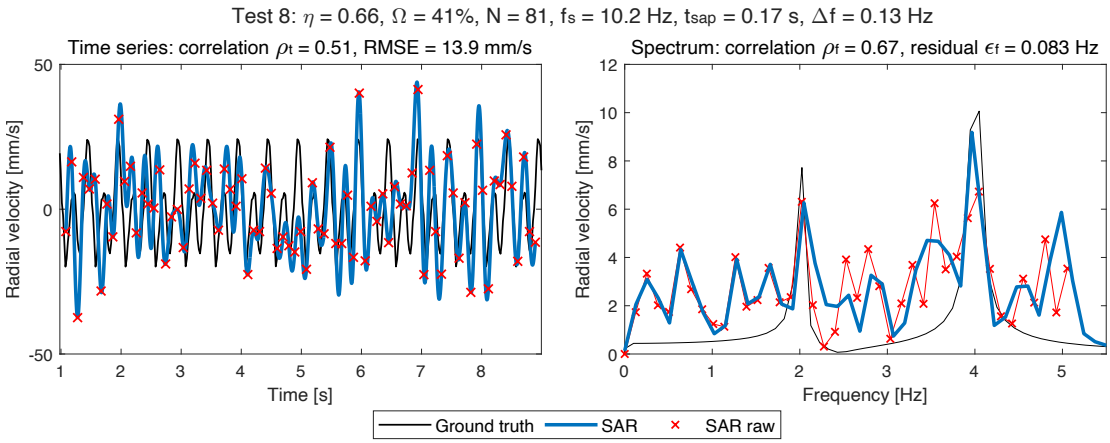


Figure 6.16: Time series and frequency spectrum results for Test 8*, for superposition of* 2 *Hz and* 4 *Hz frequencies, shaker motion with a* $v_{r,max} = 21.99$ *mms*$^{-1}$ *and* $v_{r,RMS} = 12.47$ *mms*$^{-1}$.

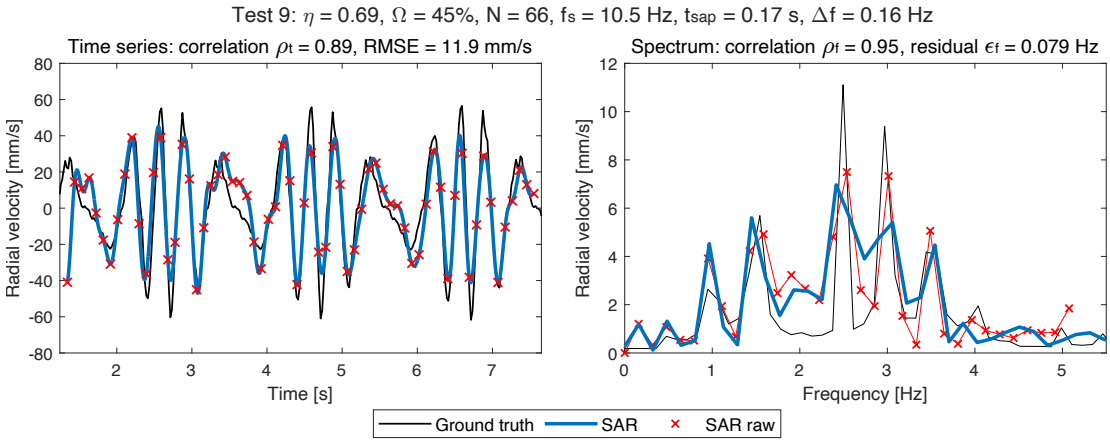


Figure 6.17: Time series and frequency spectrum results for Test 9*, for linear frequency sweep* $1 - 5$ *Hz, shaker motion with a* $v_{r,max} = 58.04$ *mms*$^{-1}$ *and* $v_{r,RMS} = 26.53$ *mms*$^{-1}$.

locities than those used for the AM motion experiments, more comparable to those for the single frequency tests. The peak radial velocity amplitudes $v_{r,\max}$ reached 21.99 mm/s for Test 8 and 58.04 mm/s for Test 9, with corresponding RMS values of 12.47 mm/s and 26.53 mm/s, respectively. The radial RMS displacements of these tests were $r_{\text{RMS}} = 0.66$ mm and 1.98 mm for Test 8 and 9, respectively. Due to the increased frequency content, higher sampling rates of 10.2 Hz and 10.5 Hz for Test 8 and 9, respectively, were necessary to guarantee the reconstruction of the full spectrum. The t_{sap} values of both tests were lower than the preceding measurements, being 0.17 and 0.15 s for Tests 8 and 9, respectively. The optimal azimuth patch sizes were once again found to

approximately scale to the target velocity, where for Test 9 this was 131 pixels, the same as Test 1 where $v_{r,\text{max}}$ was $95.52\ \text{mm/s}$ and $v_{r,\text{RMS}}$ was $64.11\ \text{mm/s}$.

Qualitative analysis

In Test 8 (Fig. 6.16), the overall agreement of the SAR measured velocity with the ground truth in the time domain was relatively poor due to the presence of significant measurement uncertainty. This is also evident in the frequency domain. Despite these limitations, the dominant frequencies of the two superposed signals of 2 Hz and 4 Hz are still correctly identified. A spurious third peak appears however at 5 Hz, reaching a magnitude comparable to the lower 2 Hz component. The amplitudes relative to the main frequency components were both well estimated, showing only slight underestimation relative to the ground truth.

The result for Test 9 shown in Fig. 6.17 showed significantly better performance in the time domain. The extracted signal closely resembled the ground truth, where the under- or overestimation of peak values was minor, although a bias towards underestimation was seen. The measurement improvement was likely due to the higher target velocity in Test 9 compared to the one in Test 8, despite the more complex signal content. In the frequency domain, all expected peaks up to 3.5 Hz were clearly identifiable. The relative amplitudes of these peaks also showed a good match, although the 1 Hz peak was nearly twice the amplitude of the ground truth, and the two most dominant components of 2.5 and 3 Hz were both underestimated. The ground truth peak at 4 Hz was not observed in the SAR data, possibly due to its relatively low amplitude compared to other components.

Quantitative results

Referring to Table 6.3, the time domain correlation for Test 8 was 0.51, which is relatively low and aligns with the qualitative assessment. The spectrum correlation of 0.67 is slightly better, reflecting the correct identification of dominant frequency components. The frequency estimation error ϵ_f for the dominant 4 Hz peak was 0.083 Hz, which is below the spectral resolution $\Delta f = 0.13$ Hz and consistent with previous tests. The RMSE was $13.8\ \text{mm/s}$, corresponding to a high relative error of 63.2%.

In contrast, Test 9 yielded significantly better results, with a time domain correlation of $\rho_t = 0.90$ and a frequency domain correlation of $\rho_f = 0.95$. The frequency estimation error of $\epsilon_f = 0.074$ Hz was also less than the spectral resolution of $\Delta f = 0.16$ Hz, supporting the robustness of the frequency extraction. The RMSE was $11.5\ \text{mm/s}$, which corresponds to a relative error of 19.8%, highlighting the improved performance over Test 8.

6.6 Discussion

6.6.1 General measurement performance

Several factors influence the LOS velocity measurement accuracy of the SPOT technique:

- oscillation amplitude of the velocity being measured,
- dominant frequency content of the vibration,
- signal complexity (e.g. sweep, superposition), and
- processing parameter selection (sampling, sub-aperture duration, overlap, etc.).

Effect of oscillation amplitude

Measurement error as defined by %RMSE increased as velocity amplitude decreased. For example, single-frequency tests (Tests 1-3) showed the %RMSE increasing from 21.6% to 45.6% for peak velocities decreasing from $95.5\ \mathrm{mm/s}$ to $10.75\ \mathrm{mm/s}$ (which in absolute terms was a decrease in RMSE from $20.6\ \mathrm{mm/s}$ to $4.9\ \mathrm{mm/s}$, respectively); a similar trend was observed for AM signals. Effectively, this means the *velocity measurement uncertainty increases with decreasing amplitude*, which is the expected result. This behavior is visible in both the time-domain and frequency-domain of the velocities measured with MDSAR, where lower amplitude oscillations are associated with more spurious content and subsequently lower respective correlation values.

Effect of dominant frequency

For AM vibrations with velocities $v_{r,\mathrm{RMS}}$ between 0.66 and $2.34\ \mathrm{mm/s}$, the carrier frequency of the vibration was shown to have a significant influence on the achievable performance of the measurement. A comparison between Test 5 and Test 6 illustrates this effect.

Test 5 featured a 2 Hz carrier and an RMS radial velocity of $1.31\mathrm{mm/s}$; its time and frequency domain correlation coefficients were 0.45 and 0.73, corresponding to an RMSE of 68.5% of the peak value. In contrast, Test 6 employed a 1 Hz carrier with a comparable RMS radial velocity of $1.46\ \mathrm{mm/s}$; here the time and frequency domain correlations increased to 0.68 and 0.75, while the RMSE dropped to 38.3% of the peak value. A further comparison with Test 7 emphasises this conclusion; Test 7 had a carrier frequency of 1 Hz and a much lower RMS radial velocity of $v_{r,\mathrm{RMS}}$ $0.66\ \mathrm{mm/s}$, resulting in time and frequency domain correlation values of 0.48 and 0.70 and an RMSE of 64.1% of the peak value – and thus a measurement quality very similar to that of Test 5, where $v_{r,\mathrm{RMS}}$ was approximately double. These results demonstrate that for comparable vibration amplitudes, *lower dominant frequencies lead to more ac-*

curate measurements of the radial velocity. Since these insights are strongly linked to the choice of optimal processing parameters, the influence of these parameters is further discussed later in Section 6.6.1.

Effect of signal complexity

For more complex motion, such as the superposition and linear frequency sweep tests, the sensitivity of MDSAR to both velocity magnitude and frequency content was demonstrated further.

The superposition test (Test 8) was carried out with a relatively high $v_{r,\mathrm{RMS}}$ of $12.47\ \mathrm{mm/s}$, however the achieved measurement quality was lower than for the simpler 1 Hz and 2 Hz cases analyzed previously. Test 8 resulted in time and frequency domain correlation values of 0.51 and 0.67, respectively, and a %RMSE of 63.2%, whereas Test 4, with $v_{r,\mathrm{RMS}} = 2.34\ \mathrm{mm/s}$, achieved higher correlation values of 0.61 and 0.71, respectively, with a lower %RMSE of 45%.

In contrast, the linear frequency modulation test (Test 9) with a $v_{r,\mathrm{RMS}}$ of $26.53\ \mathrm{mm/s}$ yielded excellent results, with a temporal correlation of 0.89, spectral correlation of 0.95, and a %RMSE of 20.5% of the peak velocity. This relative RMSE value was the lowest of all the tests, which is notable given that Test 9 combined higher complexity and lower target velocity than Test 1. This insight suggests that other measurement variables, such as the observation geometry, likely have an impact on the results which has not been controlled for in these experiments.

Processing parameters

A presentation of the full optimisation of the processing parameters, namely sub-aperture duration and overlap ratio, was outside the scope of this work. Nevertheless, the results presented revealed several phenomena resulting in the three points below, related to choosing appropriate processing parameters.

1. Nyquist sampling: the sampling frequency (f_s) must be above the Nyquist rate for the given waveform to be correctly sampled.

2. Azimuth cross-correlation precision: cross-correlation processing, and thus the pixel displacement measurement, is more accurate when the sub-aperture image has a finer azimuth resolution. A longer t_sap results in better azimuth resolution (see Eq.6.1).

3. Motion-induced artifacts: longer sub-aperture times can make the feature less distinct and reduce tracking accuracy since the changing signal phase is integrated over a greater period. This imposes an upper bound on t_sap.

These effects compete, thus need to be optimised. Considering first effects

1 and 2, these are in opposition such that 1 favours shorter t_{sap} values for higher sampling rates whereas 2 favours the t_{sap} values which are as long as possible for greater azimuth precision. This conflict is resolved by allowing the overlap of sub-apertures, as increasing the overlap allows for a greater sampling frequency without reducing t_{sap}, therefore helping to satisfy both conditions simultaneously. Effect 3 then further constrains the overlap values allowed by effects 1 and 2 by its restriction on t_{sap}, and can be considered to be in opposition to effect 2. The combined result of all three effects is a moderate overlap value and an optimal f_{s} near the Nyquist rate. The upper bound on t_{sap} duration imposed by effect 3 increases for low frequency motion since the phase evolves more slowly, where in this case a higher azimuth resolution is then permitted, resulting in a higher quality measurement as the cross-correlation is more accurate. If t_{sap} is too long, the target motion initially becomes blurred in the sub aperture image, and in the extreme case as t_{sap} approaches t_{a} the target becomes multiple or indistinct targets, as seen in the full aperture image (see Fig. 6.5).

The results of these effects are evident in Test 5 and 6, where carrier frequencies were 2 Hz and 1 Hz, respectively, and the RMS velocities were very similar. Both cases resulted in a sampling frequency near the Nyquist rate, whilst for the 1 Hz motion t_{sap} was approximately twice that of the 2 Hz case, which resulted in fewer sub-apertures. The resulting observation ratio (η) was similar for the two tests, indicating that t_{sap} scaled proportionally with the vibration period of the carrier. Due to the shorter t_{sap} required for the 2 Hz carrier motion, the azimuth resolution of each sub-aperture frame was reduced in comparison to that for 1 Hz. This resulted in slightly poorer results in terms of %RMSE and ρ_t (whilst ρ_f was about the same).

The sampling phenomena also explain the results for the more complex signals, for instance the high f_{s} for Test 8 and 9 of 10.2 Hz and 10.5 Hz, respectively. This is greater than expected compared to the AM signals, and is more similar to the single frequency tests. This is due to the greater target velocities which those two groups share, which increases azimuth displacements in the image. The tracking precision required is then reduced, allowing for higher sampling rates. This combination resulted in $t_{\text{sap}} = 0.17$ s for each test, the lowest values recorded.

Regarding Test 8, the 2 Hz peak is possibly lower proportionally than the 4 Hz peak since the optimal parameters chosen by the metric would have been most sensitive to the match to the 4 Hz signal, and thus were likely not optimal for the measurement of the 2 Hz component, resulting in a bias. For Test 9, the amplitude discrepancies and the non-existent 4 Hz component were likely the result of the algorithm being optimised for compromise values to measure

a range of frequencies concurrently, and the tracking precision was likely restricted by lower t_{sap} values resulting in less accurate estimations of the displacements. Additionally, since the 4 Hz component was of a low amplitude relative to the other frequencies, this would have had a lower weighting from the metric used to assess it. These findings suggest that improved results may be obtained by using multiple measurements on the same data which are optimised for small frequency ranges, and then synthesising these into one spectrum.

Apart from the sampling effects listed above, the tracking performance of cross-correlation is also closely related to the patch size (predominantly in the azimuth dimension). If the patch is too small, it will not be able to fully track the motion of a target since, in the extreme case, this will go beyond the bounds of the patch. If the patch is too large however, the tracking is more prone to confusion from noise or other bright targets in the image.

Whilst the optimum processing parameters were chosen for these results, in general a small range of values produced measurements approaching a similar quality. Given this and the difficulty in controlling all variables, some uncertainty in the conclusions about processing parameters remains.

6.6.2 Frequency measurement performance

The frequency measurement precision is fundamentally limited by the observation duration. In these experiments, the maximum SAR acquisition time was 16.01 s, giving a frequency resolution of roughly 0.064 Hz. This could limit distinguishing closely spaced modes in large civil structures. Longer effective acquisitions (up to ~ 30 s in principle, system permitting [21, 20]) would proportionally refine the spectrum resolution. In the context of civil SHM, the frequency accuracy achievable with this technique cannot be smaller than the spectral resolution dictated by the observation time.

Despite these limitations, the dominant frequency was correctly measured in every test, including reliable (negligible error ϵ_f) measurements for AM signals with sub-millimetre radial displacements ranging from r_{RMS} from 0.23 to 0.10 mm. These results are the smallest confirmed displacements measured by this method and are a good indication of its potential suitability to SHM applications.

6.6.3 Suitability for SHM

This section discusses the practical suitability of the SPOT MDSAR technique for VBSHM, particularly its potential to either substitute or complement conventional contact-based vibration monitoring. Using the presented results, this discussion focuses on whether SAR measurements can meet the typical

requirements of SHM. It is reasonable to assume that the following findings extend only to large and slender structures such as long-span bridges or tall buildings, with expected LOS velocity values within the tested range, frequencies between 0.1 to 2.4 Hz, and exhibiting millimetre or sub-millimetre displacements. These assumptions however, will require future testing on real structures, which is outside the scope of this work.

Regarding the efficacy of MDSAR for VBSHM, it is essential to clarify that the required measurement accuracy depends on the monitoring objective. VBSHM generally aims to extract modal parameters such as natural frequencies, damping ratios, and mode-shapes; not to reconstruct the full time-history of structural vibrations. These parameters can be obtained using time-domain methods (e.g. stochastic subspace identification, SSI) or frequency-domain methods (e.g. frequency domain decomposition, FDD), each with different sensitivity to signal sampling, length, and noise. Time-domain methods require high temporal resolution and low-noise signals, which is difficult to satisfy with current SAR acquisition limitations. Frequency-domain methods, conversely, depend more on the spectral content and signal resolution, making them more suitable for MDSAR data.

The experimental results showed that radial RMS velocities as low as 3 $\mathrm{mm/s}$ could be measured with time-domain relative RMSE ¡ 45%. Lower target velocities reduced the time-domain reconstruction accuracy, reaching an RMSE of 68.5% in the worst-case scenario. Notably, the dominant frequencies were consistently identified with frequency residuals below the spectral resolution, confirming the reliability of frequency measurement. This suggests that while MDSAR measurements may not yet be suitable for full time-history reconstructions or time-domain modal analyses, they are better-suited to frequency-domain SHM approaches, where the successful frequency measurement for a radial RMS velocity of 0.81 $\mathrm{mm/s}$ (radial RMS displacement of 0.10 mm) is an excellent indicator that MDSAR can be sensitive enough to measure SHM relevant motion.

Some practical considerations to note before applying this approach to real structures:

- Sampling frequency (f_s) and sub-aperture duration (t_sap) influence the sub-aperture azimuth resolution (see Section 6.6.1). Lower aperture fractions improve f_s but degrade image resolution, hindering the tracking of the scatterers. Therefore, when low vibration frequencies are of interest, it is preferable to use longer sub-apertures to preserve a finer image resolution.
- The technique is inherently limited to measuring radial velocities, mean-

ing that sensitivity depends on the satellite's viewing geometry. For vertical motion (e.g. bridges), near-nadir observations are ideal, while for horizontal ones (e.g. tall buildings), the orbit should be as tilted as possible for a high incidence angle.

- The high RMSE values of time-domain results prevent the precise extraction of mode-shapes and damping values but does not prevent the identification of dominant frequencies.
- The frequency resolution is limited by the achieved acquisition time, t_{a}. For structures with natural modes with a spacing more than that of the frequency resolution, the measured dominant frequency can serve as a key parameter for early-stage damage detection.

In conclusion, while SPOT MDSAR does not yet match the precision of traditional contact-based methods for full modal identification (specifically damping values and mode-shapes), it demonstrates strong potential for large-scale, remote measurement of dominant frequencies. This could support SHM frameworks where SAR data is paired with occasional on-site measurements to confirm or calibrate more detailed analyses.

6.6.4 Future developments

The presented results demonstrate the capability of measuring vibration signatures comparable to those of real infrastructure from spaceborne SAR imagery, establishing a well-validated foundation for future work. Given the limitations of the presented technique for vibration measurements, there are several strategies that could be employed to improve the performance and practicality of MDSAR for VBSHM:

- *Algorithm improvements*: the SPOT algorithm, as an image-domain method, requires patch-size optimisation and is inherently limited by image resolution. Future research could explore phase-domain methods, which may offer greater sensitivity for micro-motions measurements, and issues arising from effect 3 in Section 6.6.1 may be alleviated. Moreover, signal enhancement techniques such as singular value decomposition (SVD) or Bayesian filtering could help mitigate noise and increase robustness.
- *Integration of knowledge of structural dynamics*: integrating structural models (e.g. simplified dynamic equations or finite element models), or simply imposing physical constraints into the velocity reconstruction workflow, may allow for better fitting of measured data.
- *Orbit planning and acquisition strategies*: since MDSAR is only sensi-

tive to the radial component of motion, observation geometry plays an important role. Future satellite tasking could prioritize near-nadir acquisitions for vertical motion measurements, or steep incidence angles for horizontal displacements. Likewise, longer-duration acquisitions would enhance spectral resolution and improve the detection of closely spaced frequency modes.

- *Combination of multiple passes*: combining measurements from different passes or viewing geometries may enable the reconstruction of full three-dimensional motion. Furthermore, these could increase redundancy and improve confidence in frequency detection.

6.7 Conclusions

This work investigated the metrological effectiveness of MDSAR for measuring target vibrations from single-pass SAR images, focusing on vibrational signals relevant to SHM of infrastructure. The SPOT algorithm was used as a representative method among various potential techniques.

To assess the performance and limitations of MDSAR, a comprehensive experimental campaign was conducted using an isolated shaker target under controlled conditions. A wide range of vibration types were generated, including single frequency sinusoids, AM signals, a frequency superposition and a linear frequency modulation. Peak radial velocities varied from high amplitudes ($95.52\ \mathrm{mm/s}$, $13.96\ \mathrm{mm}$ radial displacement) to very low amplitudes ($1.42\ \mathrm{mm/s}$, radial displacement of $0.19\ \mathrm{mm}$), reflecting SHM relevant ranges.

MDSAR measured the time history of LOS velocity, with RMSE errors of $20.6\ \mathrm{mm/s}$ (21.6% of ground truth peak value) and $0.9\ \mathrm{mm/s}$ (63.2%), for the highest ($95.52\ \mathrm{mm/s}$, single frequency) and lowest ($1.42\ \mathrm{mm/s}$, AM) amplitudes, respectively. Percentage RMSE increased in relative terms as the velocity amplitude decreased and the signal complexity increased. Signals dominated by lower frequencies produced better results than those with higher-frequency content.

The dominant frequency was correctly identified in all test cases, down to RMS radial displacements of $0.10\ \mathrm{mm}$ for two AM signals with RMS radial velocities of 1.31 and $0.66\ \mathrm{mm/s}$. Frequency peak residuals consistently fell below the spectral resolution limit. The SAR acquisition duration (longest recorded $\sim 16\ \mathrm{s}$) constrains frequency resolution ($\sim 0.064\ \mathrm{Hz}$), which may not be sufficient for distinguishing closely spaced structural modes in civil SHM, although longer acquisitions of $\sim 30\ \mathrm{s}$ are feasible. Spectral correlation values (ρ_f) were consistently higher than the temporal correlation values (ρ_t), indicat-

ing that the technique is better at reconstructing the frequency content of the signal, rather than the full time-history of the radial velocity.

Overall, this work demonstrated that information relevant for VBSHM can be measured from SAR data, even with a relatively simple approach like the SPOT technique. The achievable level of accuracy – compared to synchronous ground truth time series data – indicated that whilst limitations remain in reconstructing full time-histories, dominant vibrational frequencies were measured effectively, even for very small displacements similar to those expected from infrastructure. These results show strong metrological evidence that MDSAR can be used for spectral SHM applications, with significant potential for continuing improvements.

Future developments include improving the accuracy and robustness of the SPOT method by incorporating knowledge of structural dynamics, exploring the choice for the optimal extraction parameters and patch size selection, extending the validation to a case study of a real bridge, and finally the use of other MDSAR techniques – for instance those which exploit the phase content of SAR data.

Bibliography

[1] J. J. Moughty and J. R. Casas, "A State of the Art Review of Modal-Based Damage Detection in Bridges: Development, Challenges, and Solutions," *Applied Sciences*, vol. 7, no. 5, p. 510, 5 2017. [Online]. Available: https://www.mdpi.com/2076-3417/7/5/510

[2] Wei Fan and Pizhong Qiao, "Vibration-based Damage Identification Methods: A Review and Comparative Study," *Structural Health Monitoring*, vol. 10, no. 1, pp. 83–111, 1 2011. [Online]. Available: https://journals.sagepub.com/doi/10.1177/1475921710365419

[3] Z. Sun, M. Mahmoodian, A. Sidiq, S. Jayasinghe, F. Shahrivar, and S. Setunge, "Optimal Sensor Placement for Structural Health Monitoring: A Comprehensive Review," *Journal of Sensor and Actuator Networks*, vol. 14, no. 2, p. 22, 2 2025. [Online]. Available: https://www.mdpi.com/2224-2708/14/2/22

[4] J. Brownjohn, "Structural health monitoring of civil infrastructure," *Philosophical Transactions of the Royal Society A: Mathematical, Physical and Engineering Sciences*, vol. 365, no. 1851, pp. 589–622, 2 2007. [Online]. Available: https://royalsocietypublishing.org/doi/10.1098/rsta.2006.1925

[5] L. Ngeljaratan and M. A. Moustafa, "Structural health monitoring and seismic response assessment of bridge structures using target-tracking digital image correlation," *Engineering Structures*, vol. 213, p. 110551, 6 2020. [Online]. Available: https://linkinghub.elsevier.com/retrieve/pii/S0141029620300444

[6] S. Jiang, J. Zhang, and C. Gao, "Bridge Deformation Measurement Using Unmanned Aerial Dual Camera and Learning-Based Tracking Method," *Structural Control and Health Monitoring*, vol. 2023, pp. 1–19, 4 2023. [Online]. Available: https://www.hindawi.com/journals/schm/2023/4752072/

[7] E. Kaartinen, K. Dunphy, and A. Sadhu, "LiDAR-Based Structural Health Monitoring: Applications in Civil Infrastructure Systems," *Sensors*, vol. 22, no. 12, p. 4610, 6 2022. [Online]. Available: https://www.mdpi.com/1424-8220/22/12/4610

[8] A. Trias-Blanco, J. Gong, and F. L. Moon, "Characterization of Operational Vibrations of Steel-Girder Highway Bridges via LiDAR,"

Remote Sensing, vol. 15, no. 4, p. 1003, 2 2023. [Online]. Available: https://www.mdpi.com/2072-4292/15/4/1003

[9] T. Panigati, M. Zini, D. Striccoli, P. F. Giordano, D. Tonelli, M. P. Limongelli, and D. Zonta, "Drone-based bridge inspections: Current practices and future directions," *Automation in Construction*, vol. 173, p. 106101, 5 2025. [Online]. Available: https://linkinghub.elsevier.com/retrieve/pii/S0926580525001414

[10] C. Gentile and G. Bernardini, "An interferometric radar for non-contact measurement of deflections on civil engineering structures: laboratory and full-scale tests," *Structure and Infrastructure Engineering*, vol. 6, no. 5, pp. 521–534, 10 2010. [Online]. Available: http://www.tandfonline.com/doi/abs/10.1080/15732470903068557

[11] C. Michel and S. Keller, "Advancing Ground-Based Radar Processing for Bridge Infrastructure Monitoring," *Sensors*, vol. 21, no. 6, p. 2172, 3 2021. [Online]. Available: https://www.mdpi.com/1424-8220/21/6/2172

[12] M. Sofi, E. Lumantarna, P. Mendis, C. Duffield, and A. Rajabifard, "Assessment of a Pedestrian Bridge Dynamics Using Interferometric Radar System IBIS-FS," *Procedia Engineering*, vol. 188, pp. 33–40, 2017. [Online]. Available: https://linkinghub.elsevier.com/retrieve/pii/S1877705817320064

[13] J. Xi, Z. Suo, and J. Ti, "The First Experimental Validation of a Communication Base Station as a Ground-Based SAR for Deformation Monitoring," *Remote Sensing*, vol. 17, no. 7, p. 1129, 3 2025. [Online]. Available: https://www.mdpi.com/2072-4292/17/7/1129

[14] D. Cusson, C. Rossi, and I. F. Ozkan, "Early warning system for the detection of unexpected bridge displacements from radar satellite data," *Journal of Civil Structural Health Monitoring*, vol. 11, no. 1, pp. 189–204, 2 2021. [Online]. Available: http://link.springer.com/10.1007/s13349-020-00446-9

[15] P. Milillo, G. Giardina, D. Perissin, G. Milillo, A. Coletta, and C. Terranova, "Pre-Collapse Space Geodetic Observations of Critical Infrastructure: The Morandi Bridge, Genoa, Italy," *Remote Sensing*, vol. 11, no. 12, p. 1403, 6 2019. [Online]. Available: https://www.mdpi.com/2072-4292/11/12/1403

[16] X. Qin, M. Liao, M. Yang, and L. Zhang, "Monitoring structure health of urban bridges with advanced multi-temporal InSAR analysis," *Annals of GIS*, vol. 23, no. 4, pp. 293–302, 10 2017. [Online]. Available: https://www.tandfonline.com/doi/full/10.1080/19475683.2017.1382572

[17] D. Tonelli, V. F. Caspani, A. Valentini, A. Rocca, R. Torboli, A. Vitti, D. Perissin, and D. Zonta, "Interpretation of Bridge Health Monitoring Data from Satellite InSAR Technology," *Remote Sensing*, vol. 15, no. 21, p. 5242, 11 2023. [Online]. Available: https://www.mdpi.com/2072-4292/15/21/5242

[18] D. Tonelli, A. Valentini, A. Rocca, S. Zorzi, A. Lotti, and D. Zonta, "Uncertainty quantification of satellite InSAR-monitoring of bridges: a case study," *ce/papers*, vol. 6, no. 5, pp. 900–906, 9 2023. [Online]. Available: https://onlinelibrary.wiley.com/doi/10.1002/cepa.1991

[19] V. C. Chen, *The Micro-Doppler Effect in Radar*, 2nd ed. Artech house, 2019, accessed: 2025.

[20] Umbra, "Delivering Global Omniscience • Umbra Space," 2023, accessed: 2025. [Online]. Available: https://umbra.space/

[21] C. Space, "Capella Space X-Band Synthetic Aperture Radar," accessed: 2025. [Online]. Available: https://www.eoportal.org/satellite-missions/capella-x-sar

[22] ICEYE, "Single Look Complex Image - ICEYE Product Documentation," accessed: 2025. [Online]. Available: https://sar.iceye.com/5.0/productFormats/slc/

[23] C. Clemente, D. Tonelli, A. Lotti, F. Rollo, C. Ilioudis, S. D. Riofrio, F. Biondi, E. Tubaldi, M. Macdonald, D. Zonta, M. Zavagli, M. Costantini, F. Minati, F. Vecchioli, P. Milillo, M. Zimmermanns, E. Imbembo, and M. Corvino, "On Micro-Motion Extraction from High Resolution X-band SAR products," in *IGARSS 2024 - 2024 IEEE International Geoscience and Remote Sensing Symposium*. Athens, Greece: IEEE, 7 2024, pp. 1182–1186. [Online]. Available: https://ieeexplore.ieee.org/document/10642825/

[24] F. Rollo, C. V. Ilioudis, G. Zefi, A. Lotti, D. Tonelli, M. Zavagli, M. Constantini, D. Zonta, E. Tubaldi, P. Milillo, M. Macdonald, and C. Clemente, "Micro-motion extraction from spotlight SAR using a modified backprojection approach," in *Microwave Remote Sensing: Data Processing and*

Applications III, E. Santi, F. Bovenga, C. Notarnicola, and N. Pierdicca, Eds. SPIE, 11 2024, p. 12. [Online]. Available: https://www.spiedigitallibrary.org/conference-proceedings-of-spie/13195/3031678/Micro-motion-extraction-from-spotlight-SAR-using-a-modified-backprojection/10.1117/12.3031678.full

[25] M. Soumekh, *Synthetic Aperture Radar Signal Processing with MATLAB Algorithms*. John Wiley & Sons, Inc., 1999.

[26] "Sensor Independent Complex Data (SICD), Volume 1, Design & Implementation Description Document, NGA.STND.0024-1_1.2.1," 12 2018. [Online]. Available: https://nsgreg.nga.mil/doc/view?i=4900

[27] M. Rüegg, E. Meier, and D. Nüesch, "Vibration and Rotation in Millimeter-Wave SAR," *IEEE Transactions on Geoscience and Remote Sensing*, vol. 45, no. 2, pp. 293–304, 2 2007. [Online]. Available: http://ieeexplore.ieee.org/document/4069119/

[28] F. Rollo, C. Ilioudis, and C. Clemente, "Advances in Micro-Doppler Processing in Synthetic Aperture Radar: A review of techniques, results, and future trends," *IEEE Geoscience and Remote Sensing Magazine*, pp. 2–24, 2025. [Online]. Available: https://ieeexplore.ieee.org/document/11029265/

[29] R. Raney, "Synthetic Aperture Imaging Radar and Moving Targets," *IEEE Transactions on Aerospace and Electronic Systems*, vol. AES-7, no. 3, pp. 499–505, 5 1971. [Online]. Available: http://ieeexplore.ieee.org/document/4103740/

[30] V. Chen, Fayin Li, Shen-Shyang Ho, and H. Wechsler, "Micro-doppler effect in radar: phenomenon, model, and simulation study," *IEEE Transactions on Aerospace and Electronic Systems*, vol. 42, no. 1, pp. 2–21, 1 2006. [Online]. Available: http://ieeexplore.ieee.org/document/1603402/

[31] A. B. Vattulainen, F. Rollo, A. Lotti, D. Tonelli, S. D. Riofrio, E. Tubaldi, D. Zonta, C. Ilioudis, P. Milillo, and C. Clemente, "Bridge Vibration Measurements from Very High-Resolution Spaceborne SAR," in *2024 IEEE SENSORS*. IEEE, 10 2024, pp. 1–4. [Online]. Available: https://ieeexplore.ieee.org/document/10785004/

[32] Q. Wang, M. Pepin, R. J. Beach, R. Dunkel, T. Atwood, B. Santhanam, W. Gerstle, A. W. Doerry, and M. M. Hayat, "SAR-Based Vibration

Estimation Using the Discrete Fractional Fourier Transform," *IEEE Transactions on Geoscience and Remote Sensing*, vol. 50, no. 10, pp. 4145–4156, 10 2012. [Online]. Available: http://ieeexplore.ieee.org/document/6185663/

[33] Q. Wang, M. Pepin, A. Wright, R. Dunkel, T. Atwood, B. Santhanam, W. Gerstle, A. W. Doerry, and M. M. Hayat, "Reduction of Vibration-Induced Artifacts in Synthetic Aperture Radar Imagery," *IEEE Transactions on Geoscience and Remote Sensing*, vol. 52, no. 6, pp. 3063–3073, 6 2014. [Online]. Available: http://ieeexplore.ieee.org/document/6555913/

[34] A. Anghel, G. Vasile, C. Ioana, R. Cacoveanu, and S. Ciochina, "Micro-Doppler Reconstruction in Spaceborne SAR Images Using Azimuth Time–Frequency Tracking of the Phase History," *IEEE Geoscience and Remote Sensing Letters*, vol. 13, no. 4, pp. 604–608, 4 2016. [Online]. Available: http://ieeexplore.ieee.org/document/7426774/

[35] A. Focsa, A. Anghel, G. Nico, I. Maggio, M. Datcu, and M. Corvino, "Vibration-Induced Micro-Doppler Estimation in Spaceborne SAR Images Using Doppler Centroid Tracking Across Azimuth Sub-Apertures," in *2025 IEEE International Radar Conference (RADAR)*. IEEE, 5 2025, pp. 1–6. [Online]. Available: https://ieeexplore.ieee.org/document/11031947/

[36] I. Djurović and L. Stanković, "Quasi-maximum-likelihood estimator of polynomial phase signals," *IET Signal Processing*, vol. 8, no. 4, pp. 347–359, 6 2014. [Online]. Available: https://onlinelibrary.wiley.com/doi/10.1049/iet-spr.2013.0104

[37] F. Biondi, P. Addabbo, S. L. Ullo, C. Clemente, and D. Orlando, "Perspectives on the Structural Health Monitoring of Bridges by Synthetic Aperture Radar," *Remote Sensing*, vol. 12, no. 23, p. 3852, Nov. 2020. [Online]. Available: https://www.mdpi.com/2072-4292/12/23/3852

[38] F. Biondi, P. Addabbo, C. Clemente, S. L. Ullo, and D. Orlando, "Monitoring of Critical Infrastructures by Micromotion Estimation: The Mosul Dam Destabilization," *IEEE Journal of Selected Topics in Applied Earth Observations and Remote Sensing*, vol. 13, pp. 6337–6351, 2020. [Online]. Available: https://ieeexplore.ieee.org/document/9224142/

[39] P. Milillo, R. Bürgmann, P. Lundgren, J. Salzer, D. Perissin, E. Fielding, F. Biondi, and G. Milillo, "Space geodetic monitoring of engineered structures: The ongoing destabilization of the Mosul dam, Iraq," *Scientific Reports*, vol. 6, no. 1, p. 37408, 12 2016. [Online]. Available: https://www.nature.com/articles/srep37408

[40] C. Shannon, "Communication in the Presence of Noise," *Proceedings of the IRE*, vol. 37, no. 1, pp. 10–21, 1 1949. [Online]. Available: http://ieeexplore.ieee.org/document/1697831/

[41] SatNOGS, "SatNOGS DB - Umbra 02," accessed: 2025. [Online]. Available: https://db.satnogs.org/satellite/TPDX-4064-2548-6167-6896

[42] APS, "APS 113-AB - SPEKTRA," accessed: 2025. [Online]. Available: https://www.spektra-dresden.com/en/product/details/calibration-solutions,device-testing/erreger-und-komponenten,kalibriererreger-und-komponenten/schwingung/aps-113-ab.html

[43] S. D. Robertson, "Targets for Microwave Radar Navigation," *Bell System Technical Journal*, vol. 26, no. 4, pp. 852–869, 10 1947. [Online]. Available: https://ieeexplore.ieee.org/document/6772350

[44] TIRA, "Inertial-Vibration Test System :: TIRA GmbH," accessed: 2025. [Online]. Available: https://www.tira-gmbh.de/en/vibration-test-systems/vibration-test-systems/inertial-vibration-test-system/

[45] APS, "APS 400 - APS Dynamics," accessed: 2025. [Online]. Available: https://www.apsdynamics.com/en/products/details/vibration-exciter/aps-400.html

7. Monitoring bridge vibrations via spaceborne SAR micro-Doppler

Context and contribution to the thesis

This chapter evaluates the applicability of MDSAR to a real full-scale bridge, following the controlled validation on the proposed technique that was presented in Chapter 6. Here, spaceborne SAR measurements are validated against synchronous in-situ sensors to assess velocity measurement and dominant frequency identification performance. The study highlights the practical feasibility and limitations of MDSAR for vibration-based monitoring of bridges.

The following pages present the post-print of

> **Lotti, A.**, Vattulainen, A.B., Diaz Riofrio, S., Suppi, C., Tubaldi, E., Zonta, D., Milillo, P., Clemente, C. (2026). Monitoring bridge vibrations via spaceborne SAR micro-Doppler, *Structural Control and Health Monitoring*, https://doi.org/10.1155/stc/3858095.

as published in the journal *Structural Control and Health Monitoring*, differing only from the published article in terms of layout, formatting, and notation.

Authors' contributions:

Lotti, A.: methodology, investigation, formal analysis, visualisation, software, data collection, writing (original draft), review. **Vattulainen, A.B.**: methodology, software, data collection, review. **Diaz Riofrio, S.**: methodology, software. **Suppi, C.**: software, data collection. **Tubaldi, E.**: methodology, data collection, review, supervision. **Zonta, D.**: methodology, data collection, writing, review, supervision. **Milillo, P.**: data collection, review. **Clemente, C.**: conceptualisation, methodology, data collection, review, supervision, funding acquisition.

Abstract

The advent of Synthetic Aperture Radar (SAR) imaging has presented the possibility of remote monitoring of civil infrastructure on a large scale. Although well established for observing slow and long-term phenomena, its application to vibration-based structural health monitoring (SHM) remains relatively unexplored in the current literature. This study demonstrates the use of micro-Doppler SAR (MDSAR) using data from spaceborne platforms for measuring structural vibrations of a real bridge, specifically the line of sight velocity time histories of the deck. These measurements are compared to synchronous ground truth data to validate the method and assess its accuracy. Experimental results show that MDSAR measures vibration with an error in velocity on the order of $1\ \mathrm{mm/s}$ and successfully identifies the bridge dominant frequencies from two separate SAR acquisitions at different times. Spectral correlation with ground truth data reaches values up to 0.88. Frequency estimation errors are essentially controlled by the resolution of the spectrum, which in turn is limited by the acquisition time. In this work, a frequency resolution of $0.06\ \mathrm{Hz}$ is achieved, for an acquisition duration of $16\ \mathrm{s}$. Given these results, it is expected that MDSAR could be suitable for monitoring natural frequencies and performing modal recognition for bridges. Further improvements in the technology and in the analysis algorithm could potentially enable the accurate measurement of mode shape components.

Keywords: structural health monitoring, SAR, micro-Doppler, micro-motion, modal extraction.

7.1 Introduction

Vibration-based Structural Health Monitoring (VBSHM) methods, which typically rely on conventional contact sensors such as accelerometers, are widely used for assessing the structural state of civil infrastructure [1].

VBSHM has long been the subject of research, with numerous studies aimed at identifying damage from vibrational features. The literature includes several comprehensive reviews that collect a variety of traditional methods used for diagnostics and damage detection [2, 3, 4, 5, 6].

Although contact measurement approaches have been proven to be effective, they also face significant limitations, which have led to the exploration of remote sensing alternatives. Firstly, the installation of sensors directly on a structure, such as a bridge, poses logistical challenges [7]. Deploying accelerometers or similar devices often requires safety precautions, traffic dis-

ruptions, and specialised workers, which collectively inflate costs and delay the operational readiness of the monitoring system. Moreover, maintaining and calibrating sensor networks introduces further complexity and long-term expenses [8]. This becomes problematic when dealing with large-scale infrastructure, where a large number of sensors are needed to achieve sufficient spatial coverage [9]. For example, the Mezcala cable-stayed bridge was instrumented with a total of 124 sensors (including accelerometers and other sensor types) at an estimated cost of 1.8 million USD, covering both installation and maintenance over an operating period of 30 years [10]. Secondly, in regions with a high concentration of ageing infrastructure – where safety concerns are important and widespread monitoring is promptly needed – conventional VBSHM becomes impractical [11], especially when resources are limited. To overcome these challenges, the focus of research has increasingly shifted towards remote sensing for SHM [12], as these technologies do not require the physical installation of the sensor on the structure. Several solutions, each based on different physical principles, exist and have been studied, including the use of Uncrewed Aerial Vehicles (UAVs) [13, 14, 15], laser vibrometers [16], Light Detection and Ranging (LiDAR) [17, 18], and ground-based Doppler radars [19, 20, 21]. As an alternative to these approaches, SAR satellite remote sensing is of particular interest due to its unique capabilities. SAR is a radar imaging technique capable of producing high-resolution images of the Earth's surface. Unlike optical sensors, which passively capture reflected sunlight, SAR systems (as well as other active sensors like ground-based radar and LiDAR) actively illuminate the scene and measure the backscattered electromagnetic signal, which is parameterised in terms of its reflectivity (magnitude) and phase. The signal carries information about the surface geometry, the electromagnetic properties, the distance between the radar and the surface targets, and the relative motion between the sensor and the target – the latter two as part of the measured phase, which is a property fundamental for generating the SAR image but also particularly relevant for this work. A major advantage of SAR lies in its ability to capture large areas (typically many square kilometres) while maintaining high-quality imaging capability. Moreover, the cost of SAR imagery is rapidly decreasing thanks to the advent of commercial providers on the scene. Generally, prices range from a few hundred up to a few thousand USD (e.g., up to $3000 - 5000$ USD [22]) depending on spatial resolution and revisit time (i.e., the time interval between successive acquisitions). In some cases, SAR data are freely available, such as from the Sentinel-1 mission [23].

In the context of SHM, one technique making use of the benefits of SAR is Interferometric SAR (InSAR). InSAR is a method that compares the phase

information of successive SAR acquisitions to detect and quantify surface displacements in the image over time [24] [25]. In previous years, advanced Multi-Temporal InSAR techniques, such as Persistent Scatterer Interferometry (PSI) and Small Baseline Subset (SBAS), have been developed to monitor surface deformation [26] with millimetre-level accuracy [27]. As a result, InSAR has been increasingly applied and validated in civil engineering applications for SHM. Literature case studies include long-term monitoring of dam foundations [28], bridge deflections [27], and even detection of scour-related features [29]. Another benefit of SAR technology is its archive of historical data, enabling retroactive analyses of collapsed infrastructure [30] and supporting the development of early warning systems for risk assessment [31]. Despite these advantages, InSAR has limitations that restrict its use for certain SHM tasks:

- It is effective for measuring slow, long-term deformations, and it is not suited for rapid and bulk movements [32].
- InSAR requires a large number of acquisitions for reliable results [33], and cannot measure displacements from a single SAR image.
- The temporal resolution of InSAR depends on the revisit time of the satellite, which is typically on the order of days.

Due to these limitations, InSAR cannot be used to assess the vibrational behaviour of structures, however a different class of techniques exists that works on single-pass (i.e. individual) SAR acquisitions and is capable of detecting vibrational information. These approaches exploit micro-Doppler (m-D) effects induced by target motion and are the focus of this study.

When a moving target is illuminated by a radar signal, the backscattered signal is subjected to a phase shift due to the Doppler effect [34], a well-known phenomenon caused by the relative motion between the sensor and the target. Standard SAR processing assumes the scene to be static, producing accurate images of stationary ground targets. When targets move during an acquisition (or vibrate, as for civil infrastructure components), uncompensated phase shifts are introduced into the receiving signal, generating artefacts in the final SAR image. These artefacts can be grouped into two types, depending on the nature of the motion: Doppler, caused by translational movement, and micro-Doppler, caused by periodic or oscillatory micro-motions (m-m) of the target [34]. Consequently, the micro-Doppler effect in SAR imagery carries kinematic information of targets such as vibrations [35], presenting the opportunity to reconstruct structural dynamics from single-pass SAR acquisitions. Several MDSAR techniques have been developed to measure micro-Doppler information from SAR imagery, where some of these have been applied to the field of

civil engineering SHM. For a comprehensive review of MDSAR methods and their working principles, the reader is referred to the recent literature review by Rollo et al. [36]. In the following, selected publications on measuring vibrational features from m-D signatures in SAR data are reported. Initial works focused mainly on demonstrating the potential of the m-D extraction techniques under controlled environments, using isolated vibrating corner reflectors (CRs) mounted on shaker devices to replicate vibration without interference from the surroundings. For example, Chen et al. [37] measured a vibration frequency of 2.3 Hz from a CR on a shaker, with an error of 0.3 Hz with respect to ground truth, although amplitude estimates were not reported. Ruegg et al. [35] studied the effects of both vibrating and rotating targets and successfully extracted a 1 Hz frequency from a rotating CR. More recently, Clemente et al. [38] and Rollo et al. [39] applied tracking and back-projection techniques to reconstruct vibrations with a frequency of 2 Hz and a vertical amplitude of 15 mm, validated against synchronous ground measurements. Finally, Lotti et al. [40] conducted experiments across a wide range of frequencies and amplitudes, extending measurements beyond simple case studies. This work included an experimental validation based on synchronous ground truth measurements and demonstrated that vibrations comparable to those found in civil infrastructure could be captured with SAR.

While m-D approaches are less mature than InSAR in the context of civil SHM, they have also been applied to real-world case studies employing methods such as the Sub-Pixel Offset Tracking (SPOT). Biondi et al. [41] used SPOT to identify cracks in the Mosul Dam, based on vibrational anomalies reconstructed from SAR imagery, and validated these crack locations with those obtained from the PSI InSAR technique. In a later work, Biondi et al. [42] examined several bridge case studies, detecting anomalies in the vibrational behaviour of the structures as determined by SAR m-m measurements. This investigation successfully identified locations of cracks and expansion joints in the deck, which were validated with photographic documentation. Focsa et al. [43] retrieved the natural frequencies of a bridge using an MDSAR method, reporting errors ranging from 0.03 to 0.5 Hz; however, the actual accuracy remains uncertain as the comparison relied on asynchronous ground-based radar measurements, and multiple spectral peaks were identified nearby the true frequencies. More recently, Vattulainen et al. [44] employed a modified back-projection algorithm (BPA) – an MDSAR technique distinct from SPOT – to estimate the dominant frequency on a bridge, reporting an error of 0.04 Hz validated against synchronous measurements. However, their work only focused on a frequency domain comparison and did not cover a time history reconstruc-

tion of the vibrations.

In summary, micro-Doppler SAR techniques offer a promising alternative to traditional VBSHM methods, enabling vibrational information to be measured both remotely and over large areas from single-pass SAR images. Prior studies have largely focused on controlled experiments, and real-world validation remains limited. Notably, no previous study has applied MDSAR to a full-scale civil structure while directly validating measured vibrations against synchronous ground truth data in the time domain. A comprehensive metrological evaluation of any MDSAR technique, including SPOT, is still missing. Furthermore, the possibility of using SAR data for modal extraction, specifically for identifying natural frequencies and mode shapes, remains largely unexplored.

The objective of this study is to address the following research questions:

(i) Can MDSAR be used to measure the vibration time series of a real-world structure?

(ii) In the context of a real-world structure, how accurate are these measurements, and what are the limitations of the technique?

(iii) What are the future possibilities for extracting modal parameters from spaceborne SAR data?

To explore these questions, the case study of the South Portland St. Suspension Bridge in Glasgow, UK, is considered. While this paper focuses on the measurement of vibrations and qualitatively discusses the extraction of individual modal parameters (i.e. natural frequencies and mode shapes) from SAR data, a detailed approach to a proper modal extraction will be presented in a future publication. This work constitutes a significant advancement in the use of SAR for VBSHM. It presents the first metrological assessment of a SAR-based micro-Doppler method for measuring the vibrations of a real, instrumented bridge under operational conditions. By comparing the SAR-derived velocities against synchronous ground truth measurements, this study confirms the potential of this technique and identifies its current limitations.

The remainder of this paper is structured as follows. Section 7.2 provides the necessary background for SAR-based vibration monitoring, including an overview of SAR principles and the effects of moving objects in SAR images. It then introduces the SPOT algorithm, covering azimuth sub-aperture segmentation, sub-pixel tracking, and velocity time history reconstruction. The section continues with a description of the South Portland St. Suspension Bridge case study, followed by the layout of the contact-based accelerometer system used for validation and the methodology used to compare SAR-derived results with ground-truth data. Section 7.3 presents and discusses the experimental results.

It begins by evaluating the SAR-measured vibrations against the ground-truth data using various metrics. It then addresses the three key research questions of the study and discusses current limitations and potential improvements for modal extraction using SAR. Finally, Section 7.4 summarises the main findings and outlines current challenges while proposing directions for future developments.

7.2 Materials and Methods

7.2.1 Principles of SAR technology

A SAR operates by transmitting and receiving radar pulses while travelling at a velocity v_{s} on a moving platform, which in this case is a satellite. SAR signals are EM waves with much longer wavelengths (see Table 7.1) than those used by optical sensors, and since they are active sensors, SAR systems are not dependent on sunlight or weather conditions.

Typically, a SAR acquisition spans several seconds for a duration t_{a} and involves the sensor collecting backscattered radar pulses while illuminating the same ground target from multiple positions along the flight path. The processing of the data – to account for the different phase changes for each pulse due to the moving platform – *synthesises* the antenna (or aperture), hence the term *synthetic aperture* in SAR. The SAR sensor is tilted with an incidence angle, β, with respect to the vertical direction of the surface, and the radial distance from the ground target (e.g., the bridge being monitored) to the sensor is referred to as the slant-range distance, $R(t)$, this direction is often referred to as the line of sight (LOS) of the sensor. Figure 7.1 shows the orbit geometry for a specific acquisition mode, known as spotlight mode, which is discussed later in this section.

SAR images are complex-valued matrices, where each pixel contains both a magnitude and a phase component. The magnitude and phase represent the re-

Table 7.1: Radar frequency bands commonly used in SAR systems, with their associated frequency and wavelength values [45].

Band	Central Frequency [GHz]	Wavelength [cm]
L	1-2	15–30
S	2-4	7.5–15
C	4-8	3.8–7.5
X	8-12	2.4–3.8

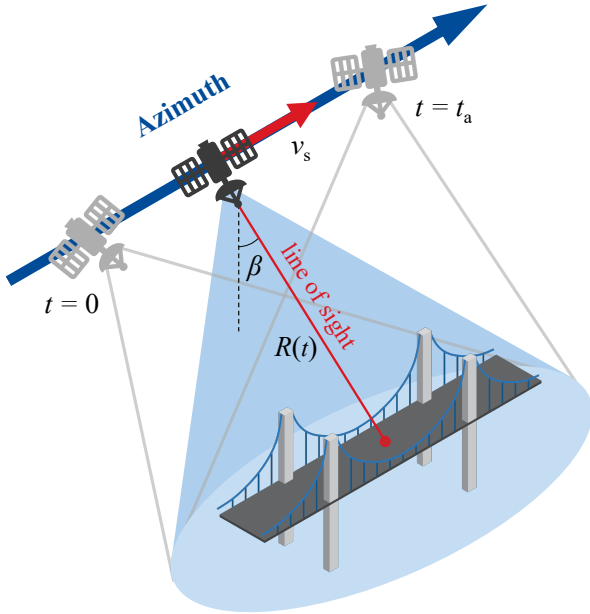


Figure 7.1: SAR spotlight mode acquisition geometry, showing the start $t = 0$ and end $t = t_a$ times of the acquisition, the platform velocity v_s, the incidence angle θ, and the slant-range distance $R(t)$ between the sensor and the ground target.

flectivity (i.e., intensity) and the delay of the backscattered signal, respectively. Figure 7.2 shows an example of a reflectivity map from spotlight acquisition of the Golden Gate Bridge compared to the corresponding optical image. In general, the reflectivity is affected by the type of material and shapes of targets; metallic objects with sharp geometries are prominently visible in the reflectivity map. The resulting complex-valued matrix is arranged in *range-azimuth* coordinates. The range direction corresponds to the radial direction from the sensor to the ground target (slant-range), while the azimuth direction aligns with the platform flight path. The resolution of the reflectivity map (i.e., the size of the pixel in azimuth and in range) is defined by the azimuth resolution, Δy, and the range resolution, Δr. These quantities both depend on the wavelength of the transmitted signal, λ, with the azimuth resolution additionally depending on the acquisition time, t_a.

Several types of acquisition mode exist, each with different trade-offs between resolution and spatial coverage [46]. In this paper, spotlight acquisitions are used, with durations ranging between 5 and 30 s. In this mode, the radar

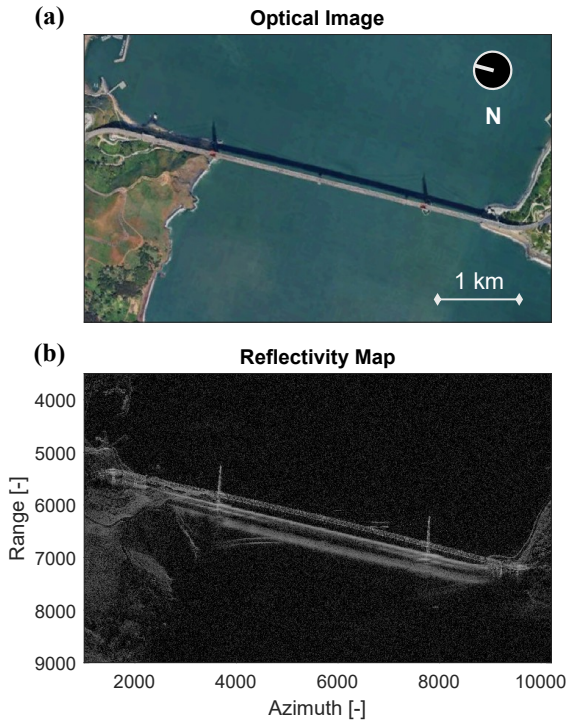


Figure 7.2: A comparison between (a) optical and (b) SAR reflectivity maps of the Golden Gate Bridge, from a spotlight acquisition by the Umbra-04 sensor ($\lambda = 31$ mm, date: March 25 2023).

beam is continuously steered ('squinted') such that it remains centred on the same area for the entire acquisition duration. Spotlight mode offers improved azimuth resolution thanks to The extended illumination time, but with reduced spatial coverage compared to other acquisition modes. Nonetheless, spotlight scenes can span areas ranging from 5 to 20 km, enabling the monitoring of multiple structures within a single image while providing finer azimuth resolution. As these acquisitions target specific areas, they are usually not available through archive data sources and must be tasked specifically.

The azimuth resolution for a spotlight acquisition is described by the following equation:

$$\Delta y = \frac{\lambda \, R(t)}{2 \, v_{\mathrm{s}} \, t_{\mathrm{a}}} \tag{7.1}$$

where the parameters are as previously defined.

7.2.2 Micro-motion in SAR imagery

Standard SAR processing is designed to produce high-resolution images of static scenes. As discussed in Section 7.1, targets undergoing some micro-motion during the acquisition period will cause characteristic artefacts in the SAR image. This phenomenon is known as the micro-Doppler effect and arises from small variations in the radial velocities relative to the SAR moving platform. In general, when a target moves at constant speed, the relative motion in the LOS direction causes an azimuth shift of the target from its true position due to the Doppler effect [34]. The azimuth shift, $y(t)$, due to constant radial velocity, v_r, of the ground target along the LOS is approximated by the relationship shown in Eq.7.2 [47].

$$y(t) = -\frac{v_r \, R(t)}{v_s} \tag{7.2}$$

In the case of a target vibrating around a static equilibrium position, the azimuth shifts in the resulting image will appear as *ghost targets* (or *paired echoes*) along the azimuth direction, centred on the true position of the target. These artefacts result from target m-m that induces periodic time-varying changes in the radial velocity. The higher the velocity of vibration, the greater the separation between these paired echoes from the true location. Figure 7.3(a) shows a clear example of this effect for a single scattering point, given by a corner reflector oscillating vertically with a constant frequency of 1 Hz, and an amplitude of 10 mm. The periodic motion generates a symmetric distribution of the echoes, observable in the reflectivity map.

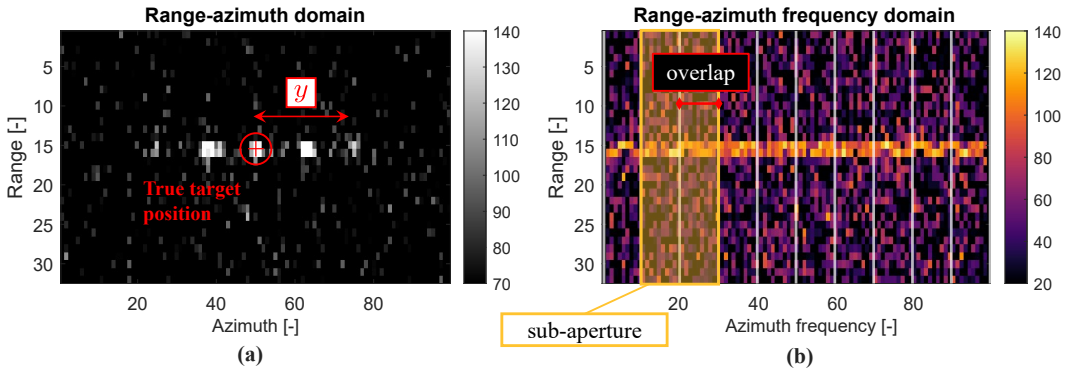


Figure 7.3: Example of micro-motion effects in a TerraSAR-X acquisition (Trento, December 18 2023, 17:09:29 UTC) of a vertically vibrating isolated target (1 Hz, 10 mm). (a) Ghost targets in the range–azimuth image; (b) range–azimuth frequency representation showing sub-aperture segmentation (yellow) and overlapping data sections (red).

It is important to note that m-m effects are best preserved in single-look data such as Single-Look Complex (SLC) images, which contain both amplitude and phase information from a single, unaveraged observation throughout the entire acquisition time. While Multi-Look Complex (MLC) products are commonly used in downstream applications due to their reduced speckle noise and lower storage requirements, they are generated by averaging independent looks, which both degrades azimuth resolution and corrupts motion information, making MLC unsuitable for micro-motion analysis. In general, motion measurements need full-resolution SLC images or even lower-level products like raw or Complex Phase History Data (CPHD) to preserve the phase modulations of interest. In this study, SLC imagery was selected as it provides the necessary requirements for m-m extraction while remaining significantly less demanding in terms of memory and processing resources compared to raw or CPHD formats.

7.2.3 Sub-Pixel Offset Tracking

The technique used in this study is inspired by the work of Biondi et al. [41] and enables the extraction of radial velocity time histories from ground targets from a focused SLC image. The main processing stages are described below.

1. Range-Azimuth frequency transformation
Starting from the SLC matrix in range-azimuth coordinates, a Fast Fourier Transform (FFT) is applied along the azimuth dimension. This results in a matrix in *range-azimuth frequency* coordinates, as shown in Figure 7.3(b). The resulting matrix already contains features related to the target vibration.

2. Sub-aperture segmentation
The *range-azimuth frequency* matrix is then split into partially overlapping azimuth sub-apertures as shown in Figure 7.3(b). Each sub-aperture represents a temporal window of the full aperture (t_{a}), with a relative width controlled by the *aperture fraction*, defined as:

$$\xi := \frac{t_{\mathrm{sap}}}{t_{\mathrm{a}}} \tag{7.3}$$

where t_{sap} is the sub-aperture duration. Adjacent sub-apertures can be processed to share a portion of the azimuth frequency domain data and therefore overlap in time, as described by the *overlap ratio*, defined as:

$$\Omega := \frac{t_{\mathrm{ol}}}{t_{\mathrm{sap}}} \tag{7.4}$$

where t_{ol} is the overlap duration between adjacent sub-apertures. Given α and Ω, the total number of sub-apertures, N, produced is given by Eq.7.5.

$$N = \frac{\xi^{-1} - \Omega}{1 - \Omega} \tag{7.5}$$

3. Range-azimuth transformation

Each *range-azimuth frequency* sub-aperture is transformed back to the spatial domain via an inverse FFT (IFFT), resulting in a series of N *range-azimuth* images that are temporally spaced. More specifically, the time vector assigned to the sub-apertures consists of N linearly spaced values, starting at $t_{\text{sap}}/2$ and ending at $(t_{\text{a}} - t_{\text{sap}})/2$. This ensures that each image corresponds to the centre time of its respective sub-aperture window, resulting in a temporal resolution, Δt, as shown in Eq.7.6.

$$\Delta t = \frac{t_{\text{a}} - t_{\text{sap}}}{N - 1} \tag{7.6}$$

It is important to note that by segmenting the full aperture image into multiple sub-apertures of duration t_{sap} (shorter than the full acquisition time t_{a}), the azimuth resolution will degrade due to the reduced observation time. It is possible to preserve the pixel spacing by applying zero-padding during the IFFT to up-sample each sub-aperture when moving to the range-azimuth domain. In this way, the granularity of the original image is maintained, although the degradation in image interpretability remains visible. Figure 7.4 shows examples of reflectivity maps of sub-apertures from a SAR acquisition over the South Portland St. Suspension Bridge, illustrating the effect of different aperture fractions: $\xi = 1$ ($t_{\text{sap}} = t_{\text{a}}$), $\xi = 0.1$ ($t_{\text{sap}} = 0.1\ t_{\text{a}}$), and $\xi = 0.01$ ($t_{\text{sap}} = 0.01\ t_{\text{a}}$). The figure demonstrates how decreasing the sub-aperture time progressively degrades the azimuth resolution of the reflectivity map.

4. Pixel tracking and velocity estimation

A target that is moving with a radial velocity v_{r} will appear displaced along the azimuth by a distance y determined by Eq.7.2. If the velocity varies over time, the shift y will also change in different sub-apertures. These displacements are tracked using 2D cross-correlation, applied to patches centred around the target in each sub-aperture. Cross-correlation is performed relative to a chosen reference sub-aperture, which in this work is selected as the central sub-aperture. This results in a time series of azimuth displacements $x(t)$, representing the shift of the target over successive sub-apertures relative to the reference image.

The corresponding radial velocity time history is then computed by invert-

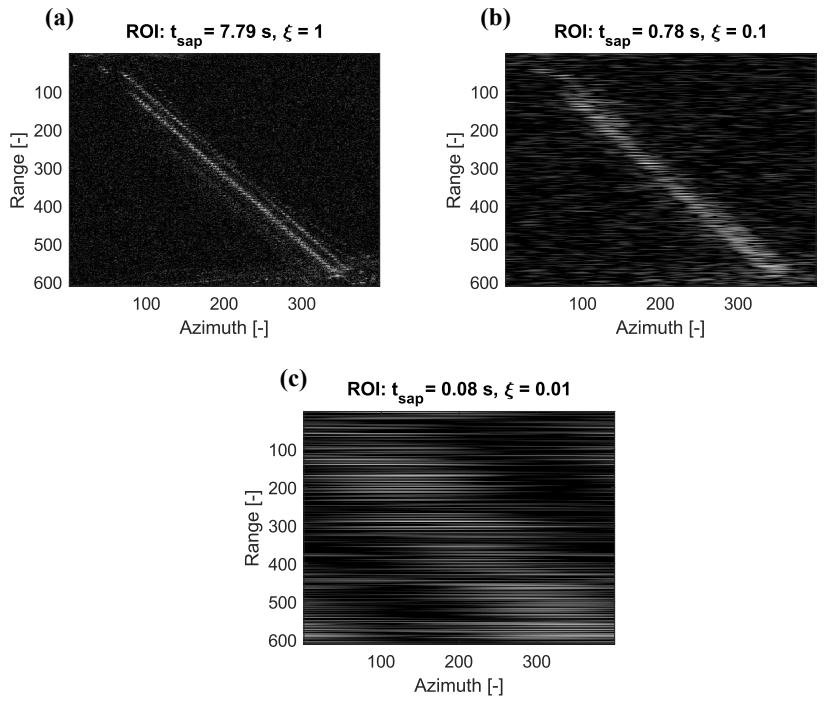


Figure 7.4: The effect of the aperture fraction, ξ, on the achieved azimuth resolution in a SAR image of the South Portland St. Suspension Bridge: (a) full-aperture image $\xi = 1$; (b) sub-aperture with $\xi = 0.1$; (c) sub-aperture with $\xi = 0.01$.

ing the azimuth shift equation Eq.7.2:

$$v_r(t) = -\frac{y(t)\, v_\mathrm{s}}{R_\mathrm{ref}} \tag{7.7}$$

assuming the platform velocity and the slant-range distance of the target, R_ref, (which in this case corresponds to the centre of the scene) are constant over the acquisition period. Each velocity estimate is mapped to its relative acquisition time based on the time vector described in Section 7.2.3. To enhance visualisation in the time domain without altering the signal bandwidth, the discrete velocity vector is up-sampled using Whittaker–Shannon (sinc) interpolation [48].

Summary of the processing chain

The key steps of the algorithm are illustrated in Figure 7.5, where, for clarity, the method is applied to a small region of interest (ROI) on one side of the bridge deck. The full processing workflow is summarised as follows:

1. Start from the full-aperture SLC image.
2. Apply an FFT along azimuth to transform the image to the range–azimuth frequency domain.
3. Divide the azimuth spectrum into N sub-apertures using parameters α and Ω (Eq.7.5).
4. Apply zero padding to maintain the original image dimensions, then perform IFFT to return each sub-aperture to the range–azimuth domain.
5. Track the azimuth displacement of bright targets across sub-apertures using 2D cross-correlation.
6. Convert azimuth shifts into line of sight velocity using Eq.7.7; optionally, apply sinc interpolation to increase the apparent sampling rate of the velocity time series.

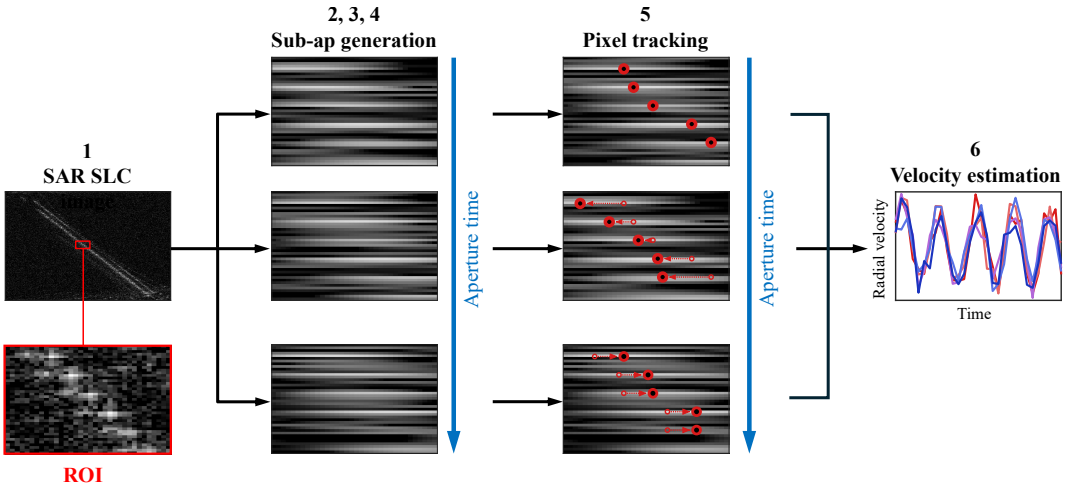


Figure 7.5: Flowchart of the SPOT processing algorithm used to extract radial velocity time histories from SLC spotlight SAR images. The sequence illustrates the workflow described in the summary of the processing chain.

7.2.4 Case Study: South Portland St. suspension bridge

The South Portland Street Suspension Bridge is a historic pedestrian suspension bridge spanning the River Clyde in Glasgow, Scotland, UK. It connects the *City Centre* district on the north bank to the southern districts of Laurieston and the Gorbals. Constructed between 1851 and 1853, the bridge was designed by engineer George Martin in collaboration with architect Alexander Kirkland.

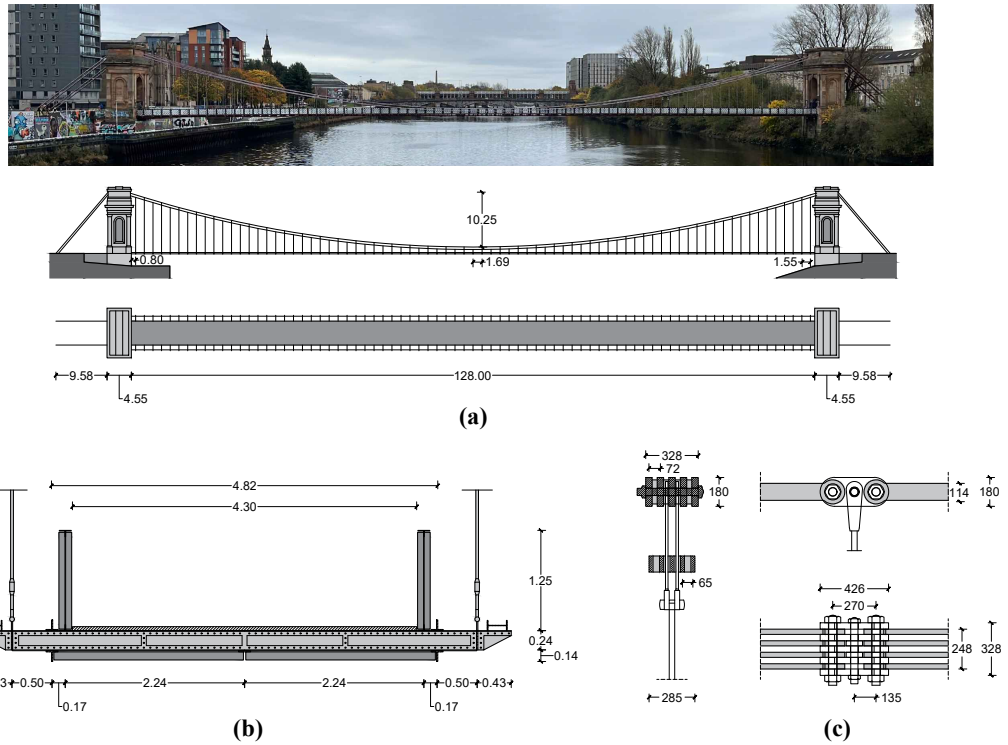
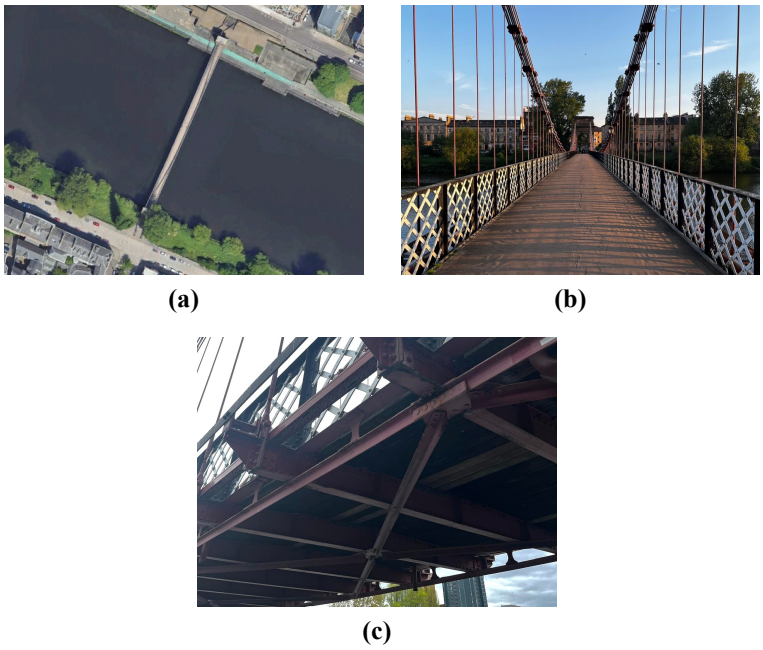


Figure 7.6: Technical drawings of the South Portland Street Suspension Bridge: (a) side view showing the span and sandstone towers over the River Clyde in Glasgow; (b) cross-sectional view of the deck; and (c) detail of the top chain connection, with dimensions in millimetres.

Originally constructed from wrought iron, the bridge has undergone several modifications, most recently in 2004[49].

The bridge features a single main span of 128 m and a deck width of 4.8 m (of which 4.3 m is walkable), as shown in the technical drawings in 7.6. The deck is suspended from four chains (two on each side), anchored into the ground, and supported by two sandstone towers located at the ends of the span. Figure 7.7 shows an aerial view of the bridge across the River Clyde, along with views from the top and underside of the deck. The maximum sag of the chains at the mid-span is approximately 10.25 m. Each side of the bridge is supported by a total of 77 vertical hangers, which are alternately connected to the upper and lower chains along the span of the bridge. The chains themselves are constructed with differing specifications:

- Lower chain: composed of five wrought iron plates, each measuring 100 mm $\times$ 25 mm.
- Upper chain: composed of four wrought iron plates, each measuring 106



(a) **(b)**

(c)

Figure 7.7: Overview and structural details of the bridge: (a) aerial view of the bridge; (b) view along the top of the bridge deck; (c) view of the underside of the steel truss deck structure.

$\mathrm{mm} \times 32\ \mathrm{mm}$ (this detail is reported in Figure 7.6(c)).

The chain node centre points are equally spaced $3.37\ \mathrm{m}$ as measured along a chain. As a result, the spacing between the hangers gradually decreases from the centre towards the towers as the inclination of the chain increases. Specifically, the horizontal spacing between adjacent hangers varies from $1.68\ \mathrm{m}$ at mid-span to $1.61\ \mathrm{m}$ near the towers. The distance from the last hanger to the tower is approximately $0.96\ \mathrm{m}$. The bridge deck consists of steel truss elements supporting a wooden walkway, which is then covered by a layer of bituminous pavement. The total mass of the bridge, supported by the four chains, has been estimated to be approximately $131.2\ \mathrm{t}$ (including the weight of the chains themselves). The main structural characteristics of the South Portland Street Suspension Bridge are summarised in Table 7.2:

The South Portland Street Suspension Bridge was selected as a case study for several reasons. First, the bridge is highly reflective in SAR images due to its steel structure and the presence of sharp features and corners, enhancing its visibility in the reflectivity map. Second, as a pedestrian bridge, it allows for the installation of monitoring equipment without the need for traffic closures,

Table 7.2: Principal features of the South Portland Street suspension bridge.

Characteristic	Description
Name	South Portland St. Suspension Bridge
Location	Glasgow, Scotland, United Kingdom
Coordinates	55°51'17.79" N, 4°15'20.11" W
River crossed	River Clyde
Type of bridge	Pedestrian suspension bridge
Materials	Wrought iron with sandstone towers
Main span length	128 m
Bridge width	4.5 m
Number of chains	2 per side
Chain sag	10.25 m
Number of hangers	77 per side

enabling the collection of vibration data under operational conditions without disruption. Finally, the long span of the bridge and its slender structure make it prone to vibrations with relatively low frequencies of oscillation, with natural frequencies ranging from approximately 0.38 Hz to 2.2 Hz (for further details on the magnitude and frequency of vibrations and mode shapes, see Section 7.2.5).

7.2.5 Operational modal analysis

A preliminary investigation of the suspension bridge dynamics was carried out by installing five pairs of wired accelerometers, model PCB 393B12 [50], along both sides of the deck. The sensors were placed at intervals of approximately one-sixth of the bridge span, as shown in Figure 7.8 and Figure 7.9. To capture both horizontal and vertical modes of vibration, two configurations were used: in Configuration 1 (Figure 7.8), both lines of accelerometers were installed vertically, while in Configuration 2 (Figure 7.9), the sensors on the western side were installed vertically and the eastern side sensors horizontally. The ends of the bridge were not instrumented, as a preliminary assessment indicated that the response at the bearings was negligible compared to that of the monitored points. Therefore, the ends were assumed to have zero displacement. Acceleration data were acquired at a sampling rate of 2048 Hz for each sensor over approximately 20 minutes, during which time the bridge remained open to pedestrian traffic. Vertical and horizontal acceleration time histories recorded under Configuration 2 are shown in Figure 7.10 and Figure 7.11, respectively.

To extract the natural frequencies and mode shapes, Frequency Domain Decomposition (FDD) was applied to the collected data [51]. The tool used for the modal extraction was pyOMA, an open-source Python library that enables Operational Modal Analysis (OMA) in both the frequency and time domains [52]. The Singular Value Decomposition (SVD) of the spectral density matrix reveals peaks corresponding to the structural modes at specific frequencies. The evolution of the first three singular values (SVs) is shown in Figure 7.12(a) and Figure 7.12(b) for Configuration 1 and Configuration 2, respectively. The figures highlight that, under operational loads, the bridge exhibits the greatest dynamic response within the frequency range of $1.5 - 2.2$ Hz. The first nine dominant mode shapes were identified through the FDD technique, and the results are summarised in Table 7.3.

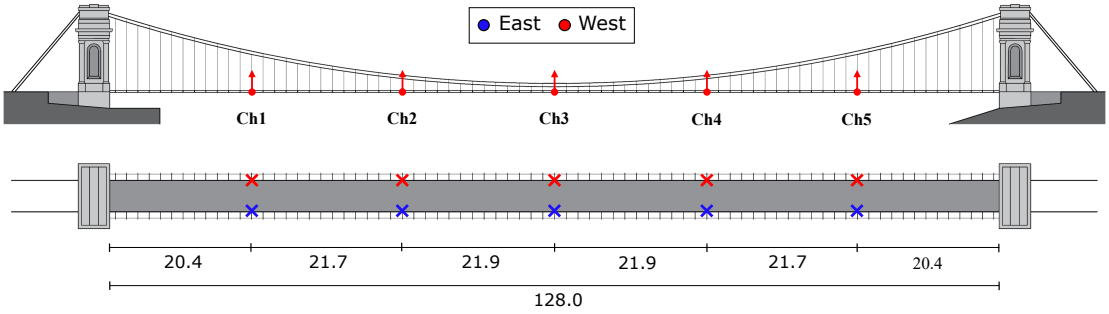


Figure 7.8: Accelerometer configuration – Vertical-Vertical (VV): schematic layout of the accelerometer installation for Configuration 1. Sensors were placed vertically on both the eastern and western sides of the bridge deck to capture vertical vibrational modes.

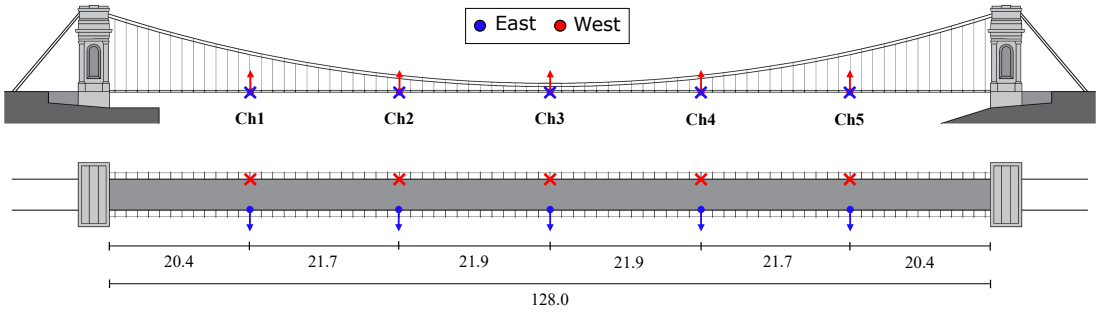


Figure 7.9: Accelerometer configuration – Vertical-Horizontal (VH): schematic layout of the accelerometer installation for Configuration 2. Vertical sensors were installed on the western side and horizontal sensors on the eastern side to capture both vertical and horizontal modes of vibration.

Table 7.3: Natural frequencies of the bridge case study, resulting from Operational Modal Analysis.

MODE	**Direction**	**Type**	**Frequency** [Hz]
1	Horizontal	Flexural	0.380
2	Vertical	Flexural	0.545
3	Vertical	Torsional	0.753
4	Vertical	Flexural	0.852
5	Vertical	Torsional	1.056
6	Vertical	Flexural	1.481
7	Vertical	Flexural	1.566
8	Vertical	Torsional	1.825
9	Vertical	Flexural	2.215

The identified mode shapes along with their associated natural frequencies are shown in Figure 7.13. It was observed that the bridge mode shapes are predominantly associated with vertical motion. Only the first mode is horizontal, corresponding to the lowest natural frequency of 0.38 Hz. The remaining modes are vertical, consisting of an alternating sequence of flexural and torsional modes. With one exception, these vertical modes show clear sinusoidal deformation patterns along the deck, with the number of nodes increasing from one to three. The single non-sinusoidal mode identified has a frequency of 1.57 Hz.

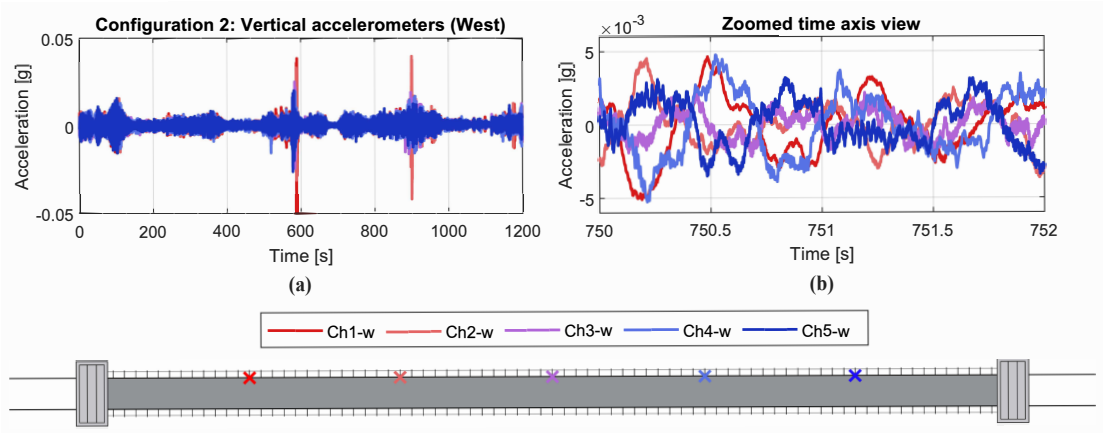


Figure 7.10: Vertical acceleration time history – west side: (a) full 20-minute time history recorded by the five vertical accelerometers on the west side during Configuration 2; (b) zoomed-in view.

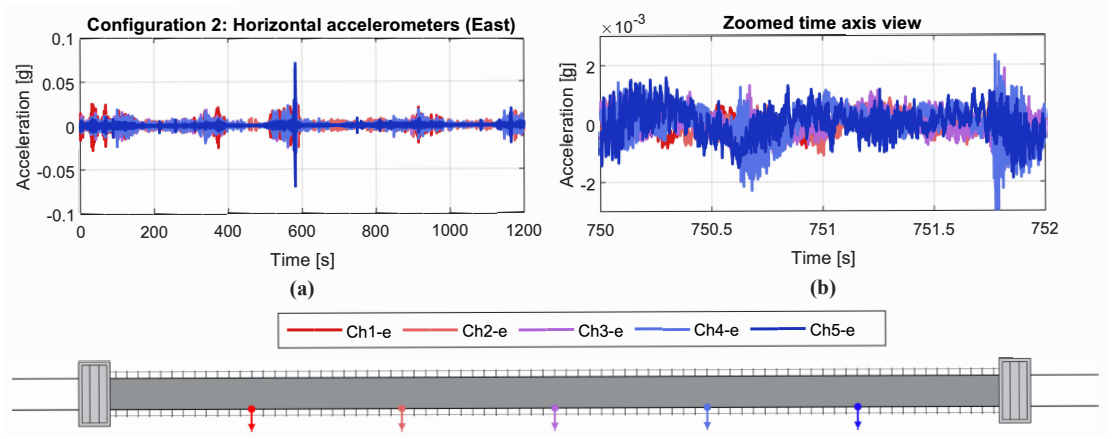


Figure 7.11: Vertical acceleration time history – east side: (a) full 20 minute time history recorded by the five vertical accelerometers on the west side during Configuration 2; (b) zoomed-in view.

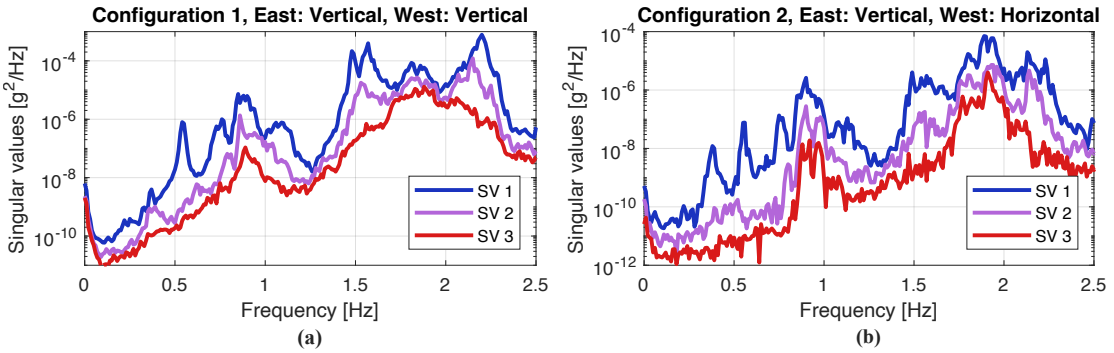


Figure 7.12: SVD of the Cross-Power Spectral Density matrix: first three singular values computed via FDD for: (a) Configuration 1 (VV May 16 2024 20:00 (UTC)) and (b) Configuration 2 (VH May 16 2024 16:00 (UTC)).

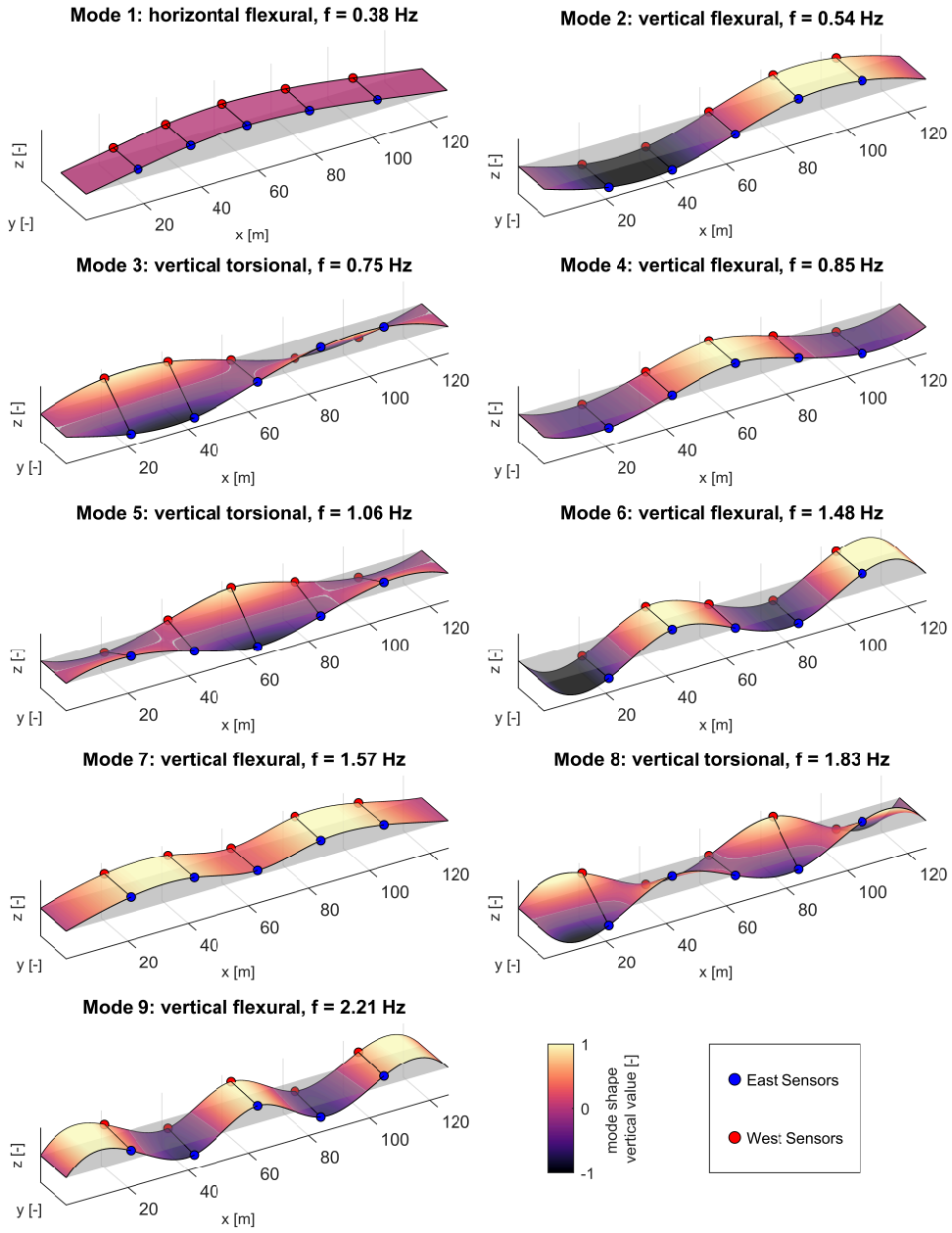


Figure 7.13: Extracted experimental mode shapes: interpolated mode shapes (coloured surfaces) identified through OMA-FDD; the colour highlights the vertical component of the deformation; east (blue) and west (red) markers indicate sensor positions.

7.2.6 SAR acquisitions and experimental validation

This section presents the SAR dataset used in this study and explains how the vibrations measured from SAR imagery were compared to ground-truth data. It first introduces the characteristics of the SAR acquisitions and the parameters used in the SPOT processing chain. Then, it describes the experimental setup, the processing of ground truth data, and the methodology adopted for validating the performance of the technique.

SAR data

The SAR dataset used in this work comprises two high-resolution spotlight mode acquisitions provided by Umbra [53], an X-band sensor constellation that delivers data both for public and private use. Both images were delivered as SLC products to preserve m-m effects and were processed independently. Spotlight mode was selected to maximise the observation time and thus azimuth resolution, as explained previously. Table 7.4 summarises the main features of the two SAR acquisitions used in the analysis.

Table 7.4: Principal features of the SAR acquisitions over the South Portland St. Suspension Bridge.

Quantity	**Acquisition 1**	**Acquisition 2**
Date	2024-May-20	2024-May-16
Time (UTC)	21:40:40	20:21:23
Acquisition time t_{a}	7.50 s	16.38 s
Center frequency f	9.6 GHz	9.6 GHz
Wavelength λ	31 mm	31 mm
Pulse Repetition frequency (PRF)	4.96 kHz	6.05 kHz
Satellite velocity v_{s}	7.65 km/s	7.67 km/s
Slant range R_{ref}	765 km	768 km
Incidence angle β	56.45 °	47.67 °
Range resolution Δr	18.8 cm	66.8 cm
Azimuth resolution Δy	19.5 cm	8.3 cm

Figure 7.14 illustrates the reflectivity maps of both SAR acquisitions with their corresponding optical images for reference. Subfigures 7.14(b) and (d) show the SAR reflectivity maps from Acquisition 1 and Acquisition 2, respectively. From the reflectivity maps, the bridge is clearly distinguishable from the water background due to its stronger backscatter. The most reflective regions of the bridge are near the connections between the hangers and the deck and

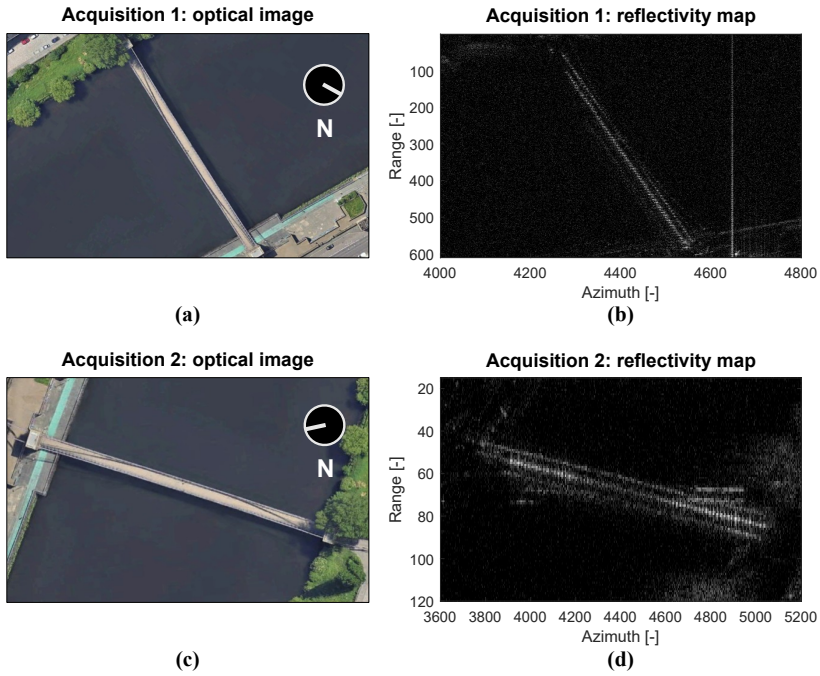


Figure 7.14: Comparison between optical and SAR imagery of the bridge: (a) optical image for Acquisition 1; (b) reflectivity map from SAR Acquisition 1; (c) optical image for Acquisition 2; (d) reflectivity map from SAR Acquisition 2.

near the ends (where the hangers are longer), while the central section appears less reflective in both acquisitions. The two sides of the deck are clearly visible; however, an additional linear feature can be observed, especially in Acquisition 2. This artefact is a mirror image of the structure reflected from the water beneath the bridge. Both edges of the deck are being reflected, but only the near edge (in terms of range) appears distinct from the other features in the SAR image, since the far edge mirror and direct images overlap. This effect must be considered, as water-related backscatter artefacts can introduce noise that affects the velocity extraction. It is acknowledged that this noise will naturally influence the performance of the final results, and in the present work, it was not removed.

To measure the SAR time histories, the SPOT method described in Section 7.2 was used. Table 7.5 provides a summary of the processing parameters applied to each acquisition. These parameters include: the aperture fraction (ξ), overlap ratio (Ω), number of sub-apertures (N), sub-aperture duration (t_{sap}). Moreover, Table 7.5 also reports the sampling frequency (f_{s}) resulting from the

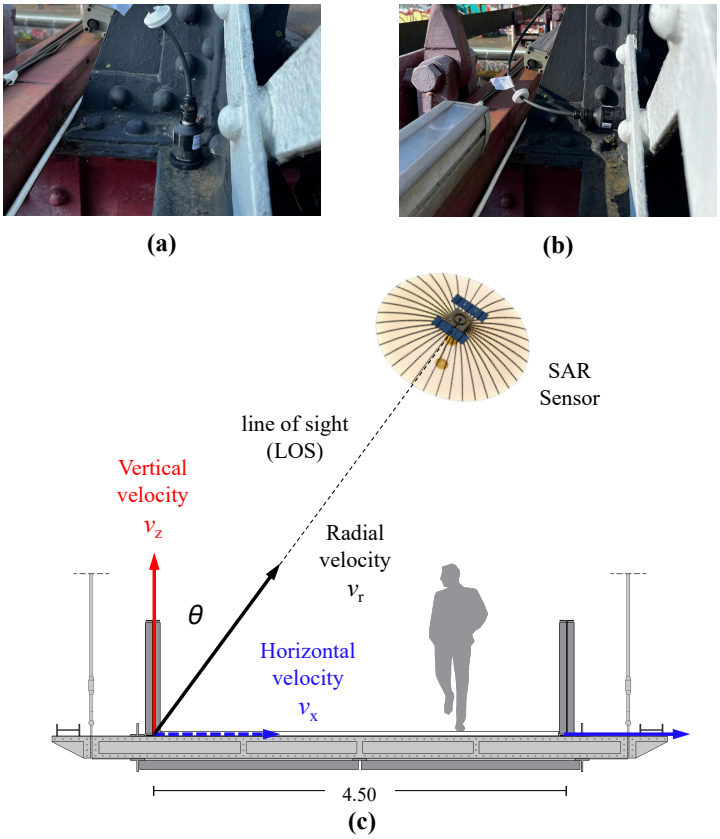


Figure 7.15: SHM system and velocity projection method: (a) vertical accelerometer setup; (b) horizontal accelerometer setup; (c) illustration of radial velocity projection from vertical and horizontal ground velocities using known satellite LOS geometry. The SAR sensor image is adapted from SatNOGS [54].

parameters, the resolution in the frequency domain (Δf), and the peak mean values of the ground velocities $v_{g,max}$ for each acquisition. Target pixels for MDSAR analysis are selected based on consistent reflectivity and the presence of vibrational signatures.

Experimental comparison

The time histories measured by SAR and the resultant spectra were then compared against ground truth measurements obtained by accelerometers. To capture the full three-dimensional dynamic response, Configuration 2 was used (Figure 7.9), which included one row of vertical and one of horizontal accelerometers (as shown in Figure 7.15(a) and Figure 7.15(b)). It was assumed that the horizontal accelerations at both the west and east sides of the deck were

Table 7.5: SPOT extraction parameters and resulting velocity time-history features. The table contains: peak ground velocity $v_{\mathrm{g,max}}$, acquisition time t_a, aperture fraction ξ, overlap Ω, number of sub-apertures N, sub-aperture duration t_{sap}, sampling frequency f_s, frequency resolution Δf.

Acq.	$v_{\mathrm{g,max}}$ [mm/s]	t_a [s]	α [%]	Ω [%]	N [–]	t_{sap} [s]	f_s [Hz]	Δf [Hz]
1	1.58	7.50	4.14	24.0	31	0.31	4.15	0.14
2	1.29	16.54	3.54	71.0	93	0.59	5.87	0.06

identical and that the structural response along the longitudinal direction of the bridge was negligible. Based on this setup, a 20-minute acquisition was performed at a sampling rate of 2048 Hz, during which time acceleration data were recorded from the 10 sensors. The acquisition window was centred around the satellite passage to ensure synchronous data collection. To compute the velocities from the acceleration measurements, the acceleration signals were numerically integrated. Prior to integration, a sixth-order Butterworth band-pass filter with cut-off frequencies of 0.1 Hz and 20 Hz was applied. To avoid introducing phase distortion, zero-phase filtering was performed by processing the data in both the forward and backward directions. The resulting vertical and horizontal velocity components were projected along the satellite LOS direction to yield the radial velocities, accounting for the azimuth and incidence angles during the acquisition. The scheme for the velocity projection is illustrated in Figure 7.15. Finally, the 20-minute radial velocity time histories were cropped to match the time of the satellite passage.

Because the radial velocity measurements were available only at a few discrete points, specifically at every sixth of the span, the full velocity profile was reconstructed by interpolating the data through a superposition of the nine mode shapes shown in Figure 7.13, with equal weighting assigned to each mode during the fitting along the bridge deck. The reconstructed ground truth radial velocities were assigned to each of the extracted pixel locations, corresponding to the points used in the MDSAR analysis.

From these, pixel velocity time histories and ground truth measurements were compared using Pearson's correlation coefficients and Root Mean Square Error (RMSE) to quantitatively assess the performance and accuracy of the SPOT method on a real-world case study.

7.3 Results and discussion

This section presents the results obtained using the SPOT technique, comparing the LOS velocity time histories measured from SAR imagery with syn-

chronous ground truth measurements. For brevity, only three representative time histories per acquisition are reported. The results are discussed separately for Acquisition 1 and Acquisition 2 in the following subsections.

7.3.1 Acquisition 1

Data for Acquisition 1 were collected over an acquisition time $t_{\mathrm{a}} = 7.50$ s. As reported in Table 7.5, the results were computed with an aperture fraction of $\xi = 4.14\%$, corresponding to a sub-aperture duration of $t_{\mathrm{sap}} = 0.31$ s. The overlap ratio Ω was set to 24%, resulting in a sampling frequency of 4.15 Hz, which was then upsampled by a factor of 20 using sinc interpolation. A patch size of 7 pixels in azimuth and 1 pixels in range was used for cross-correlation tracking. This configuration was selected to ensure tracking accuracy given the expected vibration amplitudes of the bridge deck. Ground measurements indicated peak radial velocities between 0.5 and 2 $\mathrm{mm/s}$, with a mean maximum value of $v_{\mathrm{g,max}} = 1.58$ $\mathrm{mm/s}$ (as reported in Table 7.5).

Figure 7.16 shows the LOS velocity time histories for three representative measurements made from different locations along the deck, with the corresponding ground truth data. These show that the SAR-measured velocities approximately match the oscillatory behaviour observed in the ground truth data; however, the velocity magnitudes are generally overestimated. To evaluate the agreement of the signals in the time domain, two metrics were used: the Pearson's correlation coefficient (ρ_t) and the RMSE, both of which are reported in each sub-figure. Starting with Figure 7.16(a), it is possible to observe that the MDSAR technique successfully captures the decreasing velocity magnitude from approximately 2 $\mathrm{mm/s}$ to 0.5 $\mathrm{mm/s}$, supporting the similarity between the two curves. The time-domain signals are, however, visibly affected by noise. This is reflected in the RMSE values, which range between 0.7 to 1.4 $\mathrm{mm/s}$ (40.1% to 76.1% of the maximum ground truth peak velocity), indicative of the challenges in measuring the precise time history of velocity. The temporal correlation ρ_t values calculated from the SAR and ground truth measurements are reasonable, with coefficients ranging from 0.46 to 0.66. In the frequency domain, performance was assessed using the absolute frequency error (ϵ_f), estimated as the residual between the highest amplitude frequency components of the SAR and ground truth measurements, and the Pearson's correlation coefficients of the respective spectra (ρ_f).

These metrics are also reported in the figures presenting the SAR measurement results. Figure 7.16 shows that the dominant peaks identified in the SAR spectra align well with those from ground truths. The residual error in the estimation of the dominant frequency ranged from 0.04 to 0.10 Hz, which is well

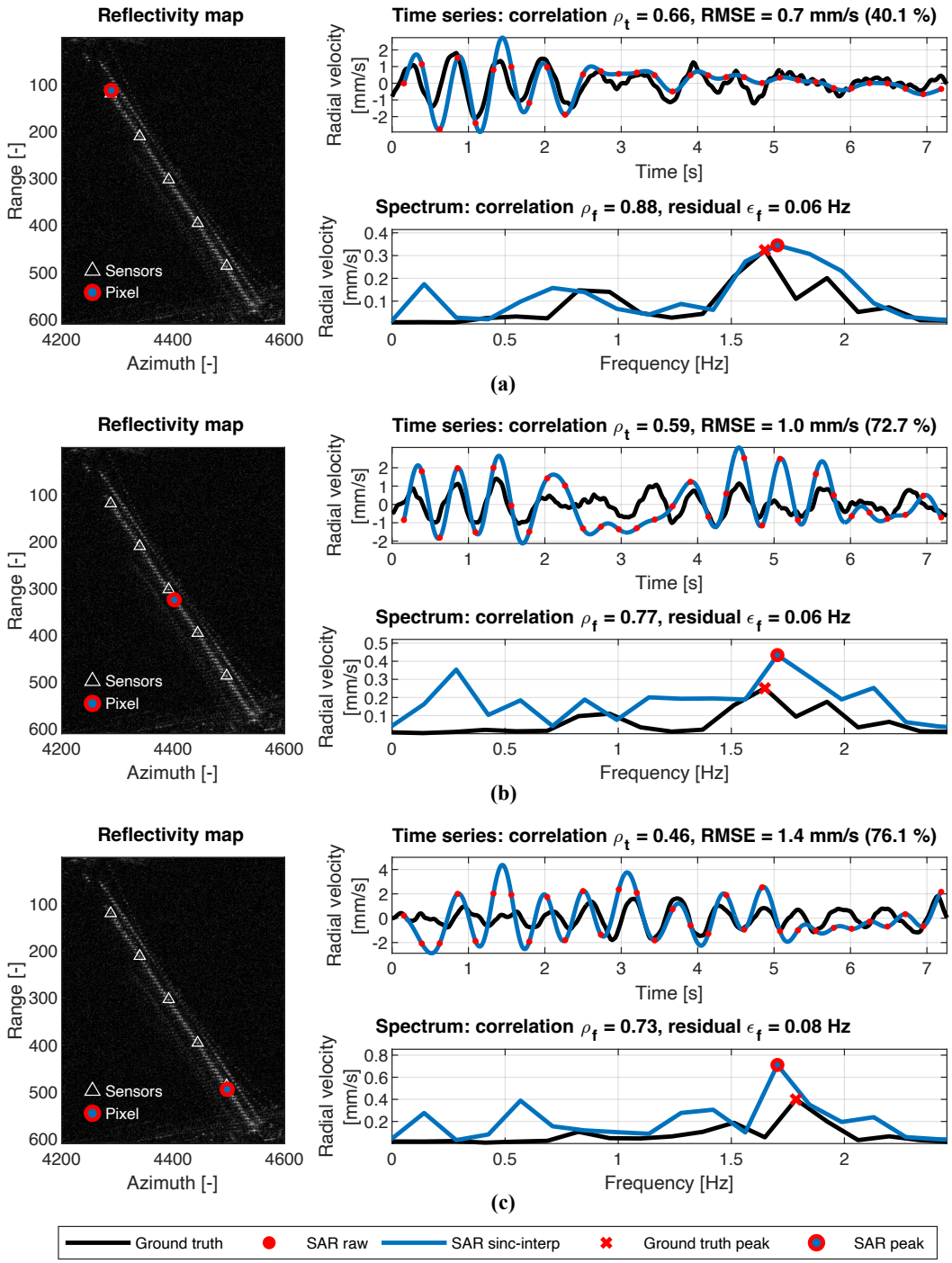


Figure 7.16: Acquisition 1 – Pixel location, SAR-measured LOS velocity, and velocity spectrum compared to ground truth measurements of a) pixel 1, b) pixel 2, and c) pixel 3. The figure includes RMSE, frequency error ϵ_f, and time/frequency correlation values.

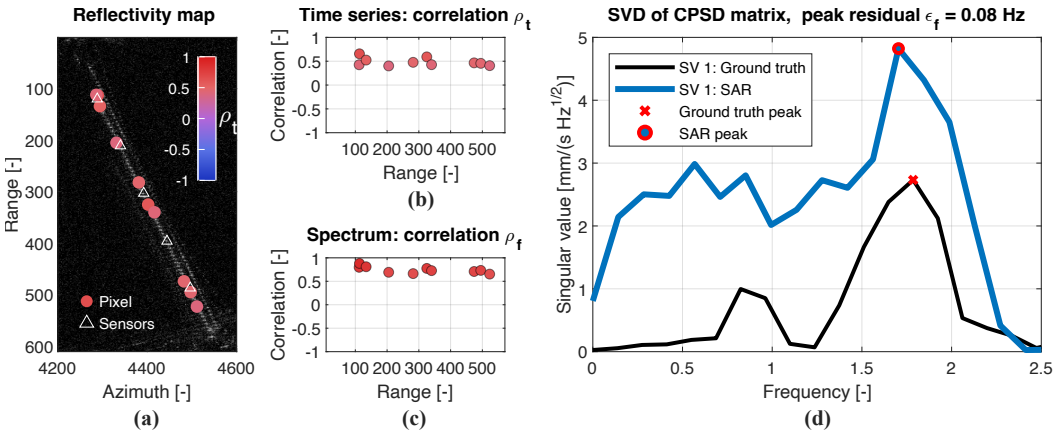


Figure 7.17: Acquisition 1 – measurement position overview and CPSD comparison: (a) locations of extracted pixels; (b) time-domain correlation; (c) frequency-domain correlation; and (d) first SV of the SAR and ground truth CPSD matrices. The figure includes the frequency residual ϵ_f.

within the spectral resolution of $\Delta f = 0.14$ Hz (limited by the short acquisition duration). For the sake of clarity, *dominant frequency* refers to the frequency that is most prominent (i.e., more visible) in the particular signal. Additional low-frequency components also appear in the SAR spectra. Whilst some of these are likely spurious (e.g., the lower frequency peaks below 0.50 Hz), minor peaks around 0.75 Hz are consistent with those observed in the ground truth data (e.g., Figures 7.16(a) and 7.16(b)). Nonetheless, the overall spectral agreement remains fairly strong, supported by high frequency-domain correlation values of ρ_f = 0.73 to 0.88.

These results are consistent across all measured pixels. Figure 7.17(a) shows the spatial location of all processed pixels, and Figures 7.17(b) and 7.17(c) show the values of correlations, with a mean ρ_t of 0.48 and ρ_f of 0.74, aligning with the representative examples. Subsequently, the analysis investigated whether the observed vibrations were consistent with the expected modal behaviour of the bridge. The Cross-Power Spectral Density (CPSD) matrix is computed from the full set of SAR-measured time histories. SVD processing was then applied to this matrix, following the approach of classical FDD used in OMA [51]. Figure 7.17(d) compares the first SV associated with SAR measurements to that obtained from the ground truth data. The two curves exhibit a strong similarity near the dominant frequency peak, with a residual error $\epsilon_f = 0.10$ Hz that is again within spectral resolution limits. The SAR SV amplitude is overestimated, likely due to residual noise. It is worth noting that the frequency peak appears broad in both SAR and ground truth datasets, sug-

gesting possible modal coupling – where vibrational modes with closely spaced natural frequencies interact and prevent full separation.

7.3.2 Acquisition 2

Data for Acquisition 2 were collected over an observation time of $t_{\mathrm{a}} = 16.54$ s, which was more than twice that of Acquisition 1. SAR time histories of velocity were measured using an aperture fraction ξ of 3.54%, comparable to the one used for Acquisition 1, resulting in a sub-aperture duration of $t_{\mathrm{sap}} = 0.59$ s (which is greater than Acquisition 1, due to the longer t_{a}). The overlap ratio Ω was increased to 71%, yielding a sampling frequency f_{s} of 5.87 Hz. As for Acquisition 1, the signal was upsampled by a factor of 20 using sinc interpolation. A patch size of 7 pixels in azimuth and 1 in range was used, consistent with the configuration in Acquisition 1. Ground truth measurements indicated similar vibrational amplitudes as those observed in Acquisition 1, with a mean peak radial velocity $v_{\mathrm{g,max}} = 1.29\ \mathrm{mm/s}$ (see Table 7.5). In this case, fewer valid pixels were identified for measurement. This reduction was primarily due to reduced deck visibility in the SAR image and a coarser range resolution Δy, which limited the number of pixels on the target.

Figure 7.18 shows the time histories and spectra of the measured radial velocities for three representative pixels, one from the southern end and two from the northern end of the deck. As for Acquisition 1, the time histories show similar issues related to noise. The RMSE values range from 1.0 to $1.1\ \mathrm{mm/s}$, comparable to those observed in the first acquisition. Due to the slightly lower peak velocities in this dataset, the corresponding RMSE percentages are higher, ranging from 73% to 95%. Temporal correlation coefficients ρ_t are slightly lower than in the previous case, ranging from 0.35 to 0.41, with a mean value of 0.38 (compared to 0.48 for Acquisition 1). Despite the lower correlation and higher error, the SAR measurements still captured the oscillatory behaviour, maintaining phase alignment with the ground truth signals.

The power spectral density comparison also produced coherent results (see Figure 7.19). The first SV of the CPSD matrix, computed across all SAR-measured time histories, aligns well with the corresponding SV from the ground truth data. The most dominant frequency peak is captured accurately, with a residual error of $\epsilon_f = 0.03$ Hz, well below the spectral resolution threshold. Moreover, the SAR SV spectrum exhibits secondary peaks in the $0.76-0.89$ Hz range, consistent with modal components observed in the ground truth signals and possibly associated with the lower frequency modes of the bridge.

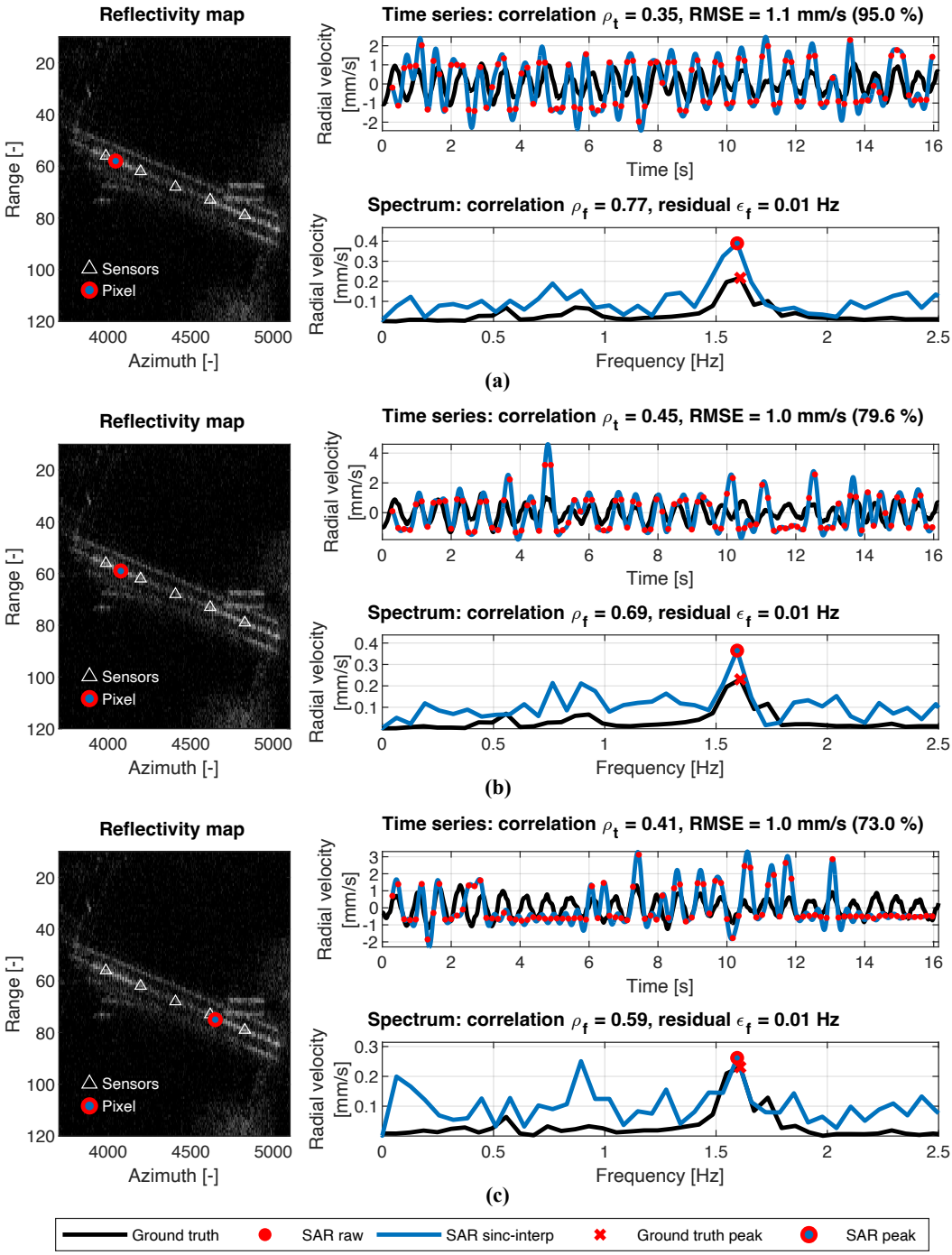


Figure 7.18: Acquisition 2 – pixel location, SAR-measured LOS velocity, and velocity spectrum compared to ground-truth measurements of (a) pixel 1, (b) pixel 2, and (c) pixel 3. RMSE, frequency error ϵ_f, and time/frequency correlation values are included.

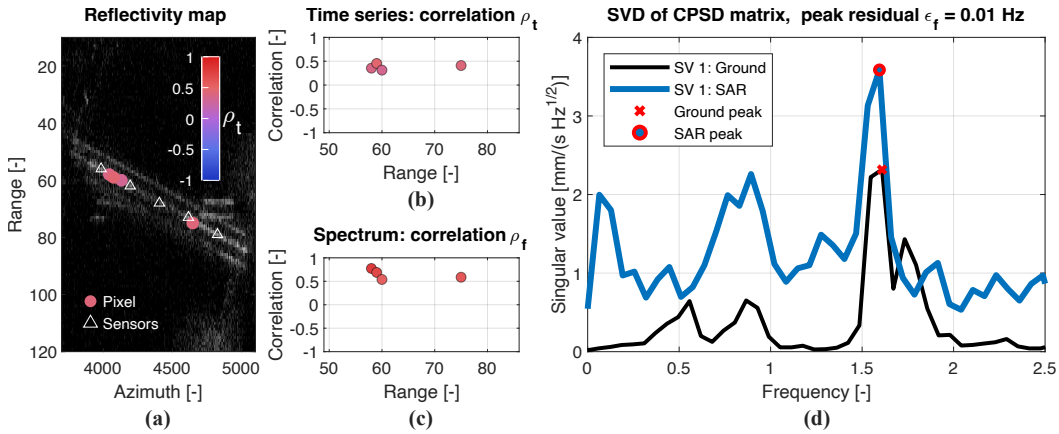


Figure 7.19: Acquisition 2 – measurement position overview and CPSD comparison: (a) locations of extracted pixels; (b) time-domain correlation; (c) frequency-domain correlation; and (d) first SV of the SAR and ground-truth CPSD matrices. The frequency residual ϵ_f is included.

7.3.3 Discussion

Three main research questions were posed at the beginning of this paper and are answered here based on the results presented.

(i) ***Can MDSAR measure the vibrations of a real-world structure?***
Yes – the experiments demonstrate that MDSAR is unequivocally capable of measuring the vibrations of a real-world bridge. No devices were installed on the structure to enhance target reflectivity during SAR collections. SAR measurements showed oscillatory behaviour consistent with the synchronous ground truth measurements, and spectral peaks from the SAR data aligned closely with the ground truth data, although some overestimation of velocity values was observed.

(ii) ***How accurate is the method, and what are its limitations?***
The discussion on the accuracy of the method and its limitations are tied in context to the specific experimental conditions and scenario of the case study, which was a full-scale suspension bridge with vibrational peak velocities along the LOS ranging from 1 to 2 $\mathrm{mm/s}$ and dominant frequencies around $1.5-2$ Hz. However, it is expected that the conclusions are applicable to similar structures.

The measured LOS velocity time histories and corresponding spectra captured the main characteristics of the bridge dynamics. In general, SAR measurements showed vibration patterns consistent with the ground truth, including visible phase alignment. The RMSE remained consistent at approximately

$1\ \mathrm{mm/s}$ across both acquisitions and at different points along the deck, aligning with previously published results focusing on controlled experiments with isolated targets [40]. It was also observed that SAR measurements tend to overestimate overall velocity amplitudes. The relative error may be considered small or large depending on the amplitude of the vibrations being measured. For these measurements, the RMSE corresponded to 40% and 95% of the true peak velocity for Acquisitions 1 and 2, respectively, which was again consistent with previous CR experimentation [40]. This resulted in temporal correlation values for the two acquisitions averaging to 0.38 and 0.48 (with the best individual pixel value reaching 0.66) for all pixels. On the other hand, spectral correlation coefficients were higher, reaching mean values of 0.65 and 0.74 (with a maximum of 0.88). It is expected that better quality results could be achieved when the bridge vibration velocities are greater in magnitude.

In general, the noise amplitude expected from this technique depends primarily on:

- The radar wavelength (λ) – longer wavelengths result in a coarser azimuth resolution (Δy, see Eq. 7.1), which increases tracking error.
- The sub-aperture duration t_{sap} – where shorter sub-apertures worsen azimuth resolution, again shown in Eq. 7.1.
- The implementation of the tracking algorithm.

In addition to coarse azimuth resolution reducing tracking precision, it also reduces tracking accuracy, especially in dense urban environments when multiple closely spaced scattering points are present (known as *cluttered* environments [36]) due to the increased risk of confusion between poorly resolved targets. Preserving a fine azimuth resolution is therefore essential. Moreover, the use of masking techniques can help identify and exclude areas or features in the SAR imagery that may interfere with the analysis or lead to false interpretations, such as the noise introduced by water backscatter.

As for the wavelength, current commercial missions do not offer sensing at shorter wavelengths than X-band ($\lambda = 24 - 38\ \mathrm{mm}$), but future missions may provide this capability.

As for sub-aperture duration, this is limited by the sampling period and by the overlap ratio. The sampling period must satisfy the Nyquist criterion and thus has to be shorter than half the minimum vibration period of interest. Also, the overlap ratio must be smaller than 100%. Therefore, the sub-aperture duration must necessarily remain shorter than the primary vibrational period of the structure. Finally, improving the tracking algorithm, either by optimisation or by substitution with more advanced techniques than SPOT, could reduce mea-

surement errors.

(iii) ***Will it be possible to extract modal parameters from spaceborne SAR data?***

The principal limitations on the use of MDSAR for the extraction of modal parameters are: the noise level and the short acquisition times available from spaceborne platforms. These factors restrict the extent to which a modal extraction can be performed.

Starting with the measurement of natural frequencies, the first observation is that the MDSAR spectra are consistent with the ground truth data, and that dominant frequency peaks are successfully identified from both acquisitions. More specifically, absolute frequency errors range from 0.03 to 0.10 Hz, below the spectral resolution (Δf) in all cases. The correlation in the frequency domain is very satisfactory, with mean values ranging from 0.65 to 0.74, indicating that the spectra are very similar. The peak frequencies of the singular values show strong agreement with those obtained through conventional OMA, indicating that the SAR data can reliably detect dominant frequencies. For example, for Acquisition 2, the first SV reveals a sharp peak at 1.59 Hz, matching the 7^{th} OMA mode at 1.58 Hz, and featuring a frequency resolution of 0.06 Hz (comparable to errors for other VBSHM techniques). This result was validated using the synchronous ground-truth accelerometers. In contrast, for Acquisition 1, the SV for both the SAR and ground truth signals (Figure 7.17(b)), each show a broader dominant peak. This is likely caused by modal coupling of the 1.57 Hz and 1.83 Hz modes, which could not be individually detected due to the limited frequency resolution of both SAR and ground truth data. The feasibility of the measurement of the natural frequencies via SAR data is inherently constrained by the short observation durations of current commercial satellite missions, which limits the resolution of the frequency spectra. For instance, a 10 s acquisition corresponds to a frequency resolution of ~ 0.1 Hz, which may be insufficient to resolve closely spaced modes, especially in complex structures where modal coupling (e.g., long-span bridges) is present. Furthermore, less excited modes were not observed from the SVs, meaning that vibrations with amplitudes below the measurement accuracy could not be detected. In summary, dominant frequencies can be reliably extracted only when the corresponding modal response along the LOS is comparable to the estimated measurement error and the acquisition duration is sufficient to achieve the desired spectral resolution.

Mode shape identification presents additional challenges, as measurement

accuracy plays a more critical role. Effectively, using MDSAR is currently equivalent to using data from very noisy ground-based sensors (with RMSE noise in the order of $\sim 1\ \mathrm{mm/s}$) for a short acquisition time (limited to $10-30$ s). Under these conditions, even advanced OMA techniques struggle to distinguish superposed modal responses with high accuracy in the presence of tightly coupled modes. It is expected that modal recognition could possibly be performed, allowing for the separation of different mode shapes and at least the identification of the phase of the modal components. It is also anticipated that accurate mode shape extraction could be possible with an appropriate extraction algorithm that could exploit multiple successive acquisitions of the same target.

The performance of MDSAR in identifying modal parameters could be improved by several strategies. One approach would be the use of corner reflectors to increase reflectivity at specific points on the structure. Placing these at antinodes, where the modal response is the highest, would enhance measurement robustness against clutter and noise. The SAR acquisition geometry could also be optimised in two ways: (i) minimising the incidence angle (θ) to maximise the projection of vertical velocity along the LOS, therefore improving the m-D measurement sensitivity; and (ii) aligning the SAR range axis with the bridge span to maximise the number of independent measurement points along its length. These improvements, however, require control of the satellite orbits and their acquisition parameters. The observation time could be increased to improve frequency resolution through several strategies. Longer duration SAR products (up to ~ 30 s) are already available for specific uses [55]. Additionally, data from multiple acquisitions with consistent geometry and closely spaced in time could be combined to effectively increase the total observation period. This is becoming increasingly feasible as satellite constellations grow, offering more frequent passes. To address the limitations imposed by modal coupling and coarse spectral resolution, super-resolution techniques in the frequency domain, such as MUSIC [56] and ESPRIT [57], could be applied to the measurements made by MDSAR to separate closely spaced frequency components. Another direction could be integrating physical models such as finite element models (FEMs) into the processing pipeline to guide pixel selection and improve tracking results by constraining the solution with additional knowledge of the expected behaviour of the target dynamics. Looking further ahead, advances in SAR satellite capabilities, such as longer acquisition durations, shorter revisit times, or higher carrier-frequency sensors providing finer spatial resolution, could support more accurate modal extraction.

7.4 Conclusions

This work presented an experimental validation and metrological assessment of an MDSAR technique for measuring vibrations from a full-scale suspension bridge. Using high-resolution spotlight SAR imagery, the SPOT algorithm was employed to reconstruct LOS vibration velocity time series of the South Portland St. Suspension Bridge. Results were then compared against synchronous ground truth measurements collected with a traditional accelerometer system. Based on the experimental results, the following conclusions were drawn:

- The study confirms that MDSAR is indeed capable of measuring real structural vibrations. The SAR-measured time histories and frequency spectra capture the main features of the bridge dynamics.
- The measurement noise of the LOS velocity in the time domain has a standard deviation of approximately $1\ \mathrm{mm/s}$, indicating that the technique is suitable for monitoring structural vibrations with amplitudes greater than this value. In this specific case, where peak velocities of $1.5 - 2\ \mathrm{mm/s}$ were recorded, the correlation between SAR measurements and ground truth time histories reached values of up to 0.66, aligning with earlier controlled experiments using corner reflectors.
- The measurement accuracy of the SPOT technique is primarily influenced by the radar wavelength, the sub-aperture duration, and the efficiency of the sub-pixel tracking algorithm. Whilst the sub-aperture duration is limited by the sampling period, future improvements could be obtained by employing satellite missions with shorter wavelengths and by refining pixel tracking techniques. Alternative MDSAR measurement methods, such as those directly based on measuring signal phase, could also be integrated into the measurement pipeline and may yield increased sensitivity.
- The technique presented is effective for estimating the dominant vibrational frequency of the structure, with a frequency resolution that essentially depends on the acquisition duration of the spotlight SAR collection. In this study, resolutions as fine as $0.06\ \mathrm{Hz}$ were achieved. With currently available missions, durations up to 30 seconds could be, in principle, reached, resulting in a frequency resolution of approximately $0.03\ \mathrm{Hz}$.
- Extracting mode shapes is more challenging. Meaningful results could be obtained in the absence of modal coupling, but the overall performance is limited by short acquisition durations and noise in the velocity

time histories.

- It is expected that modal recognition could be performed and that this would allow the separation of different modes and at least the identification of their phase components. The accurate estimation of mode shapes, however, would require the development of an appropriate extraction algorithm.

In summary, future developments to improve the quality of the MDSAR measurement would involve the testing of other processing strategies developed in the literature, deploying corner reflectors at selected locations to enhance reflectivity, applying masking techniques to reduce noise in SAR imagery, integrating physical models, and exploiting multiple acquisitions to extend effective observation time.

Bibliography

[1] Wei Fan and Pizhong Qiao, "Vibration-based Damage Identification Methods: A Review and Comparative Study," *Structural Health Monitoring*, vol. 10, no. 1, pp. 83–111, 1 2011. [Online]. Available: https://journals.sagepub.com/doi/10.1177/1475921710365419

[2] R. Hou and Y. Xia, "Review on the new development of vibration-based damage identification for civil engineering structures: 2010–2019," *Journal of Sound and Vibration*, vol. 491, p. 115741, 2021. [Online]. Available: https://linkinghub.elsevier.com/retrieve/pii/S0022460X2030571X

[3] J. J. Moughty and J. R. Casas, "A State of the Art Review of Modal-Based Damage Detection in Bridges: Development, Challenges, and Solutions," *Applied Sciences*, vol. 7, no. 5, p. 510, 5 2017. [Online]. Available: https://www.mdpi.com/2076-3417/7/5/510

[4] Y. Bao and H. Li, "Machine learning paradigm for structural health monitoring," *Structural Health Monitoring*, vol. 20, no. 4, pp. 1353–1372, 2021. [Online]. Available: https://journals.sagepub.com/doi/10.1177/1475921720972416

[5] S. S. Saidin, A. Jamadin, S. Abdul Kudus, N. Mohd Amin, and M. A. Anuar, "An Overview: The Application of Vibration-Based Techniques in Bridge Structural Health Monitoring," *International Journal of Concrete Structures and Materials*, vol. 16, no. 1, p. 69, Dec. 2022. [Online]. Available: https://link.springer.com/10.1186/s40069-022-00557-1

[6] E. Ozer, A. G. Özcebe, C. Negulescu, A. Kharazian, B. Borzi, F. Bozzoni, S. Molina, S. Peloso, and E. Tubaldi, "Vibration-Based and Near Real-Time Seismic Damage Assessment Adaptive to Building Knowledge Level," *Buildings*, vol. 12, no. 4, p. 416, Apr. 2022, number: 4 Publisher: Multidisciplinary Digital Publishing Institute. [Online]. Available: https://www.mdpi.com/2075-5309/12/4/416

[7] J. Brownjohn, "Structural health monitoring of civil infrastructure," *Philos Trans A Math Phys Eng Sci*, vol. 365, no. 1851, pp. 589–622, Dec. 2006. [Online]. Available: https://doi.org/10.1098/rsta.2006.1925

[8] T. Nagayama, S. Sim, Y. Miyamori, and B. J. Spencer, "Issues in structural health monitoring employing smart sensors," *Smart Structures and Systems*, vol. 3, no. 3, pp. 299–320, Jul. 2007. [Online]. Available: https://doi.org/10.12989/SSS.2007.3.3.299

[9] Z. E. Foden A., "Value and challenges of structural monitoring for long-span bridges," in *Risk-based strategies for bridge maintenance*. Boca Raton: CRC Press, Taylor & Francis Group, 2023.

[10] F. J. Carrión, J. A. Quintana, and S. E. Crespo, "Techno-economical and practical considerations for SHM systems," *Journal of Civil Structural Health Monitoring*, vol. 7, no. 2, pp. 207–215, Apr. 2017. [Online]. Available: http://link.springer.com/10.1007/s13349-017-0215-x

[11] D. Li, B. Li, T. Wang, and J. Zhang, "Lightweight structural health monitoring and safety evaluation: Review and case studies," *Advances in Structural Engineering*, p. 13694332251325043, Mar. 2025. [Online]. Available: https://journals.sagepub.com/doi/10.1177/13694332251325043

[12] J. Valença, X. Qin, L. Chang, J. Dong, X. Shi, and J. R. Casas, "Remote Sensing-Based Structural Health Monitoring and Damage Assessment," *Remote Sensing*, vol. 16, no. 7, p. 1146, Mar. 2024. [Online]. Available: https://www.mdpi.com/2072-4292/16/7/1146

[13] T. Panigati, M. Zini, D. Striccoli, P. F. Giordano, D. Tonelli, M. P. Limongelli, and D. Zonta, "Drone-based bridge inspections: Current practices and future directions," *Automation in Construction*, vol. 173, p. 106101, 5 2025. [Online]. Available: https://linkinghub.elsevier.com/retrieve/pii/S0926580525001414

[14] H. Kim and G. Kim, "Reliability Assessment of a Vision-Based Dynamic Displacement Measurement System Using an Unmanned Aerial Vehicle," *Sensors*, vol. 23, no. 6, p. 3232, Jan. 2023, number: 6 Publisher: Multidisciplinary Digital Publishing Institute. [Online]. Available: https://www.mdpi.com/1424-8220/23/6/3232

[15] S. Ri, J. Ye, N. Toyama, and N. Ogura, "Drone-based displacement measurement of infrastructures utilizing phase information," *Nature Communications*, vol. 15, no. 1, p. 395, Jan. 2024, publisher: Nature Publishing Group. [Online]. Available: https://www.nature.com/articles/s41467-023-44649-2

[16] T. Miyashita and M. Nagai, "Vibration-based Structural Health Monitoring for Bridges using Laser Doppler Vibrometers and MEMS-based Technologies," *International journal of steel structures*, vol. 8, pp. 325–331, Dec. 2008.

[17] E. Kaartinen, K. Dunphy, and A. Sadhu, "LiDAR-Based Structural Health Monitoring: Applications in Civil Infrastructure Systems," *Sensors*, vol. 22, no. 12, p. 4610, 6 2022. [Online]. Available: https://www.mdpi.com/1424-8220/22/12/4610

[18] A. Trias-Blanco, J. Gong, and F. L. Moon, "Characterization of Operational Vibrations of Steel-Girder Highway Bridges via LiDAR," *Remote Sensing*, vol. 15, no. 4, p. 1003, 2 2023. [Online]. Available: https://www.mdpi.com/2072-4292/15/4/1003

[19] S. Sotoudeh, L. Lantini, S. Uzor, and F. Tosti, "A Systematic Review into the Application of Ground-Based Interferometric Radar Systems for Bridge Monitoring," *Remote Sensing*, vol. 17, no. 9, p. 1541, Apr. 2025. [Online]. Available: https://www.mdpi.com/2072-4292/17/9/1541

[20] C. Michel and S. Keller, "Advancing Ground-Based Radar Processing for Bridge Infrastructure Monitoring," *Sensors*, vol. 21, no. 6, p. 2172, 3 2021. [Online]. Available: https://www.mdpi.com/1424-8220/21/6/2172

[21] A. Beni, L. Miccinesi, L. Pagnini, A. Cioncolini, J. Shan, and M. Pieraccini, "Interferometric Radars for Bridge Monitoring: Comparison among X-Bands, Ku-Bands, and W-Bands," *Remote Sensing*, vol. 16, no. 17, p. 3323, Jan. 2024, number: 17 Publisher: Multidisciplinary Digital Publishing Institute. [Online]. Available: https://www.mdpi.com/2072-4292/16/17/3323

[22] D. Amitrano, G. Di Martino, R. Guida, P. Iervolino, A. Iodice, M. N. Papa, D. Riccio, and G. Ruello, "Earth Environmental Monitoring Using Multi-Temporal Synthetic Aperture Radar: A Critical Review of Selected Applications," *Remote Sensing*, vol. 13, no. 4, p. 604, Feb. 2021. [Online]. Available: https://www.mdpi.com/2072-4292/13/4/604

[23] E. S. Agency, "Sentinel-1," https://www.esa.int/Applications/Observing_the_Earth/Copernicus/Sentinel-1, 2025.

[24] G. Chen, Y. Zhang, R. Zeng, Z. Yang, X. Chen, F. Zhao, and X. Meng, "Detection of Land Subsidence Associated with Land Creation and Rapid Urbanization in the Chinese Loess Plateau Using Time Series InSAR: A Case Study of Lanzhou New District," *Remote Sensing*, vol. 10, no. 2, p. 270, Feb. 2018. [Online]. Available: https://www.mdpi.com/2072-4292/10/2/270

[25] K. Malik, D. Kumar, D. Perissin, and B. Pradhan, "Estimation of ground subsidence of New Delhi, India using PS-InSAR technique and Multi-sensor Radar data," *Advances in Space Research*, vol. 69, no. 4, pp. 1863–1882, Feb. 2022. [Online]. Available: https://linkinghub.elsevier.com/retrieve/pii/S0273117721006827

[26] X. Qin, M. Liao, M. Yang, and L. Zhang, "Monitoring structure health of urban bridges with advanced multi-temporal InSAR analysis," *Annals of GIS*, vol. 23, no. 4, pp. 293–302, 10 2017. [Online]. Available: https://www.tandfonline.com/doi/full/10.1080/19475683.2017.1382572

[27] D. Tonelli, V. F. Caspani, A. Valentini, A. Rocca, R. Torboli, A. Vitti, D. Perissin, and D. Zonta, "Interpretation of Bridge Health Monitoring Data from Satellite InSAR Technology," *Remote Sensing*, vol. 15, no. 21, p. 5242, 11 2023. [Online]. Available: https://www.mdpi.com/2072-4292/15/21/5242

[28] P. Milillo, R. Bürgmann, P. Lundgren, J. Salzer, D. Perissin, E. Fielding, F. Biondi, and G. Milillo, "Space geodetic monitoring of engineered structures: The ongoing destabilization of the Mosul dam, Iraq," *Scientific Reports*, vol. 6, no. 1, p. 37408, 12 2016. [Online]. Available: https://www.nature.com/articles/srep37408

[29] S. Selvakumaran, S. Plank, C. Geiß, C. Rossi, and C. Middleton, "Remote monitoring to predict bridge scour failure using Interferometric Synthetic Aperture Radar (InSAR) stacking techniques," *International Journal of Applied Earth Observation and Geoinformation*, vol. 73, pp. 463–470, Dec. 2018. [Online]. Available: https://linkinghub.elsevier.com/retrieve/pii/S0303243418303052

[30] P. Milillo, G. Giardina, D. Perissin, G. Milillo, A. Coletta, and C. Terranova, "Pre-Collapse Space Geodetic Observations of Critical Infrastructure: The Morandi Bridge, Genoa, Italy," *Remote Sensing*, vol. 11, no. 12, p. 1403, 6 2019. [Online]. Available: https://www.mdpi.com/2072-4292/11/12/1403

[31] D. Cusson, C. Rossi, and I. F. Ozkan, "Early warning system for the detection of unexpected bridge displacements from radar satellite data," *Journal of Civil Structural Health Monitoring*, vol. 11, no. 1, pp. 189–204, 2 2021. [Online]. Available: http://link.springer.com/10.1007/s13349-020-00446-9

[32] T. Carlà, E. Intrieri, F. Raspini, F. Bardi, P. Farina, A. Ferretti, D. Colombo, F. Novali, and N. Casagli, "Perspectives on the prediction of catastrophic slope failures from satellite InSAR," *Scientific Reports*, vol. 9, no. 1, p. 14137, Oct. 2019. [Online]. Available: https://www.nature.com/articles/s41598-019-50792-y

[33] D. Perissin, "Geometric Processing: Active Sensor Modeling and Calibration (SAR)," in *Comprehensive Remote Sensing*. Elsevier, 2018, pp. 61–76. [Online]. Available: https://linkinghub.elsevier.com/retrieve/pii/B9780124095489103367

[34] V. C. Chen, *The Micro-Doppler Effect in Radar*, 2nd ed. Artech house, 2019, accessed: 2025.

[35] M. Rüegg, E. Meier, and D. Nüesch, "Vibration and Rotation in Millimeter-Wave SAR," *IEEE Transactions on Geoscience and Remote Sensing*, vol. 45, no. 2, pp. 293–304, 2 2007. [Online]. Available: http://ieeexplore.ieee.org/document/4069119/

[36] F. Rollo, C. Ilioudis, and C. Clemente, "Advances in Micro-Doppler Processing in Synthetic Aperture Radar: A review of techniques, results, and future trends," *IEEE Geoscience and Remote Sensing Magazine*, pp. 2–24, 2025. [Online]. Available: https://ieeexplore.ieee.org/document/11029265/

[37] V. Chen, Fayin Li, Shen-Shyang Ho, and H. Wechsler, "Micro-doppler effect in radar: phenomenon, model, and simulation study," *IEEE Transactions on Aerospace and Electronic Systems*, vol. 42, no. 1, pp. 2–21, 1 2006. [Online]. Available: http://ieeexplore.ieee.org/document/1603402/

[38] C. Clemente, D. Tonelli, A. Lotti, F. Rollo, C. Ilioudis, S. D. Riofrio, F. Biondi, E. Tubaldi, M. Macdonald, D. Zonta, M. Zavagli, M. Costantini, F. Minati, F. Vecchioli, P. Milillo, M. Zimmermanns, E. Imbembo, and M. Corvino, "On Micro-Motion Extraction from High Resolution X-band SAR products," in *IGARSS 2024 - 2024 IEEE International Geoscience and Remote Sensing Symposium*. Athens, Greece: IEEE, 7 2024, pp. 1182–1186. [Online]. Available: https://ieeexplore.ieee.org/document/10642825/

[39] F. Rollo, C. V. Ilioudis, G. Zefi, A. Lotti, D. Tonelli, M. Zavagli, M. Constantini, D. Zonta, E. Tubaldi, P. Milillo, M. Macdonald, and C. Clemente,

"Micro-motion extraction from spotlight SAR using a modified backprojection approach," in *Microwave Remote Sensing: Data Processing and Applications III*, E. Santi, F. Bovenga, C. Notarnicola, and N. Pierdicca, Eds. SPIE, 11 2024, p. 12. [Online]. Available: https://www.spiedigitallibrary.org/conference-proceedings-of-spie/13195/3031678/Micro-motion-extraction-from-spotlight-SAR-using-a-modified-backprojection/10.1117/12.3031678.full

[40] A. Lotti, A. B. Vattulainen, C. Suppi, S. Diaz Riofrio, P. Milillo, E. Tubaldi, D. Zonta, and C. Clemente, "Feasibility of micro-motion from SAR imagery for vibration-based SHM," in *13th International Conference on Structural Health Monitoring of Intelligent Infrastructure SHMII-13*. SHMII, 2025, publisher: Verlag der Technischen Universität Graz.

[41] F. Biondi, P. Addabbo, C. Clemente, S. L. Ullo, and D. Orlando, "Monitoring of Critical Infrastructures by Micromotion Estimation: The Mosul Dam Destabilization," *IEEE Journal of Selected Topics in Applied Earth Observations and Remote Sensing*, vol. 13, pp. 6337–6351, 2020. [Online]. Available: https://ieeexplore.ieee.org/document/9224142/

[42] F. Biondi, P. Addabbo, S. L. Ullo, C. Clemente, and D. Orlando, "Perspectives on the Structural Health Monitoring of Bridges by Synthetic Aperture Radar," *Remote Sensing*, vol. 12, no. 23, p. 3852, Nov. 2020. [Online]. Available: https://www.mdpi.com/2072-4292/12/23/3852

[43] A. Focsa, A. Anghel, G. Nico, I. Maggio, M. Datcu, and M. Corvino, "Vibration-Induced Micro-Doppler Estimation in Spaceborne SAR Images Using Doppler Centroid Tracking Across Azimuth Sub-Apertures," in *2025 IEEE International Radar Conference (RADAR)*. IEEE, 5 2025, pp. 1–6. [Online]. Available: https://ieeexplore.ieee.org/document/11031947/

[44] A. B. Vattulainen, F. Rollo, A. Lotti, D. Tonelli, S. D. Riofrio, E. Tubaldi, D. Zonta, C. Ilioudis, P. Milillo, and C. Clemente, "Bridge Vibration Measurements from Very High-Resolution Spaceborne SAR," in *2024 IEEE SENSORS*. IEEE, 10 2024, pp. 1–4. [Online]. Available: https://ieeexplore.ieee.org/document/10785004/

[45] N. Earth Science Data Systems, "Synthetic Aperture Radar (SAR) | NASA Earthdata," https://www.earthdata.nasa.gov/learn/earth-observation-data-basics/sar, May 2021, publisher: Earth Science Data Systems, NASA.

[46] A. Moreira, P. Prats-Iraola, M. Younis, G. Krieger, I. Hajnsek, and K. P. Papathanassiou, "A tutorial on synthetic aperture radar," *IEEE Geoscience and Remote Sensing Magazine*, vol. 1, no. 1, pp. 6–43, 2013.

[47] R. Raney, "Synthetic Aperture Imaging Radar and Moving Targets," *IEEE Transactions on Aerospace and Electronic Systems*, vol. AES-7, no. 3, pp. 499–505, 5 1971. [Online]. Available: http://ieeexplore.ieee.org/document/4103740/

[48] C. Shannon, "Communication in the Presence of Noise," *Proceedings of the IRE*, vol. 37, no. 1, pp. 10–21, 1 1949. [Online]. Available: http://ieeexplore.ieee.org/document/1697831/

[49] "Glasgow, Upper Harbour, South Portland Street Suspension Footbridge | Canmore," 2025, accessed: 2025. [Online]. Available: https://canmore.org.uk/site/44349/glasgow-upper-harbour-south-portland-street-suspension-footbridge?utm_source=chatgpt.com

[50] P. Piezotronics, "Model 393B12," 2025, accessed: 2025. [Online]. Available: https://www.pcb.com/products?m=393b12

[51] R. Brincker and C. E. Ventura, *Introduction to Operational Modal Analysis*. Wiley, Aug. 2015. [Online]. Available: https://onlinelibrary.wiley.com/doi/book/10.1002/9781118535141

[52] D. P. Pasca, A. Aloisio, M. M. Rosso, and S. Sotiropoulos, "PyOMA and PyOMA_gui: A Python module and software for Operational Modal Analysis," *SoftwareX*, vol. 20, p. 101216, Dec. 2022. [Online]. Available: https://linkinghub.elsevier.com/retrieve/pii/S2352711022001340

[53] U. Space, "Umbra Synthetic Aperture Radar (SAR) Open Data - Registry of Open Data on AWS," accessed: 2025. [Online]. Available: https://registry.opendata.aws/umbra-open-data/

[54] SatNOGS, "SatNOGS DB - Umbra 02," accessed: 2025. [Online]. Available: https://db.satnogs.org/satellite/TPDX-4064-2548-6167-6896

[55] Capella Space, "What are Capella's collection types?" accessed: 2025. [Online]. Available: https://support.capellaspace.com/what-are-capellas-collection-types

[56] R. Schmidt, "Multiple emitter location and signal parameter estimation," *IEEE Transactions on Antennas and Propagation*, vol. 34, no. 3, pp. 276–280, Mar. 1986, publisher: Institute of Electrical and Electronics Engineers (IEEE). [Online]. Available: https://ieeexplore.ieee.org/document/1143830/

[57] R. Roy, A. Paulraj, and T. Kailath, "Estimation Of Signal Parameters Via Rotational Invariance Techniques - ESPRIT," in *SPIE Proceedings*, J. M. Speiser, Ed., vol. 0696, SPIE. San Diego: SPIE, Apr. 1986, p. 94, iSSN: 0277-786X. [Online]. Available: http://proceedings.spiedigitallibrary.org/proceeding.aspx?doi=10.1117/12.936880

Part III

Summary, conclusions and future perspectives

8. Summary and discussion of research results

At the beginning of this thesis, the two research questions were formulated, regarding the enhancement of InSAR and the feasibility of MDSAR for structural monitoring applications. To answer these questions, three distinct research works were carried out, some of which have been published in international peer-reviewed journals. Detailed analyses and discussions of the results are provided in the corresponding chapters (Chapters 5–7). Building on those discussions, this chapter presents a global synthesis of the research outcomes, highlighting the main achievements of the thesis and their implications for SAR-based bridge monitoring.

For reference, the main achievements associated with each research question are summarised in Table 8.1. The table summarises the research questions, the experimental validation strategies, principal limitations, and future research directions for both ST-InSAR and MDSAR approaches.

Table 8.1: Comparison between the research questions addressed in this thesis and their main outcomes.

Aspect	**Question 1 (ST-InSAR)**	**Question 2 (MDSAR)**
Research Question	Is it possible to overcome InSAR current limitations for bridge monitoring?	Is MDSAR suitable for vibration monitoring?
Thesis Chapter	3	4–5
Experimental validation	Pre-stressed reinforced concrete cantilever bridge	Shaker tests and steel suspension bridge
Answer	Yes, by integrating a more comprehensive model that accounts for the spatial correlation of PSs displacement	Yes, for measuring vibrations with an accuracy of 1 $\mathrm{mm/s}$ and information on modal parameters with limitations
Main limitations	Model assumptions, scatterers visibility	SAR sensor features, tracking algorithm
Future developments	Model non-thermal effects, Bayesian parameters estimation	Exploit phase content, physics-based structural models

8.1 Research question 1: Is it possible to overcome InSAR current limitations for bridge monitoring?

The first research question examined the limitations of conventional persistent scatterer interferometry for bridge monitoring. Conventional PSI estimates time series of LOS displacement by analysing the phase content of persistent scatterers across multiple SAR acquisitions. This approach relies on two fundamental assumptions:

- Displacements along the LOS between consecutive acquisitions are relatively small to avoid phase ambiguity (i.e. below $\lambda/4$).
- The LOS displacement model is primarily correlated with time and air temperature.

However, these assumptions are frequently violated when this approach is applied to bridge monitoring. Bridges may experience displacements exceeding the ambiguity limit (e.g., $\lambda/4 \approx 8\ \mathrm{mm}$ for X-band sensors), and their deformation behaviour is often governed by the structural temperature rather than by ambient air temperature alone. Temperature gradients within the structure can induce thermal deflections that are not adequately captured by simple linear models.

8.1.1 Answer to question 1

This thesis demonstrates that the limitations of InSAR for bridge monitoring can be overcome. The proposed spatio-temporal InSAR framework relaxes the fundamental assumptions of conventional PSI by incorporating a structural displacement model and by jointly estimating the displacements of spatially correlated scatterers from the interferometric phase time series. This strategy significantly improves the robustness of phase unwrapping and mitigates coherence loss and measurement accuracy issues that standard PSI fails to address.

The proposed ST-InSAR method was tested and validated on the Colle Isarco viaduct, where its performance was compared with PSI using independent topographic benchmarks. The viaduct was selected because it exhibits large deflections that violate the fundamental PSI assumptions. As a consequence, PSI exhibits very poor temporal coherence (as low as 0.08) and weak, or negligible, correlations with topographic measurements (0.08 and 0.24). The RMSE error ranges from 6.65 to $7.85\ \mathrm{mm}$.

In contrast, ST-InSAR can retrieve temporal coherence values of up to 0.95 at the same locations, along with high correlations ranging from 0.78 to 0.81.

Regarding the measurement error, experimental results show that ST-InSAR achieves displacement accuracy on the order of $2\ \mathrm{mm}$ for all scattering points on the viaduct. This level of accuracy is comparable to that of ground-based topographic surveys, provided that suitable conditions are met (e.g., clear visibility of the structure, a sufficient number of acquisitions and an appropriate displacement model). Under these conditions, ST-InSAR can be considered a valid alternative to traditional topographic surveying for long-term monitoring of bridge displacements.

Moreover, the proposed ST-InSAR approach uses a structural displacement model that depends not only on air temperature, as in conventional PSI, but also on the thermal gradient across the deck. This last quantity is unknown and is estimated as an additional parameter for each acquisition within the interferometric stack. Results presented in Chapter 5 show that the temperature gradient estimated using ST-InSAR is consistent with the actual gradient, with a deviation of less than $1\ ^{\circ}\mathrm{C}$. This suggests that, in principle, ST-InSAR could also serve as a tool for assessing the thermal field of bridges, possibly decreasing the need for expensive contact-based temperature sensors.

Overall, the results of this thesis demonstrate that ST-InSAR yields a robust and accurate framework for long-term bridge displacement monitoring, extending the application of spaceborne InSAR beyond the limitations of conventional PSI.

One limitation relative to PSI is that the bridge structural components must be clearly visible and identifiable in the SAR images. This is essential to link scatterers to the corresponding elements in the model accurately. Additionally, if a deformation effect is not represented in the model, its contribution to the overall displacement can't be estimated using the framework. This highlights the need for a sufficiently detailed structural model.

8.1.2 Evaluation of ST-InSAR

Based on the experimental evidence presented and discussed in Chapter 5, the main metrological characteristics of the proposed ST-InSAR method are identified and discussed in the following. These provide a quantitative assessment of ST-InSAR performance for bridge monitoring.

Quantity of Interest

ST-InSAR measures the LOS displacement time series of stable scatterers (e.g., showing high and consistent reflectivity throughout the interferometric stack) relative to the reference acquisition.

Direction of Measurement

Displacements are measured exclusively along the sensor line of sight.

Accuracy

The accuracy of ST-InSAR depends on a number of factors, including acquisition mode, sensor frequency band, number of acquisitions, and density of persistent scatterers. For X-band stripmap data, the results presented in this thesis indicate an accuracy on the order of $2\ \mathrm{mm}$ along the LOS.

Sampling frequency

The sampling frequency depends on the satellite revisit time and ranges from 16 days to approximately 1 day (or even less), depending on the mission:

- Sentinel-1: 12 days.
- TerraSAR-X: 11 days.
- SAOCOM: 16 days.
- Umbra and Capella Space: down to 1 per day or even less, depending on tasking availability.

By combining multiple orbits and/or missions, it is in principle possible to further reduce the revisit time, although the data require further processing.

SAR acquisition compatibility

ST-InSAR can be effectively applied to all principal SAR acquisition modes, including:

- *ScanSAR*: wide coverage, with a swath size of approximately 100–$200\ \mathrm{km}$, but lower spatial resolution (10–$20\ \mathrm{m}$ pixel size).
- *Stripmap*: moderate coverage, with a swath size of approximately $40\ \mathrm{km}$, and a spatial resolution of 1–$3\ \mathrm{m}$.
- *Stripmap*: limited coverage, swath size of 5–$10\ \mathrm{km}$, but finest spatial resolution due to the longer observation time, reaching sub-metre resolution.

Temporal coverage

Various SAR missions have been operative for more than a decade, allowing the monitoring of past deformation states depending on the mission launch date:

- Sentinel-1: from 2014.
- COSMO-Skymed: from 2007, now continued with the COSMO-SkyMed Second Generation.
- PAZ: from 2018.
- Capella Space: from 2018.

To ensure satisfactory results from the ST-InSAR analysis, it is preferable to have a large number of acquisitions evenly spaced in time (densely sampled). Avoiding temporal gaps is important. While an exact minimum number of images is not defined in this thesis, in theory, the dataset should include at least as many acquisitions as required to estimate the phase model parameters unambiguously. In practice, a significantly higher number is expected, typically on the order of 15–20 acquisitions or more [1, 2].

Summary table of metrological characteristics of ST-InSAR

Table 8.2 summarises the main metrological characteristics of ST-InSAR measurements discussed in the previous sections.

Table 8.2: Main metrological characteristics of ST-InSAR measurements.

ST-InSAR features			
Quantity of interest		Displacement	
Measurement direction		LOS	
Accuracy		2 mm	
SAR acquisition mode	**ScanSAR**	**Stripmap**	**Spotlight**
Sampling period	12–16 days	12–16 days	up to 1 day
Spatial resolution	5–20 m	1–3 m	0.2–0.6 m
Image swath size	up to 200 km	up to 40 km	up to 10 km
Past data availability	2007–2014	2007–2014	not available

8.2 Research question 2: Can MDSAR be used for vibration-based monitoring of bridges?

The second question addresses the feasibility of micro-Doppler SAR for vibration-based monitoring of bridges. More specifically, this second part of the work focuses on demonstrating whether MDSAR can measure structural vibrations with sufficient accuracy and extract information about dynamic features of bridges – in terms of modal parameters – from spaceborne observations.

Although in principle, MDSAR could represent a valid solution for remote vibrational monitoring of civil infrastructure, the existing literature still presents several limitations. Most previous studies, as mentioned in Section 3.7, focused on controlled experiments or on simplified vibrating targets, which do not fully replicate bridge operational conditions. Moreover, these studies mainly assessed MDSAR performance in the frequency domain, without validating the reconstructed vibration time histories against synchronous ground-truth measurements. As a result, the actual accuracy and reliability of MDSAR for real-world bridge monitoring remain largely unquantified.

Additionally, only a limited number of case studies on full-scale civil structures have been reported, and none have provided systematic validation of MDSAR vibration measurements in the time domain.

These gaps motivate the experimental and methodological investigations presented in this thesis.

8.2.1 Answer to question 2

The results of this thesis indicate that MDSAR can detect structural vibrations from spaceborne SAR data. However, there are important limitations that constrain its use for VBSHM of bridges.

Experimental evidence from both controlled shaker tests on isolated corner reflectors and from a real bridge case study demonstrates that structural vibrations are measurable using MDSAR. The discussion of the overall performance of the technique, however, is limited to the specific experimental conditions investigated in this work. The following vibration characteristics were tested:

- *Controlled shaker tests*: frequencies between 1–4 Hz and sub-millimetric LOS displacement amplitudes.
- *Bridge tests*: dominant frequencies between 1.5–2 Hz and peak LOS velocities ranging from 1 $\mathrm{mm/s}$ to 2 $\mathrm{mm/s}$.

Nevertheless, the observations that follow are likely representative of similar

structures.

A first important finding is that the measured LOS velocity time series exhibit significant measurement noise. For vibration amplitudes comparable to those experienced by bridges in operational conditions, the error in the estimated LOS velocity was found to be on the order of $1\ \mathrm{mm/s}$. This level of error is comparable to the magnitude of the true vibrations and, therefore, results in noisy time-domain signals. Percentage RMSE values ranged 38–69% for low-amplitude shaker tests and 40–95% for the bridge case, relative to the true peak velocity. Consequently, MDSAR is not suited for precise velocity tracking. Whilst the method tends to overestimate peak velocity amplitudes, consistent vibrational patterns (relative to the ground truth) were identified, with time-domain correlation values up to 0.66 for the bridge case.

Frequency-domain analysis produced more reliable results. In all investigated cases, both for the shaker and bridge experiments, the dominant vibrational frequencies extracted from MDSAR closely matched those measured by ground truth sensors. The identified frequencies consistently fell within the frequency resolution determined by the SAR acquisition time, which achieved $0.07\ \mathrm{Hz}$ for the shaker and $0.06\ \mathrm{Hz}$ for the bridge. Spectral correlations yielded better results than those of time-domain, reaching values of 0.75 for small-amplitude shaker tests and 0.88 for the bridge. Furthermore, spectral correlation was seen to improve with increasing vibrational amplitude.

This evidence indicates that MDSAR is more suitable for detecting dominant vibrational frequencies than accurately reconstructing vibrational amplitudes. However, frequency identification is constrained by the acquisition time of spaceborne SAR sensors. Since frequency resolution is inversely proportional to the acquisition duration, currently available spotlight acquisitions – typically limited to acquisition times of up to $30\ \mathrm{s}$ – offer a resolution of approximately $0.03\ \mathrm{Hz}$. which, with current technology, is expected to be limited to a maximum of $30\ \mathrm{s}$ for spotlight modes. Moreover, MDSAR captures the dominant vibration frequency within the SAR acquisition window, which does not necessarily correspond to the true natural frequency of the structure.

With respect to modal parameters, it is expected that only limited modal information – such as qualitative indications of mode shape components – may be identified from MDSAR data. However, noisy, short-time histories from MDSAR undermine the possibility of precise modal extraction of damping ratios and detailed mode shapes. Robust modal extraction requires the development of new processing techniques specifically suited to MDSAR.

An additional important observation is that the findings of this thesis suggest that the performance limitations observed for the employed MDSAR ap-

proach, based on sub-pixel offset tracking, are not primarily due to current signal processing techniques but rather to SAR system parameters, including wavelength, acquisition duration, and scene clutter. This reflects the fact that existing SAR missions were not designed with MDSAR applications in mind.

Finally, it is reminded that this study relied exclusively on reflectivity-based MDSAR. It is expected that approaches that exploit phase information – potentially operating directly on raw SAR data (e.g., CPHD products) – could offer greater sensitivity to small-amplitude vibrations. Additionally, as demonstrated in persistent scatterer interferometry, integrating structural physical models into the processing pipeline is another approach to enhance vibration and modal parameter extraction from MDSAR data.

8.2.2 Evaluation of MDSAR

This section reports the metrological characteristics of the MDSAR technique for bridge monitoring, based on the experimental results and discussions presented in Chapters 6 and 7.

Quantity of Interest

MDSAR measures the time history of the LOS velocity of scattering points on the structure during the SAR acquisition. The measurement is limited to the observation time of a single SAR acquisition.

Indirectly, MDSAR enables estimation of the vibrational spectrum of the structure within the acquisition window. In principle, this information can be exploited for modal analysis, including the identification of dominant frequencies and qualitative indications of mode shape components.

Direction of Measurement

Velocity is measured exclusively along the sensor line of sight. As MDSAR does not provide sensitivity to motions orthogonal to the LOS (i.e., azimuth direction), the full three-dimensional velocity cannot be reconstructed from a single acquisition geometry.

Accuracy in the time domain

Experimental evidence, from both controlled laboratory experiments and full-scale bridge monitoring, suggests that the velocity measurement uncertainty is on the order of $1\ \mathrm{mm/s}$ for bridge-related vibrations. Measurement accuracy results from the sub-aperture segmentation process and the SAR data SNR.

Accuracy in the frequency domain

When the objective of the monitoring is to identify dominant vibration frequencies, the achievable frequency resolution depends on the SAR acquisition

duration. The uncertainty in frequency estimation Δf is inversely proportional to the total acquisition time t_{a}.

$$\Delta f = \frac{1}{t_{\mathrm{a}}} \tag{8.1}$$

With current spaceborne SAR technology, the maximum achievable acquisition duration is approximately 30 s, corresponding to a frequency resolution of approximately 0.03 Hz. Beyond the resolution, the total acquisition time t_{a} also governs the *theoretical* limits of the detectable frequency range. The *minimum* detectable frequency is determined by the frequency resolution itself:

$$f_{\min} = \frac{1}{t_{\mathrm{a}}} \tag{8.2}$$

since the acquisition duration must cover at least one complete oscillation cycle of the target of interest. The *maximum* detectable frequency is governed by the Nyquist criterion applied to the sub-aperture time series:

$$f_{\max} = \frac{f_{s,\max}}{2} \tag{8.3}$$

where $f_{s,\max}$ is the maximum achievable sampling frequency of the sub-aperture series and is discussed below.

Sampling frequency

The effective sampling frequency of the MDSAR velocity time series depends on the temporal spacing Δt between consecutive sub-aperture centres and is a function of the sub-aperture duration t_{sap} and the overlap ratio Ω. By substituting in Eq. 7.5 into Eq. 7.6 one obtains:

$$\Delta t = t_{\text{sap}} \cdot (1 - \Omega) \tag{8.4}$$

The maximum sampling frequency is therefore:

$$f_{s,\max} = \frac{1}{\Delta t_{\min}} = \frac{1}{t_{\text{sap}} \cdot (1 - \Omega)} \tag{8.5}$$

Increasing the overlap ratio Ω reduces Δt and therefore raises $f_{s,\max}$, while preserving the azimuth resolution of each sub-aperture (since t_{sap} is unchanged). In principle, Ω can be increased arbitrarily close to 100%, at the cost of greater computational load. In practice, overlap ratios between 23% and 71% were used in this work, yielding values of $f_{s,\max}$ just above the dominant natural frequencies of the case studies investigated here.

SAR acquisition compatibility

MDSAR can be applied exclusively to spotlight SAR acquisitions, which provide longer observation times and, therefore, enable finer frequency resolution. Spotlight images typically cover swath widths ranging from 5 to 10 km, with sub-metre spatial resolution in both range and azimuth.

SAR revisit time

Spotlight acquisitions are generally performed via tasking, resulting in flexible – but not periodic – revisit times. The achievable revisit time, therefore, depends on the tasking availability rather than on fixed orbital repeat cycles.

Temporal coverage

Although several SAR missions have been operational for more than a decade, spotlight acquisitions are significantly less frequent than stripmap or ScanSAR. Hence, the availability of historical spotlight data is limited, and MDSAR analyses are typically feasible only for dedicated tasking acquisitions.

Summary table of metrological characteristics of MDSAR

Table 8.3 summarises the main metrological characteristics of MDSAR measurements discussed in the previous sections.

Table 8.3: Main metrological characteristics of MDSAR measurements.

MDSAR features	
Quantity of interest	Velocity
Measurement direction	LOS
Accuracy	1 $\mathrm{mm/s}$
SAR acquisition mode	**Spotlight**
Sampling period	Function of ξ and Ω
Spatial resolution	0.1–0.6 m
Image swath size	up to 10 km
Past data availability	not available

8.3 Are spaceborne SAR techniques ready to replace contact-based SHM?

Based on the results presented in this thesis, spaceborne SAR methods are not yet capable of fully replacing conventional contact-based SHM systems. However, this answer depends strongly on the scope of the monitoring: whether

the objective is long-term displacement monitoring or vibration-based monitoring.

8.3.1 SAR and long-term displacement monitoring

Under optimal conditions, the proposed ST-InSAR framework has demonstrated accuracy comparable to that of traditional topographic surveys for long-term displacement monitoring. In this context, spaceborne SAR methods can effectively substitute topographic survey-based monitoring, offering wider coverage, historical data, and lower operating costs.

The main drawback, however, is that interferometric SAR measures displacement only along the satellite's line of sight. This implies that, to recover the three-dimensional structural response fully, some simplifying assumptions about the bridge behaviour must be introduced. Although in principle ascending and descending orbit data can be combined to retrieve additional displacement components, this approach poses practical difficulties. Dual-orbit coverage is not always available, specifically in areas with complex orography, and temporal asynchrony between acquisitions may compromise the reconstructed motion. Furthermore, identical structural targets are not always visible in both geometries, thereby limiting the robustness of orbit-merging strategies.

8.3.2 SAR and vibration-based monitoring

Measuring the time history of vibration

MDSAR already allows measurement of the time history of the radial velocity within the SAR acquisition window. It is preferable, though, that the velocity of vibration is sufficiently greater than the accuracy of the technique, which is on the order of $1\ \mathrm{mm/s}$.

Extract natural frequencies

In principle, the dominant frequency of the vibration can be extracted using MDSAR. Whether the dominant frequency of the SAR acquisition window coincides with the natural frequency of the structure is the same issue as measuring with contact-type sensors over a short period of time. The main drawback relative to contact-type technologies is that contact SHM systems are permanently installed and can operate continuously, whereas MDSAR depends on tasking availability and, for now, can achieve only up to $30\ \mathrm{s}$ of acquisition. For now, until this limitation is overcome, MDSAR cannot replace contact-type sensors for detecting natural frequencies.

Reconstruct mode shapes

The main limitations of MDSAR stem not only from the processing algorithm employed but also from SAR system parameters, including wavelength, acquisition duration, and observation geometry. As a result, robust modal identification from MDSAR data remains an open problem, primarily due to the available technology and requiring technological developments beyond those currently available. For now, only limited information about the mode shapes could be retrieved, such as the sign of the mode shape components. It is expected that using more advanced SAR sensor technologies will leave plenty of room for improvement. For example, future missions that support higher central frequencies or longer acquisition times (or combined acquisitions)

From a practical perspective, the results of this thesis suggest that, with current technology, SAR should be considered as a complementary tool rather than as a replacement for contact-based SHM. If integrated with in-situ measurements, SAR data could reduce the need for extensive on-site instrumentation and enhance support decision-making.

Bibliography

[1] F. Raspini, F. Caleca, M. Del Soldato, D. Festa, P. Confuorto, and S. Bianchini, "Review of satellite radar interferometry for subsidence analysis," *Earth-Science Reviews*, vol. 235, p. 104239, 2022. [Online]. Available: https://www.sciencedirect.com/science/article/pii/S0012825222003233

[2] M. Crosetto, O. Monserrat, M. Cuevas-González, N. Devanthéry, and B. Crippa, "Persistent Scatterer Interferometry: A review," *ISPRS Journal of Photogrammetry and Remote Sensing*, vol. 115, pp. 78–89, May 2016. [Online]. Available: https://www.sciencedirect.com/science/article/pii/S0924271615002415

9. Conclusions and Future Works

The main motivation for this thesis is the growing global need for scalable, cost-effective, and non-invasive monitoring systems to ensure the safety of civil infrastructure. Spaceborne SAR is a valid solution to such a problem, providing an entirely remote alternative. However, SAR methods currently face important limitations that hinder their application to structural health monitoring of bridges. To tackle these limitations, this thesis developed and validated novel frameworks for long-term and vibrational monitoring using SAR imagery and conducted experimental research under both controlled and real-world conditions.

With reference to the research questions formulated at the beginning of the thesis, the conclusions are as follows:

1. Can InSAR be enhanced for bridge monitoring applications? In particular, is it possible to overcome the limitations that currently restrict its reliability and applicability in bridge structural health monitoring?

- This thesis demonstrated that spatio-temporal InSAR (ST-InSAR) can effectively overcome the limitations of persistent scatterer interferometry (PSI) for bridge monitoring, namely, ambiguity due to large deformations and complex thermal behaviour that is not directly correlated with air temperature.
- This can be achieved via integrating structural knowledge into the processing framework.
- ST-InSAR allows for relaxing the restrictive displacement assumptions of conventional PSI, while enabling accurate displacement monitoring even in scenarios where PSI fails.
- Under optimal conditions, ST-InSAR can correctly measure the deflection of the bridge along the LOS with an accuracy on the order of $2\,\mathrm{mm}$, which is comparable to traditional topographic surveying.

2. Can MDSAR be employed for VBSHM of bridges? Specifically, can satellite SAR sensors measure structural vibrations with sufficient accuracy, and can dynamic features, such as modal parameters, be extracted from spaceborne observations?

- It was proved that Micro-Doppler SAR (MDSAR) can measure bridge vibrations from spaceborne SAR imagery.
- MDSAR is equivalent to a noisy sensor, constrained by short acquisition

durations, currently up to approximately 30 s with available satellite SAR technology.

- MDSAR can measure the velocity time histories of the bridge along the LOS with an accuracy of of $1\ \mathrm{mm/s}$.
- MDSAR can identify the dominant vibrational frequencies with an accuracy that depends on the achievable frequency resolution, which is limited by the SAR acquisition duration. With current technology, the finest achievable frequency resolution is approximately 0.03 Hz, corresponding to a 30 s acquisition time.
- Estimating damping ratios and detailed mode shapes is not easily achievable with current MDSAR technology and conventional modal extractions. It is expected that limited information on mode shapes could be retrieved.

9.1 Open challenges and future directions

9.1.1 ST-InSAR

ST-InSAR shows significant potential when compared to PSI; however, it requires a physics-based structural model capable of capturing all relevant deformation mechanisms acting on the structure of interest. Any deformation mechanism that is not explicitly modelled may not be estimated from the displacement extraction process. A further constraint is that ST-InSAR requires structural components to be clearly visible in SAR imagery to be correctly associated with the elements of the structural model. A limited number of PSs is expected to reduce the method performance.

Future research should expand structural models to account for non-thermal deformation mechanisms and adopt probabilistic or Bayesian frameworks for parameter estimation and uncertainty propagation.

9.1.2 MDSAR

The evidence presented in this thesis suggests that the main limitations of MDSAR are given by the currently available SAR system features, such as wavelength, acquisition duration, and observation geometry: existing spaceborne SAR missions were not designed with vibration monitoring or modal extraction as primary objectives.

Two main development paths can be identified: advancing sensor technology and refining processing methodologies.

Significant improvements could be achieved, for example, by mounting

future missions with SAR sensors with shorter wavelengths (e.g., Ku-band), longer acquisition times and greater flexibility in tasking and acquisition geometry. Until such technology becomes available, subsequent research should investigate approaches that exploit phase information rather than reflectivity alone, potentially operating directly on raw SAR data products. Physics-based vibration models and model-driven processing strategies may help stabilise time-domain estimates and improve the extraction of modal parameters.

A. Appendix

A.1 Scopus search and queries

Bibliometric data were retrieved from the Scopus database in November 2025. The search was conducted using the `TITLE-ABS-KEY` fields and was limited to: journal articles (`DOCTYPE = ar`) written in English and published between 2005 and 2022.

Query 1: InSAR-based bridge displacement monitoring

```
( TITLE-ABS-KEY ( insar OR "interferometric sar" OR
"interferometric synthetic aperture radar" )
AND TITLE-ABS-KEY ( bridge OR viaduct )
AND TITLE-ABS-KEY ( monitoring OR displacement ) )
AND PUBYEAR > 2005 AND PUBYEAR < 2023
AND ( LIMIT-TO ( DOCTYPE , "ar" ) )
AND ( LIMIT-TO ( LANGUAGE , "English" ) )
```

Query 2: SAR micro-Doppler and vibration monitoring of bridges

```
( TITLE-ABS-KEY ( ( "micro-Doppler" OR
"micro-motion" ) AND "SAR" )
AND TITLE-ABS-KEY ( bridge OR viaduct )
AND TITLE-ABS-KEY ( monitoring OR vibrations ) )
AND PUBYEAR > 2005 AND PUBYEAR < 2023
AND ( LIMIT-TO ( DOCTYPE , "ar" ) )
AND ( LIMIT-TO ( LANGUAGE , "English" ) )
```

A.2 Publications list

As a result of the work conducted during my PhD program, the following research products have been produced from the following research projects: the ReLUIS Interuniversity Consortium under the agreement *DPC-ReLUIS 2024-2026 WP 6 "Monitoring and satellite data"*, funded by the italian Civil Protection Department, and the European Space Agency (ESA) under the project *Bridge Monitoring Based on Single Pass SAR Images*. From this research activity the following research products have been produced.

Journal Papers and Manuscripts

The following are the main journal papers produced. Papers J.1, J.2 and J.3 have been published in the journals *Structural Health Monitoring* (SAGE), *IEEE Access* (IEEE) and *Structural Control and Health Monitoring* (John Wiley & Sons), respectively.

(J.1) **Lotti, A.**, Zorzi, S., Tubaldi, E., Rocca, A., Perissin, D., Zonta, D. (2026). Spatio-temporal InSAR for bridge monitoring: integrating physics-based models with persistent scatterer interferometry, *Structural Health Monitoring*, https://doi.org/10.1177/14759217261453023.

(J.2) Vattulainen, A.B., **Lotti, A.**, Diaz Riofrio, S., Suppi, C., Tubaldi, E., Zonta, D., Milillo, P., Clemente C. (2026). Assessment of spaceborne SAR micro-motion measurement for vibration-based SHM, *IEEE Access*, Volume: 14, https://doi.org/10.1109/ACCESS.2026.3652346.

(J.3) **Lotti, A.**, Vattulainen, A.B., Diaz Riofrio, S., Suppi, C., Tubaldi, E., Zonta, D., Milillo, P., Clemente C. (2026). Monitoring bridge vibrations via spaceborne SAR micro-Doppler, *Structural Control and Health Monitoring*, https://doi.org/10.1155/stc/3858095.

In addition to these, during my PhD period, I have been working on a cross-disciplinary project completed EU-funded project ERIES-FLEJOI (Flexible joints for seismic-resilient design of masonry-infilled RC frames) led by the University of Strathclyde. From this project two Journal papers were produced, one published and one under review:

(J.4) Manojlovski F, Tubaldi E, Sheshov V, Rakicevic Z, Bogdanovic A, Bojadjieva J, Shoklarovski A, Poposka A, Ivanovski D, Kitanovski T, Markovski I, Filipovski D, Naumovski N, Turchetti F, Marinković M, Bošković M, Butenweg C, Gams M, Krtinić N, Freddi F, Pieroni L, Losanno D,

Parisi F, Dhir P, Pantó B, Ahmadi H, Patel J, Schroeder M, Meyer UJ, Rosen B, **Lotti A.** (2025). Flexible joints for seismic-resilient design of masonry-infilled RC frames, *Nature Scientific Data*, 19;12(1):1266, https://doi.org/10.1038/s41597-025-05515-6.

(J.5) Tubaldi, E., Marinković, M., **Lotti, A.**, Galano, S., Freddi, F., Losanno, D., Ahmadi, H., Gams, M.,Krtinić, N., Bošković, M.,Butenweg, C., Dhir, P.K., Manojlovski, F., Bogdanovic, A., Rakicevic, Z., Sheshov, V., Bojadzieva J. (2026). Shaking Table Testing of Masonry-Infilled RC Frames with Rubber Joints, *Earthquake Engineering and Structural Dynamics*, (Under review).

Conference papers

The following are the main conference papers produced.

(C.1) **Lotti, A.**, Tonelli, D., Zorzi, S., Zonta, D., Tubaldi, E. (2023). Pre-Posterior Effectiveness of Modal Extraction Techniques for Vibrational Tests Design, *In Life-Cycle of Structures and Infrastructure Systems, CRC Press*, https://doi.org/10.1201/9781003323020-49

(C.2) Valentini, A., Tonelli, D., Rocca, A., **Lotti, A.**, Zorzi, S., Zonta, D. (2023). Satellite InSAR technology for displacements monitoring of bridges: a comparison with onsite topographic measurements and uncertainty quantification, *In Proceedings of the 14th International Workshop on Structural Health Monitoring, Destech Publications*, https://doi.org/10.12783/shm2023/37057.

(C.3) Tonelli, D., Valentini, A., Rocca, A., Zorzi, S., **Lotti, A.**, Zonta, D. (2023). Uncertainty Quantification of Satellite InSAR-monitoring of Bridges: A Case Study, *ce papers 2023, 6 (5), 900–906*, https://doi.org/10.1002/cepa.1991.

(C.4) **Lotti, A.**, Zorzi, S., Tonelli, D., Tubaldi, E., Zonta, D. (2024). Development of a Bayesian Framework for Kinematic Data Fusion, *Proceedings of the 10th European Workshop on Structural Health Monitoring (EWSHM 2024)*, e-Journal of Nondestructive Testing Vol. 29(7). https://doi.org/10.58286/29643.

(C.5) **Lotti A.**, Tonelli D., Tubaldi E., Zorzi S., Zonta D. (2024). Pre-posterior Approach for Designing Forced Vibration Tests in Structural Health Monitoring. *On-line proceeding of the 18th World Conference on Earthquake*

Engineering (WCEE2024), IAEE. International Association for Earthquake Engineering. E-ISSN 3006-5933, https://proceedings-wcee.org/view.html?id=22663.

(C.6) Vattulainen, A. B., Rollo, F., **Lotti, A.**, Tonelli, D., Riofrio, S. D., Tubaldi, E., Zonta, D., Ilioudis, C., Milillo, P., Clemente, C. (2024). Bridge Vibration Measurements from Very High-Resolution Spaceborne SAR, *In 2024 IEEE SENSORS*, IEEE: Kobe, Japan, 2024, pp 1–4, https://doi.org/10.1109/SENSORS60989.2024.10785004.

(C.7) **Lotti, A.**, Vattulainen, A. B., Suppi, C., Diaz Riofrio, S., Milillo, P., Tubaldi, E., Zonta, D., Clemente, C. (2025). Feasibility of Micro-Motion from SAR Imagery for Vibration-Based SHM, *The 13th edition of the International Conference on Structural Health Monitoring of Intelligent Infrastructure*, https://doi.org/10.3217/978-3-99161-057-1-142.

(C.8) Suppi, C., **Lotti, A.**, Vattulainen, A., Riofrio, S. D., Rollo, F., Ilioudis, C., Tonelli, D., Tubaldi, E., Clemente, C., Zonta, D., Milillo, P. (2025). Vibrational Monitoring of Isolated Targets Using Single-Pass SAR Images, *In Proceedings of the 15th International Workshop on Structural Health Monitoring*, Destech Publications, Inc., 2025. https://doi.org/10.12783/shm2025/37524.

(C.9) Clemente, C., Vattulainen, A. B., Rollo, F., **Lotti, A.**, Zonta, D., Milillo, P. (2025). Micro-Motion Extraction from Land and Maritime Targets with Spaceborne SAR Using Sub-Aperture Phase Analysis, *22nd European Radar Conference (EuRAD)*, https://doi.org/10.23919/EuRAD65285.2025.11234218.

(C.10) Lotti, A., Vattulainen, A., Riofrio, S. D., Suppi, C., Tonelli, D., Rollo, F., Ilioudis, C., Milillo, P., Tubaldi, E., Clemente, C., Zonta, D. (2025). Vibration-Based Structural Health Monitoring from Single-Pass SAR Images, *In Experimental Vibration Analysis for Civil Engineering Structures*, Lecture Notes in Civil Engineering, Springer Nature Switzerland: Cham, 2025, Vol. 674, pp 402–411, https://doi.org/10.1007/978-3-031-96110-6_38.

During my Ph.D. program, I also participated in the writing of the following conference papers, contributing only to a limited extent.

(C.11) Zorzi, S., Tonelli D., **Lotti A.**, Broccardo M., Zonta D. (2023). Closed form solution for SHM-based Bayesian reliability assessment, *Proceedings of the 14th International Workshop on Structural Health Monitor-*

ing 2023: Designing SHM for Sustainability, Maintainability, and Reliability, DES tech Publications, Inc. https://doi.org/10.12783/shm2023/37010.

(C.12) Zorzi, S., Rossi, F., Tonelli, D., **Lotti**, A., Zonta, D. (2023). Metrological validation of Non-Destructive Testing techniques for assessing the condition state of pre-stressing systems, *Proceedings of the 14th International Workshop on Structural Health Monitoring 2023: Designing SHM for Sustainability, Maintainability, and Reliability.* DES tech Publications, Inc. https://doi.org/10.12783/shm2023/37011.

(C.13) Zorzi S., Tonelli D., **Lotti A.**, Broccardo M., Zonta D. (2024). Bayesian Estimation of Structural Reliability Using SHM Observations and Linear Models, *On-line proceeding of the 18th World Conference on Earthquake Engineering (WCEE2024)*, IAEE. International Association for Earthquake Engineering. E-ISSN 3006-5933, https://proceedings-wcee.org/view.html?id=25392.

(C.14) Clemente, C., Tonelli, D., **Lotti, A.**, Rollo, F., Ilioudis, C., Riofrio, S. D., Biondi, F., Tubaldi, E., Macdonald, M., Zonta, D., Zavagli, M., Costantini, M., Minati, F., Vecchioli, F., Milillo, P., Zimmermanns, M., Imbembo, E., Corvino, M. M. (2024). On Micro-Motion Extraction from High Resolution X-Band SAR Products, *In IGARSS 2024 - 2024 IEEE International Geoscience and Remote Sensing Symposium*, IEEE: Athens, Greece, pp 1182–1186, https://doi.org/10.1109/IGARSS53475.2024.10642825.

(C.15) Rollo, F., Ilioudis, C. V., Zefi, G., **Lotti, A.**, Tonelli, D., Zavagli, M., Constantini, M., Zonta, D., Tubaldi, E., Milillo, P., Macdonald, M., Clemente, C. (2024). Micro-Motion Extraction from Spotlight SAR Using a Modified Backprojection Approach, *In Microwave Remote Sensing: Data Processing and Applications III*, SPIE: Edinburgh, United Kingdom, 2024, p 12. https://doi.org/10.1117/12.3031678.

(C.16) Tubaldi, E., Manojlovski, F., Bogdanovic, A., Rakicevic, Z., Bojadjieva, J., Sesov, V., Marinković, M., Bošković, M., Butenweg, C., Gams, M., Krtinić, N., Freddi, F., Losanno, D., Dhir, P., Ahmadi, H., **Lotti, A.** (2024). Shake Table Testing of Masonry-Infilled RC Frames with Flexible Joints for Seismic-Resilient Structural Performance, *In Engineering Research Infrastructures for European Synergies*, Lecture Notes in Civil Engineering, Springer Nature Switzerland: Cham, 2025, Vol. 718, pp 144–158. https://doi.org/10.1007/978-3-031-98893-6_15.

(C.17) Suppi, C., Girardi, C., **Lotti, A.**, Zonta, D., Prada, A. (2025). Statistical Models for Temperature Prediction in Civil Structures, *In Proceedings of the 15th International Workshop on Structural Health Monitoring*, Destech Publications, Inc., 2025, https://doi.org/10.12783/shm2025/37514.